Phenomena in the Solar Corona: characteristic structure and dynamic evolution

Caroline Elizabeth Alexander

A thesis submitted in partial fulfilment

of the requirements for the degree of

Doctor of Philosophy

Jeremiah Horrocks Institute for Astrophysics and Supercomputing

University of Central Lancashire

August 2012

Declaration

The work presented in this thesis was carried out in the Jeremiah Horrocks Institute for Astrophysics and Supercomputing, University of Central Lancashire.

I declare that while registered as a candidate for the research degree, I have not been a registered candidate or enrolled student for another award of the University or other academic or professional institution.

I declare that no material contained in the thesis has been used in any other submission for an academic award and is solely my own work.

Abstract

This thesis presents a study of multiple phenomena that exist within the solar corona. The structures explored in this work cover a range of sizes from a small-scale X-ray bright point (<10 Mm), to medium-scale coronal loops (10–100 Mm), and finally to a large-scale prominence (>100 Mm). Observational data and numerical simulations were utilised in order to investigate the structure and evolution of each type of feature.

A small-scale X-ray bright point (XBP) was investigated using complete Hinode observations in order to examine it over its entire lifetime (~12 hours). The XBP was found to be formed directly above an area of cancelling magnetic flux on the photosphere. A good correlation between the rate of X-ray emission and decrease in total magnetic flux was found. The magnetic fragments of the XBP were found to vary on very short timescales (minutes), however the global quasi-bipolar structure remained throughout the lifetime of the XBP. Electron density measurements were obtained using a line ratio of Fe XII and the average density was found to be $5\pm1\text{x}10^{9}\text{cm}^{-3}$ with the volumetric plasma filling factor calculated to have an average value of 0.04±15%. Emission measure loci plots were then used to infer a steady temperature of $\log T_e[K] \sim 6.1\pm0.1$. The calculated Fe XII Doppler shifts show velocity changes in and around the bright point of ±15 kms^{-1} which are observed to change on a timescale of less than 30 minutes.

The results indicate that higher cadence spectroscopic measurements are required if the velocity flows are to be related to corresponding changes in the magnetic field.

The next feature investigated was a 100 Mm multistranded coronal loop that was simulated in order to investigate how changing the various model parameters would affect the resulting differential emission measure (DEM) distributions and intensity values. Once the model was fully understood, it was used to test a DEM solver and quantify the 'goodness-of-fit' that could be achieved. This allowed the limitations of the DEM method to be understood. As the model parameter space was altered, a number of changes in the resulting synthetic DEMs were observed. In most cases these changes were subtle and could be explained by the changing physics of the system. The cooling simulation showed the most unique changes where the total energy of the system could be identified by examining the evolution of the intensity values and DEM shape. The iterative solver solution XRT_DEM_iterative2 did an excellent job of reconstructing the original model intensity values and DEM distributions in the majority of cases. The only instance where the solver did not do well was when the synthetic DEM was very narrow i.e., only covering a few temperature bins. This highlights the under-constrained problem of using DEM solvers and shows that this particular solver works best when the original DEM being reconstructed is smoother and more multithermal.

Finally, a large-scale prominence eruption was investigated using observations from two points of view. The structure and evolution of the prominence material and cavity were examined over the eruption process. Many possible initiation methods were investigated to see if the cause of the prominence eruption could be pinned down. It was found that the polar-crown cavity could be defined as a density depletion sitting above denser polar-crown filament plasma which has drained down from the cavity due to gravity. The eruption of the polar crown cavity as a solid body can be decomposed into two phases: a slow rise at a speed of 2 ± 0.2 km s^{-1} , and an acceleration phase at a mean speed of 15–25 ± 0.6 km s^{-1} . The initiation of the prominence was concluded to be caused by a combination of mass un-loading and a type of kink instability.

Contents

List of Tables

List of Figures

Acknowledgements

I have thoroughly enjoyed my time at UCLan- both the work side and the social side. I would like to thank all the people who have supported me during the course of my PhD. In no particular order I would like to thank:

- Robert Walsh my supervisor for his encouragement and enthusiasm. The other members of my supervisory team Silvia Dalla, Gordon and Barbara Bromage for their guidance and support.
- The rest of the UCLan solar group for their support, friendship and the interesting discussions over the years.
- I would like to thank my institution, the Jeremiah Horrocks Institute for Astrophysics and Supercomputing for the studentship award as well as the STFC for the 3.5 years of funding I had.
- All the staff and students at JHI who made me feel very welcome and made it a fun place to work.
- In particular, thanks to the amazing friends I've made at the JHI. Gareth, Nicky, and Mike in particular. You guys are awesome and I'm really going to miss you.
- My collaborators Giulio, Rhona, Mark, and Aveek for their help and expertise on various projects.
- Helen Mason and Dan Brown for agreeing to read this slightly long thesis.

- Special thanks to my Mum, Dad, and brother Douglas for being a never-ending source of encouragement and emotional support. I couldn’t have come this far without you all.

- Thanks also to my extended family and all my friends. It always felt like you guys were rooting for me and I thoroughly appreciate it.

Chapter 1

Introduction

This thesis presents results concerning the dynamics and evolution of various phenomena of the solar corona. The features analysed cover a range of sizes from small-scale (<10 Mm), to medium-scale (10–100 Mm), and finally to large-scale (>100 Mm). These structures take the form of observations of an X-ray bright point, modelling of multi-stranded coronal loops, and observations of a large prominence eruption. These three features are different in terms of their scale, origin, evolution and dynamics but they all form part of the corona - a highly complicated and interconnected region of the solar atmosphere. Similar use of satellite observations, data analysis techniques and evaluation methods were employed in each investigation which allowed a common thread to link the different features.

This chapter gives a general introduction to the Sun, particularly the corona, while more thorough introductory material is presented at the beginning of each of the main chapters.

1.1 The Sun

For the entire span of human history, mankind has been enraptured by the beauty and complexity of the Sun. It has played an important role in the myths and religion of many ancient civilisations, who viewed the Sun in awe. Today we know that the Sun is the same as the millions of stars seen in the night sky - a sphere of hot ionized gas powered by nuclear fusion that releases energy in the form of electromagnetic radiation. A slightly less romantic description but one that many scientists have spent their lives trying to understand further.

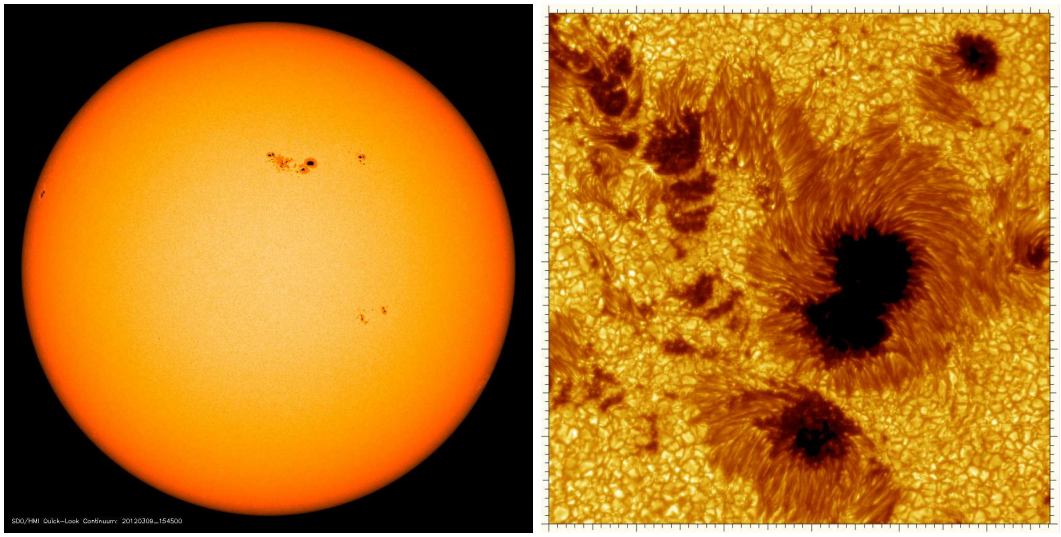

Figure 1.1: *Left:* Continuum image from the SDO/HMI instrument showing the surface of the Sun with few sunspot groups taken on the 9 March 2012. Image credit: NASA. *Right:* Small field-of-view image showing a different sunspot group on the 15 July 2002 by the Swedish 1-meter Solar Telescope. The distance between the tick marks is 1000 km.

The left panel of Figure 1.1 shows a familiar view of the Sun with a smooth yellow disc and a couple of dark sunspot groups. The right panel shows an image taken with the Swedish Solar Telescope of a close up of a similar sunspot group. To put these sunspots in perspective, their sizes are on a par with the size of the Earth. The granulation pattern seen in this image gives an indication that the surface of the Sun is not as quiet as it appears in the left-hand figure. The granulation is observational evidence of convective motions at work in the upper part of the solar interior, and the sunspots are evidence of

regions of intense magnetic field. This gives a glimpse at the complicated nature of the Sun which is explained in more detail in the rest of this chapter.

1.1.1 Overview

The Sun is a spectral class G2V star meaning that it is on the main sequence and has a surface temperature of around 5778 K. These features make the Sun an 'average' star which is about half-way through its main sequence stage. The Sun was formed around 4.7 billion years ago and has an average diameter of 1.392 x 10^6 km making it 109 times wider than the Earth. The Sun-Earth distance defines the unit of AU (astronomical unit) and has a mean value of 149,600,600 km.

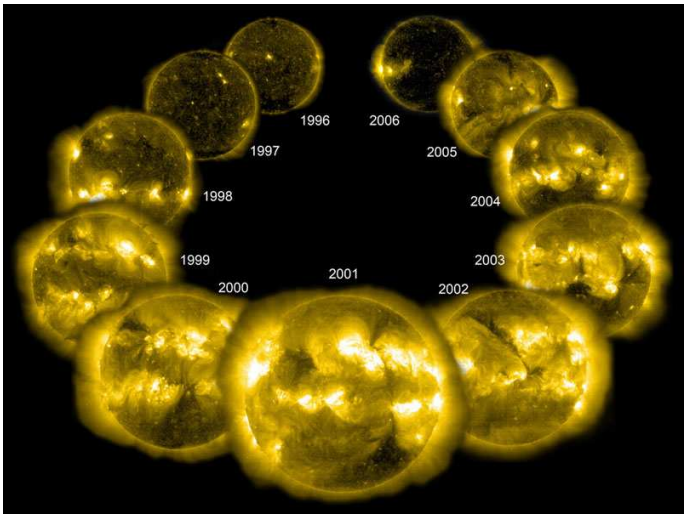

Figure 1.2: Series of full-disc images taken with the SoHO/EIT instrument in the 284Å waveband. As time progresses over the 11 year solar cycle it can be seen that the activity levels on the Sun (indicated by the number and size of the active regions) goes from a minimum value to a maximum (in 2001) and then back to a minimum again.

The internal dynamo mechanism of the Sun powers its complicated magnetic field. Unlike the simple bipole-type magnetic field of the Earth, the differential rotation of the Sun causes its field to wind up and intensify. The five stages of this process are described by the Babcock-Leighton model (Babcock 1961; Leighton 1964).

The level of magnetic activity on the Sun (i.e., indicated by the sunspot number) is not

constant and varies on a cycle of around 11 years. Figure 1.2 shows observations of the solar cycle by the SoHO satellite where the activity can be seen to go from a minimum in 1996 to a maximum in 2001 and then back to a minimum.

1.1.2 Composition

The mass of the Sun is around 1.989 x 10^{30} kg which accounts for 99.86% of the total mass in the solar system. Its chemical composition is made up of hydrogen (~75%) and helium (~24%) with other metals making up less than 2% of the mass. Helioseismology has allowed the complex internal structure of the Sun to be inferred (Leighton et al. 1962). The Sun is powered by nuclear fusion which takes place in the core. This core extends out to about $0.25R_{sun}$ and the energy released is transported outwards firstly by radiation (from $0.25–0.7R_{sun}$) and then by convection to the solar 'surface' where it is emitted from the photosphere (see e.g., Miesch 2005).

The atmosphere of the Sun is stratified into numerous layers that differ in terms of temperature and density. The way in which the temperature of the atmosphere changes as height increases above the surface is shown in Figure 1.3 where the photosphere, chromosphere, transition region and corona are labelled as well as the positions of various observational wavelengths that are referred to throughout this work.

The Photosphere:

The photosphere is typically regarded as the visible 'surface' of the Sun as it is where the bulk of the Sun's energy is radiated and is the deepest layer that can be directly imaged with observations. This layer has an average temperature of 6000 K and is thought to have a thickness value of 10s-100s of kilometers (see e.g., Solanki 1998).

The Chromosphere:

Above the photosphere lies the chromosphere which has an average temperature of

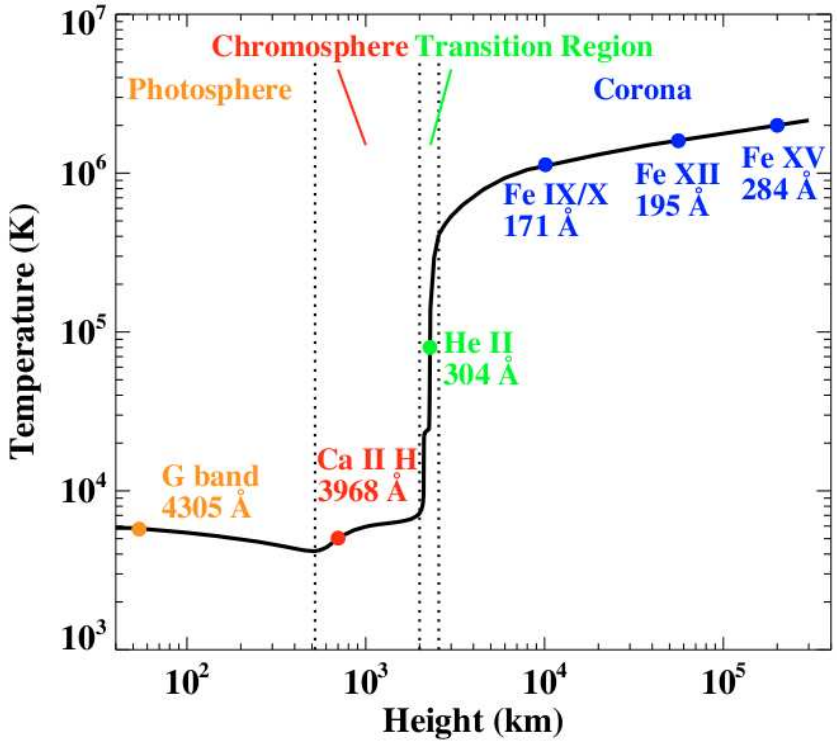

Figure 1.3: Temperature change with height through the different layers of the solar atmosphere. The characteristic temperature and formation height of various observational wavelengths are also noted. Image from Yang et al. (2009).

around 10,000 K and a density that is typically around 10^4 times that of the photosphere. Features seen at this height include spicules and the large-scale chromospheric network. More details on the chromosphere can be found in Judge (2010) and references therein.

The Transition Region:

The transition region is the interface between the chromosphere and corona that encompasses the area of vast temperature difference between them (for more details see e.g., Peter 2001). This is clearly shown in Figure 1.3 where the drastic increase in temperature can be seen as an almost vertical line connecting the chromosphere and corona. The process or processes responsible for this sharp increase in temperature is one of the most sought after answers in modern solar physics.

Figure 1.4 shows an illustration of these different layers and how they appear in observations. Some of the features described in this thesis (loops and prominences) are also shown in the figure.

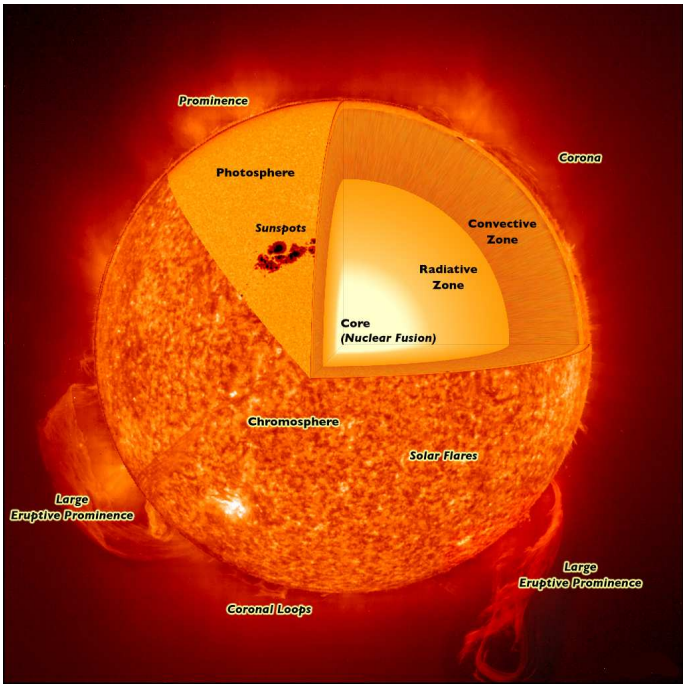

Figure 1.4: Illustration showing the different layers of the Sun as well as some of the features that are described in this thesis. Credit: NASA/ESA.

1.2 The Corona

1.2.1 Overview

The corona is the outermost layer of the Sun's atmosphere and begins at the transition region, before extending outwards for hundreds of thousands of kilometres into interplanetary space. This layer consists of extremely hot, tenuous plasma with an average temperature of 1-2 MK. The total radiation from the corona is only a small fraction of that outputted by the photosphere meaning that the corona can only be seen in white light during an eclipse or with an occulting disc. Despite having significantly less radiative output than the photosphere, the corona radiates in a much wider range of wavelengths (i.e., from radio waves to gamma rays). This allows a wide range of observational tools to be employed to investigate the corona and the various features that are formed there.

The high temperature of the corona is reached over a height of only one thousandth of a solar radii (Golub 1996). This forms the basis of what is known as "the coronal heating problem" which concerns the fact that as yet, no process has been identified that can account for the sudden temperature change between the photosphere and corona. The temperature of the corona has been inferred due to the presence of highly ionized elements e.g., Fe xv which could only have been created in temperatures exceeding one million degrees Kelvin (see e.g., Noci 2003, and references therein).

1.2.2 Features of the Corona

Before the advancements in rocketry of the 1950s and 60s, the only way to view the corona was with a coronagraph or during a solar eclipse. Figure 1.5 shows an image taken of a total solar eclipse which allows the emission from the white light corona to be seen. Magnetic structures such as large helmet streamers can be seen as well as some areas of open magnetic field. The white light portion of the corona is visible as scatted

light and constitutes only a small part of the total coronal emission, with the bulk of the radiation in the ultraviolet and soft X-ray region of the spectrum.

Figure 1.5: Image of a total solar eclipse showing the white-light corona. Credit: NASA

This type of emission cannot be viewed with ground-based instruments as the Earth's atmosphere absorbs them. Various rocket flights in the 1960s and 70s allowed scientists to glimpse the hot X-ray corona for the first time. Using data from these rocket flights, Vaiana et al. (1973b) classified the various features seen in the X-ray corona. A brief overview of these coronal features is given here.

Active Regions

Active regions appear throughout the solar cycle, first at high latitudes but then at progressively lower latitudes as the cycle progresses. Each hemisphere of the Sun has its own active region belt (i.e., a strip of latitude where active regions are more likely to be found/emerge) as shown in Figure 1.6.

The first dedicated mission to study active regions and the solar corona in general was Skylab. Skylab (1973-1979) was the USA's first space station and provided the first data on coronal active region loops. The station's slitless spectrometer was used to

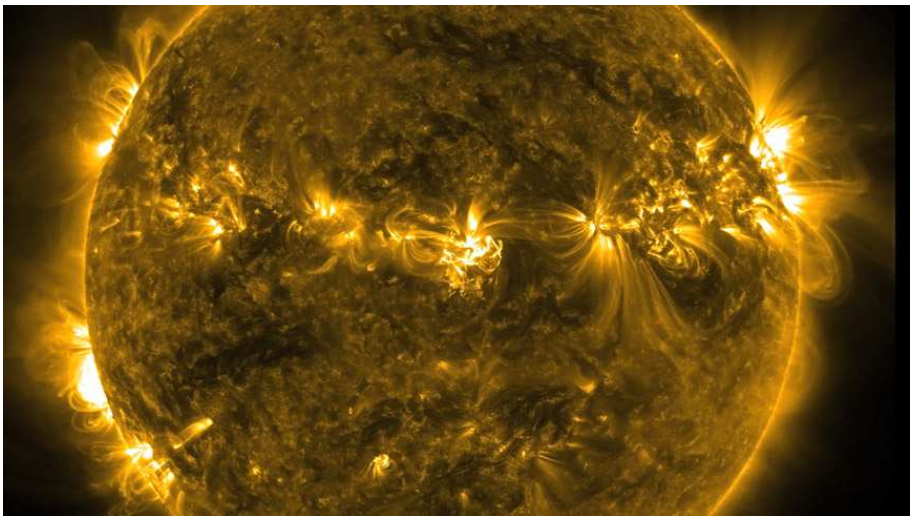

Figure 1.6: Image of the Sun taken with the SDO/AIA instrument in the 171Å wavelength (T~1MK) showing the northern hemisphere active region belt on the 1 Oct 2011, Credit: NASA/SDO.

produce spectroheliograms that only provided partial information about the loops bright footpoints (Vaiana et al. 1973a; Cheng 1980). This gave a rather incomplete view of coronal loops although a baseline for the properties of these footpoints was established.

The in-depth study of coronal loops really began with the launch of TRACE (Transition Region and Coronal Explorer; Handy et al. 1999) in 1998 as this satellite had high spatial resolution. Before this, the delicate structure of the loops could not be accurately resolved with the available instrumentation.

Active regions are composed of loop structures of varying sizes. Figure 1.7 shows two examples of active region loops captured by the SDO/AIA satellite. Table 1.1 shows the classification of different types of loop structure according to parameters such as length, temperature and density. Many studies have been made to observe and analyse coronal loops (see e.g., Reale 2010, for a review of subject). These studies highlight the different methods used to measure physical parameters such as density, temperature, and velocity flows. Some of the issues and methods involved in this type of analysis are detailed in Section 1.3 below.

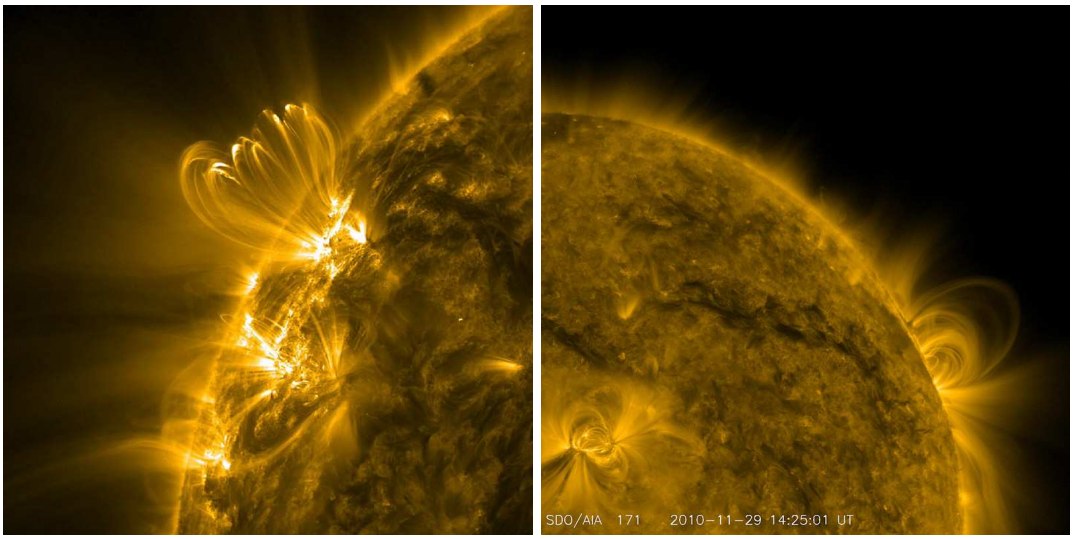

Figure 1.7: SDO/AIA images of active region loops in the 171Å channel. *Left:* post flare loops seen on the Eastern limb. *Right:* active regions observed with two orientations - one straight on and one side on. Credit: NASA/SDO

Table 1.1: Typical X-ray coronal loop parameters. From Reale (2010).

Type	Length [10^9 cm]	Temperature [MK]	Density [10^9 cm^{-3}]	Pressure [dyne cm^{-2}]
Bright points	0.1 – 1	2	5	3
Active region	1 – 10	3	1 – 10	1 – 10
Giant arches	10 – 100	1 – 2	0.1 – 1	0.1
Flaring loops	1–10	> 10	> 50	> 100

X-ray Bright Points

X-ray bright points (XBP) are small, compact loop systems seen all over the solar disc. Figure 1.8 shows an image from the Hinode/XRT instrument which highlights how numerous these features are. Chapter 3 concerns work done on examining a particular XBP and so a fuller introduction to the topic is given there.

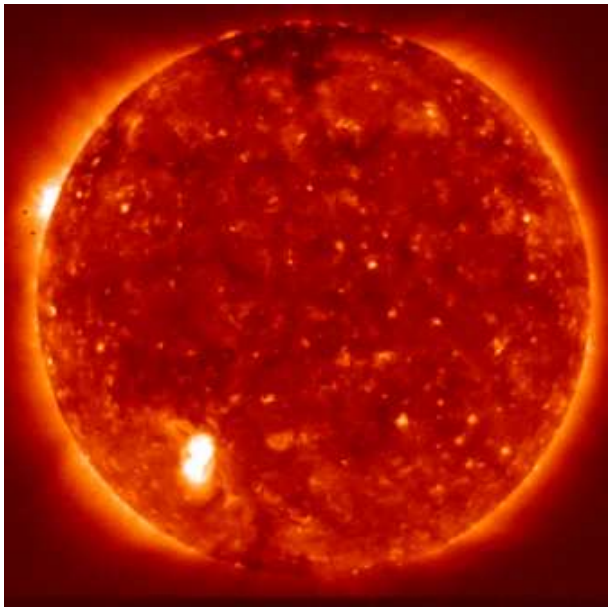

Figure 1.8: X-ray image of the solar disc showing a number of X-ray bright points over the solar surface. The bright feature in the lower left of the image would be classified as a small active region and not a bright point. Bright points are typically around 10-15" in size. Credit: Hinode/XRT.

Coronal Holes

Coronal holes are large areas of open magnetic flux on the Sun and are the origin of the fast solar wind (Krieger et al. 1973). There are two types of coronal hole: polar, and mid-latitude such as those seen in Figure 1.9. They appear in EUV images as large, dark areas because they are cooler than the surrounding plasma.

Coronal holes change their position and size as the solar cycle progresses with polar coronal holes being present and most prominent at solar minimum. At this time the

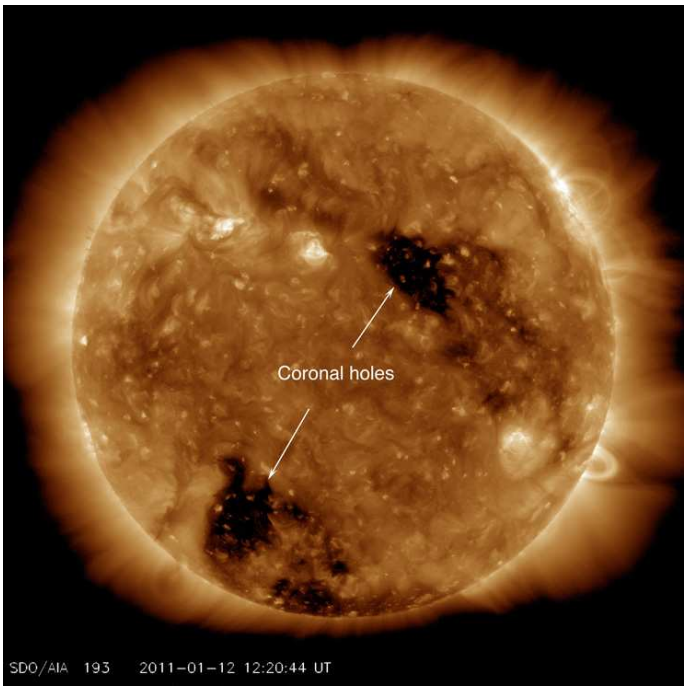

Figure 1.9: Two mid-latitude coronal holes observed in the 193 Å channel of SDO/AIA.Credit: NASA/SDO.

northern and southern polar coronal holes will have opposite magnetic polarities. As the solar cycle progresses, these polar holes shrink and more mid-latitude coronal holes appear - sometimes joining with a polar hole to create an equatorial extension coronal hole (EECH). Towards solar maximum the polar holes disappear and then reappear towards solar minimum with opposite polarities (Wang et al. 1996).

Coronal Mass Ejections

Coronal Mass Ejections (CMEs) are large bursts of plasma that are released from the corona and expand outwards into interplanetary space. Figure 1.10 shows a series of images taken in white light by a coronagraph of an expanding CME. The black circle is the occulting disc which covers 1.6 solar radii in order to block out the intense light from the disc to allow the faint CME to be seen. The release of plasma from CMEs can lead to changes in the solar wind with the effects of an Earth-directed CME reaching us in 3-4 days (Gilbert et al. 2000).

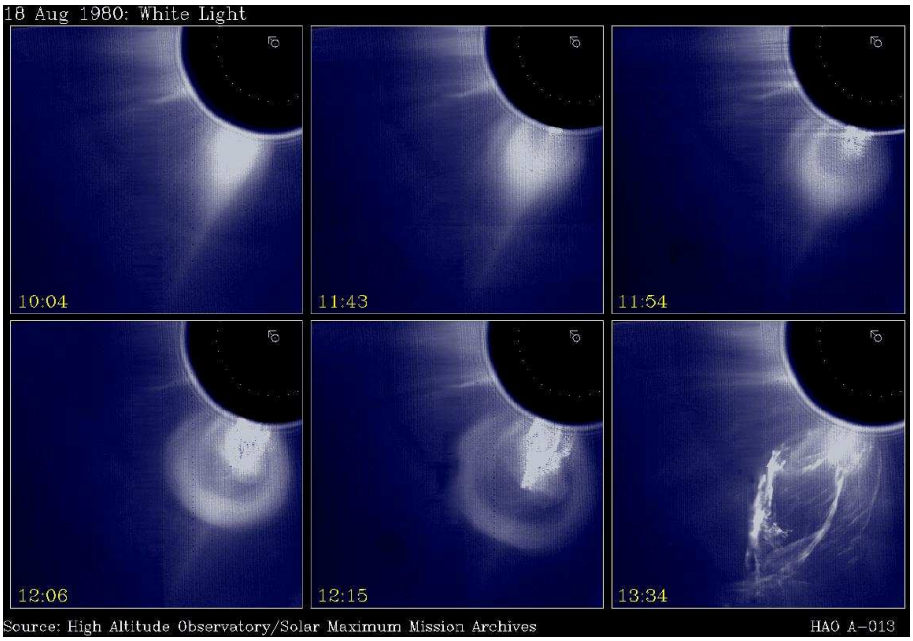

Figure 1.10: Series of images of an expanding CME. The dark occulting disc is used to allow the faint CME structure to be seen in white light. The three part structure of core, cavity and front is clearly seen at 12.06. Credit: HAO/SMM.

This can have an effect on space weather with the high energy plasma potentially causing satellites to be affected. The origins of CMEs are not fully understood and they have been linked with solar flares and prominence eruptions but no definitive link has been established. This correlation between eruptive events is detailed further in Chapter 6.

Prominence/Filaments

Solar prominences are composed of plasma with chromospheric temperature and density values but which are found at coronal heights, suspended in the magnetic field. Prominences and filaments are the same structure observed from different points of view i.e., prominence is the term for the structure seen off the limb (as shown in Figure 1.11), while filaments are seen on the disc. Chapter 6 concerns the study of a particular prominence where this topic is discussed in more detail.

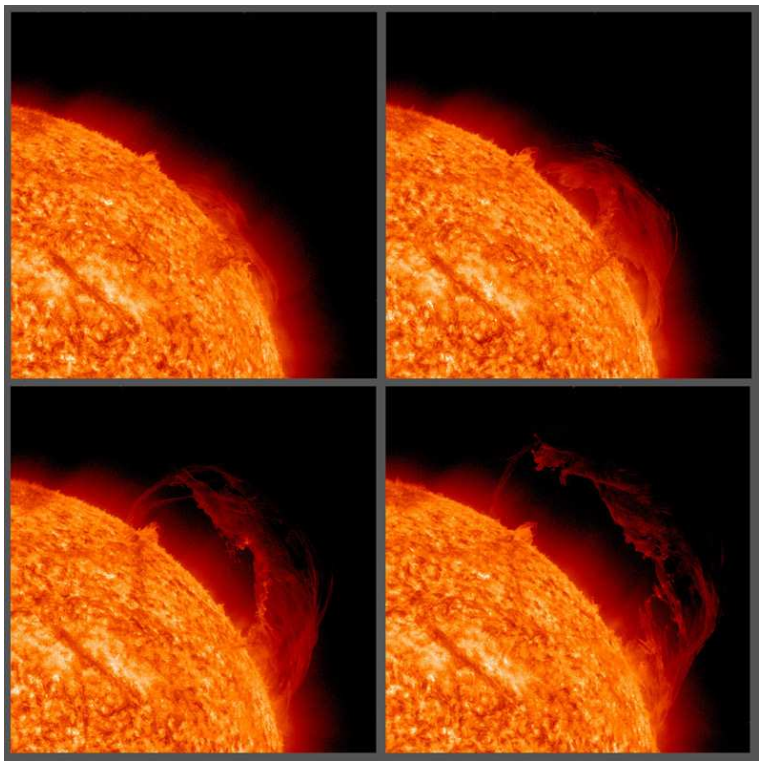

Figure 1.11: Series of images taken with SDO/AIA showing the eruption of a prominence on the 15 September 2010. Credit: NASA/SDO.

Solar Flares

Solar flares are characterised by a sudden burst of energy on the Sun which is observed as a release of radiation across the entire electromagnetic spectrum (i.e., from radio, through optical, up to X-ray and gamma-ray). Solar flares are associated with active regions and are therefore more numerous at solar maximum (Charbonneau et al. 2001).

The total energy released by a flare can vary widely with the occurrence of smaller events being much higher than larger ones (Fletcher et al. 2011). The size of a flare is denoted by its classification: A (for background level flares), followed by B, C, M and X. Each level represents a flare with ten times more energy than the previous level. Figure 1.12 shows observations from the SoHO satellite of the Sun on the 28 October 2003 when an X17 class flare was observed. The active region it occurred in released many flares around this time including the 'Halloween' flare which caused the aurora to be seen at much lower latitudes than usual (Tsurutani et al. 2006). Studying solar flares

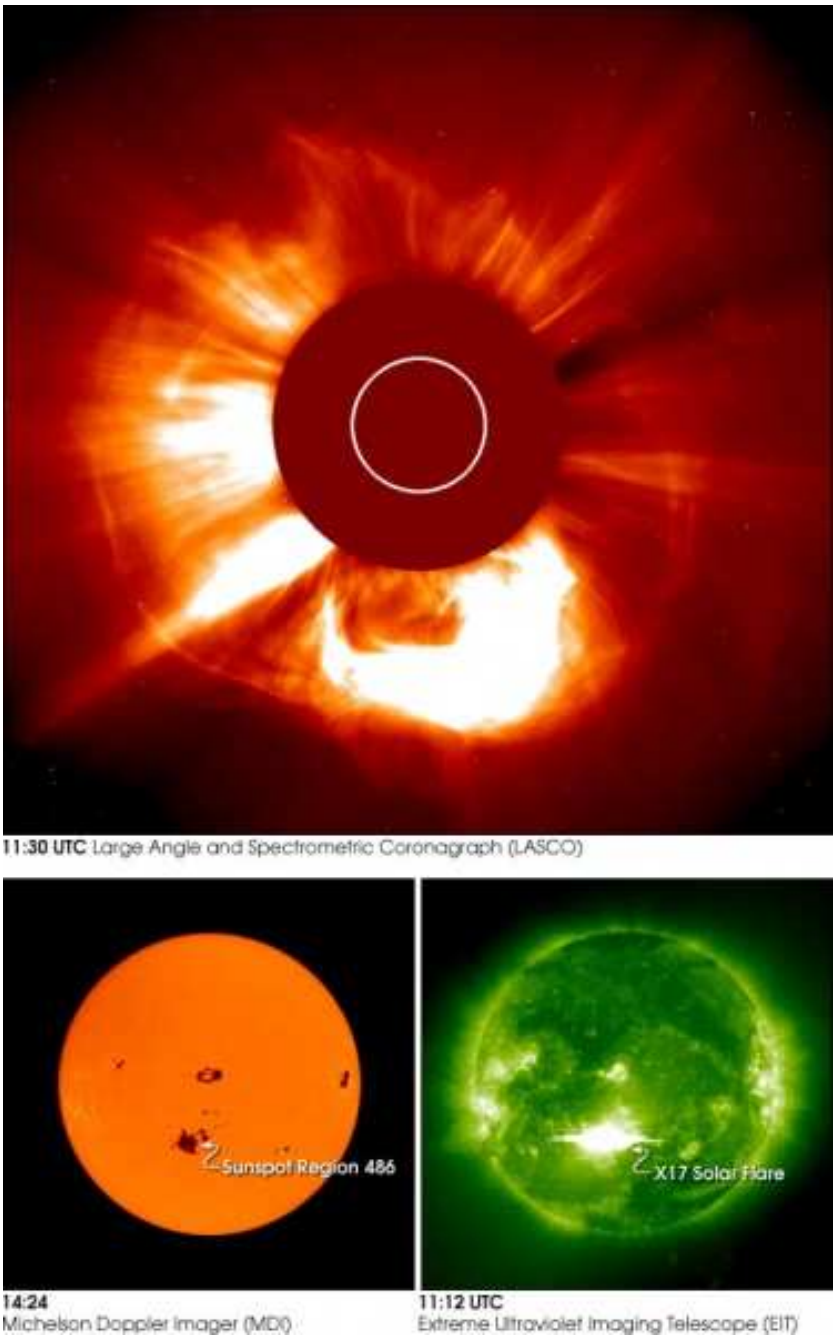

Figure 1.12: Images from three of the SoHO instruments showing a solar flare on the 28 October 2003. Top image shows the resultant CME imaged by LASCO while the bottom-left panel shows a continuum image from MDI showing the sunspot group the flare originated from. The bottom-right image shows the saturation caused by the flare in EIT. Credit: NASA/SoHO

is an important area of research as they have a profound effect on space weather. Understanding the mechanisms responsible for them would allow more accurate predictions to be made which would help to safeguard future space missions and satellites.

1.3 Measuring Coronal Parameters

Today, with the abundance of solar observations available to scientists, there are numerous ways in which this data can be analysed in order to infer the physical parameters of the plasma. This section briefly outlines the primary methods used to study coronal features such as loops and various considerations that should be kept in mind.

1.3.1 Background subtraction:

Before analysis can begin on a coronal structure a suitable method of background subtraction is needed. This is due to the overlying intensity caused by other bright structures lying along the line of sight of the observation and can be corrected in a number of ways.

Cirtain et al. (2007) used the standard approach where they defined a quiet area near the loop they were studying and used the average value of intensity within this region as their value for background emission. They also picked an area over some moss structure (the area around loop footpoints) and defined this as the maximum background emission. Reale et al. (2000) decided against this method and instead picked a quiet frame from their data set where the loop they were studying could not be seen and took the value of each pixel to be the background value. A different approach was conducted by Tripathi et al. (2009) where the background levels were found by following a path alongside the loop being analysed in order to get accurate results for the background levels at different heights throughout the plasma. Del Zanna (2003) also noted that the effect of foreground and background emission was a greater problem for observations

on the limb while on-disk measurements were less obstructed. This can be an important consideration when choosing data or planning observations.

1.3.2 Density determination:

The density of coronal plasma can give a lot of information on the structure and filling mechanism of the loop. Throughout the literature the majority of authors have used the same method: the line ratio method. This involves using data from a spectrometer (e.g., SoHO/CDS or Hinode/EIS) and using the ratio of the intensity values from a density sensitive pair (described in detail in Young et al. 2007) in order to calculate the density.

An example of a coronal loop study which employed this method is Tripathi et al. (2009) who measured several density sensitive pairs (Mg VII 280/278, Si X 258/261 and Fe XII 186/195) along one specific loop. They found that electron density varied from 10^{10}cm^{-3} at the footpoints to $10^{8.5}$cm^{-3} higher up on the loop apex. They noted a variation within the density values from the three ratios that did not always fall within the error range. This suggests it is worthwhile trying out a few different methods in order to check the accuracy of the results. Results from other authors covering the topic of density diagnostics can be found in Del Zanna & Mason (2005), Young et al. (2007), and Tripathi et al. (2008).

1.3.3 Temperature determination:

One of the main issues surrounding the temperature determination of coronal loops is whether or not the loops are isothermal or multi-thermal along the line of sight. It can be difficult to differentiate between an isothermal distribution and a narrow distribution measured by spectrometers due to limitations in the resolution of current instrumentation.

Certain studies such as Warren et al. (2008) concluded that loops were not isothermal in contrast to most of the literature. For example, Del Zanna (2003) and also Del Zanna & Mason (2003) looked at active region loops using SoHO/CDS and TRACE in order to accurately calculate density and temperature within loops and found that many previously published results were overestimated due to poor background subtraction methods. They also found the the '1 MK loops' seen most clearly in TRACE 171Å were nearly isothermal along their lengths with a constant density across the loop. They made note of the poor diagnostic ability of TRACE for temperature determination.

Accurately determining the temperature of coronal loops is an important area of research as pinning down this factor will help to understand the heating mechanisms at work. This is not an easy thing to do however, as direct measurements cannot be taken. The information gathered by solar instruments is integrated along the line of sight so contributions may be counted from other sources. Information from imagers and spectrometers can be used to infer a plasma temperature of a particular structure.

The five main diagnostic methods used to infer plasma temperature are:-

- **Bandpass observations:** where the temperature of the plasma is inferred by the wavelength of the bandpass filter the feature appears in. This can be useful as an indicator but cannot give an accurate measurement. Problems such as line-of-sight effects and contributions from double-peaked instrument response functions can cause inaccurate conclusions.

- **Filter ratio:** authors such as Noglik & Walsh (2007) and Aschwanden et al. (2000b, 2001) used the ratio of intensities seen in TRACE EUV channels to infer plasma temperature. This method can be unreliable as it is compromised if one of the filters has inherent inaccuracies.

- **Line ratio:** similar to the density determination described above, this method uses the ratio of two temperature sensitive spectral lines to infer the thermal structure

of the plasma. See Young & Landi (2009) for more details.

- **Emission Measure Loci:** the EML method (see e.g., Jordan et al. 1987; Del Zanna et al. 2002) uses information from spectral lines of an observation. This method is very useful for determining isothermal plasmas but Landi et al. (2012b) point out that this method fails at giving a measure of the uncertainty in the results. This method is described in more detail in Section 3.3.1.

- **Differential Emission Measure (DEM):** this technique has a few different methods of reconstructing the thermal structure of coronal plasma i.e., iterative, direct inversion (see Section 5). The distributions calculated by this method give an indication of the spread of the plasma over different temperatures and also allows conclusions to be drawn about whether plasma is isothermal or multithermal. A full description of this method is given in Section 4.1.3.

1.4 Remaining issues in solar physics

The incredible advances in solar physics over the last 50 years make it a very exciting field to work in. With more and more data coming in of higher and higher resolution, scientists are in a unique position to try and tackle some of the remaining unknowns. Aschwanden (2008) outlined the ten outstanding problems in solar physics over the past 60 years - only two of which have been solved.

The list includes remaining issues such as understanding the coronal heating problem, magnetic reconnection processes, particle acceleration in flares, CME mechanics, and the hydrodynamics of coronal loops to name just a few. This last point in particular is very relevant to the work presented in the bulk of this thesis. The issue of whether coronal loops are in hydrostatic equilibrium or not is one that is very important to theorists and observers alike.

1.5 Synopsis of thesis

This thesis is arranged as follows. In Chapter 2 the solar observation satellites used within this work are described with special attention paid to the particular instruments utilised in the four main science chapters. These main science chapters (3-6) progress from examining small-scale (<10 Mm) coronal features up through medium-scale (10–100 Mm) and finally to large-scale (>100 Mm) ones in order to tie together the common observational techniques and analysis methods used throughout this thesis.

Chapter 3 presents a case study of a small-scale coronal X-ray bright point (XBP). Results concerning the evolution and plasma parameter changes observed within the XBP over its entire lifetime are detailed and various science questions are addressed. Findings concerning how the physical attributes of the bright point (e.g., temperature, density, filling factor) change over time are used to infer its origins and track its evolution.

Chapter 4 explores the parameter space of a multi-stranded loop simulation in order to achieve a number of goals: (i) to check the model is behaving in a physically realistic way, (ii) to determine in what way the model 'observables' (e.g., DEM distribution and intensity values) change due to the changing input parameters, and (iii) to see if these changes constitute a 'unique signature' that could be useful for interpreting real data.

Chapter 5 tests the accuracy of applying an iterative DEM solver code to the results already produced by the loop simulation. By comparing the DEM solutions of the solver with the 'true' DEM the simulation has calculated, the applicability of the solver to interpret real data can be tested. Firstly, a detailed case study is conducted to define all the parameters relevant to determining the 'goodness-of-fit' of each DEM solution to the original. Secondly, the solver is applied to various runs of the simulation in order to see where it does and does not do well.

Chapter 6 moves on to study a large-scale coronal structure in the form of an erupting

polar-crown prominence. The structure and evolution of the prominence material and cavity are investigated over the course of the eruption. The most likely trigger mechanism of the eruption is also investigated using dual satellite observations.

Lastly, Chapter 7 summaries the final conclusions reached concerning the structure and evolution of the various coronal features investigated. Various future directions that each chapter could take (and the upcoming missions that will facilitate this future work) are also detailed.

Chapter 2

Solar Observations: Satellites and Instrumentation

Observations of our nearest star underwent a serious transformation in the mid-20th century due to the advancement in rocket technology. Before this time, ground based observations were the only available source of information on solar activity. The Earth's atmosphere and magnetic field help to ensure that high-energy radiation and particles cannot reach the ground. This means that any instrument wishing to observe the solar corona and the high energy phenomena that occur there need to be placed into orbit.

The early solar observation programs of the 1960's and 70's laid the foundations for later missions and uncovered the first views of the dynamic solar corona. Later missions such as Skylab (1973–1979), the Solar Maximum Mission (1980–1989) and Yohkoh (1991–2001) to name only a few, were instrumental in discovering and analysing many different types of coronal phenomena.

Today, we are lucky to have many operational solar satellites, each contributing to the vast knowledge base of observational solar physics. This chapter describes the main missions and instruments associated with the work presented in this thesis, as well as a

brief summary of some of the future missions to look forward to that would complement and help to extend this work.

2.1 SoHO

The Solar and Heliospheric Observatory (SoHO) satellite (Domingo et al. 1995), launched in 1995 and still operational today, has made an incredible contribution to the field of solar physics due to both the large number of instruments it carries, and its location.

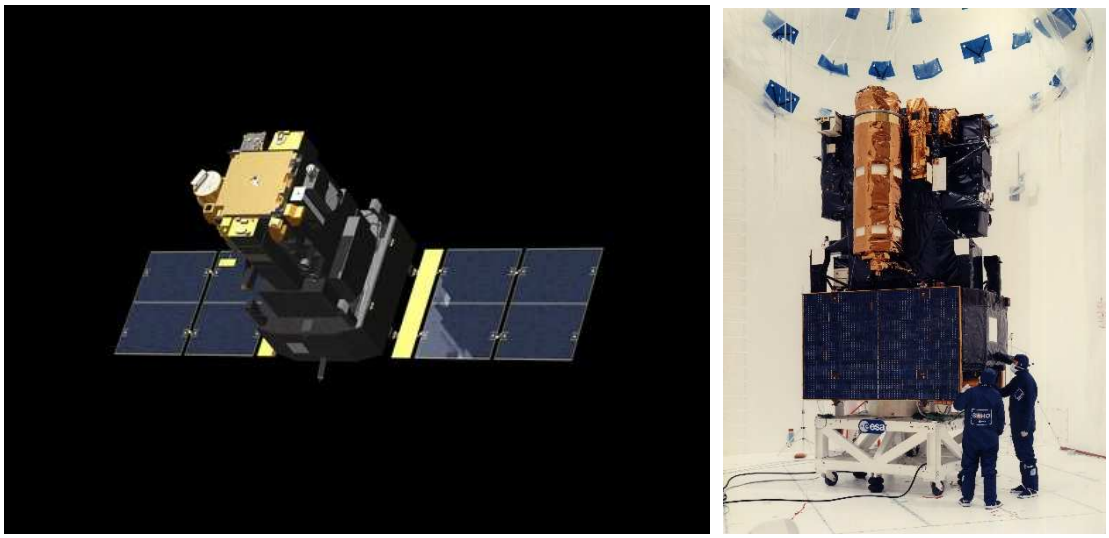

Figure 2.1: *Left:* artist's impression of the SoHO satellite in space. *Right:* photograph of the SoHO satellite being prepared for launch. The satellite dimensions are approximately 4.3 x 2.7 x 3.7 metres with the solar arrays taking the width to 9.5m when deployed.

SoHO orbits around the First Lagrangian Point (L1) which is located along the Earth-Sun line at around 1.5 x 10^6 km from Earth. This allows the satellite to have an uninterrupted view of the Sun with no eclipse periods causing gaps in the data. The satellite houses twelve different instruments, each capable of working together in order to measure different observables. The names of these instruments are given in Table 2.1. SoHO has been operational for 17 years due to the number of extensions the mission has been given. This has allowed the satellite to observe the Sun over an entire solar cycle. The instruments onboard SoHO are still operational but a few are starting to have their

operations scaled back due to newer satellites being launched with similar (but better resolution) instruments.

Instrument	Full name
CDS:	Coronal Diagnostic Spectrometer
CELIAS:	Charge, Element, and Isotope Analysis System
COSTEP:	Comprehensive Suprathermal and Energetic Particle Analyzer
EIT:	Extreme ultraviolet Imaging Telescope
ERNE:	Energetic and Relativistic Nuclei and Electron experiment
GOLF:	Global Oscillations at Low Frequencies
LASCO:	Large Angle and Spectrometric Coronograph
MDI/SOI:	Michelson Doppler Imager/Solar Oscillations Investigation
SUMER:	Solar Ultraviolet Measurements of Emitted Radiation
SWAN:	Solar Wind Anisotropies
UVCS:	UltraViolet Coronograph Spectrometer
VIRGO:	Variability of Solar Irradiance and Gravity Oscillations

Table 2.1: List of the instruments that make up the scientific payload of the SoHO satellite.

Two of the instruments onboard SoHO are described in more detail in the following paragraphs as they have a bearing of some of the details of this work. Descriptions of the other instruments onboard SoHO are outside the scope of this work but more information can be found in Domingo et al. (1995).

2.1.1 EIT

The Extreme ultraviolet Imaging Telescope (Delaboudinière et al. 1995) observes the full-disc of the Sun in four EUV wavelengths (171Å, 195Å, 284Å, and 304Å- shown in Figure 2.2) allowing plasma from the transition region to the low corona to be viewed. Table 2.2 gives more details of the particular temperatures and observational targets that each channel has.

EIT is currently on reduced operations (due to the launch of the improved imager SDO/AIA, see below) but at its peak it took a full-disc image of the Sun in each channel with spatial resolution of ~5 arcseconds approximately every 12 minutes. Since

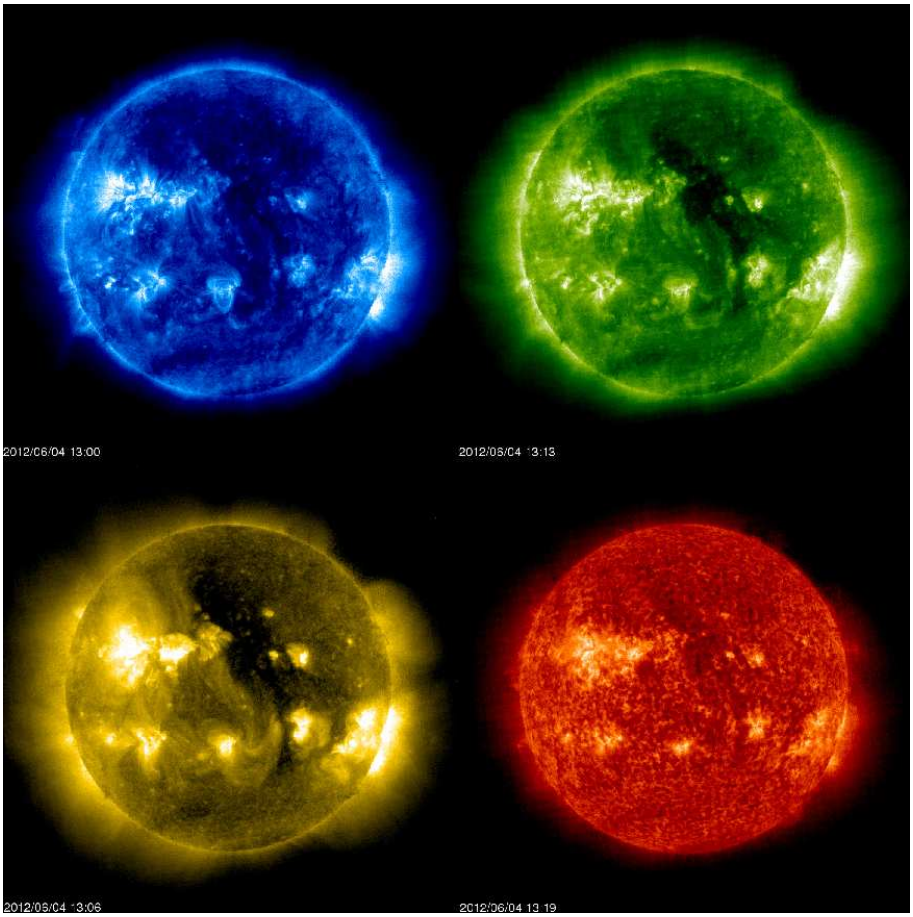

Figure 2.2: Images taken with the SoHO/EIT instrument in the four wavelength channels available- 171Å (top-left), 195Å (top-right), 284Å (bottom-left), and 304Å (bottom-right).

Wavelength	Ion	Peak temperature	Target observation
304 Å	He II	8.0 x 10^4 K	chromospheric network; coronal holes
171 Å	Fe IX-X	1.3 x 10^6 K	corona/transition region boundary; structures inside coronal holes
195 Å	Fe XII	1.6 x 10^6 K	quiet corona outside coronal holes
284 Å	Fe XV	2.0 x 10^6 K	active regions

Table 2.2: SoHO EIT bandpass information. Adapted from Delaboudinière et al. (1995).

August 2010, most of EIT's telemetry bandwidth has been allocated to the LASCO instrument with only a couple of EIT images being taken a day for synoptic purposes. EIT provided almost 15 years of observations and revolutionised the way the corona was viewed. Originally designed to provide context for the other instruments, its workload was increased after the amazing imaging power of its four channels was seen. Many major discoveries have been made with EIT. One example is the first observations of travelling waves (Thompson et al. 1998), correspondingly named 'EIT waves'.

2.1.2 MDI

The Michelson Doppler Imager (Scherrer et al. 1995) measures line-of-sight (los) motions on the solar surface as well as measuring the los magnetic field of the Sun. The first measurement is very useful for solar oscillation studies while the second is crucial for modelling the magnetic field of the Sun as well as interpreting coronal images. Figure 2.3 shows an MDI magnetogram (left) and continuum image (right). The black and white pattern on the magnetogram represents areas of positive (white) and negative (black) polarity which can be thought of as magnetic field going out of and into the solar surface respectively.

MDI magnetograms were used in this work primarily to give context to other smaller field-of-view magnetograms (e.g., from Hinode/SOT, see below), as SoHO has very accurate pointing and MDI has been well calibrated over the years. This allows cross-calibration of coordinates and magnetic field strength levels to be made between instruments. As of early 2011, MDI ceased normal science operations due to the launch of a higher resolution magnetograph aboard SDO (see below). MDI's spatial resolution of 4" (full-disc) and 1.2" (high resolution partial disc) has been surpassed as well as its temporal resolution. MDI typically produced a full-disc magnetogram every 96 minutes (although it was also capable of making one per minute) so it is generally not very useful for studying small-scale changes that occur on short (i.e., minutes) timescales.

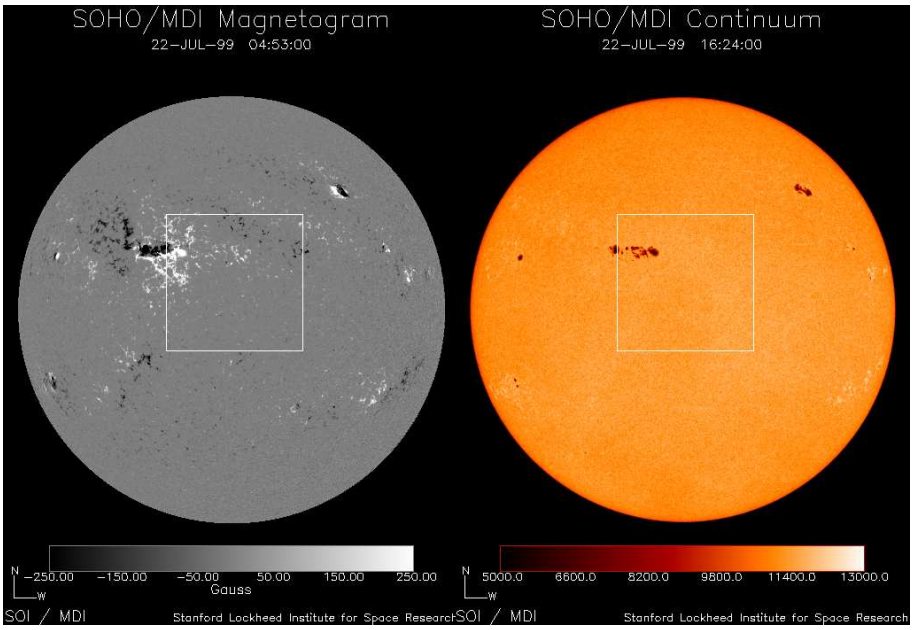

Figure 2.3: *Left:* SoHO/MDI magnetogram taken on the 22 July 1999. *Right:* continuum image taken with MDI twelve hours later.

2.2 Hinode

The Hinode satellite is a joint mission between the space agencies of Japan, the US, Europe and the UK. It was launched on the 22nd September 2006, under its development name Solar-B, into a polar sun-synchronous orbit. This orbit was chosen to allow 9 months of continuous observation of the Sun with 3 months of eclipse seasons each year.

The satellite observes the Sun at visible, EUV and X-ray wavelengths with its three instruments: the X-Ray Telescope (XRT), the Solar Optical Telescope (SOT), and the EUV Imaging Spectrometer (EIS). Hinode was designed for its three instruments to work together as an observatory in order to observe solar phenomena from the photosphere up through the chromosphere and transition region to the corona. The left image of Figure 2.4 shows the layout of the satellite's instruments on the satellite test model. The 'FPP' (Focal Plane Package) and 'OTA' (Optical Telescope Assembly) make up the SOT instrument.

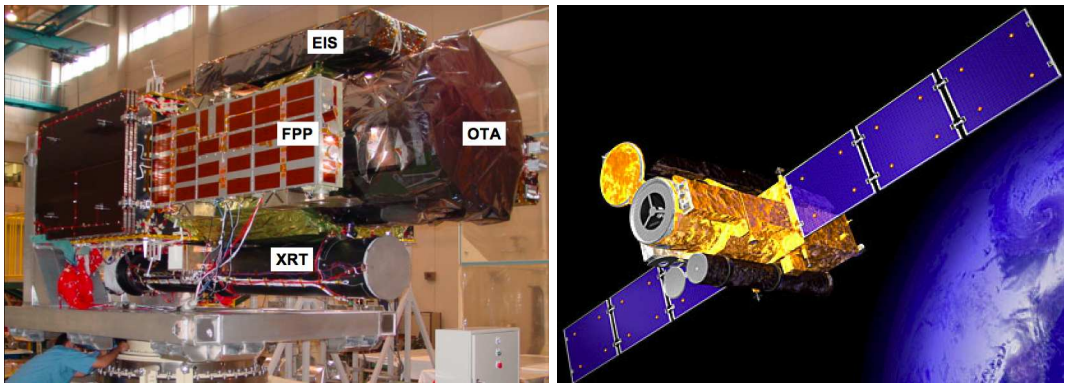

Figure 2.4: *Left:* photograph of the Solar-B Mechanical Test Model which shows the relative position and scale of the instruments. *Right:* artist's impression of the satellite in orbit. Image credits: JAXA.

2.2.1 EIS

Hinode's EIS instrument observes emission lines with wavelengths in the ranges 170–210Å and 250–290Å (Culhane et al. 2007). The instrument can be used to measure spectral line intensities, Doppler velocities, and line widths. These measurements can then be used to calculate values of temperature and density within the plasma being imaged.

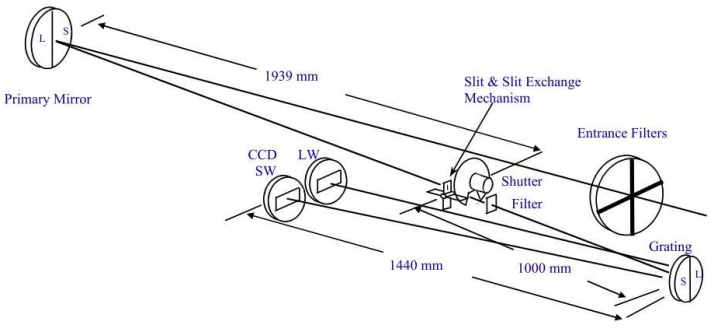

Figure 2.5: The Optical Layout of Hinode EIS. S\SW and L\LW refer to the short (170-210Å) and long (250-290Å) wavelength bands of the two CCDs. Image from Culhane et al. (2007).

The instrument can observe plasma within a temperature range of 0.1MK up to 10MK (Kosugi et al. 2007), has a spatial resolution of 2", and can be used to measure plasma velocity flows to an accuracy of $\pm 5 \mathrm{kms}^{-1}$ (Culhane et al. 2007). All these factors go towards making the EIS instrument an improvement upon other spectrometers such as

the CDS (Coronal Diagnostic Spectrometer) aboard SoHO.

2.2.2 SOT

Hinode's Solar Optical Telescope (Tsuneta et al. 2008) provides various information on the magnetic field of the Sun. Unlike SoHO's MDI, the SOT only has a partial field-of-view of approximately 360x200 arcsec^2 meaning that features up to the size of small active regions can be viewed at any particular instance.

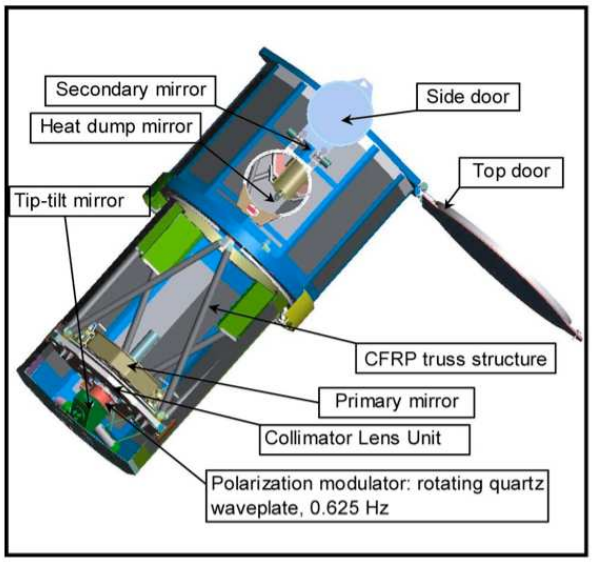

Figure 2.6: The Optical Telescope Assembly (OTA) for the SOT instrument. The aperture of the telescope is 50cm. Image credit: JAXA.

The instrument comprises of two parts: the OTA (Optical Telescope Assembly) and the FPP (Focal Plane Package). The SOT's instrument package contains three main sub-systems:

- The Broad-band Filter Imager (BFI),
- The Narrow-band Filter Imager (NFI),
- The Spectropolarimeter (SP).

The spatial resolution of the SOT is 0.25” (c.f. SoHO’s MDI which has a resolution of ~1” for high resolution images and 4” for full-disc) and has a time cadence range from tens of seconds (for NFI) to a few hours for a wide-field scan with SP (Tsuneta et al. 2008).

2.2.3 XRT

The X-Ray Telescope aboard Hinode images high temperature plasma and can be used to study changes in the morphology and temperature of solar features. The XRT is a grazing incidence telescope with an aperture of 50cm (see Figure 2.7). It focuses soft X-rays from the Sun onto a CCD array and has nine X-ray analysis filters (of varying thickness and material) which allows plasma of different energies to be viewed.

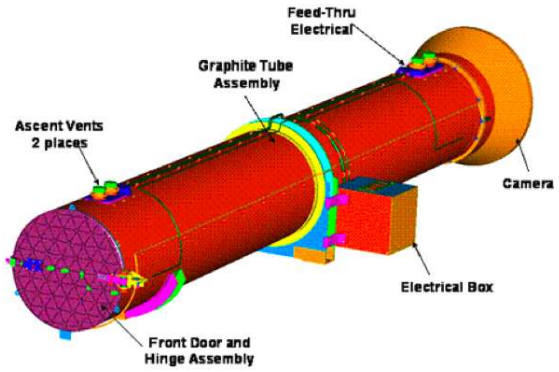

Figure 2.7: The Hinode XRT Instrument. Image from Golub et al. (2007).

The XRT instrument is able to image features with temperatures ranging from $6.1 \leq \text{LogT/K} \leq 7.5$ and is able to discriminate between temperatures of LogT=0.2K (Golub et al. 2007). The XRT has the highest resolution of any solar X-ray telescope to date with the optical design and mirror quality allowing coronal plasmas to be images with a resolution of 2” (Golub et al. 2007). The XRT has many improvements on previous coronal imagers: it has the broadest temperature range to date which allows many different types of feature to be studied as well as a high data rate and image cadence to allow the study of features that show rapid changes in structure and temperature.

2.3 SDO

The Solar Dynamics Observatory was launched on the 11th February 2010 and is now studying the solar atmosphere at high spatial and temporal resolution in multiple wavelengths simultaneously. The satellite comprises of three instruments: the Atmospheric Imaging Assembly (AIA), the Helioseismic and Magnetic Imager (HMI), and the Extreme Ultraviolet Variability Experiment (EVE). These instruments are described in more detail below except for EVE which is outside the scope of this work. More details on this instrument can be found in Woods et al. (2012).

The left panel of Figure 2.8 shows the satellite being prepared for launch and gives an idea of the scale of the structure. The satellite measures 2.2 x 2.2 x 4.5 metres and the solar arrays are 6.5 metres across when deployed. The right panel of this figure shows an illustration of where the three instruments are located on the satellite.

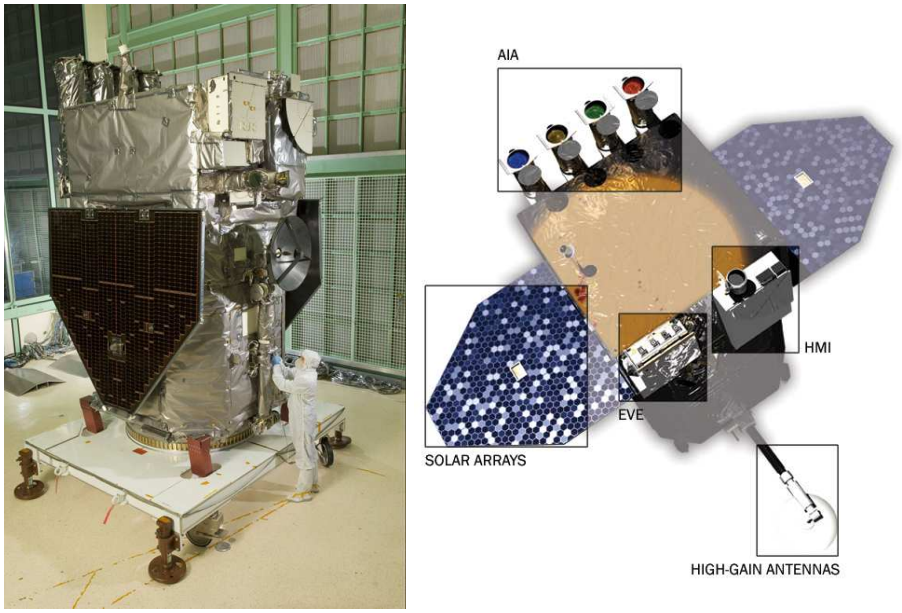

Figure 2.8: Images of the SDO satellite. *Left:* photograph of the finished satellite before being stowed for launch. *Right:* illustration of the satellite with the three instruments highlighted.

The amazing stride forward that the AIA and HMI instruments represent in terms of spatial and temporal resolution, is detailed below.

2.3.1 AIA

The Atmospheric Imaging Assembly instrument (Lemen et al. 2012a) consists of four telescopes that are designed to observe plasma in several narrow band passes in the EUV range. Figure 2.9 shows two representations of the AIA instrument. The top image shows a photograph of the telescopes during the testing phase of the mission while the lower image shows exactly which of the telescopes produces each wavelength.

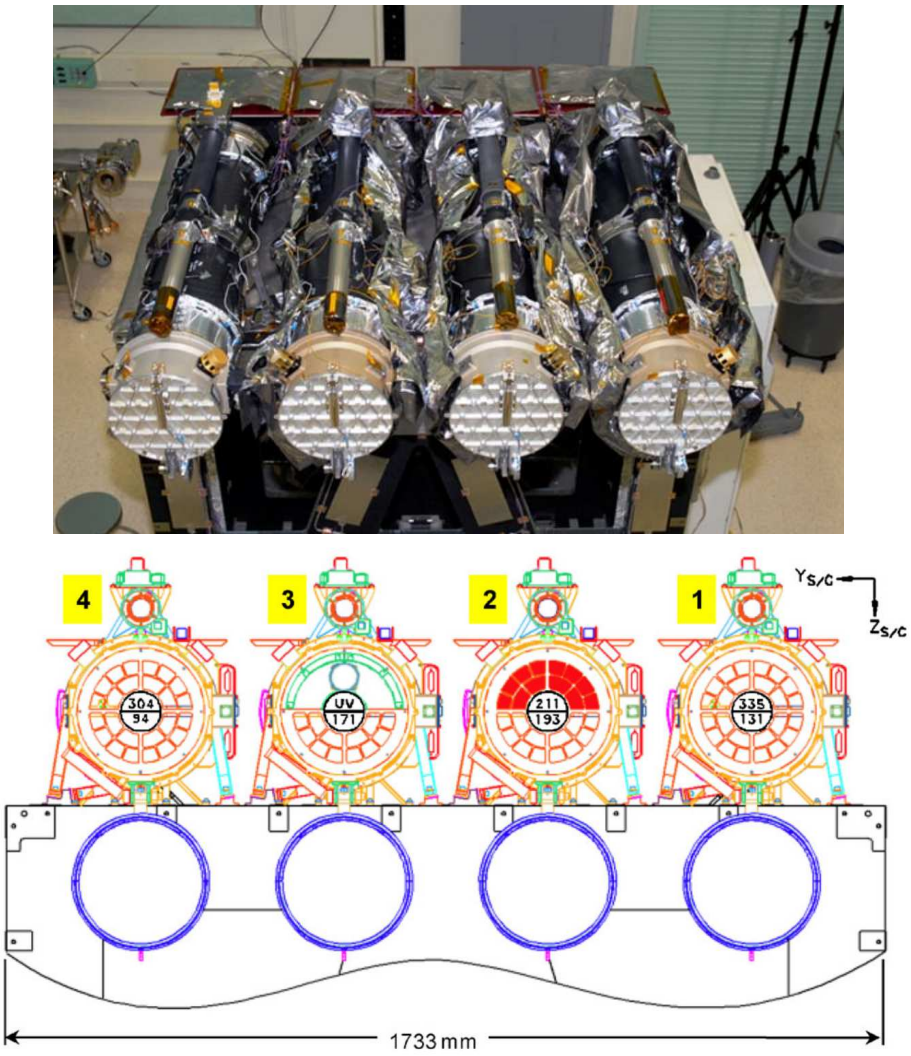

Figure 2.9: *Top:* photograph of the AIA telescopes taken during the satellite integration. *Bottom:* Layout of the channels in the four telescopes. Telescopes 1, 3 and 4 rely on filter wheels to change between channels while telescope 2 employs an aperture blade to select the different wavelength channels.

Table 2.3 lists the different wavelengths imaged by AIA and the primary ions that contribute to each particular channel. The characteristic temperatures that these ions represent are also noted. It can be seen that some channels have multiple contributions which can create problems when trying to interpret observations from these channels.

Channel name	Primary ion(s)	Region of atmosphere	Char. log(T)
4500 Å	continuum	photosphere	3.7
1700 Å	continuum	temperature minimum, photosphere	3.7
304 Å	He II	chromosphere, transition region	4.7
1600 Å	C IV+CONT.	transition region, upper photosphere	5.0
171 Å	Fe IX	quiet corona, upper transition region	5.8
193 Å	Fe XII,XXIV	corona and hot flare plasma	6.2, 7.3
211 Å	Fe XIV	active-region corona	6.3
335 Å	Fe XVI	active-region corona	6.4
94 Å	Fe XVIII	flaring corona	6.8
131 Å	Fe VIII,XXI	transition region, flaring corona	5.6, 7.0

Table 2.3: Information on the wavelengths imaged by AIA and the primary ions included in each band pass. The target observation of each channel and its characteristic temperature are also noted. Table from Lemen et al. (2012a).

Figure 2.10 shows a selection of images taken with the ten channels listed in Table 2.3. As with all solar images, the false colours are indicative of the channel being used.

The main advantage that AIA has over previous coronal imagers is the very high spatial and temporal resolution of the instrument. Although the TRACE satellite (Handy et al. 1999) had a similar high spatial resolution (close to 1”), it only had a partial field-of-view (8.5 x 8.5 arcminutes). TRACE also only took an image every minute (although in certain studies it could take images much faster e.g., every ten seconds) and only imaged in three EUV channels (at 171Å, 195Å, and 284Å) as well as at various continuum and UV wavelengths.

SDO/AIA takes full-disc images of the Sun in six EUV channels every 10 seconds making it a vastly superior imager compared to both TRACE and SoHO/EIT. The high spatial and temporal resolution combined with its full-disc field-of-view, allows both large and small-scale changes to be observed with an unprecedented level of detail. An

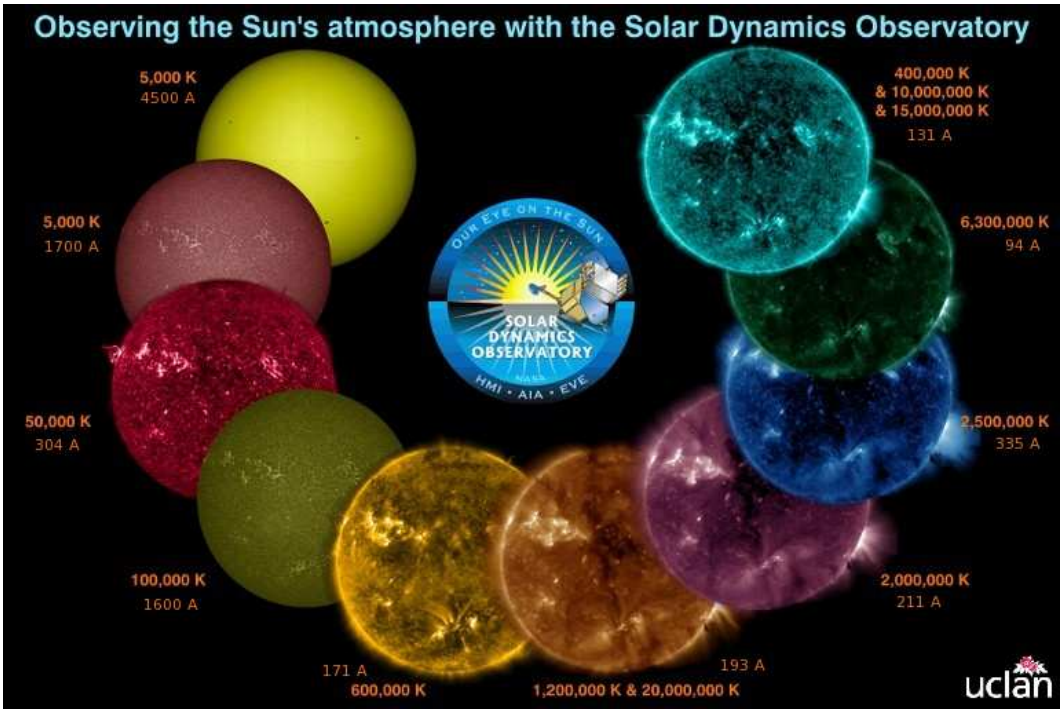

Figure 2.10: Selection of SDO/AIA images taken in the ten channels listed in Table 2.3. The wavelength and characteristic temperature of each channel are noted next to each image. Image credit: Dan Brown, UCLan.

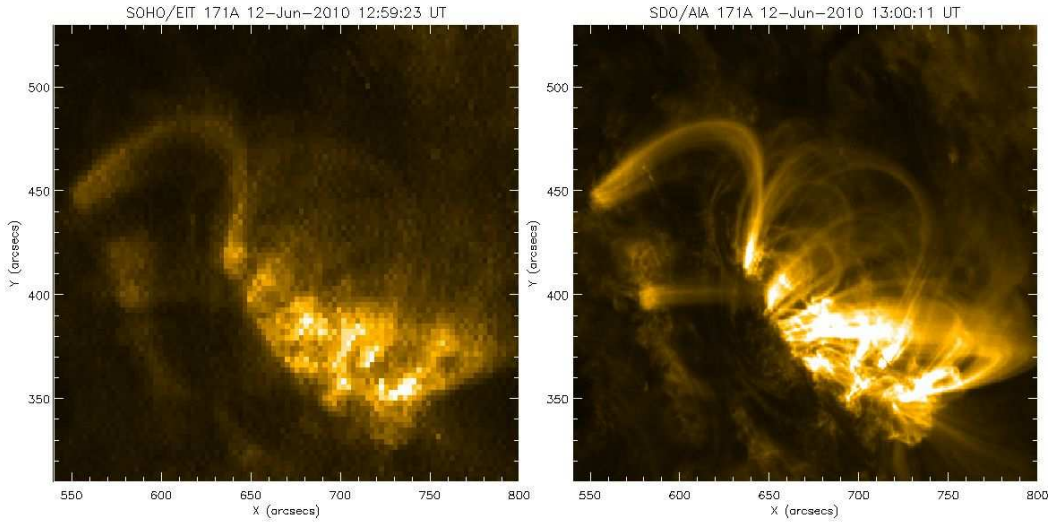

Figure 2.11: Comparison between the SoHO/EIT imager in the 171Å channel (left) and the SDO/AIA imager in the same channel. The feature imaged is an active region located towards the Western limb of the Sun on the 12 June 2010. The difference between EIT's 5" spatial resolution and the 1" resolution of AIA is very apparent. The field-of-view of each image is 260" x 220".

example of this is shown in Figure 2.11 where an active region has been imaged by both SDO/AIA (right) and SoHO/EIT (left) in the 171Å channel. The improvement in spatial resolution from EIT to AIA is very clear.

Figure 2.12 shows a quick-look comparison between SDO/AIA and the other major solar imagers of the last decade. As mentioned previously, EIT is now in semi-retirement due to the launch of AIA. For the same reason, TRACE ceased operations in July 2010.

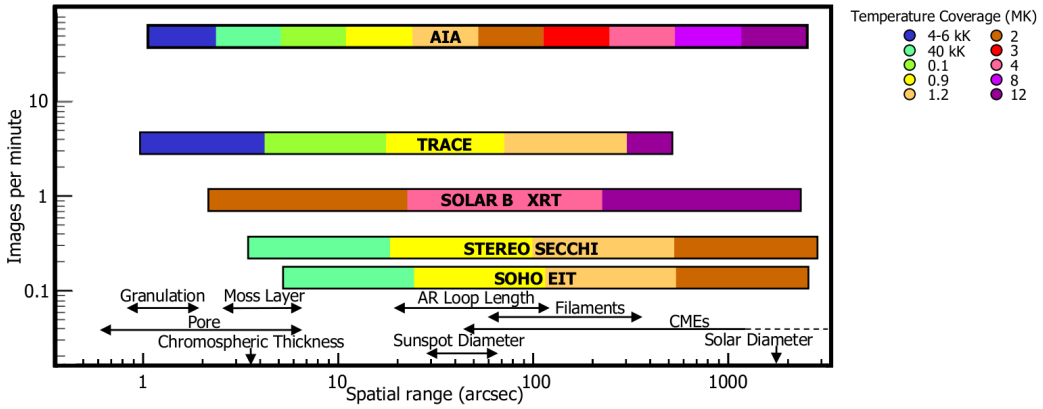

Figure 2.12: Comparison of traits of the five major coronal imagers of the past decade. Image credit: K. Schrijver, LMSAL.

AIA Temperature Response:

The AIA wavelengths and characteristic temperatures listed in Table 2.3 indicate that one or more of the channels may have contributions from multi-thermal plasma. The effect of this is explored by looking at the temperature response of the instrument in the six EUV channels dominated by iron emission. Figure 2.13 shows a plot generated from the aia_get_response.pro routine where each channel's response is calculated from the effective-area functions coupled with the solar emissivity calculated from the CHIANTI (Dere et al. 1997; Landi et al. 2012a) model.

Since the satellite was launched, a number of issues with these response functions have been raised. Aschwanden & Boerner (2011) detailed a problem with the 94 Å channel

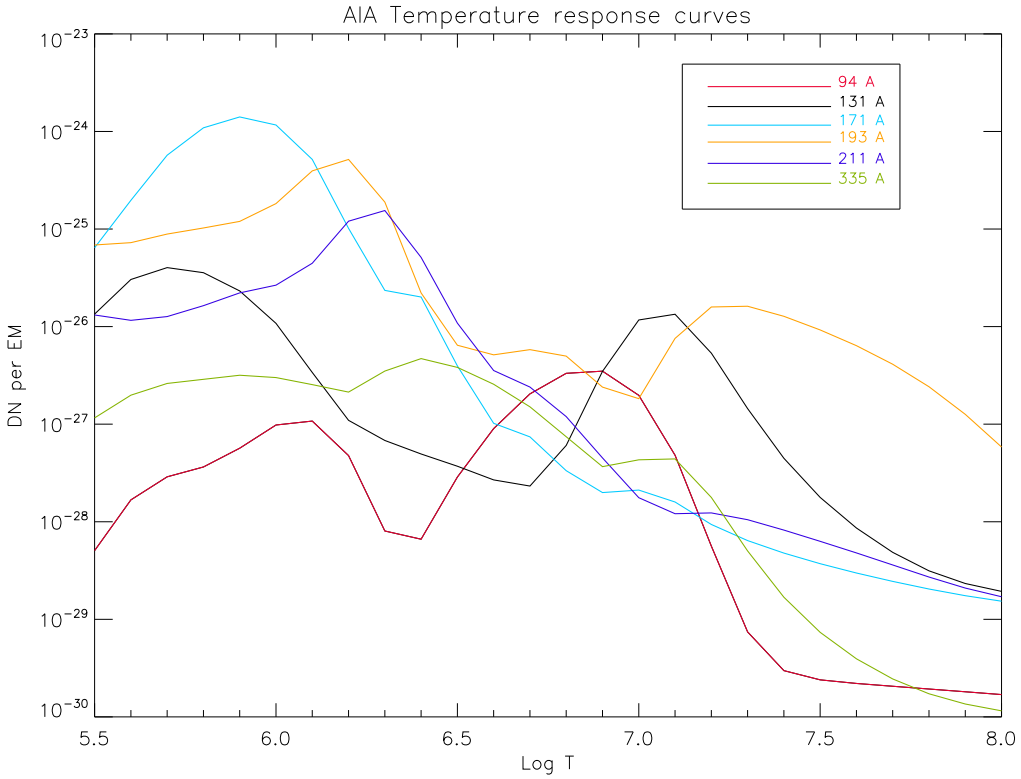

Figure 2.13: Plot of the temperature response functions for the six EUV channels. These functions are generated using the aia_get_response.pro routine within SSWIDL.

where the effect of the lower temperature contribution was questioned. They noted that the double peak in the temperature response function is caused by the Fe x lines at log(T)~6.1 and the Fe xviii lines at log(T)~6.8, but that the strong emission seen at log(T)~6.0 in 94 Å suggests that some of the Fe x transitions are missing from the CHIANTI (v7.0) atomic database code. They offer a correction factor of:

$$q_{94} = 6.7 \pm 1.7 \tag{2.3.1.1}$$

which should be applied to the data as follows,

$$R_{94}(T)^{emp} = \begin{cases} q_{94} R_{94}(T)^{nom} & \text{for } \log(T) \leq 6.3 \\ R_{94}(T)^{nom} & \text{for } \log(T) > 6.3 \end{cases} \tag{2.3.1.2}$$

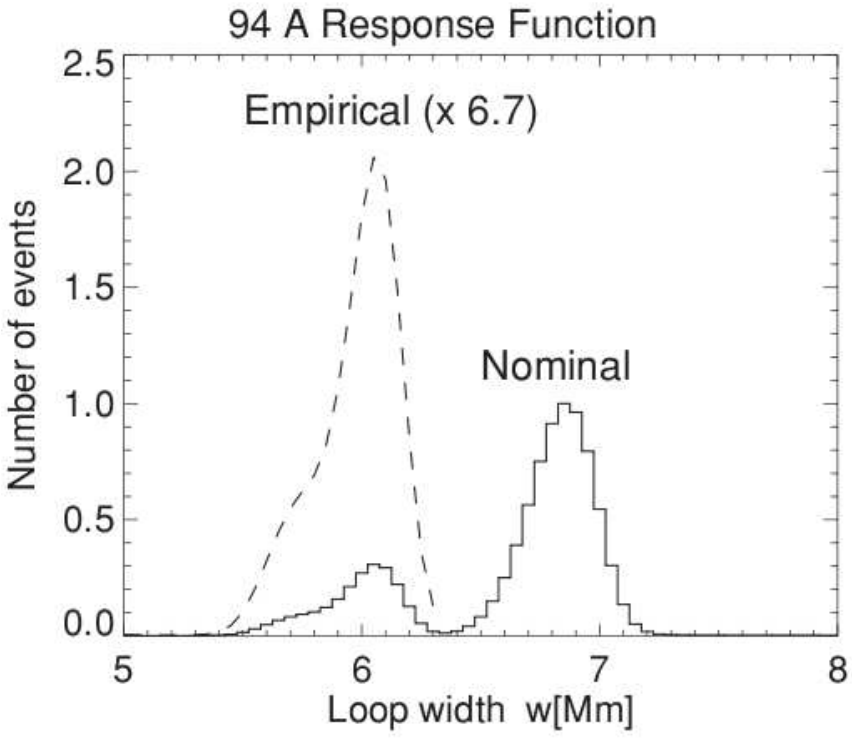

Figure 2.14: Plot from Aschwanden & Boerner (2011) showing the empirical fix applied to the nominal temperature response function in the 94 Å channel using the correction factor given in Equation 2.3.1.1.

As of February 2012, the aia_get_response.pro routine included keywords to update the emissivities to the newest version of CHIANTI (v7.0) as well as offering an empirical fix for the missing emission lines in the 94 and 131 Å channels. Figure 2.15 shows the replotted temperature response curves (calculated with the /chiantifix keyword) as dashed lines over the older values (solid lines). The work in this thesis relating to the AIA temperature response functions was begun before this empirical fix was available. For consistency, all calculations were carried out using the temperature response curves seen in Figure 2.13.

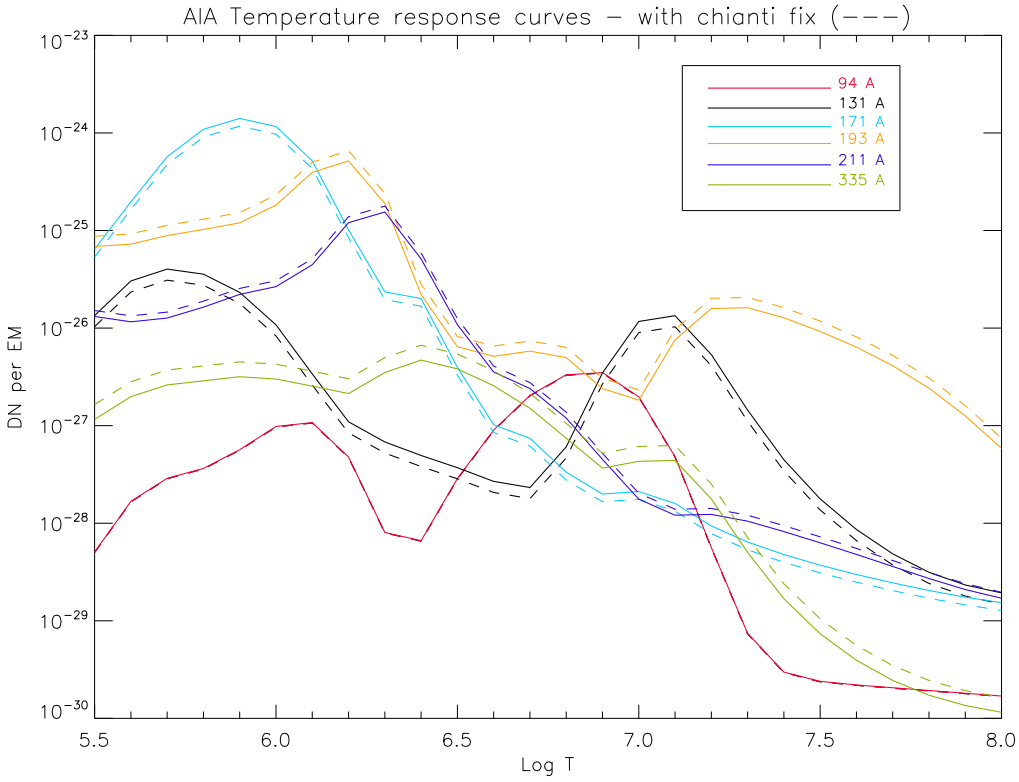

Figure 2.15: Plot of the temperature response functions for the six EUV channels generated with aia_get_response.pro routine and utilising the /chiantifix keyword. Dashed lines are the corrected values with the solid lines representing the nominal responses.

The details of the spectral lines included in each of the AIA channels has been looked at in detail by O'Dwyer et al. (2010) and Del Zanna et al. (2011). O'Dwyer et al. (2010) highlighted the dominant contributions to each filter and how they depend on the region of the atmosphere being imaged (e.g., quiet sun, active region, coronal hole, or flaring

region). They advised caution when using the channels to observe different types of feature as the dominant ion in each case can change. Del Zanna et al. (2011) extended this work and noted that due to the unidentified lines in the 94Å, 171Å, and 211Å channels, as well as the cross-talk identified between the 131Å and 335Å channels, that care should be taken when drawing conclusions from the data. The issue of the uncertainties with the AIA temperature response functions will be further investigated and corrected for in all future work.

2.3.2 HMI

The Helioseismic and Magnetic Imager (Scherrer et al. 2012) onboard SDO is designed to investigate the Sun's interior as well as measure various aspects of the magnetic activity. The instrument makes full-disc observations of the Sun in the Fe I 6173 Å absorption line and can measure oscillations and the magnetic field on the photosphere.

The instrument was developed from the heritage of the SoHO/MDI instrument but has significant improvements in terms of spatial and temporal resolution. HMI produces a full-disc Doppler velocity, line-of-sight magnetic flux, and continuum image every 45 seconds. It also produces vector magnetic field maps every 90-135 seconds depending on the observing run selected. The spatial resolution is ~1" compared to MDI's 4".

Another difference between the two instruments was noted by Fleck et al. (2011) who concluded that the formation height of the spectral line utilised in HMI is slightly lower (~100km above the visible solar surface) than the spectral line used in the MDI instrument (~125km). The Fe I 6173 Å line was chosen for HMI as it is more magnetically sensitive than the Ni I 6768 Å and is better at measuring the vector magnetic field (Norton et al. 2006).

2.4 STEREO

Launched in October 2006, NASA's STEREO (Solar TErrestrial RElations Observatory) satellites are providing a unique view of the Sun from their two vantage points. Launched as a pair, the nearly identical satellites orbit the Sun both ahead (STEREO-A) and behind (STEREO-B) the Earth in order to offer a 3D view of the Sun and the Earth-Sun line. The separation of the satellites is increasing over time (around 22° per year) with the angle of separation between the Earth and each satellite at 116 ° on the 1st of June 2012 (see Figure 2.16).

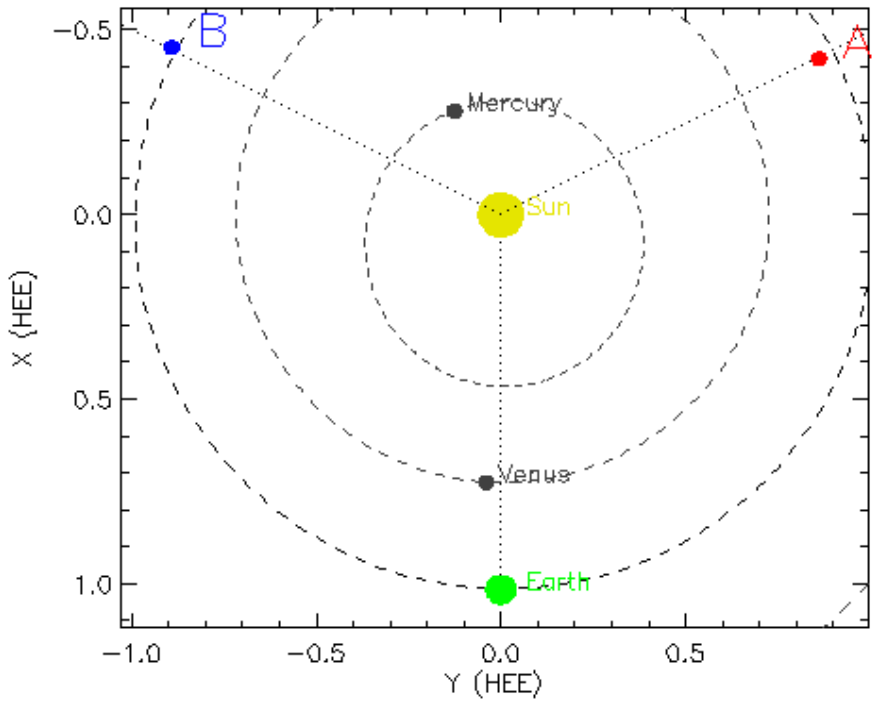

Figure 2.16: Image showing the positions of the STEREO A and B satellites relative to Earth on the 1 June 2012.

The STEREO satellites carry a host of instrument packages identified in Figure 2.17. These packages are named:

- SECCHI: Sun Earth Connection Coronal and Heliospheric Investigation, (Howard et al. 2008)

- SWAVES: STEREO/WAVES, (Bougeret et al. 2008)
- IMPACT: In-situ Measurements of Particles and CME Transients, (Luhmann et al. 2008)
- PLASTIC: PLAsma and SupraThermal Ion Composition, (Galvin et al. 2008)

Details of all these instruments can be found within the relevant references but most are outside the scope of this work. Information on SECCHI/EUVI is detailed here as this instrument was utilised in Chapter 6.

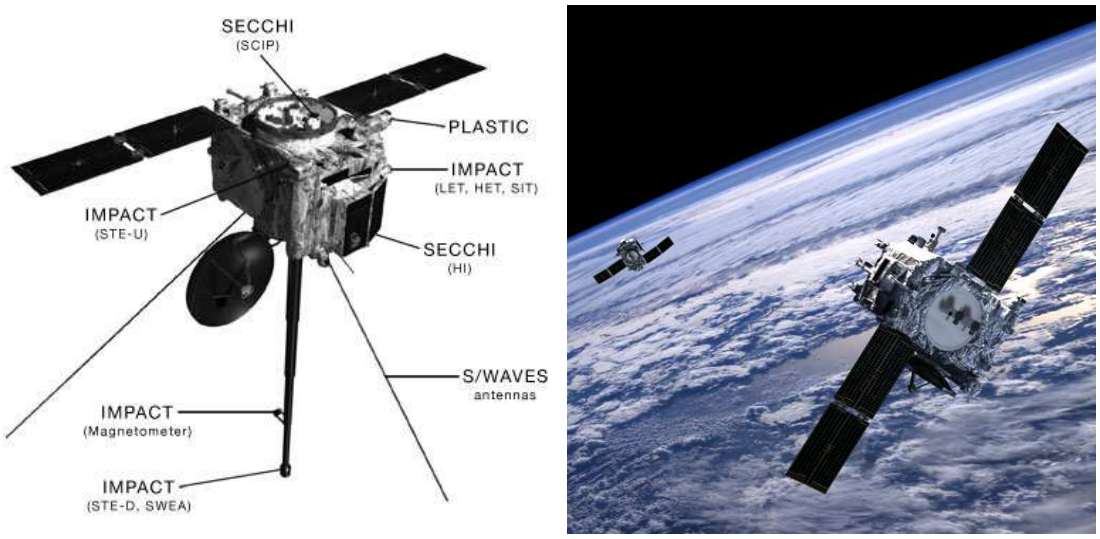

Figure 2.17: Images of the STEREO satellites. *Left:* schematic of the location of the various instrument packages onboard STEREO-A and B. *Right:* artist's impression of the two satellite in orbit before they move apart.

EUVI

The Extreme Ultraviolet Imager (EUVI; (Wuelser et al. 2004)) forms part of the SECCHI instrument package onboard both STEREO satellites. The telescope is designed to image the surface of the Sun in four wavelength channels in order to view structures at different temperatures - particularly areas where Coronal Mass Ejections are thought to have initiated from. The wavelengths imaged by EUVI are the same as those seen by SoHO/EIT i.e., He II 304Å, Fe IX 171Å, Fe XII 195Å, and Fe XV 284Å.

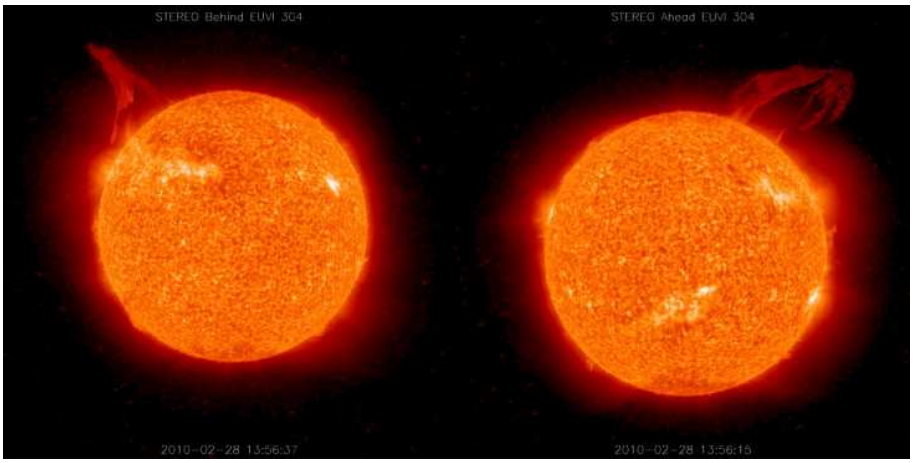

Figure 2.18: Image taken on 28 February 2010 of a prominence seen from the two points-of-view of STEREO/EUVI in the 304Å channel. *Left:* view from the STEREO-B EUVI instrument showing a rising prominence. *Right:* same-time image of the prominence seen by STEREO-A EUVI revealing another perspective. This helps to show the importance of a multi-viewpoint observation as the structure of the prominence is seen differently by both satellites.

The instrument was a significant improvement on SoHO/EIT with higher spatial resolution and temporal cadence, as well as offering a unique dual-perspective of the full solar disc. The spatial resolution of the instrument is ~3.2" (Aschwanden et al. 2008) compared to the 5" resolution of EIT. The temporal resolution of the telescope is also higher than EIT at 4 minutes (compared to 12 minutes). An example of the dual point-of-view of the satellites is shown in Figure 2.18 where a prominence eruption is observed in the 304 Å channel. The apparent structure of the prominence is very different depending on the viewing angle. This shows why the STEREO satellites are so useful for interpreting the 3D morphology of coronal structures.

The temperature response functions for the four EUVI channels are shown in Figure 2.19 where it can be seen the imager covers temperatures between $4.5 < \log T(K) < 7.5$ but that there is a lot of overlap between the each of the four functions (most of which are also very wide). This suggests that the imager can be used to infer temperature but that robust calculations cannot be made based on the imager data alone.

2.5 Future Missions

Our understanding of the solar atmosphere has advanced significantly in the last 10-15 years with observations reaching a higher level of precision every time a new mission is launched. This progress is showing no signs of slowing, with many new and exciting missions planned in the next ten years alone.

A feature a lot of the upcoming solar missions have in common is a shift towards studying the chromosphere. This is an important layer that has been somewhat sidelined by more high temperature observations in the past. The new generation of missions feature instruments which aim to study the dynamic chromosphere/transition region in more detail than ever before in order to study the flow of mass and energy between the different layers of the Sun.

Several of the upcoming missions that are pertinent to the type of work discussed in this thesis are described in Chapter 7 where relevant details of these missions are provided as well as how they could help to facilitate the proposed future work on each topic.

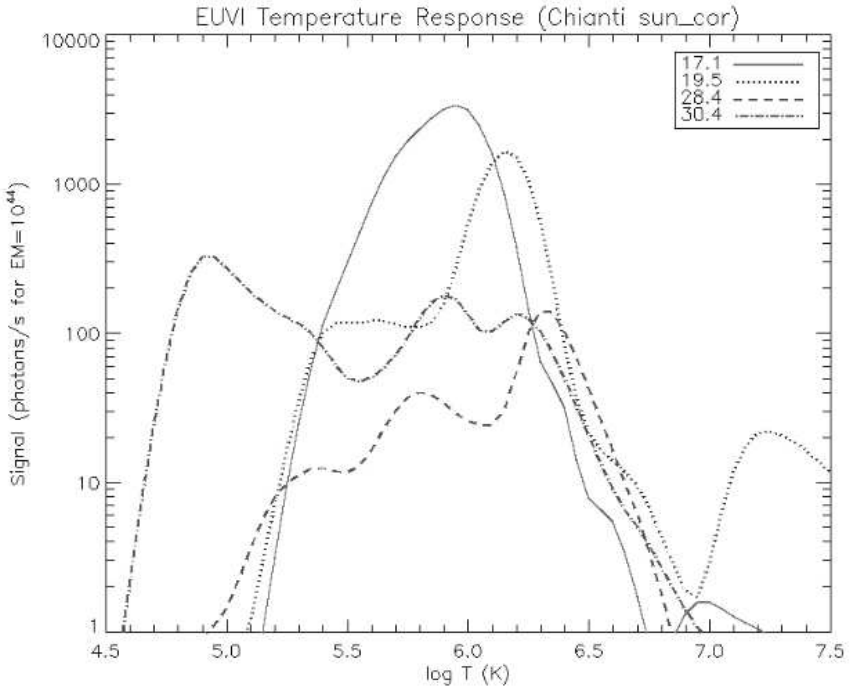

Figure 2.19: EUVI temperature response functions of the four channels. Legend notes channel wavelengths in nm. Graph from Wuelser et al. (2004).

Chapter 3

X-Ray Bright Point work

The corona is an inhomogeneous and dynamic part of the solar atmosphere containing a vast array of features. As previously mentioned, this thesis looks at coronal features ranging from small (a few Mm), to medium (10–100 Mm) and to large (>100 Mm) scale. This chapter showcases an example of a small-scale coronal feature called an X-ray bright point. This work was written up and accepted for publication in January 2011 and all figures and text have been adapted from the article Alexander, Del Zanna, and Maclean 2011. This article and the work presented in this chapter is a full re-analysis and major extension of work begun in Alexander (2008). The latter work involved a preliminary analysis of the XBP at one point in time. Much more detailed analysis, covering a fuller range of topics, is presented in this chapter where the bright point has been analysed over its entire lifetime to study its evolution.

3.1 Introduction

X-ray bright points (hereafter XBPs) were first observed by Vaiana et al. (1970) while studying images of the X-ray corona taken during an Aerobee rocket flight in 1969.

The first detailed study was from Golub et al. (1974) using data from Skylab. They found that XBPs have an average lifetime of 8 hours, an average size of 30", and are composed of a diffuse aspect and a bright core. The enhanced X-ray emission that they exhibit is due to their electron density being typically 2-4 times higher than the coronal average (around 5 x 10^8 cm^{-3}). NIXT (Normal Incidence X-Ray Telescope), as well as TRACE (Transition Region and Coronal Explorer) observations later showed that XBPs are composed of multiple compact loops (see e.g., Brown et al. 2001a; Parnell et al. 1994).

About one-third of bright points are associated with emerging ephemeral regions, while two-thirds are associated with cancelling magnetic fragments (see e.g., Harvey 1985; Brown et al. 2001b). The process of flux emergence and cancellation in connection with XBP occurrence is quite complex, as shown by Harvey et al. (1994): XBPs can occur from magnetic bipoles emerging, cancelling, emerging then cancelling, or even when no visible bipole exists. They also stated that two thirds of all magnetic bipoles observed have no corresponding XBP and that bright points only occur when the magnetic field lines of the bipoles interact and reconnect with the overlying global magnetic field.

As in the general case of the solar corona, it is quite clear that the XBP emission is powered by the release of magnetic energy, however the details are elusive. Various models have been put forward such as the Converging Flux Model (Priest et al. 1994) to explain the interaction of the magnetic field and the creation of an XBP. The model consists of three main stages: (1) "The Pre-interaction Phase" where the two unconnected areas of opposite magnetic polarity approach one another, (2) "The Interaction Phase" where energy is released as the fields of the two areas reconnect creating the XBP, and (3) "The Cancellation Phase" where the fragments cancel each other and disappear. Another possibility is 'stick slip' magnetic reconnection, which should occur along separator field lines and should be associated with sporadic energy releases, as proposed by Longcope (1998).

It is still not clear if XBPs are heated in a steady or impulsive way. For example, Nolte et al. (1979) used X-ray imaging at about 90 seconds cadence for a period of 25 minutes for a few XBPs to show that the emission appeared as steady, although rapid disappearances were found, following brightening. Habbal & Withbroe (1981), on the other hand, found evidence of variations of EUV emission in chromospheric, transition region and coronal lines, on timescales as short as 5.5 minutes (the cadence of their Skylab observations). Some work based on SoHO/CDS and SUMER spectroscopic observations to study XBPs at transition region temperatures followed (see e.g., Madjarska et al. 2003; Ugarte-Urra 2004; Ugarte-Urra et al. 2005).

In this chapter, a case study of one particular X-ray bright point observed with the Hinode satellite over a period of 12 hours is presented. All three instruments onboard Hinode were utilised in order to investigate the measurable physical characteristics of the feature such as temperature, density, filling factor, Doppler velocities, cooling timescales and magnetic field strengths over the entire lifetime of the XBP. Once these measurements have been made, conclusions can be drawn about the likely source of the XBPs heating.

Measurements of EUV coronal line profiles and photospheric magnetic fields, together with estimates of coronal magnetic fields are fundamental to test theories. A large literature exists, however a comprehensive study has been lacking. The suite of instruments aboard Hinode (Kosugi et al. 2007) is extremely well suited to study XBPs for a variety of reasons. First, XPBs small sizes and short lifetimes mean that their entire evolution, from birth to disappearance, can be followed with the Hinode instruments. Indeed, telemetry limitations and high temporal cadence normally constrain the FOV of the Hinode instruments to be of the order of a few arcmin^2, meaning that large regions cannot be observed.

Second, the temporal cadence and spatial resolutions of the Hinode X-Ray Telescope (XRT) and the Solar Optical Telescope (SOT) are higher compared to what was available

with previous instruments. XRT has a resolution of 2” (Golub et al. 2007) while SOT provides imaging and spectropolarimetry at 0.32 and 0.16” resolution, i.e., far superior than what was previously achieved with e.g., the SoHO/MDI instrument.

As described below, SOT data show that the rate of magnetic flux density emergence and cancellation in quiet Sun areas, where most XBPs are formed, occur on timescales much shorter (i.e., minutes) than previously thought (clearly seen in the SOT Movie xbp_sot.mov). Third, the Hinode EIS instrument (Culhane et al. 2007) is far superior than any previous spectrometers flown on satellites in providing accurate measurements of coronal densities and temperatures for XBPs. Also, for the first time it allows detailed studies of line widths and Doppler-shifts in coronal lines, something that has already added a new dimension into the problem of understanding how plasma is heated and cools in active regions (see e.g., Del Zanna 2008b).

The entire Hinode database was surveyed to find a suitable well-observed case to be studied. From the Hinode observations, described in Section 3.2, the physical properties of an XBP such as density, temperature, velocity flows, magnetic field strengths were obtained for its entire lifetime. Cooling times were also estimated. This is the first time that such a complete set of physical parameters has been presented for the entire lifetime of an XBP.

As regards measurements of electron temperatures, in most previous literature they were obtained with broad-band filter ratios, which are inherently subject to large uncertainties. A few more direct measurements using spectral lines exist, however this is the first time that the emission measure loci (EML) method (see Section 3.3.1) is applied to measure the temperature of an XBP at different times over the feature’s lifetime.

Few results exist in the literature regarding direct measurements of XBP electron densities at coronal temperatures. In most cases, only measurements at one point in time are provided, whilst here several measurements which span the lifetime of an XBP are calculated.

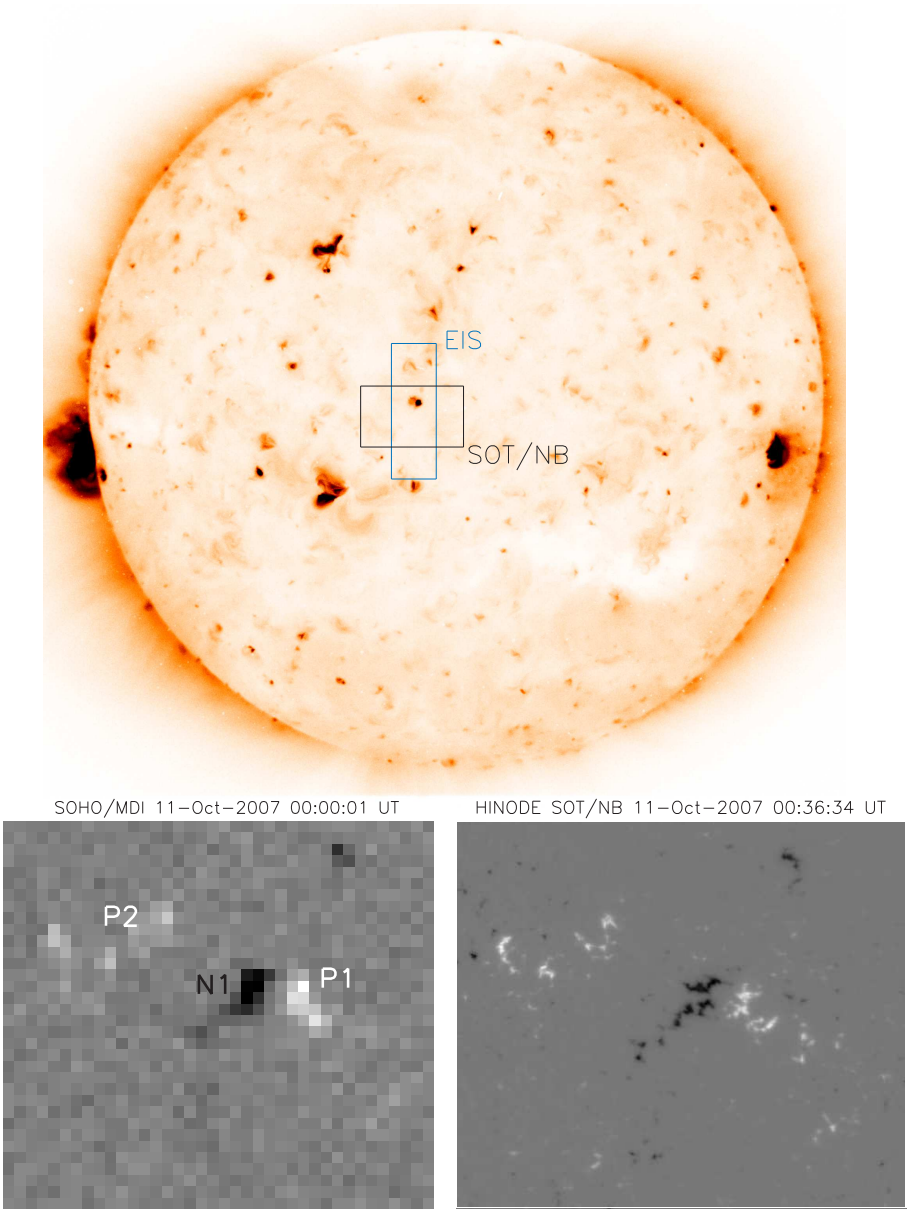

Figure 3.1: The top panel shows a negative image of full disc XRT Al_poly/Open filter showing the location of the XBP at 00:07:11 UT on 11 October 2007. The over-plotted boxes show the EIS and SOT full fields of view. The lower left panel shows SOHO/MDI data with the three magnetic source regions labelled as they are referred to in the text. The lower right panel shows same-time SOT/NFI data. The field-of-view of both lower images is 100" x 85".

In most cases, estimates of cooling times have not been based on direct measurements of densities and temperatures. For example, Habbal et al. (1990) assumed the temperature was the peak formation temperature of the lines, while the density was estimated from an assumed constant pressure. Also, most previous estimates of radiative losses have used power-law fits, whilst here the coronal radiative losses with the latest atomic data (CHIANTI v.6) have been calculated.

In terms of Doppler-shifts, very few previous measurements of XBPs exist in the literature. A few measurements from SoHO/SUMER (e.g., Madjarska et al. 2003) have been published, but were limited to low-temperature lines. Brosius et al. (2007) provided Doppler measurements at 'coronal' temperatures during an EUNIS rocket flight, but lacked spatial and temporal information.

Pérez-Suárez et al. (2008) presented one Dopplergram in Fe XII from a single observation, and found spatially-variable red and blue-shifts. Here, for the first time a complete sequence of Dopplergrams of an XBP is presented. It has been unclear whether the observed velocities are a direct measure of reconnection outflows or if they are signatures of chromospheric evaporation, or something else entirely.

To gain an additional perspective on the processes at work, the similarity of the X-ray structure of the XBP was compared to a potential field model. This work was done by Dr Rhona Maclean (previously of the University of St. Andrews) and is presented in Section 3.3.5 where the evolution of the coronal magnetic field with potential field extrapolations is modelled, and Section 3.4.2 where a discussion is given on the energetics and correlations between magnetic fields and coronal emission.

3.2 Observations and data analysis

The online Hinode SDC Europe Archive was used to search for good observations of XBPs. The criteria were that the XBP should be well within the field-of-view of the Hinode instruments and observed over many hours. Here, the results concerning one such XBP are presented. The X-ray bright point studied here was observed with Hinode between 2007 October 10 18:45 UT and 2007 October 11 07:17 UT. Figure 3.1 shows the location of the XBP on the 11th October 2007, in a quiet Sun region close to Sun centre. This position makes line-of-sight analysis more accurate.

The Hinode observations consist of a long sequence of XRT, SOT and EIS observations. The Hinode spacecraft in its normal mode tracks a solar feature, as the Sun rotates, so in theory the FOV should be the same over time for the various instruments. However, thermal changes along the orbit affect each of the instruments in different ways, creating a considerable 'jitter' of a few arcseconds over short (minutes) time-scales. The fact that the pointing of the instruments is not stable requires a significant amount of extra analysis, described below.

3.2.1 XRT

The XRT data considered here were taken with the Al-poly/Open filters and a FOV of 384" x 256". The XRT has a lower energy X-ray cut-off than the SXT (Soft X-Ray Telescope) aboard Yohkoh meaning that the XRT can observe coronal plasma with temperatures of 1 x 10^6 K or lower (Kosugi et al. 2007).

The data were processed using XRT_PREP and the XRT jitter has been corrected for by cross-correlating successive images. The pointing of the partial-frame images were obtained by cross-correlating with available full-disc data. The pointing of the partial-frame images is susceptible to error due to spacecraft movement. In order to correct

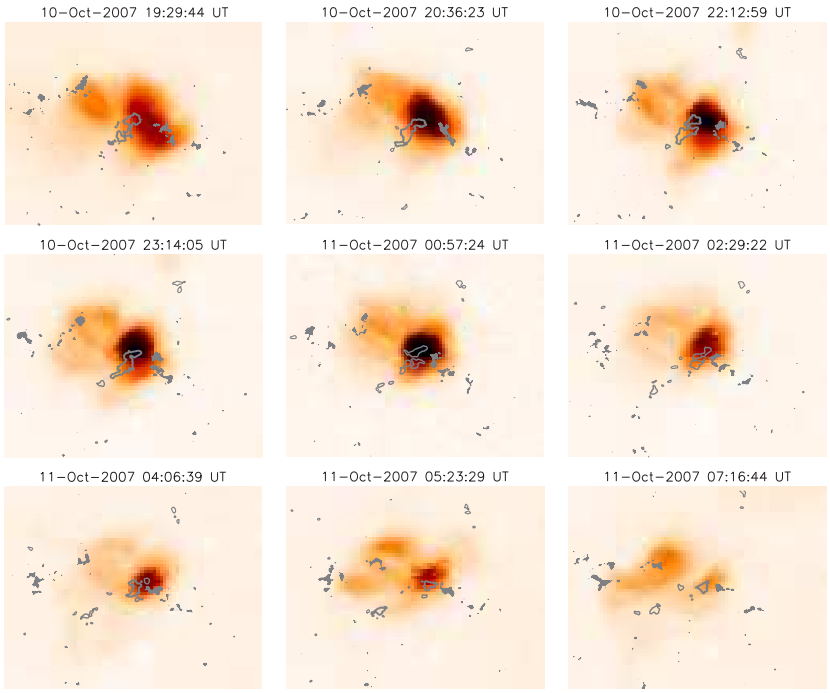

Figure 3.2: Evolution of negative XRT images with co-aligned SOT contours overlaid. Unfilled grey contours indicate negative magnetic flux and the filled grey contours represent positive flux (contours are at level ±250 G). The FOV is 80” x 70”.

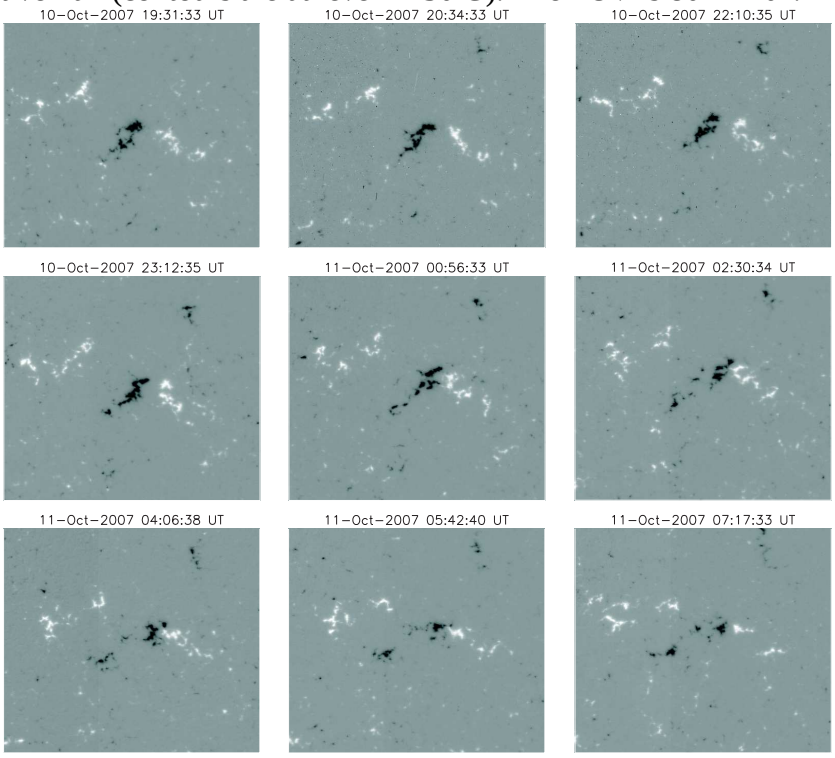

Figure 3.3: Hinode SOT/NFI Stokes V filtergram images of the bright point during times corresponding to those of the X-ray XRT images of Fig. 3.2. The FOV is 80” x 70” and the range of the data is ±350 Gauss.

for this, each partial-frame image must be aligned with a similar full-disc image. The pointing of the full-disc images can be trusted more due to the visible limb offering context. In the case of XRT, each partial-frame image was compared to a same-time full-disc XRT image (or a SoHO/EIT 195 Å image if no full-disc XRT was available). By matching up the features, the partial-frame images can be corrected to full-disc pointing. Figure 3.2 shows a sequence of XRT images (negative) over a time-span of 12 hours. The XBP was composed of two main areas, a compact bright structure (size ∼10 Mm) and a secondary, fainter loop system to the East. The secondary one is clearly increasing in brightness as the XBP evolves.

3.2.2 SOT

The SOT observed the XBP with both the Narrow-band Filter Imager (NFI) and the Spectropolarimeter (SP). The NFI was used in the narrowband (NB) mode, where imaging in the V, I Stokes parameters is performed in the Na I line. The FOV was 276" x 164" and the temporal cadence was about 1 minute. The filtergram (FG) data were processed using the standard processing routine FG_PREP. The Stokes I and V data were used to obtain, as described below, line-of-sight (LOS) magnetic field density maps. The SOT has an internal mechanism which can track solar features. Despite this, a considerable 'jitter' of a few arcseconds over short (minutes) time-scales is still present in both the SP and FG data. This jitter in the FG data was corrected for by cross-correlating successive images. Figure 3.3 shows a selection of these images with the same FOV and timings of the XRT images of Figure 3.2 for comparison.

As with the partial-frame XRT images, the SOT/FG Stokes V images are likely to have slight errors in their pointing values. This can again be corrected for by aligning each SOT magnetogram with a same-time SoHO/MDI LOS magnetogram which has more accurate pointing values as it is full-disc. The pointing of the full-disc images was

obtained by fitting the visible limb. The features of the bright point seen in each magnetogram can easily be matched up in order to check how misaligned each partial-frame image is and correct for it.

Figure 3.1 shows two near-simultaneous observations of SoHO/MDI and Hinode SOT/NB. Notice the striking difference in resolution between the full-disc MDI and SOT/NB. Once all the corrections were applied, and the FOV reduced, a movie of the SOT/FG V images was made (see Movie xbp_sot.mov). Notice in Figure 3.2 that the brightest part of the XBP is associated with the largest magnetic fragment concentrations, which are converging and cancelling over time. The fainter XRT loops connect the main negative polarity (N1) with the fragments of positive polarity located NE of the main feature (P2).

The SOT contours in Figure 3.2 are coloured to show the different polarities (unfilled grey contours for negative flux, and filled grey contours for positive flux). It can be seen that over time the main negative polarity splits into two segments: one that goes on to cancel with the west positive fragments (P1), and one that moves towards the secondary positive fragments in the east (P2). It can be seen that the bright point does not occur exactly in-between the cancelling magnetic features as one would expect. The XBP seems to be concentrated over the central area of negative flux which is most likely due to the influence of the secondary positive flux fragments. It may also be a line of sight difference between the fragments which are observed on the photosphere and the XBP on the corona.

The SP provides the line profiles in all Stokes parameters (I, Q, U, V) and is sensitive to magnetic flux of 1-5 Gauss (longitudinal) and 30-50 Gauss (transverse) (Tsuneta et al. 2008). The SP performed various scans over the XBP, with the 0.16” slit over a FOV of 157” x 162”. The data can provide vector magnetograms but there are drawbacks in using the SP data: the long time (typically 30 mins - 1 hour) to scan an area means fast-changing features are missed, and the thermal/orbital effects that exist are difficult

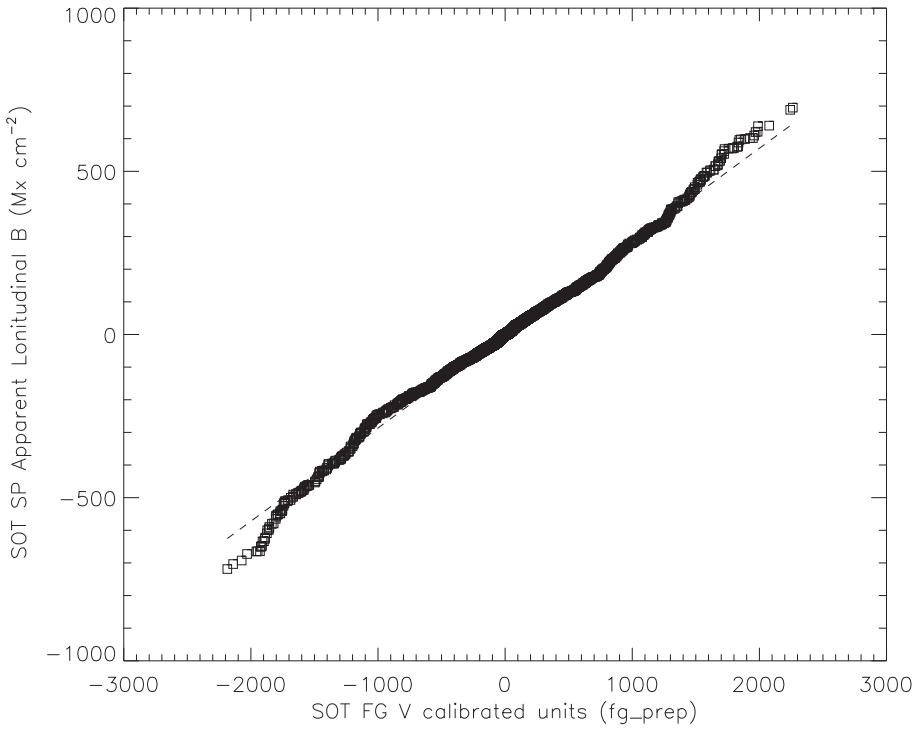

Figure 3.4: Graph showing linear relation between SOT/SP data and SOT/NB data used for calibration.

to correct for.

The SP data was processed in the standard way within SolarSoft. This processing makes various corrections, including an approximate one for the instrument jittering, and provides apparent longitudinal and transverse magnetic field density maps. The SP longitudinal maps were then used to calibrate the NFI data. A section of the SP longitudinal map that passed over the XBP took approximately 15 minutes to be rastered over. Averaged FG V, I images were obtained during this time and used to obtain a calibration of the FG data using the apparent SP longitudinal map. Firstly, the FG data were re-binned to the same spatial scale as the SP data. Secondly, the two datasets were co-aligned, and an area centred on the XBP selected. Then, a linear correlation between the SP density and the V/I values was performed (see e.g., Chae et al. 2007). This linear relation can be seen in Figure 3.4.

Small discrepancies between the SP and FG dataset are present, due to the different scales and method of observations, as well as the fast temporal evolution of the magnetic

fragments. The calibration leaves an uncertainty of the order of 10-20 Gauss. It was found that the stronger magnetic fragments (i.e., the main polarity fragments labelled P1 and N1 in Figure 3.1) have typical flux densities of 100–250 Gauss.

3.2.3 EIS

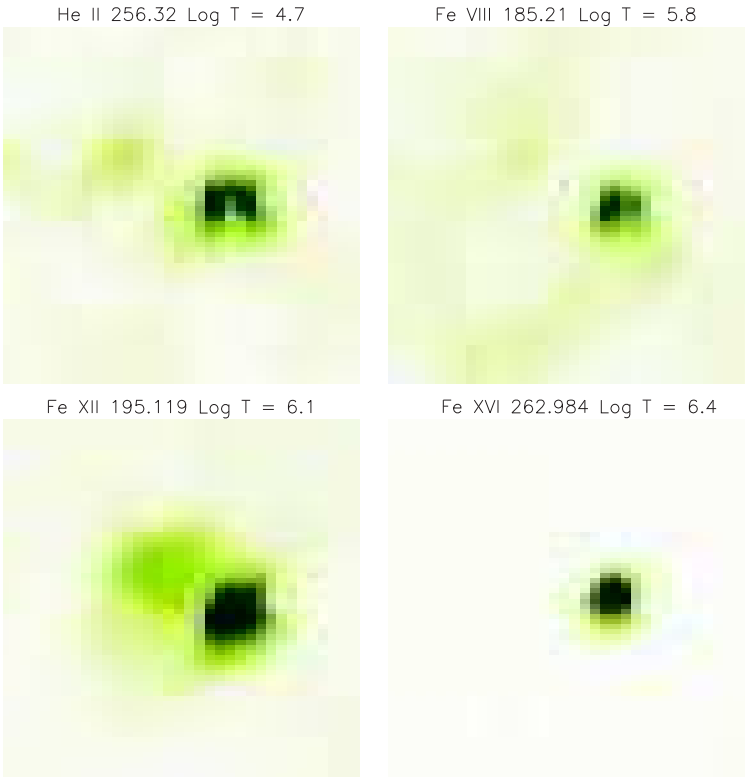

Figure 3.5: Negative EIS intensity maps of the XBP in different spectral lines observed on 11-Oct-2007 at 00.10.47 UT. The FOV is 70” x 70”.

The EIS instrument aboard Hinode observes emission lines with wavelengths in the ranges 165–211Å and 246–291Å (Culhane et al. 2007). EIS is used to measure line intensities, Doppler velocities (i.e., to show plasma flows), temperatures and densities in the upper transition region and coronal part of the solar atmosphere. The spatial resolution is only of the order of 3-4”, however the spectral resolution is very high and allows measurements of Doppler-shifts of only a few km s^{-1}.

The EIS observations were successive repetitions of an EIS study (CAM_QS_2AS_CONTEXT) which was designed by Dr Giulio Del Zanna, as part of a campaign to observe the quiet

Sun. This study included 32 spectral windows and lines formed over a range of temperatures. The 2" slit covered a field of view of 120" x 360" with an exposure time of 30 seconds. The time between successive files was 30 minutes with a total of 22 rasters being performed.

The SolarSoft routine EIS_PREP was used to process the raw data. The *cfit* package (Haugan 1997) was then used to fit Gaussian profiles to all the lines observed, using custom-written programs to obtain intensity, position and width.

Ion	λ(Å)	Waveband	Region	log T_{max}(K)
He II	256.320	lw	Chromosphere	4.9
O V	192.910	sw	TR	5.4
Fe VIII	185.216	sw	Low Corona	5.6
Si VII★	275.35	lw	Corona	5.8
Mg VII★	278.395	lw	Corona	5.8
Fe X★	184.543	sw	Corona	6.0
Fe XII	186.880	sw	Corona	6.2
Fe XII★	195.119	sw	Corona	6.2
Si X★	261.056	lw	Corona	6.2
Fe XIII★	202.044	sw	Corona	6.2
Fe XV★	284.160	lw	Hot Corona	6.4
Fe XVI★	262.984	lw	Hot Corona	6.8

Table 3.1: Some of the prominent EIS lines present in the CAM_QS_2AS_CONTEXT study used. TR refers to the transition region while SW and LW refer to the short and long wavebands of the EIS CCDs. The approximate temperature $T_{\max}$ of line formation is also shown.★ indicates that these lines were used in the Emission Measure Loci discussed in Section 3.3.1.

The line fitting produced information on 32 spectral lines and from these results, a few lines were chosen to be looked at in more detail. These lines, along with their wavelengths and approximate temperatures, are shown in Table 3.1. These lines show how the features of the bright point change at different wavelengths and represent the XBP from the chromosphere, through the transition region to the corona.

The EIS instrument has a complex internal and external jittering to which only some corrections can be applied. This was done by co-aligning the monochromatic EIS images in the hot lines with XRT images taken at similar times. The co-alignment is very

accurate (1–2”), however the fast jittering of the EIS instrument while it scans means that locations of EIS features can only be obtained with an accuracy of 3-4”.

As described in Del Zanna (2008a), one of the problems in the analysis of EIS data is the offset in both N-S (18”) and E-W (2”) directions between the two channels. The offset in the E-W direction means that observations in the two channels are not simultaneous nor co-spatial however this only affects rapid variations and not the observations considered here.

Figure 3.5 shows monochromatic images of a selection of EIS lines. The primary part of the XBP is very compact in the hottest lines (e.g., Fe xvi). The transition region lines (e.g., Fe viii) and particularly the chromospheric He ii consistently show a bipolar structure in the main body of the XBP, which can be interpreted as the footpoint locations of the (unresolved) system of hot loops. The strong He ii 256.32 Å line (seen in the top-left panel of Figure 3.5) is blended with many coronal transitions, from Si v, Fe xiii, Fe xii, and Fe x at least, the dominant one being Si x.

However, at the footpoints of coronal loops, the He ii emission is so bright that blending with coronal lines can become negligible. Indeed the morphology of this line is similar to that of lines formed in the transition region. This morphology is also similar to that noticed by Kankelborg et al. (1996) in the high-resolution (1”) images obtained by the MSSTA rocket. XBPs have associated very strong neutral hydrogen Lyα emission, often resolved as a pair of footpoints. Fe xii 195.119 has the most intense emission suggesting that the bright point has a maximum temperature within the range $6.1 \leq \log T/K \leq 6.3$ and very little plasma emitting above 3 MK. The secondary loop structure to the east of the main bright point is also clearly shown in this image.

3.3 Results

3.3.1 Temperatures

The temperature of the XBP was investigated using the emission measure loci (EML) method (see e.g., Jordan et al. 1987; Del Zanna et al. 2002). Figure 3.6 shows an example of one of the 22 plots that was made for each time-step. It was constructed by plotting the ratio of the background-corrected intensity values of the bright point in eight strong emission lines (see Table 3.1) with the calculated contribution function, and plotting these against an array of temperatures as shown in the equation:

$$EM(\lambda, T) = \frac{I_\lambda}{G(\lambda, T)} \tag{3.3.1.1}$$

where EM is the emission measure of a spectral line (at wavelength λ) at a given temperature (T), I_λ is the background corrected intensity measurement in that spectral line, and G is the contribution function calculated for that spectral line over a range of temperatures. See Del Zanna et al. (2002) for a more detailed discussion on the various ways in which to define emission measure.

In order to determine the temperature where the greatest number of intersections occurred, a simple histogram plot was made (Figure 3.6 lower panel). This histogram has a bin size of log T/K = 0.05 and clearly shows that the specific temperature of log T/K = 6.05 has the most intersections. This method was applied to each of the 22 EIS files studied and it was found that over the time period (12 hours) the XBP was nearly isothermal (i.e., each histogram was constricted to a narrow temperature range) with an average temperature of 1.3 MK. The crossing point of the EM loci curves was found to shift slightly from file to file meaning the indicated temperature varied from 1.2-1.7 MK. The ionization equilibrium values of Mazzotta et al. (1998) were used, together

with elemental abundances of Grevesse & Sauval (1998).

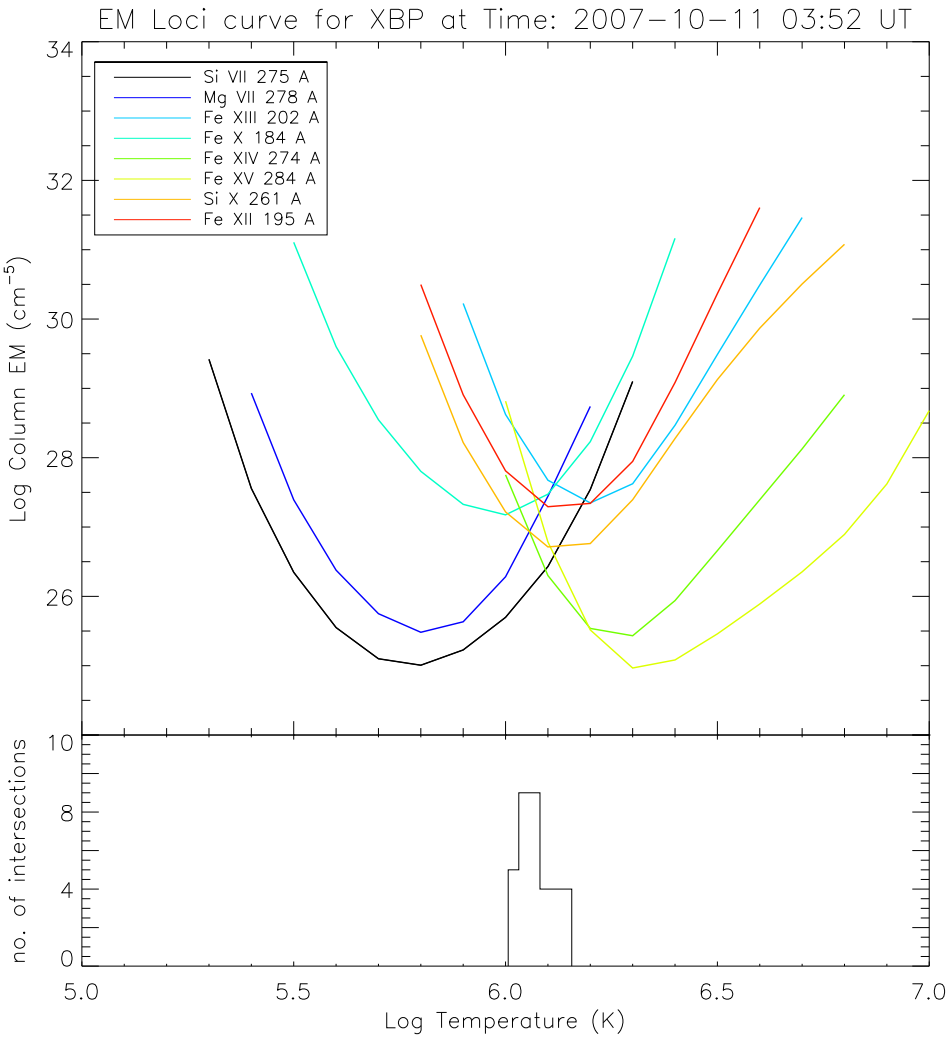

Figure 3.6: Example Emission Measure Loci curves of the XBP for temperature analysis made with information from eight EIS spectral lines. The lower plot shows a histogram of the location of the intersections of the loci curves. This example indicates the plasma is near-isothermal at log T/K = 6.05. The degree of isothermality is inferred from the tight distribution of the histogram over the temperature range.

The EML method is a direct and accurate way of determining the plasma thermal distribution, although it still relies on the accuracy of the atomic calculations and on the validity of ionization equilibrium in a low-density plasma. One important result of the EML method is that the XBP was nearly isothermal during its entire lifetime. It should

be noted that the assumption that a plasma's temperature can be inferred from the characteristic temperature of the spectral line in which it can be seen is not consistent with the data here. In this case the temperature of the bright point is found to have an average value of 1.3 MK even though it can be seen in much hotter lines such as Fe XVI 262.98 Å which is formed around 2.5 MK. This point is made to advise caution when interpreting temperature results.

3.3.2 Electron densities and spectroscopic filling factors

The CHIANTI (v6) package (Dere et al. 1997; Landi et al. 2006) was used to calculate the density of the central part of the bright point using the Fe XII (186.854 + 186.887 Å) / (195.119 + 195.179 Å) line intensity ratio, with the values of intensity corrected for background emission. The variation of this line ratio with density is shown in Figure 3.7.

This calculation was done for each of the 22 EIS rasters. The density of the bright point was found to have an average value of 5±1 x $10^9 cm^{-3}$, although it did decline by around 40% in the last hour of the data set (see Table 3.2), when the main part of the XBP became faint. It should be noted that the Fe XII lines used here often produce densities higher than other ions (see e.g., Young & Landi 2009), when densities are of the order of $10^{10} cm^{-3}$ or more, so it is possible that the XBP electron densities are slightly overestimated here.

The XBP densities are, however, similar to those found in the literature. For example, Ugarte-Urra (2004) used various instruments on-board SoHO to observe two bright points. For one of the XBPs they used the Si IX (349.86/345.10) line ratio to calculate a density value of ~5 x 10^8 cm^{-3} which they found to be in agreement with the result of Del Zanna & Mason (2003) for a similar bright point.

Ugarte-Urra et al. (2005) measured electron densities for six bright points observed

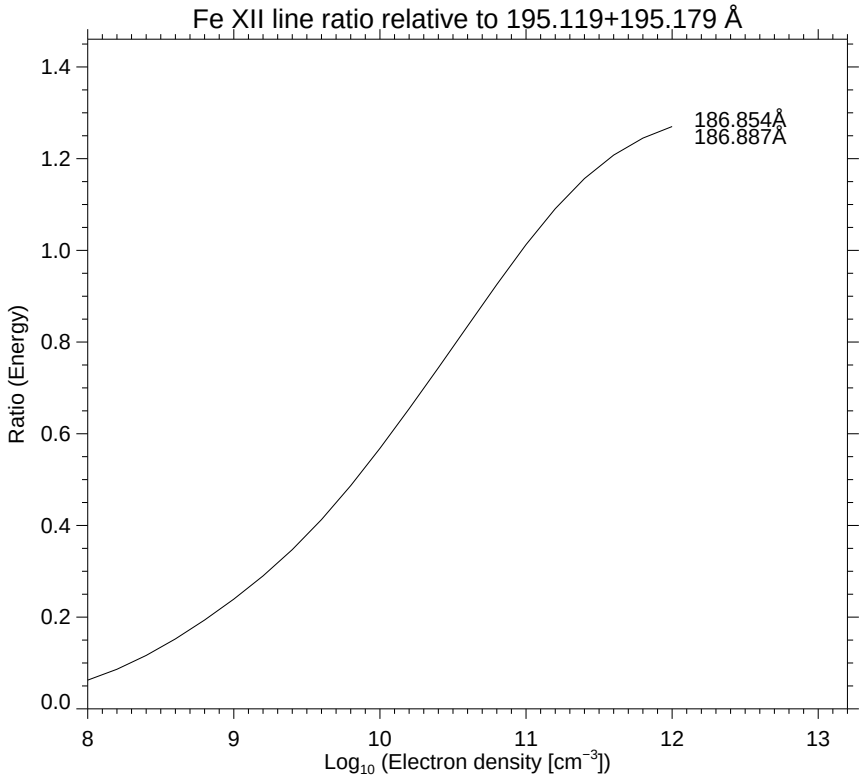

Figure 3.7: Plot showing the variation of the Fe XII ratio (186.854 + 186.887 Å) / (195.119 + 195.179 Å) with plasma density. This plot was generated using the CHIANTI (v7.0) DENS_PLOTTER procedure.

with SoHO/CDS, obtained with a range of ions. Values ranged between 10^9 and $10^{9.9}$ cm^{-3}. Pérez-Suárez et al. (2008) found values around $10^{9.5}$ cm^{-3} for one XBP using Hinode/EIS lines from Fe xii and Fe xiii. Tian et al. (2008) found values around $10^{9.4}$ cm^{-3} for one XBP using a few Hinode/EIS line ratios. Dere (2008) and Dere (2009) used the Fe xii ratio to provide densities for several XBPs which were also in-line with these values.

Using the densities calculated from the Fe xii line ratio together with the calibrated intensity seen with EIS Fe xii 195.119 Å, an estimate of the spectroscopic filling factor for the bright point in each EIS raster can be made. The average filling factor for this bright point was found to be 0.04. This is in excellent agreement with the results of both Dere (2008) and Dere (2009) who studied various quiet sun coronal bright points using EIS. The filling factor was found using the equation:

$$I = 0.86\, G(T_{\max})\, N_e^2\, f\, w \qquad (3.3.2.1)$$

where I is the intensity (ergs cm^{-2} s^{-1} sr^{-1}) of the Fe xii 195.119 Å, G is the contribution function (ergs cm^3 s^{-1} sr^{-1}), N_e is the electron density (cm^{-3}), f is the filling factor, and w is the width of the XBP along the line of sight (cm). Approximating that the depth of the bright point is equal to the observed width, this width at different times was found by using the method described by Dere (2008). This defines the width of the XBP as the width of the feature at half the maximum intensity (see Figure 3.8).

In Dere (2008) an average density of $4x10^9$ cm^{-3} and an average filling factor of 0.015 was found. Dere (2009) used the better spatial resolution of TRACE to recalculate the bright point widths of the same data set (plus an additional EIS raster) and found a lower average density of $3x10^9$ cm^{-3} and an average filling factor of 0.04.

Table 3.2 shows a summary of the values of filling factor found for the bright point over the time series as well as listing information on how the other plasma parameters of the

XBP changed over time.

File	Time	$I_{\lambda 195}$	N_e	log T_e	w	f
		(ΔI=0.1I)	(ΔN_e=0.2N_e)	($\Delta log T_e/K$=0.1)	(Δw=2)	(Δf=0.15f)
1	18:45:27	1201	3.89×10^9	6.15	11	0.094
2	19:17:11	978	3.89×10^9	6.15	10	0.102
3	19:48:56	999	3.89×10^9	6.14	12	0.077
4	20:20:40	1026	5.01×10^9	6.08	13	0.049
5	20:52:24	1498	6.31×10^9	6.08	12	0.038
6	21:24:08	1173	6.31×10^9	6.17	14	0.031
7	21:55:52	947	6.31×10^9	6.08	16	0.025
8	22:27:36	1023	6.31×10^9	6.17	12	0.032
9	22:59:19	856	5.01×10^9	6.23	13	0.029
10	00:10:47	1126	1.00×10^{10}	6.15	12	0.016
11	00:42:31	866	6.31×10^9	6.09	7	0.038
12	01:14:15	922	5.01×10^9	6.08	8	0.060
13	01:45:59	867	6.31×10^9	6.11	9	0.040
14	02:17:43	902	3.89×10^9	6.13	13	0.051
15	02:49:28	705	3.89×10^9	6.12	10	0.055
16	03:21:11	744	5.01×10^9	6.10	14	0.024
17	03:52:55	580	5.01×10^9	6.07	15	0.023
18	04:24:39	506	3.89×10^9	6.08	15	0.025
19	04:56:23	452	5.01×10^9	6.08	14	0.019
20	05:28:07	362	3.89×10^9	6.12	15	0.023
21	06:32:27	216	2.51×10^9	6.14	16	0.031
22	07:04:11	165	1.99×10^9	6.07	15	0.034

Table 3.2: Values calculated for the 22 EIS files observed over the 10-11 October 2007. Intensities ($I_{\lambda 195}$) observed in the Fe XII 195.119Å line are in ergs cm^{-2} s^{-1} sr^{-1}, densities N_e in cm^{-3}, temperatures T_e in K, and widths (w) of the XBP observed by EIS (see Figure 3.8) are given in arcseconds. The filling factor (f) for each time is also shown.

The errors calculated for each measurement are also given in this table. The error on the Intensities ($I_{\lambda 195}$) observed in the Fe XII 195.119Å line were estimated at 10% due to the level of background noise in the data. This uncertainty is carried forward into the density calculation which is based on the ratio of two values of intensity (so therefore has an uncertainty of 20%). The uncertainty in the temperature measurements was estimated as the size of two temperature bins in log T space where the location of the EM loci curves was evaluated. The temperature bins were log Δ T/K = 0.05 in size so the uncertainty on each temperature estimate is ±0.1 log T/K. The uncertainty in the width of the XBP was estimated as one EIS pixel which is 2". Since the average width of the XBP was

15” this was approximated as an error of 15%. These percentage uncertainties were then combined to find the uncertainty in the filling factor which is based on measurements of intensity, density squared and width. The resulting uncertainty for the filling factor was found to be 12%.

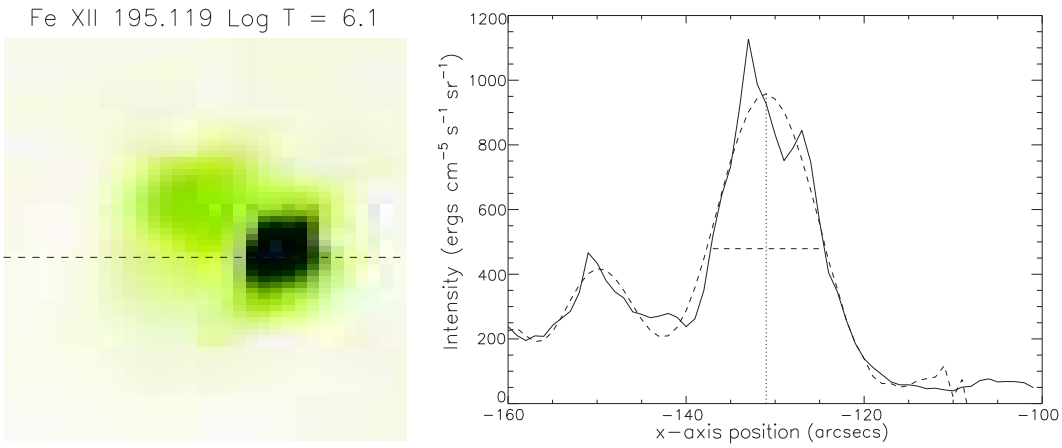

Figure 3.8: Example showing how the width of the XBP was calculated. The left figure shows an EIS Fe XII 195.119 Å image with a cross-section taken through the middle of the bright point. The right figure is the intensity plotted along this cross-section. A fit of the curve was made and the FWHM of this curve was determined to be the width.

3.3.3 Timescales of energy losses

With the information already calculated it is trivial to calculate the timescales of energy losses within the XBP. This will give a more thorough view of the processes at work within the XBP. The timescale for radiative losses is given by the following equation:

$$\tau_{\mathrm{R}} = \frac{3\, N_{\mathrm{e}}\, k_{\mathrm{B}}\, T_0}{N_{\mathrm{e}}^2\, \Lambda(T_0)} \qquad (3.3.3.1)$$

This timescale represents how long a feature should last if its primary method of energy loss is through radiation. In the equation, $\Lambda(T_0)$ stands for the radiative loss function (ergs cm^3 s^{-1}). This was calculated using the CHIANTI RAD_LOSS procedure. Also in the equation, T_0 represents the measured temperature, k_B represents Boltzmann’s constant, and N_e is the measured electron density.

The equation to calculate the timescale of the bright point if its primary method of energy loss is through conduction is given by the following equation:

$$\tau_{\mathrm{C}} = \frac{3\, N_{\mathrm{e}}\, k_{\mathrm{B}}\, T_0}{K_{\mathrm{c}}\, T_0^{-7/2}\, L^{-2}} \qquad (3.3.3.2)$$

In this equation K_{c} represents the coefficient of classical heat conductivity and has a value of 8 x 10^{-7} ergs $cm^{-1}s^{-1}$ $K^{-7/2}$. The L represents the approximate size of the bright point in centimetres and was valued at 1.09 x 10^{9}cm for a bright point of 15" size.

The results of these timescale calculations at three instances over the XBP observations are given in Table 3.3. An additional entry is shown in order to compare these cooling timescales with a similar bright point studied by Ugarte-Urra (2004).

Ion: source	N_e (cm^{-3})	$\Lambda(T_0)$ (ergs cm^3 s^{-1})	T_0(K)	τ_R (s)	τ_C (s)
Mg x: Ugarte-Urra (2004)	1.6x10^{9}	2.1x10^{-22}	1.3x10^{6}	2000	377
Fe xii: 10-Oct-07 18.45.27	3.95x10^{9}	3.365x10^{-22}	1.39x10^{6}	408	1002
Fe xii: 11-Oct-07 00.10.47	9.00x10^{9}	3.365x10^{-22}	1.41x10^{6}	155	2636
Fe xii: 11-Oct-07 05.28.07	3.72x10^{9}	3.365x10^{-22}	1.31x10^{6}	323	1263

Table 3.3: Density and temperature values and corresponding timescales for radiative and conductive processes. N_e is the calculated electron density, $\Lambda(T_0)$ stands for the radiative loss function, T_0 represents the measured temperature, τ_R is the timescale of energy loss due to radiation, and τ_C due to conduction.

The various cooling timescales calculated for the XBP in Table 3.3 range from 6–43 minutes which are very short compared to the lifetime of the bright point which is observed to be around 12–15 hours. The fact that the XBP lives longer than the cooling times suggests that some kind of heating factor is present within the bright point.

3.3.4 Velocities

Changes in the Doppler-shifts and line widths were also examined. As described in Del Zanna (2008a), a strong (75 km s^{-1}) orbital variation of the wavelength scale is present in EIS data. This variation is non-reproducible and is different for the two bands. It has been corrected for (with custom-written software) by obtaining an average time-dependent wavelength scale for the two bands using the brightest lines and the standard wavelength-to-pixel calibration. Rest wavelengths were obtained from a quiet Sun area far away from the XBP. Count rates were such that Doppler-shifts in only a few stronger lines could be measured. The best measurements are those from the strongest line in the EIS wavelengths, the Fe XII 195.12 Å self-blend.

The line widths do not vary significantly over time and in the XBP location, however Doppler-shifts do. The velocity flows in and around the bright point were studied over a 12 hour period at intervals of 30 minutes (the minimum time between the rasters). Figure 3.9 shows a time series of the red-shifts and blue-shifts that were observed. It can be seen that even on the relatively short timescale of 30 minutes, changes are observed in the strength and structure of the velocity flows suggesting that these flows are occurring on timescales smaller than the observations available here.

It can be clearly seen that initially there are blue-shifts observed in the boundary between the two loop systems as well as on the other side of the cooler loop system (i.e., above the magnetic area P2). It can also be seen that there is a persistent red-shift observed in the main part of the XBP which also corresponds to the area where the polarities N1 and P1 are meeting and cancelling. Figure 3.9 shows that these red and blue-shifts are changing in strength and position from one image to another. As the cancellation of the XBP magnetic fragments progresses, it can be seen that a new area of red-shift has emerged in the secondary loop area. This is most likely due to the migration of part of N1 that splits off and moves towards P2 at around 03.00 UT. This new red-shift indicates that a secondary cancellation is occurring.

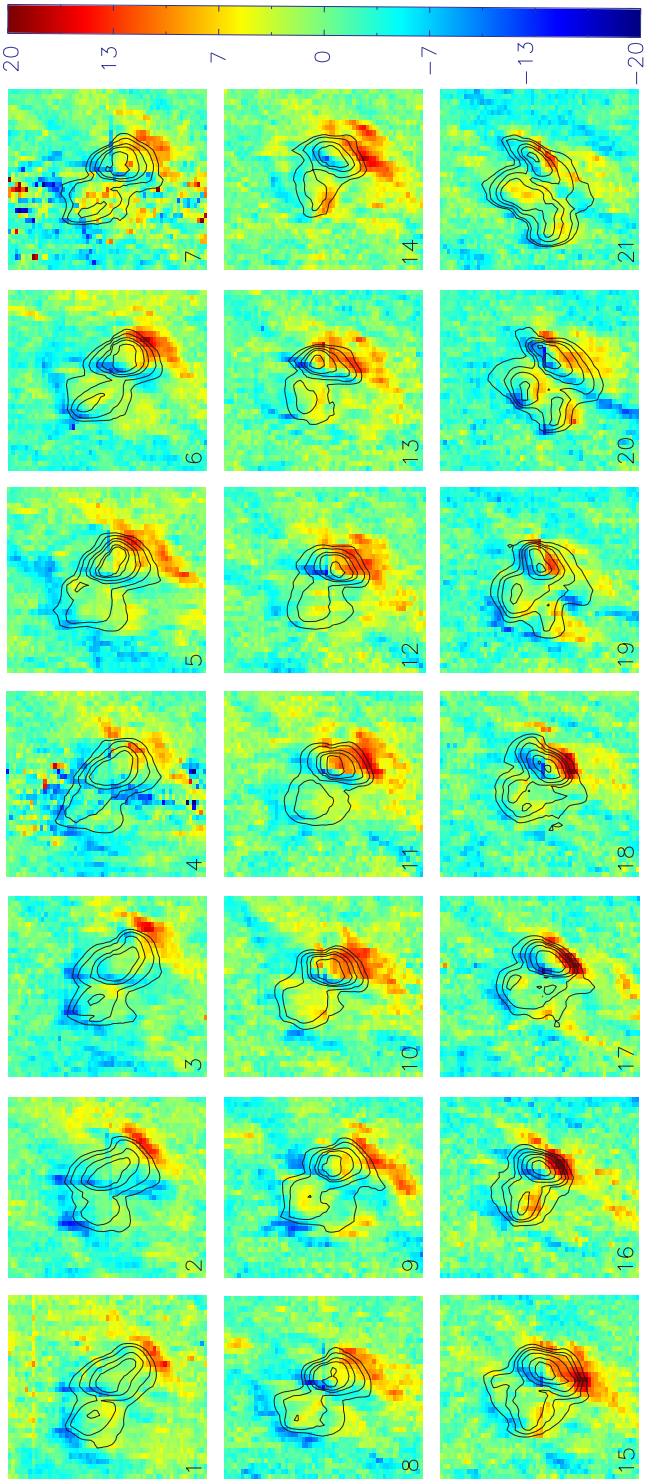

Figure 3.9: Sequence of Dopplergrams of area around XBP from 18:45 on the 10-October-2007 every 30 minutes until 06:32 on the 11-October-2007. The numbers in the bottom-left of each image correspond to their entries in Table 3.2 (NB file 22 is not shown in this plot but is very similar to file 21). Velocities were found using EIS Fe XII 195.119 Å . The velocities shown are between ±20 km $s^{-1}$and are over-plotted with intensity contours. The field-of-view of each box is 70” x 70”.

3.3.5 3D magnetic field structure

This section was written by a coauthor of the paper this chapter is based on. Dr Rhona Maclean contributed a potential magnetic field extrapolation in order to investigate the similarity of this extrapolation to the X-ray structure of the bright point. Her work (this section and also section 3.4.2) and figures (3.10 and 3.11) are included here for completeness as her work is necessary for full conclusions to be drawn.

The coronal magnetic field near the bright point was reconstructed from the SOT/NFI data which had already been calibrated. By identifying the strong photospheric magnetic features, tracking them in time, and modelling them as point magnetic sources, a sequence of potential magnetic fields for the solar atmosphere close to the bright point were extrapolated.

This was useful for the analysis because the 3D magnetic topological structure of these fields could then be calculated. Such a topology consists of magnetic null points (where the magnitude of the magnetic field is zero, Parnell et al. 1996) and their associated field-lines: spines, separatrix surfaces, and separators (a good review is given by Longcope 2005). These elements together make up the topological skeleton of the magnetic field, and they are prime locations for magnetic reconnection (Priest et al. 2005). As the heating of the bright point could have been caused by magnetic reconnection (Brown et al. 2001b), it makes sense to use topological analysis to determine where the likely reconnection sites are and how they change in time. These can be compared with the observed heating/brightening locations (from XRT) to determine the role of magnetic reconnection in heating the bright point.

In order to take advantage of the simultaneous observations available for this bright point, XRT and SOT/NFI data taken as close to the EIS file times as possible were chosen for the extrapolation. The SOT/NFI data were analysed using the YAFTA feature tracking algorithm (Welsch et al. 2004), which was set to detect and track magnetic

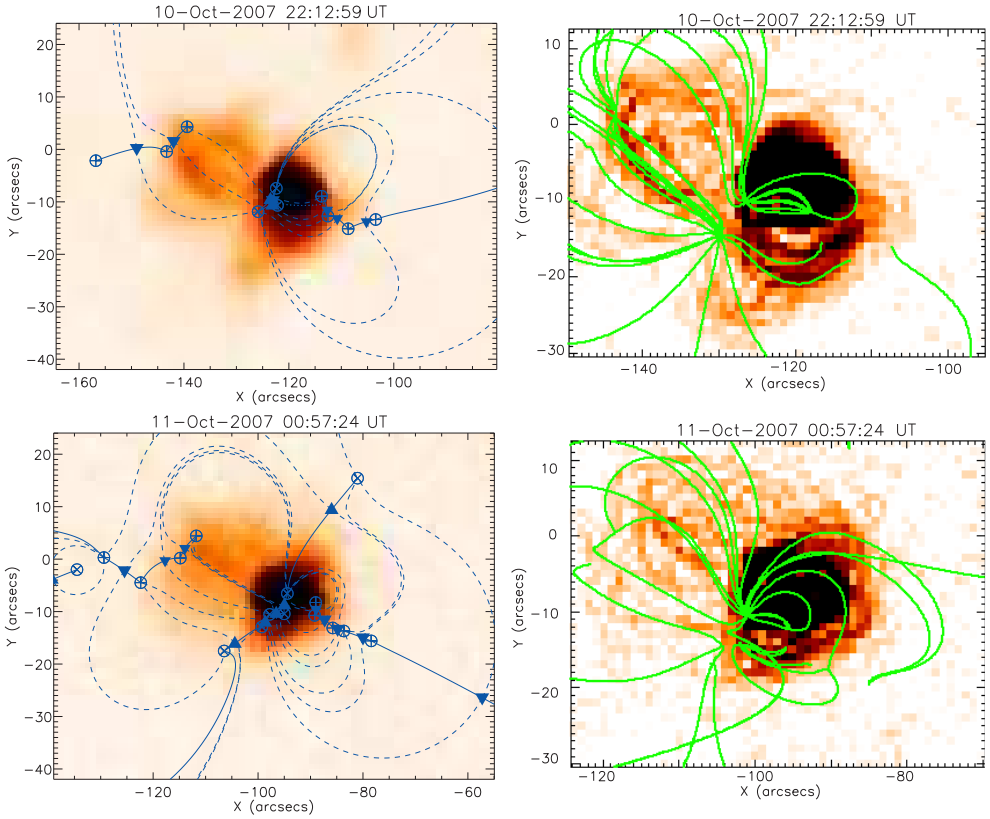

Figure 3.10: Figure by Dr Rhona Maclean showing two examples of our comparison between the X-ray emission seen in XRT and the similarities to the potential field model we applied. The two figures on the left show negative XRT images overlaid with the photospheric footprints of the calculated topological structure of the extrapolated magnetic field. Positive magnetic sources are labelled as ⊕, negative magnetic sources as ⊗, positive null points as ▼, negative null points as ▲, spines as solid curves, and the intersections of separatrix surfaces with the photosphere as dashed curves. It is possible to form a good impression of the whole 3D magnetic field structure, given that each null point's associated 3D separatrix surface must close via spine field-lines in the photosphere in cases where its own two separatrix traces do not terminate at the same source. No field-line can cross a separatrix surface or a spine. The two figures on the right show the same XRT images after being put through an edge-detection process (by CEA). These images have then been overlaid with field-lines (in green) generated by the potential field model to identify any structural similarities

.

features with a minimum magnetic flux density of 250 G in each pixel, and a minimum size of 20 pixels. Ten or more strong magnetic features were detected in all frames.

The tracked features were then modelled as point magnetic sources, with magnetic field strengths and (flux-weighted) locations determined by their parent features. MPOLE (Longcope & Klapper 2002) was used to extrapolate a potential magnetic field for each time-frame and calculate its topological skeleton. Figure 3.10 (left column) shows the photospheric footprints of the topological skeletons of the magnetic fields, superimposed on the XRT emission, for two representative time-frames within the observation period. The photospheric footprint of the topological skeleton means that only those parts of the skeleton that lie in the photospheric plane are shown; magnetic sources, null points, spines, and the intersections of the separatrix surfaces with the photosphere. The right-hand column in Figure 3.10 shows the same XRT images after being processed with edge-detection software. Over-plotted on these figures are example field-lines based on the calculated topological skeleton. This is to look for similarities between the observed loop structure and that predicted by the potential field model.

3.4 Discussion and conclusions

3.4.1 Energy timescale

It can be seen in Table 3.3 that the average results for the bright point for both τ_R and τ_C are different to the values calculated for a similar bright point studied by Ugarte-Urra (2004). This is due to the slight differences in density and temperature of the two bright points as well as having a more up-to-date figure for the radiative loss function Λ. The size of the bright point in the study was also smaller so the timescales involved could differ due to factors such as the bright point containing less magnetic flux which would affect the temperature and overall lifetime of the XBP. The figures calculated for

our bright point indicate that the corona cools via conduction in around half an hour whereas energy is lost via radiative methods over a manner of minutes. This illustrates that there must be a continuous heating method present in the XBP for it to last longer than these timescales.

3.4.2 Magnetic Topology

This section was written by Dr Rhona Maclean to analyse her work on the potential field extrapolation she performed.

The fundamental large-scale structure of the bright point's magnetic field is two sets of magnetic loops sitting next to each other length-ways, and orientated approximately east-north-east to west-south-west on the Sun. These loops spring from three main regions of strong magnetic field on the photosphere; a central negative region (N1) flanked by positive regions to both west (P1) and east (P2), as can clearly be seen in Figure 3.1 (lower panels).

Early on, the strongest brightening in XRT issues from the loops joining N1 to P1; this can be considered as the main bright point. However, fainter loops can also be seen joining N1 to P2 (seen clearly in Figure 3.2). As time goes on, the brightening in the N1-P1 loops become more concentrated close to N1, and eventually dims to about the same level as the N1-P2 loops, which remain faint but distinct throughout.

Figure 3.11(a) shows how the magnetic fluxes of N1 (solid curve), P1 (dot-dot-dashed curve) and P2 (dashed curve) varied over time. After 23:00 UT, the fluxes of N1 and P1 are both clearly decreasing, suggesting that magnetic cancellation took place between the two main bright point sources at least from 23:00 to 07:00 UT.

The distances between N1 and P1 (solid curve) and between N1 and P2 (dashed curve) can be seen in Figure 3.11(b). This graph shows that both pairs of sources moved closer

together during the observational period, although the change was more steady and significant for N1 and P1. So we have a pair of sources moving closer together while their magnetic fluxes are decreasing; both indications of magnetic cancellation. Finally, topological model of the bright point's magnetic field was used to calculate the changing amounts of flux joining each pair of sources. This is shown in Figure 3.11(c), with the flux joining N1 to P1 shown as a solid curve, and the flux joining N1 to P2 shown as a dashed curve. The magnetic connection between N1 and P1 steadily weakens over the whole observation period. After 23:00 UT, the magnetic connection between N1 and P2 also weakens. This weakening must be due to magnetic cancellation between both source pairs.

3.4.3 Relation between photospheric fields and coronal signatures

Several authors have found it useful to study the magnetic field of an area of coronal activity and use the extrapolated field lines to look for similarities in the coronal emission. Pérez-Suárez et al. (2008) used SoHO/MDI to compare the extrapolated field lines of an XBP with what they saw in XRT images. They found that the bright point X-ray structure was very similar to that predicted by the potential field model used.

It is very clear that the XRT brightenings join the two pairs of magnetic source regions. As can be seen in Figure 3.10, the XBP shows a good agreement between the positions and angles of the observed magnetic loops and the extrapolated magnetic field-lines of the potential-field model. This implies that the potential field model used does a good job of capturing the large-scale features of the XBPs 3D magnetic field for most of its observed lifetime.

The Hinode/XRT observations of the XBP do not show significant variations on short timescales (the same was found by Nolte et al. 1979 with X-ray imaging). This is in disagreement with the 'stick slip' magnetic reconnection model proposed by Longcope

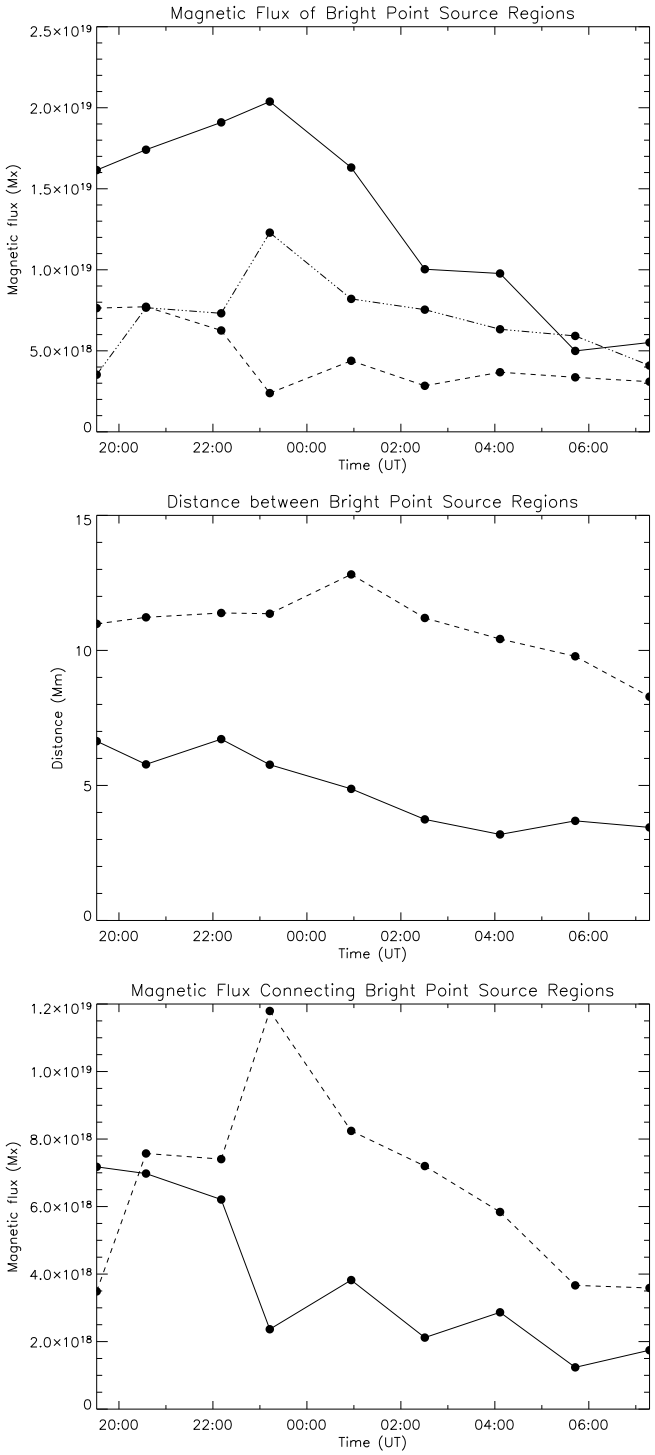

Figure 3.11: From top to bottom: (a) Evolution of the magnetic flux of each source region. N1 = solid curve, P1 = dot-dot-dashed curve, P2 = dashed curve. (b) Evolution of the distances between the source regions. N1-P1 = solid curve, N1-P2 = dashed curve. (c) Evolution of the magnetic flux joining the pairs of source regions. N1-P1 = solid curve, N1-P2 = dashed curve. Figure by Dr Rhona Maclean.

(1998). This of course does not mean that impulsive heating does not occur, but if it does, it does on very short time-scales (seconds) and/or sub-resolution spatial scales.

It is interesting to look for correlations between the X-ray emission and the total magnetic flux density over time. An area around the main polarity of the XBP was selected (areas P1 and N1 in Figure 3.1), and the light curve of the XRT count rates obtained. This is shown in Figure 3.12 which shows the evolution of the magnetic flux and the X-ray emission over time.

It can be seen that the positive (blue triangles) and negative (black squares) magnetic flux of the bright point show a significant decrease after around 00:30 UT which indicates that the XBP is indeed formed over an area of cancelling magnetic flux. What is interesting to note is that the XRT data shows a significant variation up until this time after which the count rates decrease in intensity then level out to background levels. This correlation between the start time of the cancellation and the sharp increase in X-ray output can be interpreted as evidence of magnetic reconnection.

In Figure 3.11, both the positive and negative SOT fluxes show the same gradual decrease after 00.00 UT suggesting this is when the cancellation begins. Figure 3.11(a) also shows that the greatest loss of magnetic flux joining P1 and N1 takes place between 23:00 UT and 01:00 UT, which suggests that the midnight spike in the XRT intensity is due to energy release from this magnetic cancellation event. There are two or three significant peaks seen in the XRT intensities before the cancellation begins which we cannot fully explain. These are most likely due to heating or reconnection events that can’t be linked to motions of the magnetic fragments.

The fact that the magnetic field of the XBP is quite close to being potential means that the energy powering the XRT spikes should come from physical cancellation of the magnetic fields rather than from magnetic reconnection converting stored magnetic energy to heat.

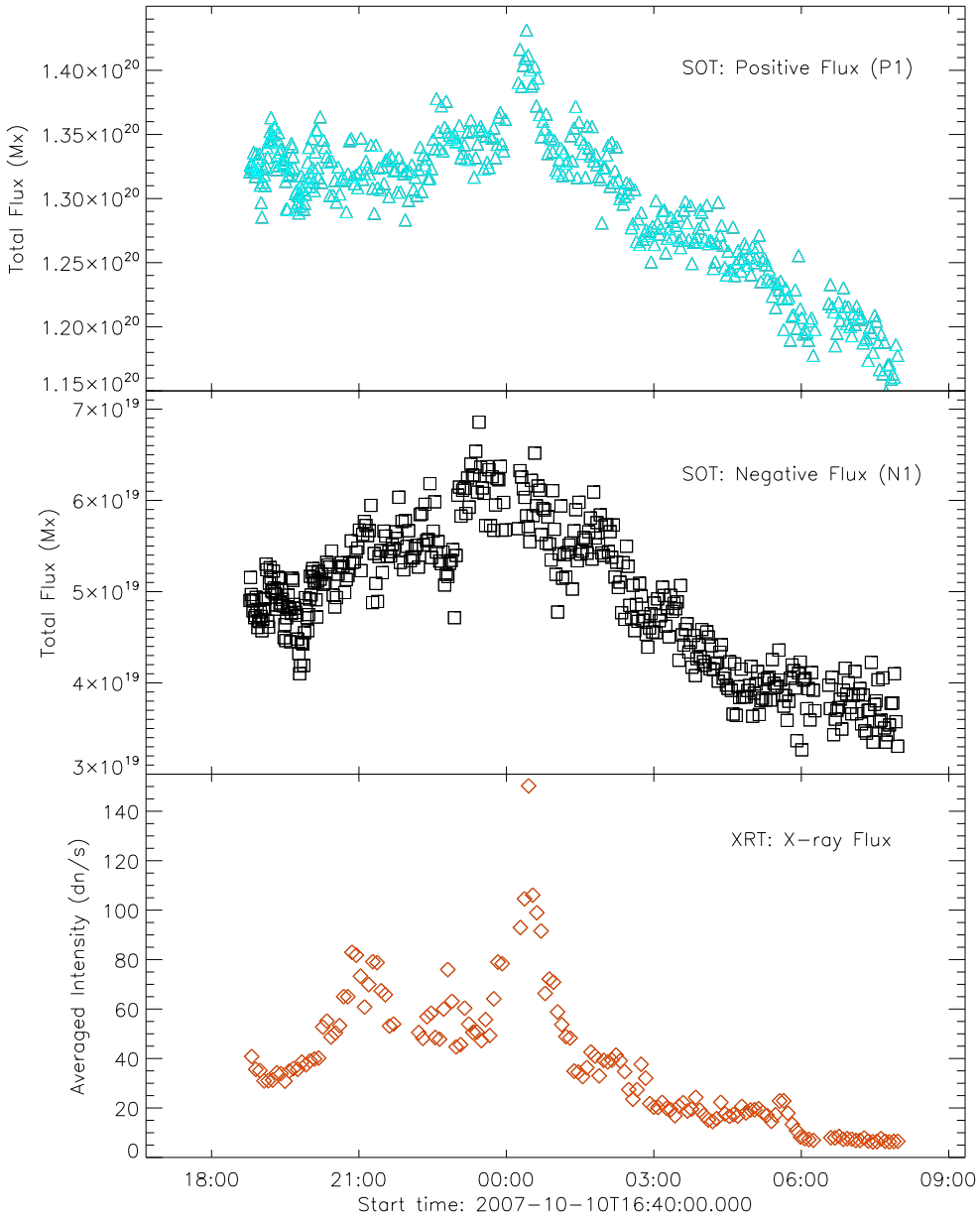

Figure 3.12: Comparison between the changing magnetic and X-ray flux of the area of the XBP over time. *Top:* plot showing how the total positive magnetic flux (designated as P1 in Figure 3.1) changes over time. *Middle:* similar plot showing how the absolute values of the total negative magnetic flux (N1) changes over time as the cancellation progresses. *Bottom:* plot showing how the total count rate of the XBP observed by the XRT instrument changes over time. The initial variations in the X-ray flux peak around 00:30 UT which coincides with the time both magnetic fluxes start to significantly decrease i.e., at the start of the cancellation. This could be a signature of magnetic reconnection.

3.4.4 Relation between magnetic field and observed plasma velocity flows

The Dopplergrams clearly indicate a variable pattern. This is somewhat puzzling, considering that the overall intensity pattern does not change so rapidly. Similar patterns of blue and red-shifts were found in active regions (see e.g., Del Zanna 2008b), but they were stationary over long time periods. It seems unlikely that the Doppler motions are related to reconnection outflows. Also, the flow patterns do not support the idea of 'stick slip' magnetic reconnection, which should occur along separator field lines.

It is quite possible that the Doppler-motions are related to chromospheric evaporation (blue-shifts) and subsequent draining (red-shifts) following cooling. However, Brosius et al. (2007) suggested the possibility that, if outflows are connected to chromospheric evaporation, they would likely decrease in time, something that is not observed.

This work found no clear correlation between the Doppler-motions and the coronal magnetic field as obtained from the extrapolations, and can give no clear explanation of the observed velocity flows. Higher cadence observations with EIS will better reveal the pattern and links between what we see in the magnetic structure on the photosphere and the corresponding changes in the plasma velocities observed in the corona. Possible future work on this topic is detailed in Section 7.1.

Chapter 4

Impact upon the Differential Emission Measure of evolving multistranded loops

4.1 Introduction

The internal structure of coronal loops and the heating processes that take place within them is an area of intense research. By understanding these two important aspects, progress can be made towards answering one of the most important questions in solar physics: how is the corona heated? The heating of coronal loops is an important part of this question, and progress has been made in both observations and theory to try and answer it.

The idea that nanoflares contribute a large portion of the energy needed to heat the corona was first suggested by Parker (1988). In this discussion the term nanoflare refers to a discrete, localised impulsive burst of energy of the order of 10^{24} ergs. Combining this power source with the idea that loops are composed of many sub-resolution strands

forms the basis of the loop simulation that is explored and then utilised in this chapter.

The aim is to use a multi-stranded hydrodynamic model in conjunction with Differential Emission Measure (DEM) analysis to examine three main areas. Firstly, the parameter space of the model is explored to see how varying the simulation inputs affects the resulting DEM. Secondly, the simulated loop is used alongside the temperature response function of the SDO/AIA instrument in order to create synthetic values of intensity. These values are then used to test the accuracy of various DEM solvers. Lastly, actual SDO/AIA data are examined to see if the model produces results which are consistent with what is observed on the Sun.

The combination of simulation and observation is the key element of this study. It is important for any model to generate observables as these can help to interpret real solar data. By varying the parameters of the model we can observe how the physics of the system affects the observables and this in turn can help to put limits on the model. The investigation of DEM solvers is another important aspect e.g., how consistent is the synthetic DEM generated from the model compared to the DEM generated by the solver on the same data? In that regard, how well can we trust the solver to interpret real observations?

4.1.1 Heating and Structure of Coronal Loops

The explanation behind the relatively high temperature of the corona is probably one of the most sought after solutions in modern solar physics. Reaching a conclusive answer to this question is no easy feat however, and a comprehensive review of the problems and current theories is given by authors such as Klimchuk (2006), Reale (2010), Priest et al. (2000), and Aschwanden et al. (2007).

Out of the many proposed methods put forward to explain how plasma within coronal loops is heated, only one method will be concentrated on in this chapter: nanoflare

heating. The goal of this chapter is not to prove that nanoflares heat the corona, but to explore the viability of the nanoflare concept within the confines of a simulation.

The term nanoflare can be misleading as it does not refer to a specific type of solar flare. In this discussion "nanoflare" is used the same way as Parker (1988) who use the term to describe an energy release (of the order 10^{24} ergs) that occurs on very small spatial scales and is in the form of many localised impulsive bursts.

The source of these nanoflares comes from the fast-moving and complicated movement of the photosphere which causes the magnetic field running through it to become twisted and braided. This results in multiple small-scale magnetic reconnections occurring to dissipate the stored energy. The timing of these nanoflares is impulsive (as photospheric motions would not cause a steady rate of reconnections to occur) and they occur on small spatial scales (i.e., on the order of flux tube width) so nanoflare heated loop models are generally also multi-stranded. Many authors have explored nanoflare models with encouraging results (see e.g., Taroyan et al. 2006; Walsh et al. 1997; Tripathi et al. 2011).

The ability of nanoflare models to accurately predict/explain the behaviour of real coronal loop observations would help to uncover the *frequency* of heating events in the corona. This would allow constraints to be put on the coronal heating mechanism (Winebarger et al. 2012). The debate over whether this mechanism is low-frequency (i.e., impulsive) or high-frequency (quasi-steady) is still ongoing but the detection of high temperature plasma would help to decide matters. High-frequency heating should keep plasma at a relatively constant temperature as the loop material doesn't have time to cool and drain in between heating events. Low-frequency heating, however, would allow the plasma to drain and cool to a greater extent as there is more time between heating events. This would mean that higher temperatures could be achieved due to the changes in density that are caused by the draining.

Klimchuk (2009) found that both high and low-frequency heating could reproduce the

observed intensities and velocities of active region loops so definitive evidence of a hot component would go a long way in supporting nanoflare heating. Evidence for this hot component has been reported by Schmelz et al. (2009b,a) and Reale et al. (2009) who have both used X-ray observations such as XRT and RHESSI. However, care should be taken when interpreting observations as Winebarger et al. (2012) detailed that current instrumentation has problems imaging high temperature plasma that has a low emission measure. They used a combination of Hinode EIS and XRT and found that the two instruments were insensitive to plasma above 6 MK (logT/K=6.8) which had an emission measure of less than $10^{27}\mathrm{cm}^{-5}$.

However, a recent study by Testa & Reale (2012) used a combination of Hinode/EIS with SDO/AIA and concluded that the hot component could be seen in active regions. They used a combination of three AIA channels (171Å, 335Å, & 94Å) to highlight the location of hot plasma and also observed it with observations in the EIS Ca XVII line. If this result is confirmed by other studies it would mean that evidence for the hot component could be identified now rather than having to wait for the next generation of instruments.

Observations show that solar flares obey a power law for their energy distribution with a slope of about α=-1.8 (see e.g., Drake 1971; Dennis 1985). Hudson (1991) examined this further and concluded that for nanoflares to power the corona, they would have to obey a power law with a more negative slope of α<-2. This relationship is shown in equation 4.1.1.1 where W refers to the nanoflare energy.

$$\frac{dN}{dW} \sim W^{-\alpha} \tag{4.1.1.1}$$

No conclusive evidence has been found to find in favour of nanoflares based on power law observations as both steeper and shallower gradients have been observed (see e.g., Aschwanden & Parnell 2002).

Other models

Most authors agree that the combination of observations with theory is the best way in which to progress our understanding of the physics of the solar corona. This can be done by either using observations as inputs to fine tune models or by using models to generate 'observables' which are compared to real data.

The model used in this chapter is described in detail in the next section but there are also many other models available, each with their own advantages and disadvantages. Simulation speed, resolution and parameter inputs are all issues that need to be considered when writing or utilising a particular model. The more detailed 3D models will take longer to run and more space to store while 1D models are quicker and take up less storage space but will contain less dimensional information on the plasma properties of the loop.

Many authors have successfully matched observations of coronal loops with multi-stranded static models (see e.g., Reale & Peres 2000; Aschwanden et al. 2000a; Winebarger et al. 2003a). At the same time other work has shown equally positive results using hydrodynamic codes such as Ugarte-Urra et al. (2006), and the 0D hydrodynamic code introduced by Cargill (1994). This code was later modified and used further by Cargill & Klimchuk (1997, 2004) and Klimchuk & Cargill (2001). In their multistrand model each strand is represented by a single temperature and density and undergoes impulsive nanoflare heating. This allows the loop to cool via conduction and then by radiation. The model calculates the parameters of many strands in order to draw conclusions about a "global loop".

4.1.2 Multistranded Hydrodynamic Loop Model

The coronal loop simulation explored in this chapter is based on the 1D hydrodynamic loop model first presented in Arber et al. (2001) and subsequently explored by Sarkar & Walsh (2008, 2009). The model consists of a loop composed of a number of individual strands that are modeled independently by a one-dimensional hydrodynamic simulation. The simulated loop is heated by localised, discrete energy bursts in the form of nanoflares which occur along individual strands.

Hereafter this simulation shall be referred to as the MSHD model (multi-stranded hydrodynamic) rather than a 1D hydrodynamic model as it is the multistrandedness that is the most important aspect. This model is not truly 1D (although each strand is 1D) as the simulation can be used to look at parameters across the loop width by studying the evolution of all the strands together. In this context 1D refers to the ability of the model to study parameters along the length of the loop i.e., parallel with the magnetic field. The hydrodynamic nature of the model means that changes in time can also be studied. Throughout this work the term ‘strand’ is used to refer to individual flux tubes containing plasma while ‘loop’ refers to the type of structures imaged by observations that are an amalgamation of these filamentary strands.

MSHD model description:

The MSHD model is very flexible so it is straightforward to change the various input parameters in order to see how the physics of the system is affected. The variable input parameters include:-

- the loop length,
- the number of individual strands,
- the total energy going into the loop,

- the number of bursts (i.e. nanoflares) in each strand,
- the energy and timescale of each burst,
- the location of the bursts i.e., apex, footpoint or uniform distribution (see Figure 4.1),
- the duration of the simulation,
- the proportion of the loop designated as the chromosphere and transition region,

In each case, the loop is modelled as a semi-circular shape as opposed to some models (e.g., Winebarger & Warren 2004), where only half the loop is modelled (i.e., footpoint to apex). The MSHD model simulates the entire length in order to study how the different parameters change at each footpoint.

In this work, the loop modelled is 100 Mm in length and is anchored in the model chromosphere and transition region which account for 5 Mm at each footpoint. The length of the loop means that the height of the loop apex above the solar surface is ~32 Mm. This means the loop does not extend beyond one pressure scale height (~47 Mm Aschwanden et al. 2001) which simplifies the pressure and gravitational constraints. In the future if larger loops were modelled this assumption would have to be revisited.

At the beginning of the simulation, the plasma within the loop has a temperature set at the chromospheric value of 10,000 K which increases sharply as the nanoflares begin to heat the loop. As mentioned in the list of model inputs above, the position along the loop where these nanoflares are deposited can be defined in three ways. Figure 4.1 shows the heating profiles where the nanoflares are spread uniformly along the loop length (green), or constrained to the apex (red) or footpoint areas (blue).

The data on this graph is plotted from -50 Mm to +50 Mm but it can be seen the nanoflare distribution is only between ± 45 Mm. This is the previously mentioned 5 Mm

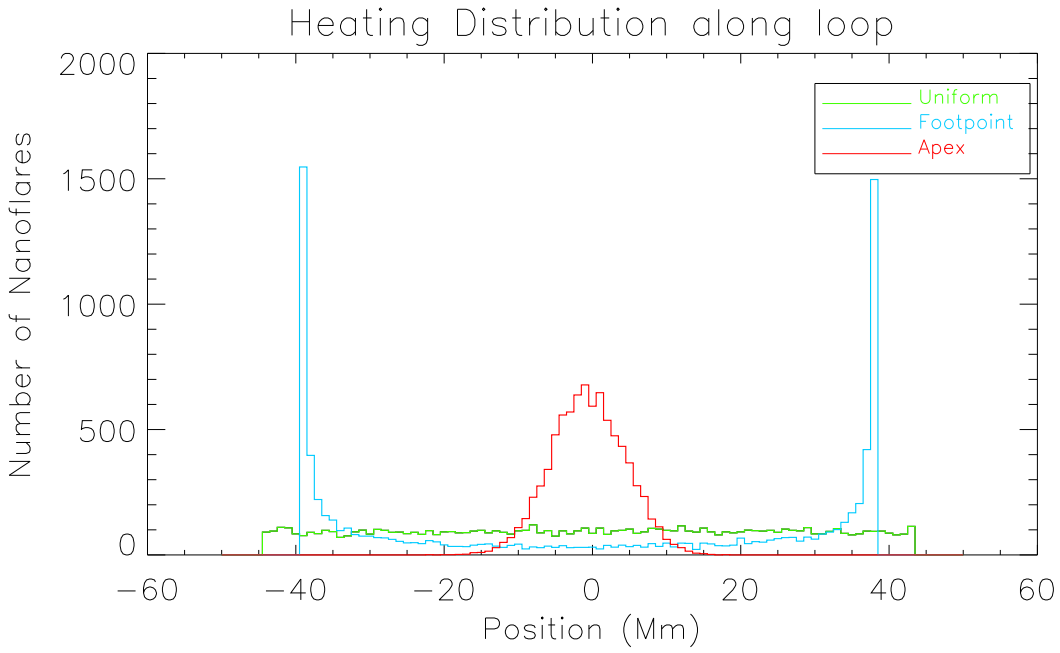

Figure 4.1: Example of how the distribution of the nanoflares can be changed to be confined to a specific area of the loop in the MSHD model.

at either end of the loop that is designated to be the chromosphere/transition region area and no nanoflares are located there.

The plasma within each individual strand is modelled according to the following time-dependent 1D differential equations of mass, momentum and energy conservation:

$$\frac{D\rho}{Dt} + \rho\frac{\partial}{\partial s}\mathrm{v} = 0 \tag{4.1.2.1}$$

$$\rho\frac{D\mathrm{v}}{Dt} = -\frac{\partial p}{\partial s} + \rho g + \rho\nu\frac{\partial^2 \mathrm{v}}{\partial s^2} \tag{4.1.2.2}$$

$$\frac{\rho^\gamma}{\gamma - 1}\frac{D}{Dt}\left(\frac{p}{\rho^\gamma}\right) = \frac{\partial}{\partial s}\left(\kappa\frac{\partial T}{\partial s}\right) - n^2\Lambda(T) + H(s,t) \tag{4.1.2.3}$$

$$p = \frac{R}{\tilde{\mu}}\rho T \tag{4.1.2.4}$$

$$\frac{D}{Dt} \equiv \frac{\partial}{\partial t} + v \cdot \frac{\partial}{\partial s} \tag{4.1.2.5}$$

where ρ, p, n, v and T represent the mass density, pressure, particle density, velocity and temperature of the plasma, s is the spatial coordinate which indicates the position along the strand, g is the component of gravity along the loop (assumed to be constant), γ is the adiabatic index (assumed to be 5/3), κ is the conductivity of the plasma (= $9.2\times10^{-7}T^{5/2}$ erg s^{-1} cm^{-1} K^{-1}), R the molecular gas constant (8.3×10^7 erg $mol^{-1}K^{-1}$), and $\tilde{\mu}$ is the mean molecular weight with $\tilde{\mu} = 0.6$ mol^{-1}. ν is the coefficient of kinematic viscosity (assumed to be uniform), Λ(T) is the optically thin radiative loss function, and H(s,t) is the coronal heating term. This has the form of Cook et al. (1989) which is shown in Figure 4.2 alongside various other forms of the radiative loss function. The MSHD model can be adapted to accept any of these functions.

Model resolution and grid spacing:

The MSHD model is relatively quick to run (~ few hours) and provides information on the temperature, density and velocity evolution of the loop plasma along each individual strand at each timestep of the simulation. The spatial resolution of the simulation (i.e., how many grid spaces are defined along the length of the 100 Mm) as well as the time resolution (i.e., how many seconds one timestep represents) are user defined to adapt the model to the type of observable required (e.g., simulation of a small-scale rapid change or large-scale, slowly-evolving type of observation). A balance must be found between the resolution requirements and the simulation run-time in order to get the best result from the model.

In this work, the spatial resolution chosen was of the same order as an SDO/AIA pixel,

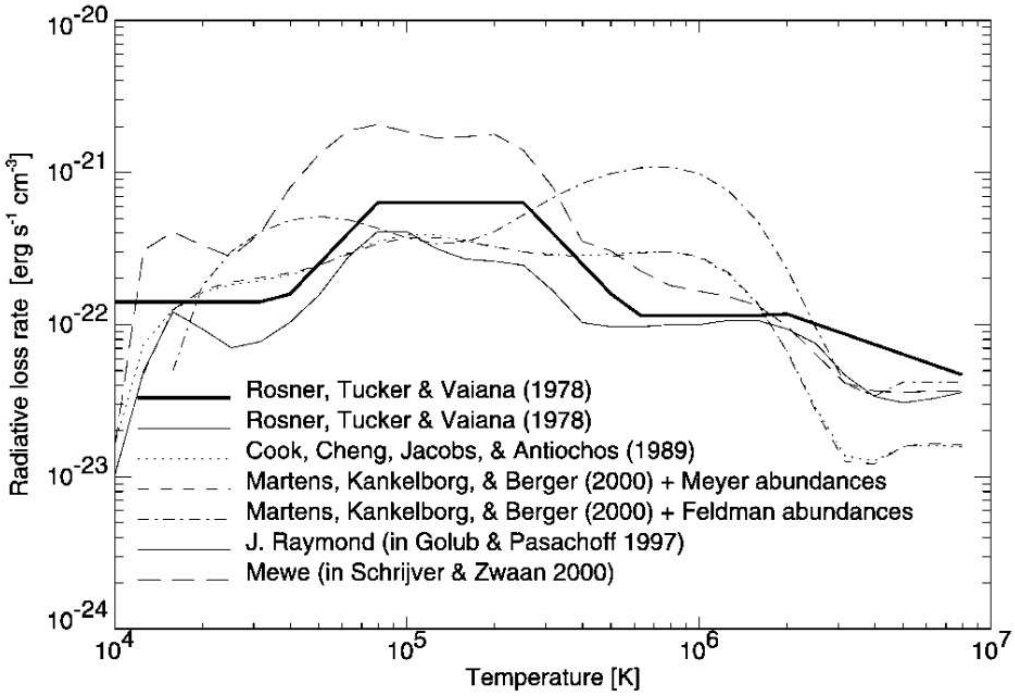

Figure 4.2: Compilation of different radiative loss functions which result from different choices of elemental abundances. The work in this thesis has been done using the Cook et al. (1989) function. Figure from Aschwanden et al. (2003).

and the time resolution was set at one second per timestep. Figure 4.3 shows a representation of the 100 Mm loop where the zoomed-in section shows a subset of five individual strands that make up the loop. The marked length segments refer to the grid size of the model where each section has its own value of temperature and density for every timestep.

The grid size in this case is 0.164 Mm but this is not uniform along the loop. Figure 4.4 shows how this factor changes along the length of the loop i.e., that the grid size is much smaller in the chromosphere and transition region portions than in the corona. This needs to be kept in mind when selecting portions of the loop for analysis. Care must be taken not to take data from the TR/chromosphere section unless the change in resolution is accounted for.

The grid size is used for calculating how many sections of length to consider in order to represent a particular observable. For example, if the MSHD loop was to be compared

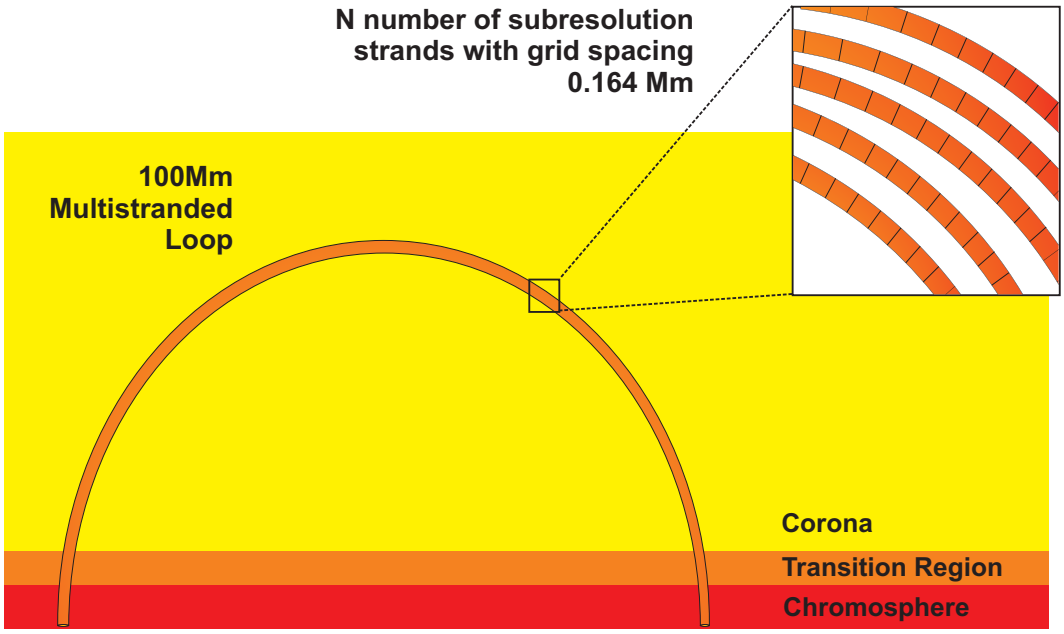

Figure 4.3: Representation of the MSHD model showing the multistrandedness and the way in which individual strands are divided up into segments according to the model grid size.

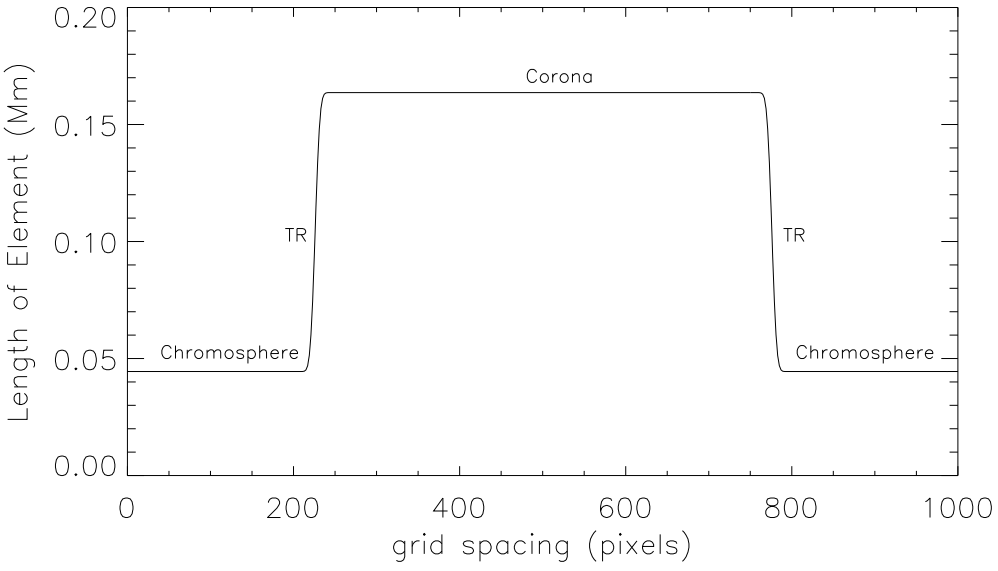

Figure 4.4: Graph showing how the 100Mm loop simulation is composed and how the sizing of the pixels/length segments in each region differs.

to 1 AIA pixel (which has a resolution of ~1” which is approximately 0.725 Mm on the Sun) then data from ~4 length segments should be analysed as 0.725 Mm/0.164 Mm ≈4.4≈4.

4.1.3 Differential Emission Measure Description

As discussed in Section 1.3, there are various ways to investigate the temperature and density distribution of coronal plasma. The filter ratio and EM Loci methods rely on the assumption that the plasma along the line-of-sight is isothermal, but this could be quite a crude approximation. A more complete analysis may be gained from using a Differential Emission Measure (DEM) distribution which describes the variation of the plasma emission within a particular temperature range.

The DEM investigates plasma along a certain line-of-sight and gives the contribution from radiation between defined temperature (T) intervals (ΔT). The DEM is only a function of temperature so information on how the plasma temperature varies along the line-of-sight (i.e., at different atmospheric heights) is not available. This is due to the fact the emission is optically thin in the corona so plasma at different positions along the line-of-sight that share a certain temperature range will all contribute to the DEM.

Subsequently, the emission measure (EM) of a plasma can be defined as a summation of the DEM over all temperatures as shown in Equation 4.1.3.1 where ρ is the density of the plasma and dh is the line-of-sight element. T is the temperature and ΔT is the defined temperature interval.

$$EM_{\Delta T}(T) = \int_{T-(\Delta T/2)}^{T+(\Delta T/2)} DEM(T)\, dT$$
$$DEM(T) = \int \rho^2 \frac{dh}{dT} \qquad (4.1.3.1)$$

Observationally the DEM can be calculated from measurements of spectral lines (e.g., from SoHO/CDS or Hinode/EIS) or from imaging instruments (e.g., Hinode/XRT or SDO/AIA). When using observations taken from imaging instruments to construct a DEM, it is important to keep in mind the fact that these filters have multiple contributions over a given temperature range.

The intensities measured from these observations can be used to construct a DEM by using an inversion technique. Equation 4.1.3.2 demonstrates this issue as the left-hand side of the equation (where I_λ is the intensity at a particular wavelength/filter) is known but the DEM(T) portion on the right-side is what is to be calculated. In this equation G_λ represents the instrument response function of a specific imager at a particular wavelength. In the case of spectra being used, this function would be replaced by the element abundance multiplied by the contribution function of the specific line being used.

$$I_\lambda = \int G_\lambda(T)\, DEM(T)\, dT \tag{4.1.3.2}$$

In this chapter, synthetic DEM distributions are constructed directly from the plasma temperature and density parameters as the MSHD model provides these values over the time and length-scales of the simulation. Using Equation 4.1.3.1, the DEM can be calculated from the model outputs. This DEM can further investigate the model parameters by using Equation 4.1.3.3 and folding this DEM through the SDO/AIA temperature response function in order to obtain synthetic intensity values. In this equation I_c is the intensity seen in a particular AIA channel (DN), t is the 'exposure time' of the synthetic observation (i.e., the length of simulation time it is constructed from in seconds), and ΔT is the width of the temperature bin the DEM is based on (in degrees Kelvin).

$$I_c = \sum DEM(T)\, G_c\, t\, \Delta T \tag{4.1.3.3}$$

Only the Fe AIA channels (e.g., 94Å, 131Å, 171Å, 193Å, 211Å, and 335Å) have been selected to investigate synthetic intensities in order to avoid abundance issues. Additionally, only simulated data with log T ≥ 5.5 have been included as below this is where the solar atmosphere becomes more optically thick and optical thinness is an important assumption of DEM analysis.

4.2 Exploration of model parameter space

The flexibility of the MSHD model allows a full examination of how the physical system reacts to changes to its input parameters. It is straightforward to perform different runs of the simulation where parameters such as loop length, number of strands, number of nanoflares per strand, energy of each nanoflare, and the distribution of the nanoflares in space and time can be altered. Table 4.1 shows a list of the four main parameters investigated for a 100 Mm length loop of fixed radius (2 Mm).

Investigation	Description
A	The effect of changing the number of strands (N_{strand}) within the loop
B	The effect of changing the location of the nanoflares along the loop
C	The effect of changing the energy balance:
i	- Changing the E_{tot} of the system by increasing the E_{burst}
ii	- Changing the number of nanoflares whilst keeping E_{tot} the same
D	Investigating the effect of turning off the heating after a prescribed period of time on the loop system

Table 4.1: List of the various investigations of the MSHD model parameter space.

The purpose of altering these parameters is to investigate how changes in the inputs of the model affect the resulting values of temperature and density which are investigated using DEM analysis. Table 4.2 gives a full list of the different simulations that were run to investigate the parameter space of the model.

Simulation No.	No. of strands	No. of bursts/strand	Heating Location	Energy Class	$E_{average}$ burst (ergs)	Total Energy in loop
1	16	64	U	10^{24}	5.20×10^{25}	5.32×10^{28}
2	32	64	U	10^{24}	2.57×10^{25}	5.28×10^{28}
3	64	64	U	10^{24}	1.25×10^{25}	5.13×10^{28}
4	128	64	U	10^{24}	6.28×10^{24}	5.14×10^{28}
5	128	64	A	10^{24}	6.16×10^{24}	5.04×10^{28}
6	128	64	F	10^{24}	6.26×10^{24}	5.13×10^{28}
7	128	64	U	10^{23}	6.28×10^{23}	5.14×10^{27}
8	128	64	U	10^{25}	6.28×10^{25}	5.14×10^{29}
9	128	64	A	10^{23}	6.16×10^{23}	5.04×10^{27}
10	128	64	A	10^{25}	6.16×10^{25}	5.04×10^{29}
11	128	64	F	10^{23}	6.26×10^{23}	5.13×10^{27}
12	128	64	F	10^{25}	6.26×10^{25}	5.13×10^{29}
13	128	64	U C	10^{23}	6.28×10^{23}	5.14×10^{27}
14	128	64	U C	10^{24}	6.28×10^{24}	5.14×10^{28}
15	128	64	U C	10^{25}	6.28×10^{25}	5.14×10^{29}
16	128	16	F	–	2.49×10^{25}	5.10×10^{28}
17	128	640	F	–	6.32×10^{23}	5.17×10^{28}

Table 4.2: Table showing all simulations run of a 100Mm loop and the important parameters involved. The fourth column details where along the loop the majority of the nanoflares were distributed. ‘U’ is a uniform distribution, ‘A’ is an apex dominated distribution, ‘F’ is a footpoint dominated distribution, and ‘U C’ refers to a uniform distribution of nanoflares which was allowed to cool after the heating had been stopped. The fifth column ‘Energy class’ is a designation to quickly show the nanoflare energy mean where 10^{24} ergs is considered as the standard value. Energies that were of an order of magnitude either side were also explored. This designation is used on various figures to differentiate between the simulations.

Each simulation produces arrays of temperature and density values that vary by strand number, location along each strand, and in time. The spatial and temporal resolution of the model is chosen to reach a balance between simulation run time and producing a dataset that is comparable to observations so that small-scale changes can be seen. The high resolution of the MSHD model, although advantageous for looking at small-scale changes, can lead to some computational difficulties if the full scope of what the model shows is to be examined.

For example, if one wishes to have a temperature and density value for every time-step, along every strand, at each grid spacing along the loop, this can lead to arrays with dimensions of T/ρ (s,t,N)=[1002,17250,128] for the case where there are 128 strands in the loop over the whole 17250 second simulation whilst looking at all 1002 length sections of the loop (including the chromospheric and transition region parts of the loop as well as the coronal part). This leads to two arrays with 2.2 x 10^9 double-precision elements which can cause some memory and CPU usage problems when run on a standard computer.

These problems can be overcome technically for example, by splitting the calculations over numerous processors/storage drives, but it is equally practical to cut down these massive data sets to something more physically useful. For example, the chromospheric and transition region portions of the loop need not be considered when constructing DEMs as these sections of the loop contain no nanoflares and are only present to set up the initial and boundary conditions for the coronal part of the loop. These areas are also not optically thin so are not suitable for DEM analysis. In terms of the time range of the simulation, this too can be cut down to something more realistic. Although it is important to look at the entire evolution of the plasma properties of the loop (to check it is running as it should and to explain any abnormalities), when constructing DEMs and examining the synthetic emission of the simulation it is more realistic to pick a fixed portion of time. The time period considered should fulfill certain criteria, namely:

(a) The time section begins after the initial start-up perturbations caused by the simulation evolving from the initial conditions to some quasi-steady equilibrium,

(b) Is comparable to the time resolution of real imager observations i.e., anywhere from the 3 second exposure time of SDO/AIA up to 1 or 2 minutes to average out short-scale anomalies,

(c) Or is longer than the acoustic travel time in order the smooth over the effects of individual nanoflare energy dissipation. This allows for any possible longer-scale general trends to be examined.

With these factors in mind, a variety of ‘cuts’ were performed on the temperature and density arrays (named in Table 4.3). Hereafter, the term ‘cuts’ will refer to a specific part of the simulation that has been trimmed down to a certain time range and section length. These cuts in space and time were picked to try and cover a variety of scenarios i.e., Cut 1 is designed to match what SDO/AIA would view and has been cut to cover the spatial resolution of one AIA pixel (i.e., equivalent to 1”~725 Km on the Sun) over the average AIA exposure time of ~3 seconds. Cuts 2 and 3 cover the equivalent of 4 AIA pixels (in order to average over any spatial anomalies) but are taken at different positions along the loop. Cut 2 is taken from the very apex of the loop while Cut 3 is taken from data on the ‘leg’ of the loop. In this case ‘leg’ refers to the area on the loop that is closest to the transition region but is still part of the coronal portion of the loop (i.e., so not quite at the loop ‘footpoint’ but as close as the simulation allows). These cuts are designed to explore the differences going on in different portions of the loop and are averaged over 500 seconds to smooth out the temporal effects of the nanoflare energy dissipation and just look at the differences caused by location. Cuts 4, 5 and 6 include data taken from the entire coronal length of the loop over a number of different timescales in order to look at more ‘global’ trends and differences between the simulations. These various cuts are also shown in Figure 4.5.

Cut No.	Equivalent length (AIA pixels)	Time sections (secs)	Position Taken
1	1	3	apex
2	4	500	apex
3	4	500	leg
4	120	100	whole loop
5	120	1000	whole loop
6	120	2000	whole loop

Table 4.3: Table showing temporal and spatial cuts of the simulations that were examined. Each cut was designed to show a different aspect of the simulated loop. Cut 1 represents 1 AIA pixel size that is cut to 3 seconds which is the approximate exposure time for AIA. This is expanded in cut 2 where the same area at the apex of the loop is increased in length and duration in order to smooth out any fluctuations in the data. This same cut is examined in cut 3 but the location of the cut is moved to the 'leg' of the loop i.e., an area closer to the transition region of the loop. Cuts 4, 5 and 6 are taken over the whole length of the coronal part of the loop simulation and is examined over 100, 1000 and 2000 seconds in order to examine 'global' trends and differences in the data.

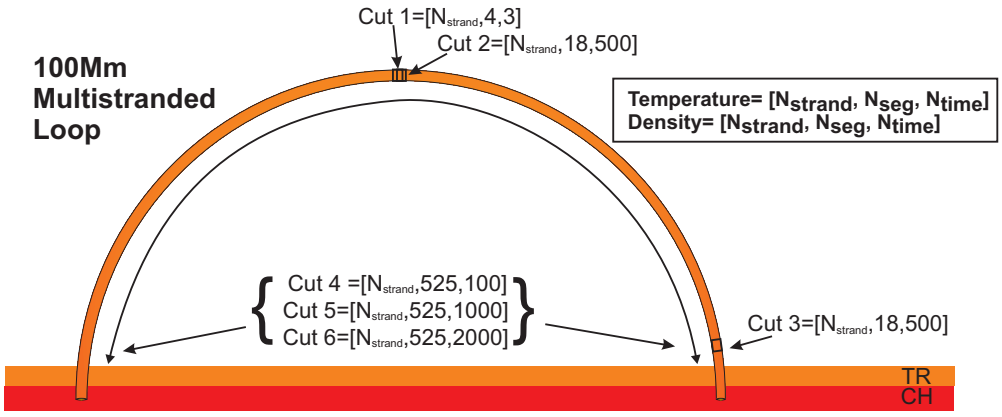

Figure 4.5: Sketch showing how the coronal part of the 100Mm loop has been cut into various sections of differing spatial and temporal sizes.

Once the simulations are run and the data has been cropped to various length and time-scales, the physical parameters outputted by the model can be extracted and examined. The main output of each simulation is an array of temperature and density which gives a single value of these quantities at each length section along each strand at each time-step. Looking at the temperature alone is not a good indicator of the plasma behaviour as density also needs to be considered. That is why an emission measure weighted temperature (as given in Equation 4.2.0.1) is the best way to characterise the overall temperature trend of the plasma. In this equation the effect of the temperature (T) and the density (ρ) along the length of the loop (s) and over time (t) is summed up over the number of strands in the loop (N_{strand}). The δl factor is the grid resolution which in the coronal part of the loop is 0.16 Mm as shown in Figure 4.4.

$$\overline{T}_{EM} = \frac{\sum_{i=1}^{N_{strand}} \rho_i^2(s,t)\, \delta l(s)\, T_i(s,t)}{\sum_{i=1}^{N_{strand}} \rho_i^2(s,t)\, \delta l(s)} \qquad (4.2.0.1)$$

By examining the trend of the emission measure weighted temperature (hereafter EMT), the broad characteristics of the plasma can be observed. These characteristics can be further examined by constructing differential emission measure plots (DEMs). General differences and unique signatures in these plots can be searched for between the different variations of the simulation. The purpose of doing this is to examine the way in which changing the physical parameters of the loop will influence the characteristics of the DEM (i.e., in terms of width, height, shape etc.). This is both a test that the MSHD model is behaving in a physically realistic way and also to put limits on what the DEM analysis can tell us about the model i.e., if some parameter is changed can it be detected just from looking at the DEM? This issue becomes very important later in this chapter when real SDO/AIA data is incorporated into the analysis. Ultimately the aim is to show that this model is valid because it can produce observations that are physically sensible and are consistent with what is seen on the Sun.

4.2.1 Investigation A: Effect of Changing Strand Number

The MSHD simulation can be used to investigate the effect of multi-strandedness by changing the number of individual strands within the fixed volume of the model loop. The effect this has on the subsequent DEM and synthetic SDO/AIA intensities can then be examined and explained by looking at the physical parameters of the model which have changed as a result of increasing/decreasing the number of strands.

The number of strands within the 100 Mm loop of fixed volume (1.26×10^{21} m^3) was increased from 16, to 32, 64, and 128 strands to measure this effect. This was done whilst keeping the radius of the overall loop the same (2 Mm) as well as the total energy that is deposited in the loop over the simulation timescale. However, this means that the radius of the individual strands decreased as strand number increased. The number of nanoflares per strand was also kept the same (64 bursts/strand) but this in turn meant that the energy of each nanoflare decreased as strand number increased in order for the total energy to remain the same in accordance with the equation:

$$E_{TOT} = (E_{burst} x N_{burst}) x N_{strands} \qquad (4.2.1.1)$$

This investigation aims to quantify the changes caused by increasing the strand number which consequently causes strand radius and nanoflare energy to decrease. The aim is to see if this change in model parameters causes a measurable effect on the outputted synthetic DEM and intensity measurements.

Comparison of general traits of simulations

As mentioned above, in each of the four simulations (of 16, 32, 64 and 128 strands) the number of bursts per strand was kept the same (64 nanoflares/strand) and each burst deposited its energy at a random time during the simulation. The size of these nanoflares

was scaled according to their number in order to keep the total energy deposited in the loop roughly the same at around 5.1 - 5.3 x 10^{28} ergs.

Strand No.	Tot. No. Bursts	Cross-sect. Area (cm^2)	Total Energy (ergs)	Ave. Burst Energy (ergs)	Power Law	Average EMT[a] (Log T/K)
16	1024	$8x10^{15}$	$5.32x10^{28}$	$5.20x10^{25}$	2.35	6.561
32	2048	$4x10^{15}$	$5.28x10^{28}$	$2.57x10^{25}$	2.39	6.562
64	4096	$2x10^{15}$	$5.13x10^{28}$	$1.25x10^{25}$	2.46	6.561
128	8192	$1x10^{15}$	$5.14x10^{28}$	$6.28x10^{24}$	2.57	6.561

Table 4.4: Model Parameters for changing strand number. EMT stands for the emission measure weighted temperature (see Equation 4.2.0.1). The cross-sectional area refers to the cross-sectional area of an individual strand in each case.

The basic parameters of the four simulations are given in Table 4.4 where it can be seen that the total energy of each simulation is around this value. It could not be exactly fixed due to the random nature employed to determine the size and timing of each specific nanoflare event. This slight difference in the total energy and also in the power law is to be expected and does not significantly impact the outcome. The columns in Table 4.4 describing how the average emission measure weighted temperature (EMT) of the loop changes between the simulations is based on the outputs of the model and is not a predefined value. This data is included to help explain the various changes in the calculated DEMs and also to show that the EMT values are almost exactly the same in each case.

The spatial distribution of the nanoflares along the loop was also kept the same in each case with the nanoflares being distributed practically uniformly over the length of the 100 Mm loop. These distributions are shown in Figure 4.6 where it can be seen that in each case nanoflares occur from -45 Mm to +45 Mm. This is due to the 5 Mm at the two ends of the 100 Mm loop being designated as the transition region/chromosphere where no nanoflares are located. As strand number increases, so too does the total number of nanoflares occurring within the loop. This increase leads to the spatial distribution of nanoflares becoming more smooth.

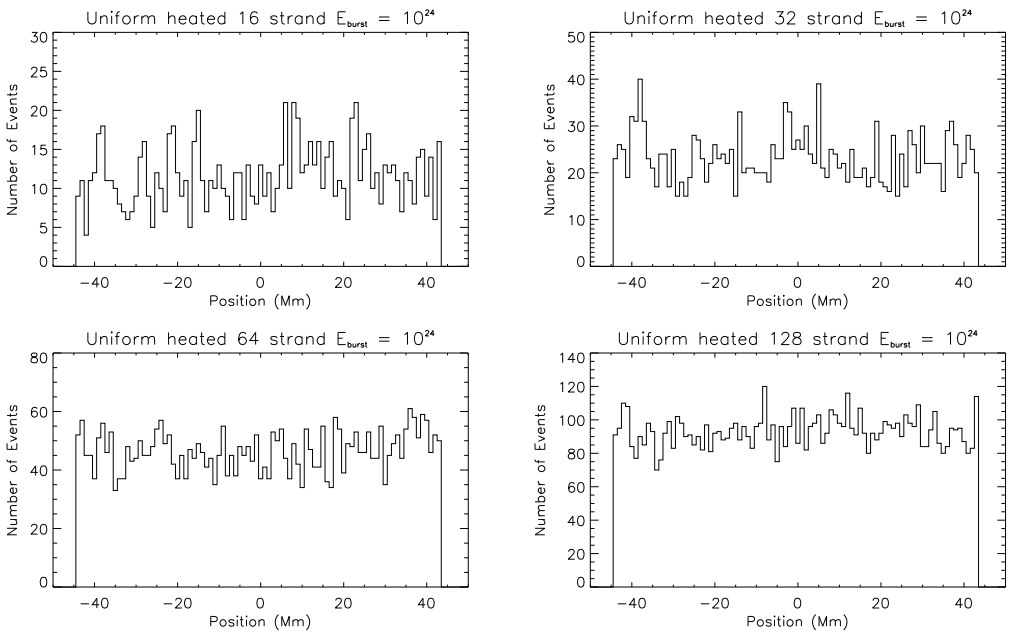

Figure 4.6: Figures showing the spatial distribution of the nanoflares along the length of the loop. It can be seen the distribution of nanoflares is uniformly spread along the length of the loop but grows more smooth as strand number increases. This is due to the number of bursts per strand remaining the same so as strand number increases there is a more uniform distribution due to more bursts going off.

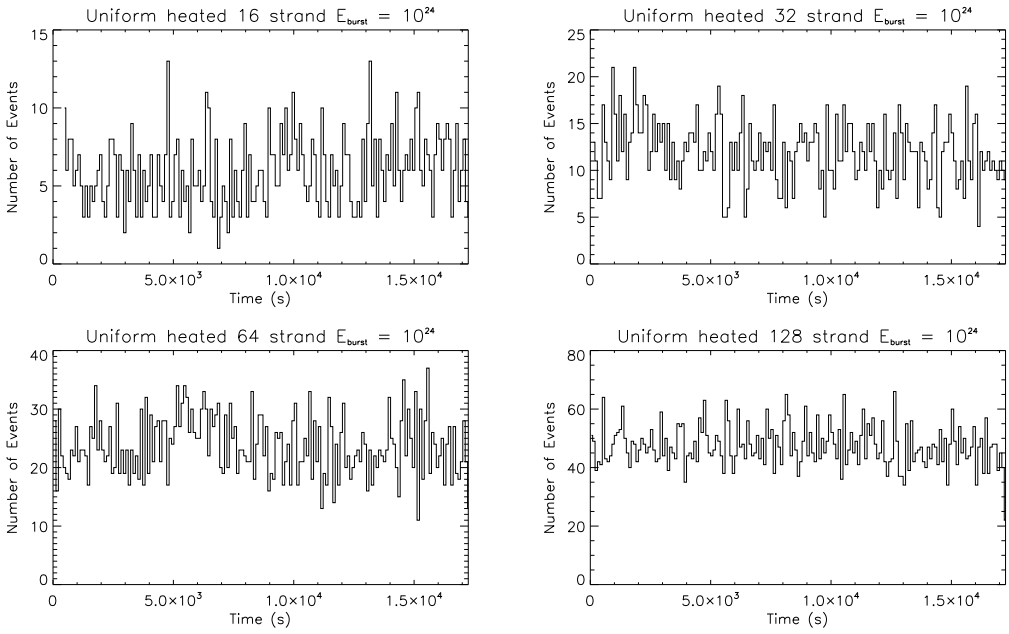

Figure 4.7: Figures showing the temporal distribution of the nanoflares over the time-length of the simulation. It can be seen the distribution smoothes as strand number increases.

Figure 4.7 shows how the nanoflares in each simulation are distributed over the simulation time. In each case they are spread over the 17,250 seconds fairly well.

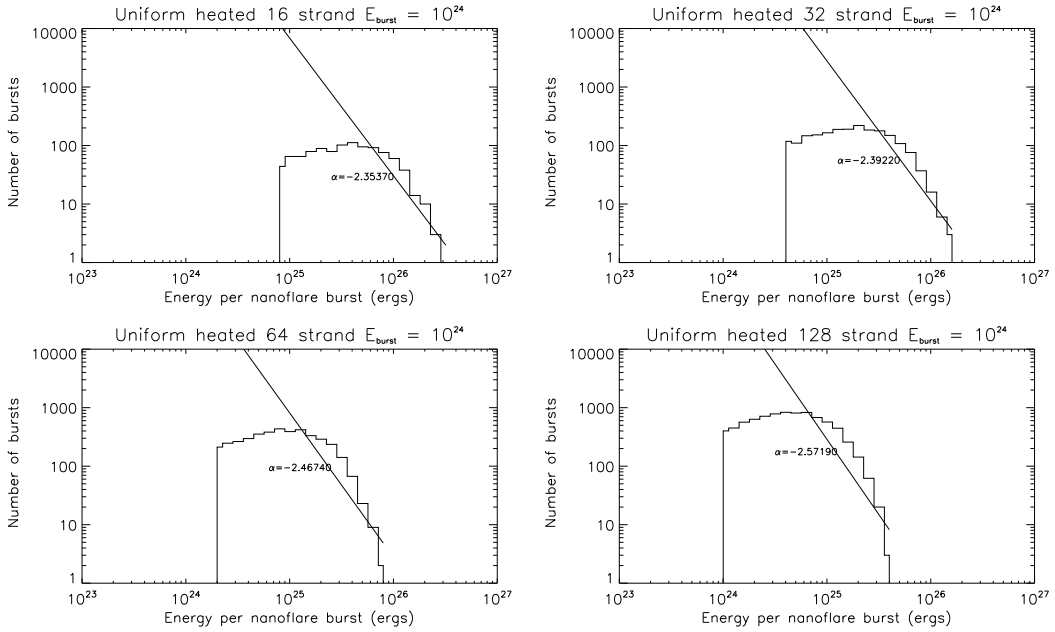

Figure 4.8: Figures showing how the power law changes as strand number increases. It can be seen that the slope in each case remains roughly the same with the distribution moving upwards (due to the number of nanoflares increasing with increasing strand number) and to the left. This shift to lower temperatures is due to the average energy per nanoflare decreasing as strand number increases.

The relationship between the number of nanoflares and the energy per nanoflare is shown in Figure 4.8 where the value of α from Equation 4.1.1.1 is given on each plot. The slope of each graph remains roughly the same but the plot moves upwards and to the left as strand number increases. The upward motion is due to the increase in the number of nanoflares occurring within the loop as strand number increases and the movement towards lower energies is due to the average energy of each nanoflare decreasing in accordance with Equation 4.2.1.1. The variation in the slope of each graph is within the bounds of what is acceptable i.e., the standard deviation of the power law as the strand number increases is only 0.1. Only changes of greater than 1 will significantly affect the simulation as shown by Sarkar & Walsh (2008).

Figure 4.9 shows the evolution of the EM weighted temperature (EMT) over time for each of the four simulations. It can be seen that the variation in the EMT becomes

less extreme as strand number increases. The reaction of the strand plasma to the nanoflare heating in the different simulations can be related back to the ratio of the cooling timescale of each nanoflare burst to the burst frequency.

The burst frequency is the same in each simulation but the time taken for a strand to cool back to its equilibrium temperature following a nanoflare is dependant on the size of the nanoflare energy. For example, a strand will have a more varied temperature evolution if the time between heating events is longer than the time taken for the strand to cool. Higher energy bursts cool faster (as conduction time is related to $T^{5/2}$) so the EMT for the 16 strand simulation (which has the highest E_{burst} size) is much more varied compared to the 128 strand model.

Another factor that will influence how the plasma behaves after a heating event is the volume each nanoflare is concentrated in. The individual strand volume decreases as strand number within the loop increases (see Table 4.4 where the cross-sectional area of the strands in each simulation is listed). The plasma within a low volume strand will have a more dramatic reaction to a particular heating event than would be seen in a higher volume strand (providing the energy burst is the same size). This effect is not seen in this investigation as both strand volume and nanoflare energy go down together as strand number increases. The effect of changing the volume of a strand while the energy bursts stay the same size is discussed further in Section 4.2.4.

The outputs from each simulation can further be used to investigate the plasma properties of the modelled loop by calculating the differential emission measure of each simulation based on particular time/space cuts of the data (as described in Table 4.3). The DEM distribution is expected to smooth out as strand number increases i.e., show less variation from temperature bin to bin.

This smoothing occurs mainly because the size of the model dataset (that goes into creating the DEM for each simulation) doubles each time the strand number does (as loop length and grid spacing along each strand is fixed) so it is statistically more likely

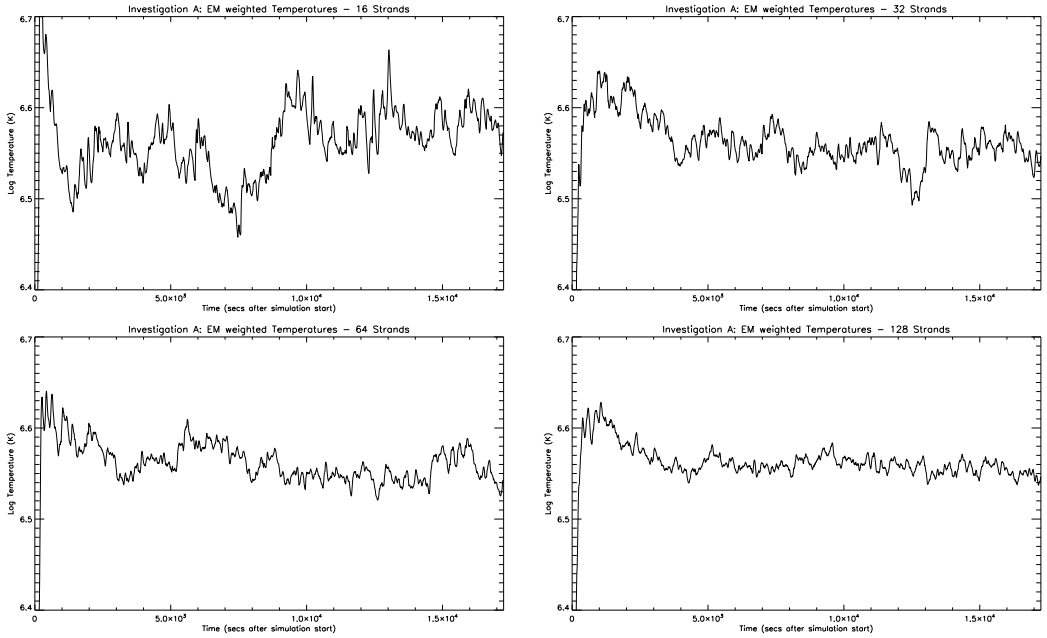

Figure 4.9: The emission measure weighted temperature of each simulation as strand number is increased.

that there will be plasma covering a wide range of temperatures centred around some average value.

The DEM of each simulation was explored over the various data cuts in order to see if any unique signatures of multi-strandedness were observed. Such signatures could be ideal indicators of multi-strandedness present in real observations. The veracity of this idea is explored in this section.

Issues with cropping/cutting MSHD model outputs

One of the aims of this chapter is to apply what the MSHD model indicates about changing plasma parameters to a real SDO/AIA data set. With this in mind, the logical temporal and spatial cut of the model would be equivalent to one AIA pixel resolution for the average exposure time of an AIA image.

Figure 4.4 showed the coronal part of the simulation has a uniform grid size of 0.164 Mm. From this the number of grid sections required to represent an AIA pixel of ~1” can be

calculated as follows:

1” = 725 Km = 0.725 Mm

0.725/0.164 = 4.4 ~ 4 length segments

The simulation duration is chosen to be 17,250 seconds long in each case but this generates a lot of output i.e., one value of temperature and density for every length section along every strand at every time-step. Picking just three of these time-steps is computationally advantageous and also represents a similar view to what would be seen by SDO/AIA which has an average exposure time of 3 seconds (Lemen et al. 2012b). As mentioned previously, this cut of the data (i.e., four length sections from all strands over three seconds) is designated as Cut 1 (see Table 4.3) and although it is comparable to what would be seen with SDO/AIA, there are inherent drawbacks in using such a small cut of the data to produce DEMs.

The DEMs in Figure 4.10 and 4.11 are examples showing the wide variation in the DEM profile that results from choosing a different three second window in the simulation. The 32 and 64 strand DEMs show a similar variation and illustrate that although the variations smooth out slightly as strand number increases (i.e., seen by comparing the size of the variations between Figures 4.10 and 4.11), the variations are not completely eliminated and therefore the choice of three seconds will not give an adequate representation of the simulation properties. Based on this, cuts of the simulation data that are averaged over a larger portion of space and time are primarily used to assess real changes in the DEM that are a result of the changing plasma properties and not just a temporal distortion.

Leg vs. Apex

An advantage of the MSHD model generating temperature and density values along the entire length of the loop is that changes in the DEM can be observed along this length

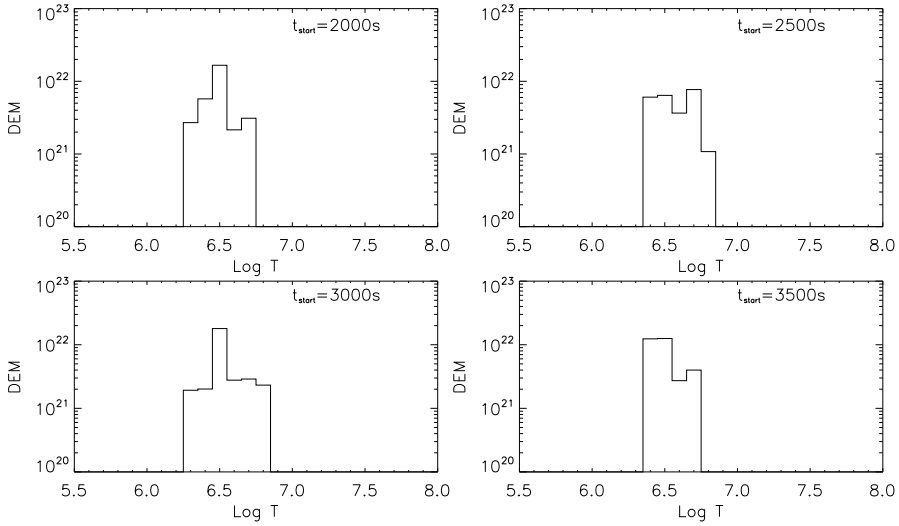

Figure 4.10: 16 strand simulation synthetic DEMs based on Cut 1 (1 AIA pix, 3 seconds) taken at different start times.

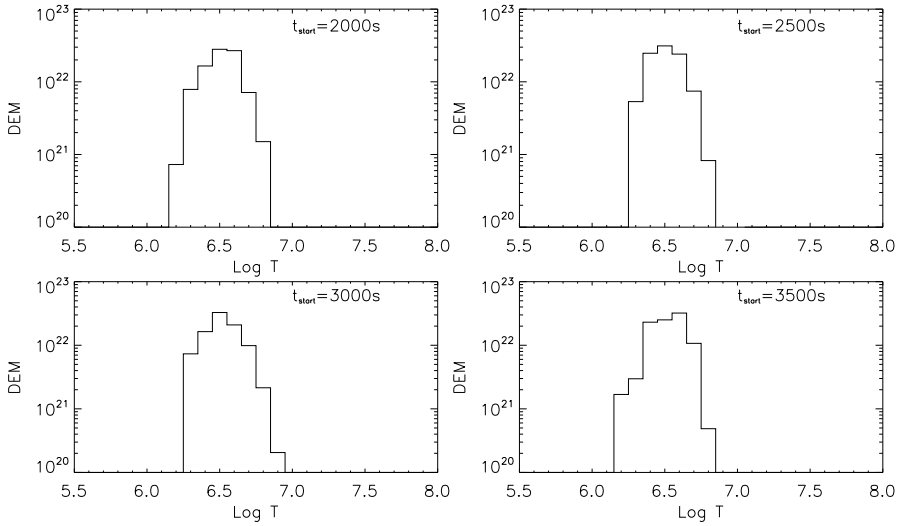

Figure 4.11: 128 strand simulation synthetic DEMs based on Cut 1 (1 AIA pix, 3 seconds) showing the difference in the DEMs due to picking a different time in the simulation to take the 3 second cut. For this reason, DEMs taken over a longer time period are considered as these have less drastic variations.

e.g., to compare the apex and footpoints of the loop. Figure 4.12 shows a comparison between DEMs constructed from data taken from the simulation apex compared to the leg. In this case 'leg' refers to the area of the simulation that is closest to the transition region but still part of the coronal portion of the loop. It can be seen that for each case of changing strand number, the DEMs exhibit a similar behaviour with the leg based DEM being wider and taller compared to the apex DEM. As strand number increases it can also be seen that the DEMs increase in height but this point will be covered in Section 4.2.1. The reason behind the shift in the 'Leg vs. Apex' DEMs becomes apparent when the spread of the data that the plots are based on is examined.

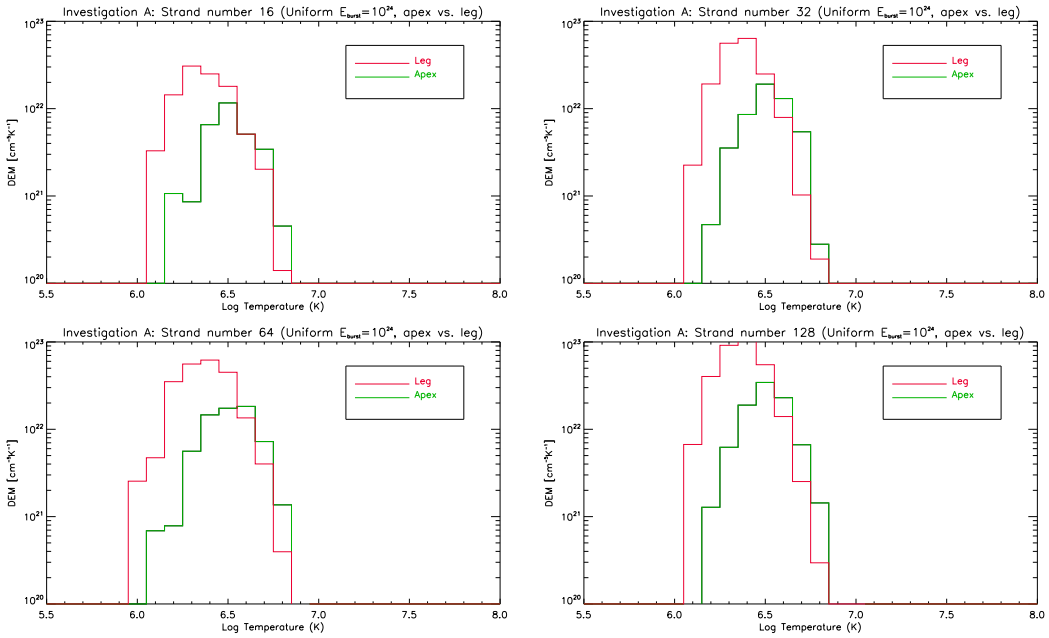

Figure 4.12: Figure showing comparison between DEMs taken from apex vs. leg of simulation for different strand lengths.

Figure 4.13 shows an example of the distribution of the temperature and density at different areas of the simulated loop. This plot was made by taking each value of the temperature and density contained in Cuts 2 and 3 (i.e., leg and apex) over four length segments and 500 seconds for the 128 strand loop, and plotting them against each other to get an indication of the spread of the data. Although this particular plot is taken from the 128 strand simulation, it is representative of what the other lower strand number plots demonstrate. It can be seen that the temperature and density of the data taken from

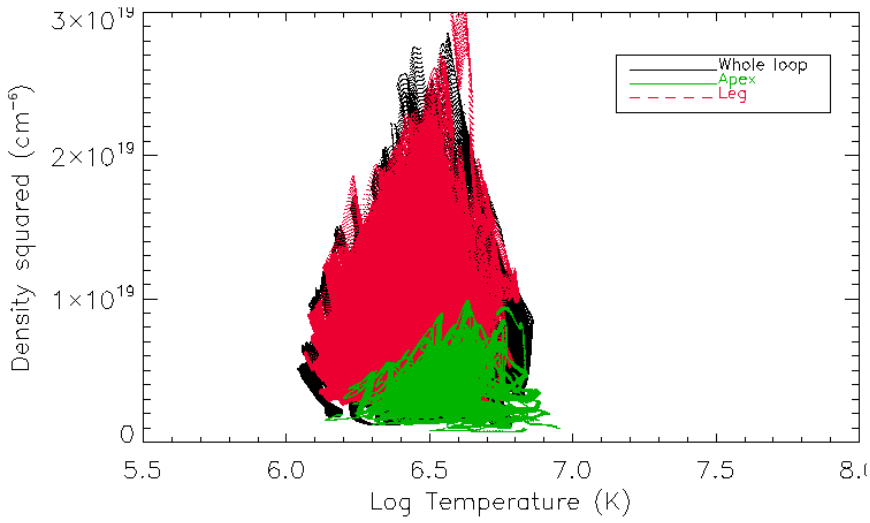

Figure 4.13: Temperature and density distribution of area of 128 strand loop at apex (green) and on the leg (red).

the apex (green) of the loop is contained within a narrower region than data taken from the leg of the loop (red). This accounts for the apex DEMs being distributed over a narrower temperature range than the leg DEMs. The increase in the DEM values of the leg data compared to the apex is also explained as it is clear the legs of the loop have a higher density than the apex which is to be expected.

Impact on DEM of changing strand number

In order to see the overall trend exhibited by increasing the strand number of the simulations, a longer time period needs to be examined to iron out any fluctuations caused by individual nanoflare energy dissipation.

Figure 4.14 shows the four simulations of increasing strand number overplotted on each other with the topmost plot showing the comparison with temperature bins of Log T/K = 0.1 while the lower plot shows a more detailed view where the temperature bins have been refined to Log T/K = 0.025. A clear trend is seen where the DEM increases in height as strand number increases. The width of the DEM also seems to increase slightly. This widening is due to an increase in the statistical significance of the data set

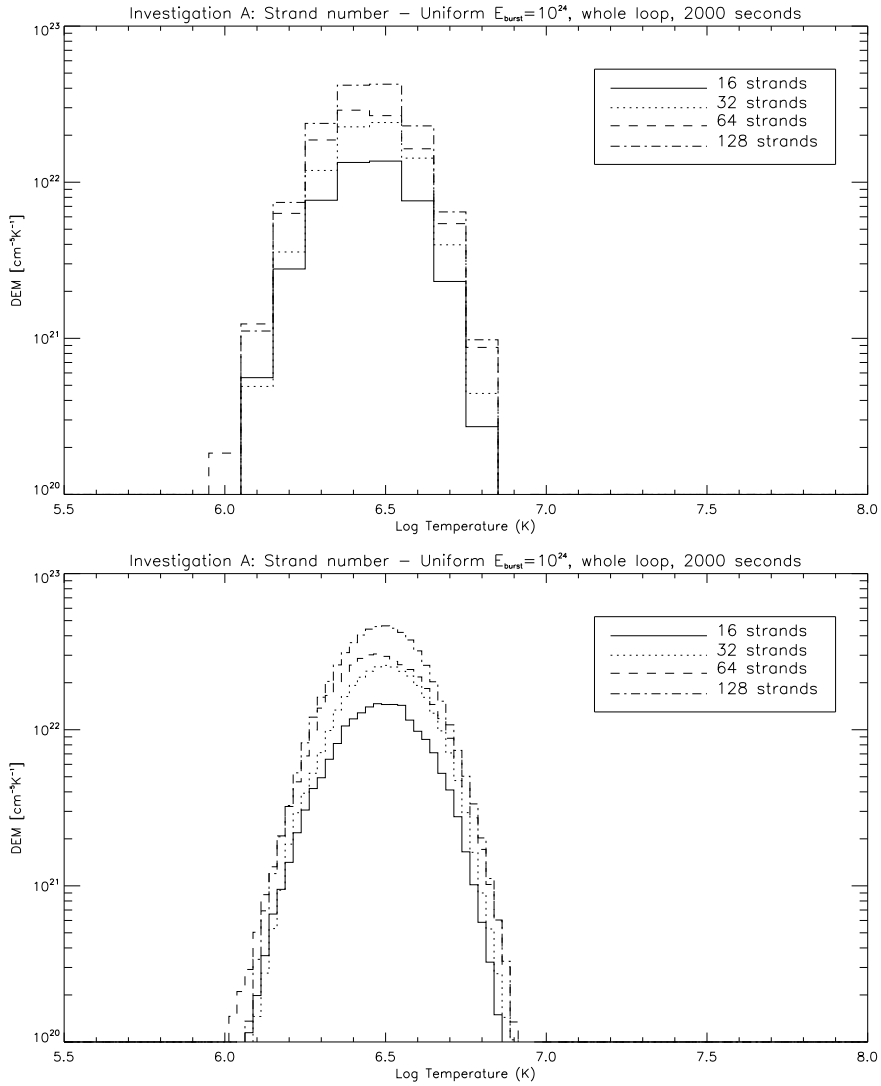

Figure 4.14: DEMs of changing strand number based on data from whole loop averaged over 2000 seconds. *Top:* DEMs with temperature bins of Log T = 0.1. *Bottom:* Same DEMs but calculated over finer temperature bins of Log T = 0.025 to highlight small-scale differences.

that each subsequent DEM in based on as strand number increases i.e., as strand number doubles so does the number of temperature and density values that the DEM is based on.

The increase in the height of the DEMs as strand number increases can be directly related to the corresponding decrease in the strand diameters. As Table 4.4 indicates, the doubling of the stand number in each subsequent simulation causes the individual strand diameters to decrease by a factor of $1/\sqrt{2}$. Since the DEM calculation includes a line-of-sight factor which is approximated as the thickness of one strand in each case, this change in strand diameter causes the DEM to increase by a corresponding factor of $\sqrt{2}$. This scaling factor is clarified below where A_L is the cross-sectional area of the whole loop, A_s is the cross-sectional area of an individual strand, R_L and R_s are the corresponding loop and strand radii (where R_L is kept constant), and N_s is the strand number.

$$A_L \approx A_s N_s$$

$$\pi R_L^2 \approx \pi R_s^2 N_s$$

$$R_s \approx \frac{R_L}{\sqrt{N_s}}$$

$$16 strands \Longrightarrow R_{16s} \approx \frac{R_L}{\sqrt{16}} = \frac{R_L}{4}$$

$$32 strands \Longrightarrow R_{32s} \approx \frac{R_L}{\sqrt{32}} = \frac{1}{\sqrt{2}} \frac{R_L}{4}$$

$$64 strands \Longrightarrow R_{64s} \approx \frac{R_L}{\sqrt{64}} = \frac{1}{\sqrt{2}\sqrt{2}} \frac{R_L}{4}$$

$$128 strands \Longrightarrow R_{128s} \approx \frac{R_L}{\sqrt{128}} = \frac{1}{\sqrt{2}\sqrt{2}\sqrt{2}} \frac{R_L}{4}$$

It can be seen that doubling the strand number in each case causes the strand radius to decrease by a factor of $\sqrt{2}$. This will have a direct result on the DEM in each case as

the line-of-sight element for the DEM calculation is approximated as the diameter of a strand. Therefore this LOS element will change by a factor of $1/\sqrt{2}$ as strand number doubles, directly impacting on the DEM.

Figure 4.15 shows this scaling clearly as the real DEM values are plotted (in black and in non-log form) while the values of the 128 strand DEM (scaled down by $\sqrt{2}$ in each case) have been overplotted in red. It can be seen that this approximation reproduces the majority of the observed increase in the DEM values suggesting that this is just an inherent effect of the simulation. The slight disparity between the DEM values (black) and their scaled counterparts (red) is due to the particular snapshot in time this plot is based on.

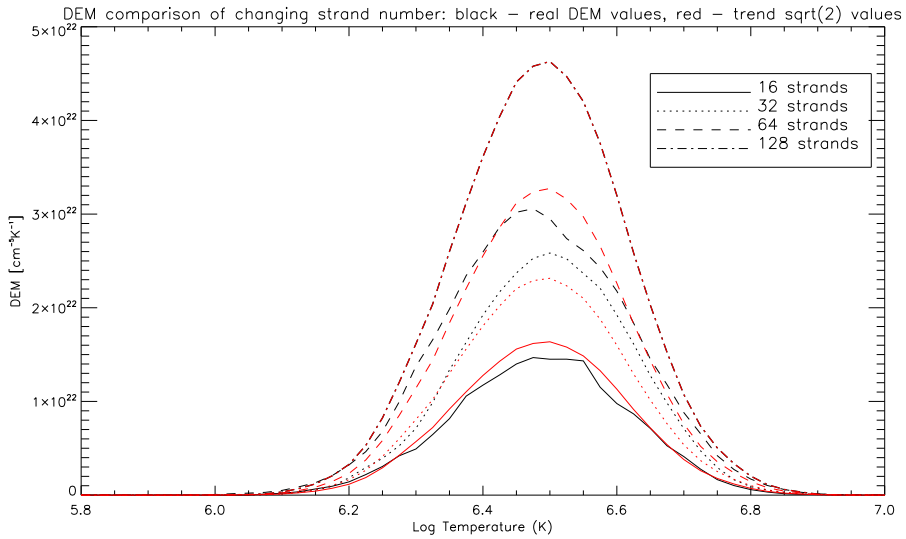

Figure 4.15: DEM values from Figure 4.14 (lower) plotted on a non-log scale in black with the 128 strand values scaled down by $\sqrt{2}$ overplotted in red. It is a close visual fit suggesting that the majority of the DEM rise is due to the $\sqrt{2}$ factor from the change in strand diameter.

Impact on SDO/AIA intensity due to changing strand number

By using the calculated DEMs and folding them through the temperature response function of the SDO/AIA imager, simulated intensities can be calculated and examined for unique signatures. These intensities are shown in Figure 4.16 where it can be seen that

the intensities seen in each channel follow the same pattern as strand number increases but with a different scaling. Once again the difference in the scaling is $\sqrt{2}$ and is due to the change in the strand diameter as strand number increases. As the DEMs (seen in Figure 4.14) cover approximately the same temperature range as the strand number increases, it is expected that the emission would follow the same pattern in each case. A difference in the ordering of the dominant intensity channels would only be expected if there was a clear shift to higher or lower temperatures seen in the DEMs.

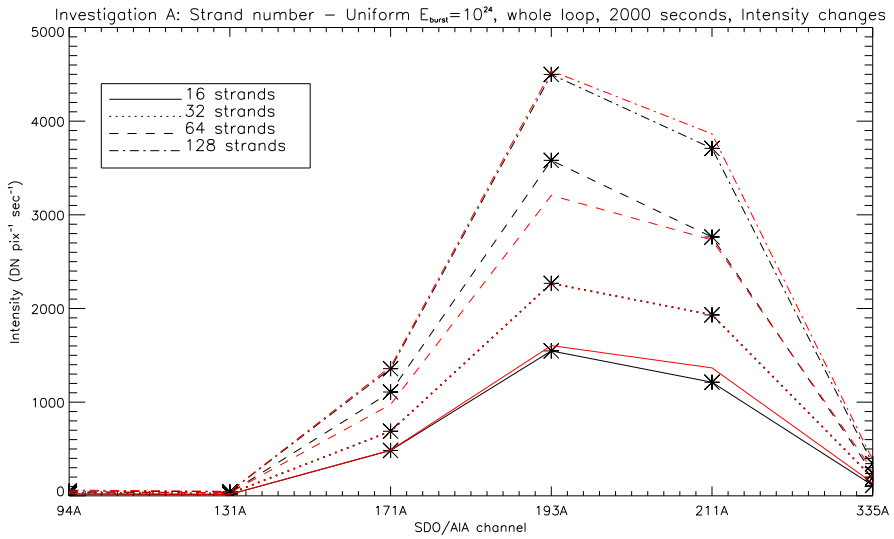

Figure 4.16: SDO/AIA simulated intensities changing as strand number increases (black). Note that these values are not continuous and are only plotted this way to indicate the general trend of each intensity set. The values of each intensity are plotted as $*$. The red lines represent the intensity values of the 32 strand loop that have been scaled up/down by $\sqrt{2}$ to show that changes in intensity as loop number increases are mostly due to the strand diameter changing in each case.

Discussion

In order to study the effect of changing the strand number within a 100 Mm loop of fixed radius and fixed total energy input, loop simulations of 16, 32, 64 and 128 strands have been run and the measurable outputs examined.

By changing the strand number (and correspondingly changing the strand diameter and average nanoflare energy in order to keep the overall loop radius and total energy the

same), the result is an increase in the calculated DEM and intensity (per pixel per second) values as strand number increases. These increases are characterised by a scaling of $\sqrt{2}$ which can be traced back to the changing strand diameter. The $\sqrt{2}$ scaling seen is a result of the strand number doubling in subsequent simulations e.g., the scaling would be $\sqrt{N}$ if the strand number had increased by a factor N each time.

The DEMs also become more smoothed as strand number increases. This is because increasing the strand number leads to many more nanoflares (of lower energy) going off along the loop which creates a smoother DEM as there is less variation in the temperatures reached.

Apart from this scaling there is no clear unique signature that would allow an identification of increasing strand number to be made. The same increase in DEM value could also be attributed to a scenario where the density of one loop was higher than another giving the same result. A larger multi-strandedness signature would be of use when looking for evidence of subresolution strands within real data sets.

4.2.2 Investigation B: Changing the Location of the Nanoflares

As previously mentioned, the location of each nanoflare along a particular strand and the time of its initiation are randomised factors in the simulation. However, the distribution of these nanoflares can be confined to a particular area of the loop such as the apex region, footpoint region, or having a uniform distribution along the loop length. In order to examine what effect, if any, this factor plays in the MSHD simulation, all three cases have been examined.

Three simulations were undertaken that kept all parameters basically unchanged except the distribution of the nanoflares along the length of the loop. Some of the basic parameters are given in Table 4.5. The average energy of each nanoflare in the three simulations was set to be around 10^{24} ergs but this is only a guide value as the simulations vary the

Strand No.	Heating Location	Total Energy	Ave. Burst Energy	Power Law	Average EMT[a]	EMT[a] range
128	Uniform	5.14×10^{28}	6.28×10^{24}	2.57	6.562	6.537–6.628
128	Apex	5.04×10^{28}	6.16×10^{24}	3.07	6.606	6.580–6.636
128	Footpoint	5.13×10^{28}	6.26×10^{24}	2.87	6.522	6.462–6.591

Table 4.5: Model Parameters for changing nanoflare location. EMT strands for the emission measure weighted temperature (see Equation 4.2.0.1).[a] at apex.

heat deposition around by a randomised amount. Due to this randomisation factor the total energy going into each simulation is slightly different (third column of Table 4.5). However, these variations are not large enough (~2% difference) to cause any substantial effects so we can be confident any changes detected in the model outputs are due to the nanoflare spatial distribution alone.

The exact differences in the nanoflare spatial distribution between the three simulations can be seen in Figure 4.17. In all figures in this section the designation 'Apex' refers to apex localised heating, 'Footpoint' to heating localised at the footpoints of the loop, and 'Uniform' to heating spread uniformly over the length of the loop. Although the distribution of the nanoflares in space is very different between the three simulations, Figure 4.18 shows that the nanoflares are distributed evenly throughout the simulation time.

Figure 4.19 shows the energy power law for each of the three simulations. The slight variation in the α value of the Apex Heating can be traced back to the slightly lower value of total energy that this simulation has compared to the other two. As mentioned in Investigation A, this slight variation causes no major effects and any influence it does have is greatly overshadowed by the effect of changing the distribution of the heating.

In order to examine how changing the spatial distribution of the nanoflares affects the outputs (e.g., temperature and density) of the MSHD model, various plots can be made. The first factor to examine is how the average emission measure weighted temperature (EMT) of each simulation changes over time. This can be seen in Figure 4.20 where the

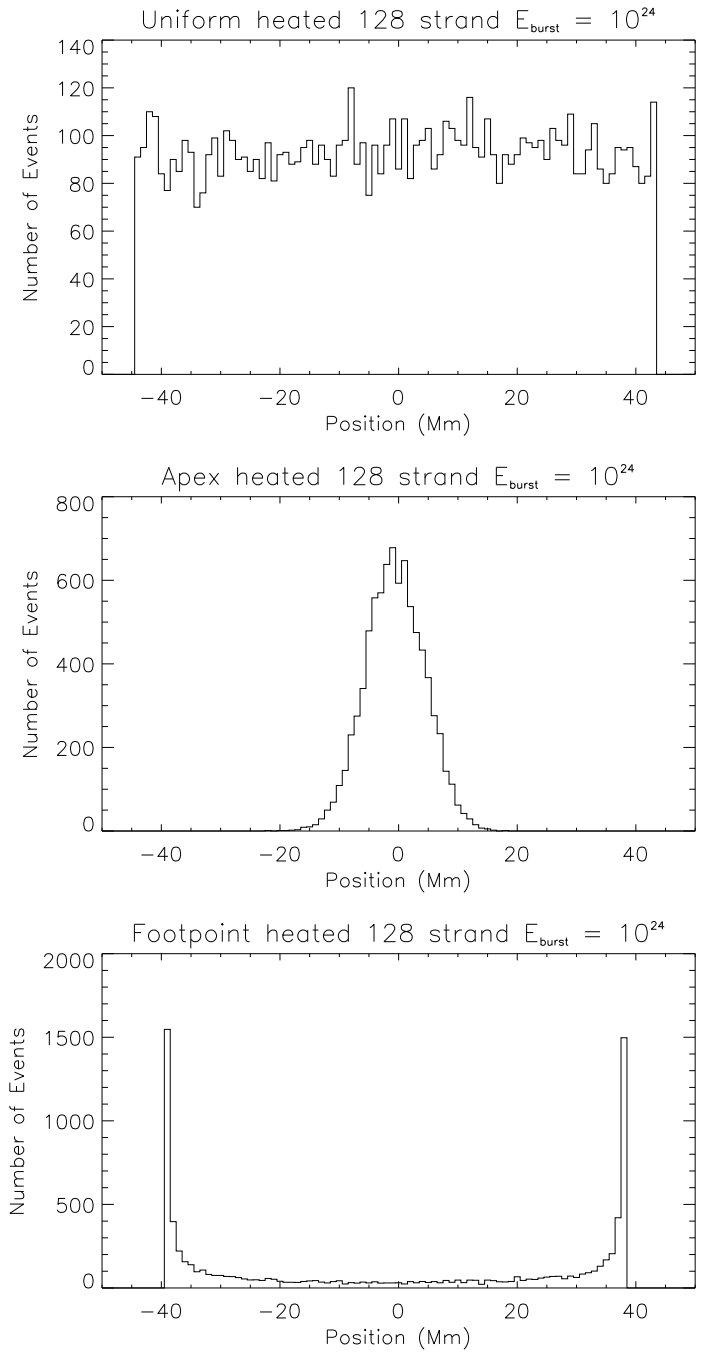

Figure 4.17: Figures showing the spatial distribution of the nanoflares over the length of the 100 Mm loop.

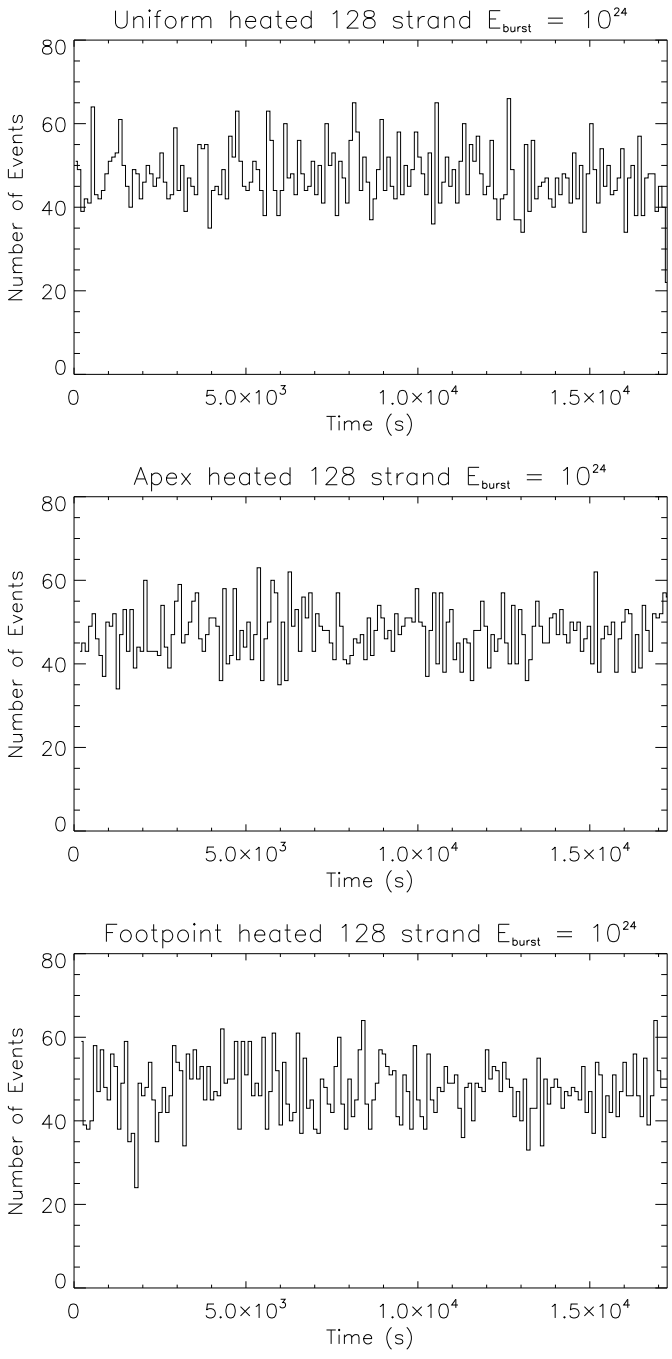

Figure 4.18: Figures showing the temporal distribution of the nanoflares over the time length of the simulation.

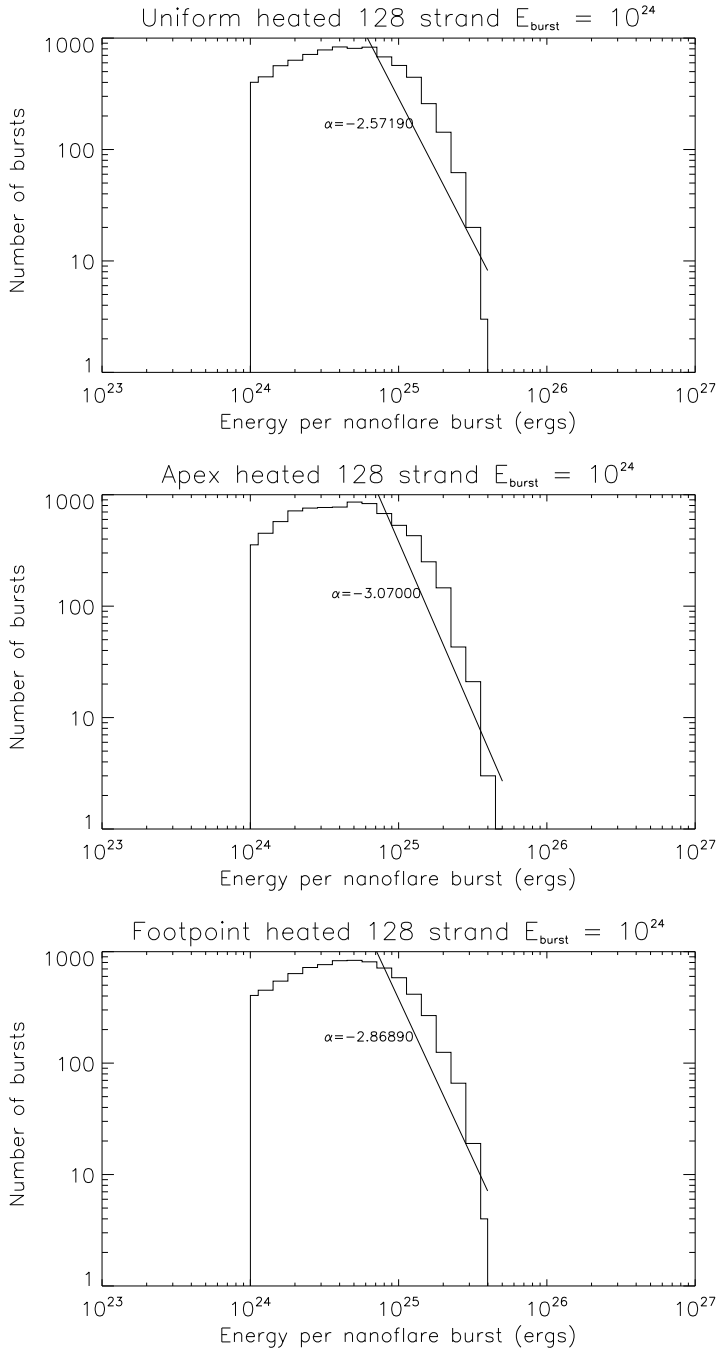

Figure 4.19: Figures showing the relationship between the number of nanoflares and the nanoflare energy in each simulation as a power law.

data is based on a region taken at the topmost portion of the loop over all strands and all time. The EMT is calculated using Equation 4.2.0.1 and it can be seen that there is a modest difference in log scale in the average EMT value between simulations. The extent of the variation in the EMT seems to be comparable in each case but the average value from the apex heated simulation is clearly the highest followed by the uniform distribution and lastly the footpoint heated case. Although Figure 4.20 is based on a section of the data at the top of the loop, this trend is seen when looking at positions at other points along the loop. The reason for this shift can be further explored by looking at the unweighted model temperature and density values as a function of loop position.

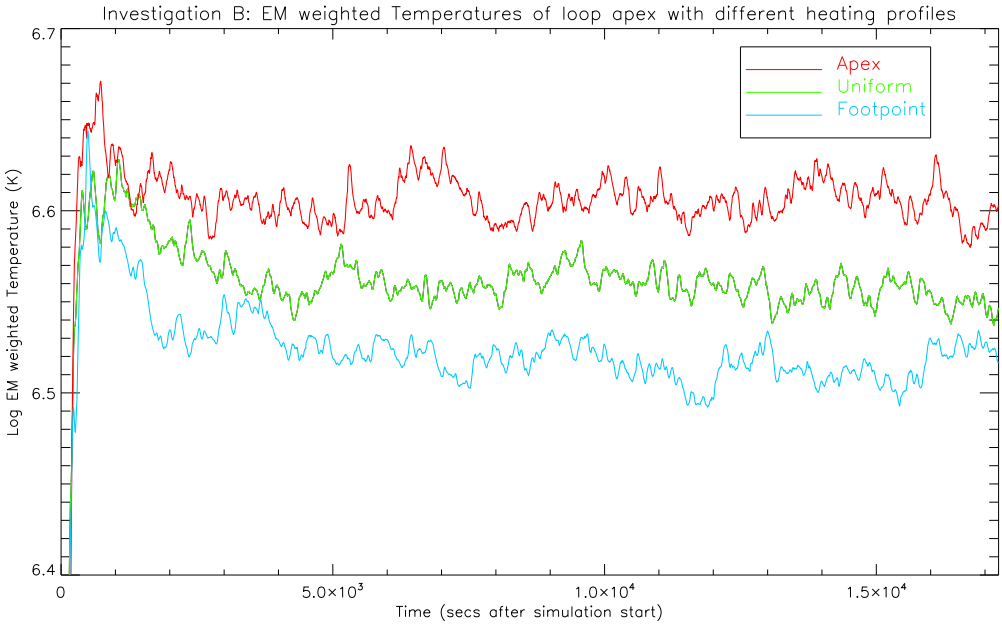

Figure 4.20: The emission measure weighted temperature of each simulation. The data for this plot has been taken from the apex of the loop simulation but is representative of what would be seen in the whole loop.

As described by other authors (Priest et al. 2000, e.g.,) there is an observable difference in the resulting long-duration temperature and density values depending on the location of the heat input. Figure 4.21 shows the variation of the temperature and density (averaged over all strands over 1000 seconds) along the length of the 100 Mm loop for each type of heating distribution.

The density values for the footpoint heating case are seen to be higher than for the

uniform and apex heating cases. This is because more mass is evaporated from the model chromosphere into the loop when the heating is focused at the footpoints. This higher density means that radiation dominates the energy dissipation throughout the loop and conduction is low. This low conduction is responsible for the flat temperature profile seen for the footpoint heating case. The temperature profile for the apex heating case is more sharply peaked around the loop apex as the plasma density in this scenario is lower meaning that conduction can dominate over radiation to dissipate the nanoflare energy.

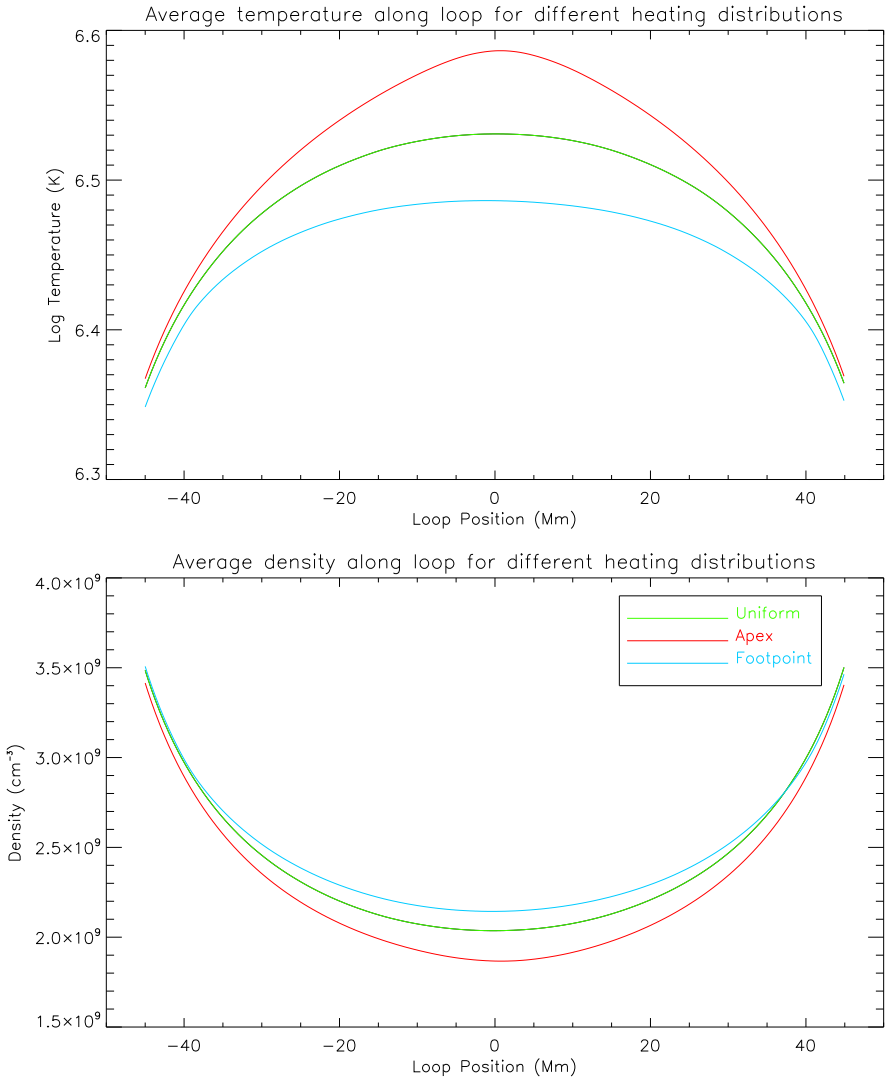

Figure 4.21: Average temperature and density over loop length for different heating profiles. Values averaged over 1000 seconds of model data over all strands.

A major advantage of studying the outputs of the MSHD model is the level of detail

available in terms of temperature and density values. These values can be put to a more practical use by using them to calculate a DEM distribution for each simulation to look for unique signatures and/or any trends observed.

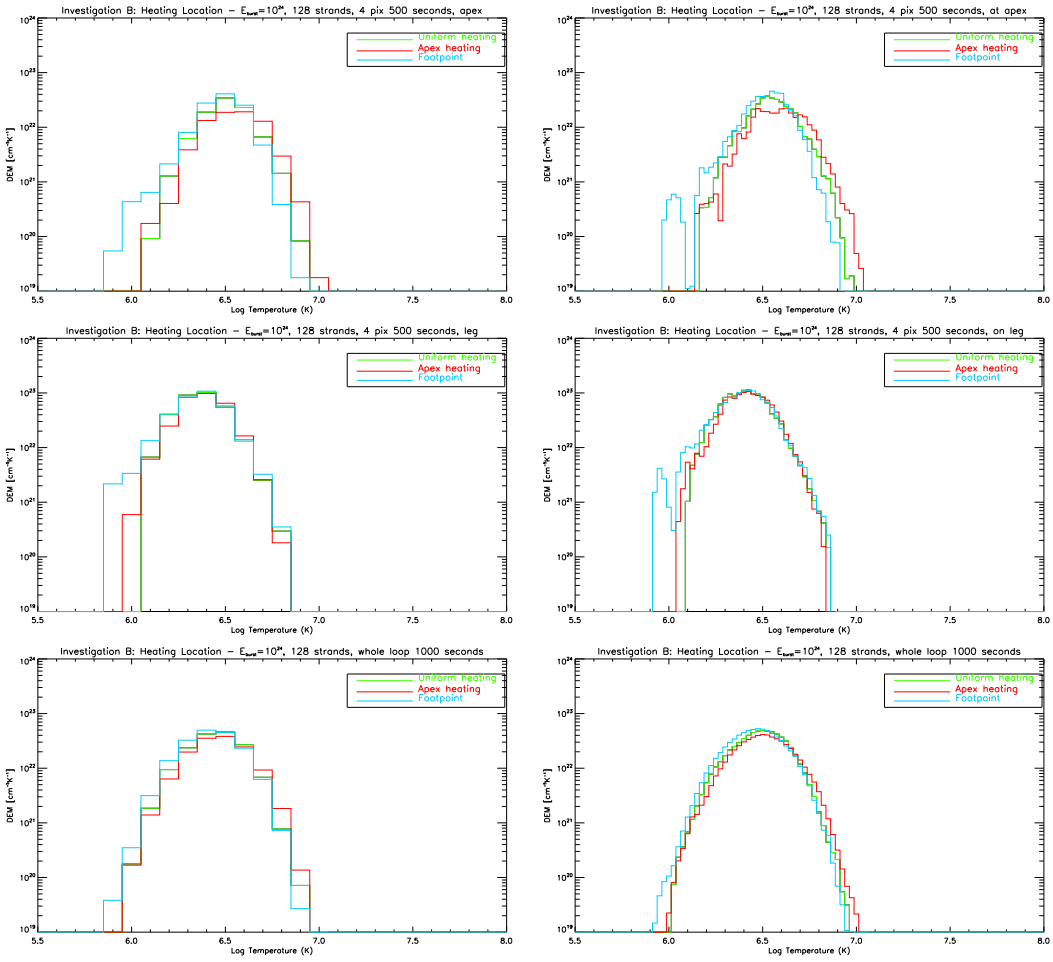

Figure 4.22: Comparison of DEMs at cuts 2 (top), 3 (middle), and 5 (bottom) (see Table 4.3 for cut specifications) for Δ Log T =0.1 and 0.025 (K) showing three simulations with the nanoflares distributed uniformly (green), at the loop apex (red) and close to the footpoints (blue).

Figure 4.22 shows DEMs for the three simulations listed in Table 4.5 based on three different cuts (cuts 2, 3 and 5 as described in Table 4.3) of the data. The left column shows the DEMs made with a bin size of Δ Log T =0.1 while the right column shows a finer binning of Δ Log T =0.025. This was done in order to examine any fine-scale changes that may be averaged over in larger temperature bins and it can be seen that much more detail is revealed in the finer DEMs. One such example is the peak at Log T =6.0 seen in

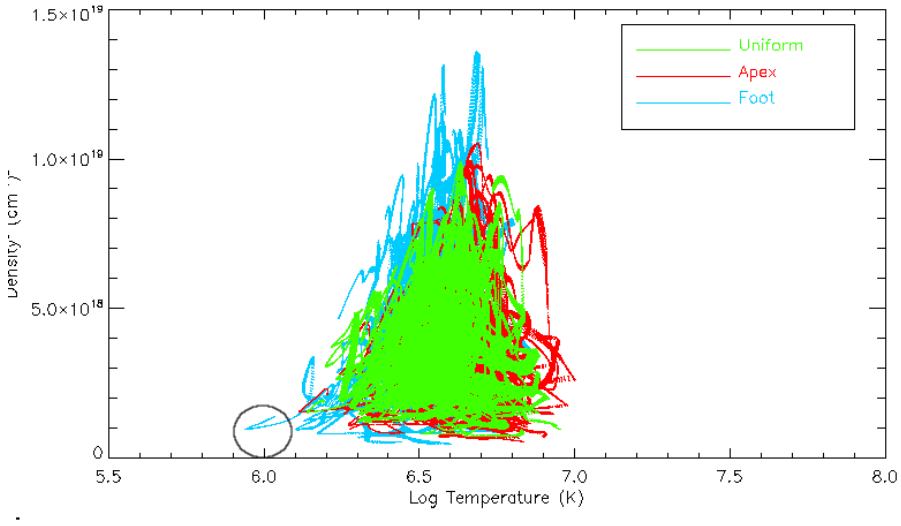

Figure 4.23: Plot showing the distribution of the temperature and density values used to create the topmost DEM in Figure 4.22. The point of this plot is to explain the erroneous DEM contribution at Log T = 6.0 for the footpoint heating distribution. This part of the DEM is created from the data within the circled area of the graph and is only due to the behaviour of one strand. This effect is magnified in Figure 4.22 as it is plotted on a log-scale.

the top and middle right-hand plots for the footpoint heated simulation (blue). This feature is an erroneous contribution to the DEM caused by the behaviour of one particular strand.

Figure 4.23 shows the distribution of the temperatures and densities of the model plasma for each heating case with the circle at Log T =6.0 highlighting the strand in question. The log-scale of the DEM plots in Figure 4.22 have exaggerated the contribution of this strand to the overall DEM and should not be over-interpreted. This feature is not seen in the lower DEM plots as these graphs are made from a much larger cut of the data (in space and time) and so have averaged out this feature to create a much smoother DEM i.e., there is much less variation from temperature bin to bin.

The top and middle rows show the DEMs created from data at the loop apex and on the loop leg respectively. A similar trend to the one seen in Investigation A is observed with the leg DEMs being taller than the apex DEMs. This is again due to the increased density in the loop legs compared to the apex.

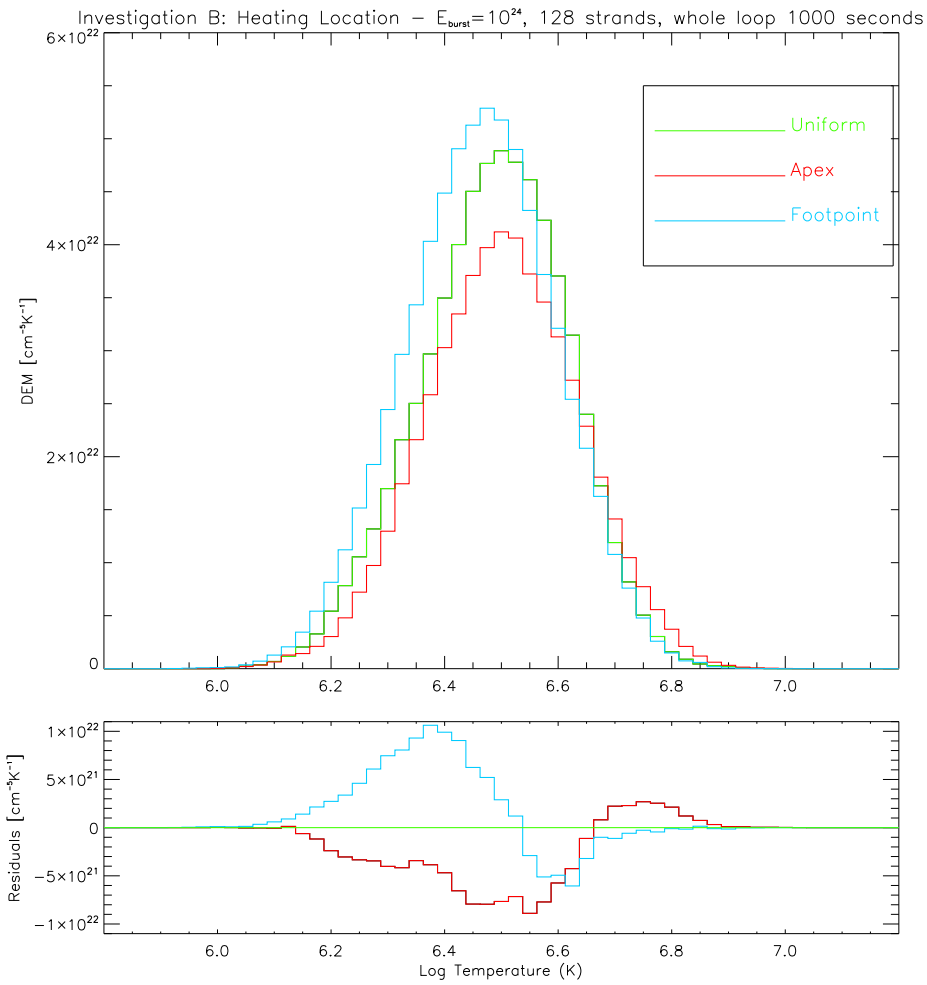

Figure 4.24: DEMs of the three simulations plotted on non-log scale. This data is based on cut 5 of the data and is the same as the lower-right plot of Figure 4.22 i.e., based on data from the whole loop over 1000 seconds. The residuals between the uniform data and the apex/footpoint data are shown in the lower panel.

The main feature to note from these DEM plots is the slight offset between the three heating distribution DEMs in each case. The apex and footpoint heated DEMs appear on either side of the uniform DEM with footpoint shifted towards lower temperatures and apex towards higher temperatures. This shift is seen more clearly in Figure 4.24 where the DEM from the lower-right panel of Figure 4.22 has been replotted on a non-log scale. The residuals between the apex and footpoint heated DEMs compared to the uniform heated case are also shown in the lower panel to highlight this offset.

The peaks and troughs of the residuals plot can be explained by considering the apex and footpoint heating cases compared to the uniform case. The small peak in the apex DEM residual seen at Log T = 6.75 highlights the shift in the DEM to higher temperatures compared to the uniform case. This can be related back to Figure 4.21 where it can be seen that the apex heated loop reaches higher temperatures than the other two heating distributions. This means that more of the plasma in the apex heated simulation is at a higher temperature leading to the DEM shifting to the right. The main peak in the footpoint heating residuals is due to the fact that the plasma in this simulation has a lower average temperature (as seen in Figure 4.21) but a higher average density than the uniform and apex heated simulations. This lower average temperature accounts for the shift to lower temperatures in the DEM and the higher average density leads to the DEM having an increased height compared to the other two simulations. This shift between the three heating distributions is not substantial and would be hard to detect in some reduced versions of the dataset.

These DEMs can then be folded through the temperature response of the SDO/AIA instrument in order to investigate how the intensity evolves as the parameter space of the model changes. Figure 4.25 shows that the three simulations display the same intensity pattern but with the footpoint heated distribution (blue) having the highest values. This can be explained by noting that the footpoint heated DEM is the largest out of the three due to this simulation having a higher overall density (see Figure 4.21).

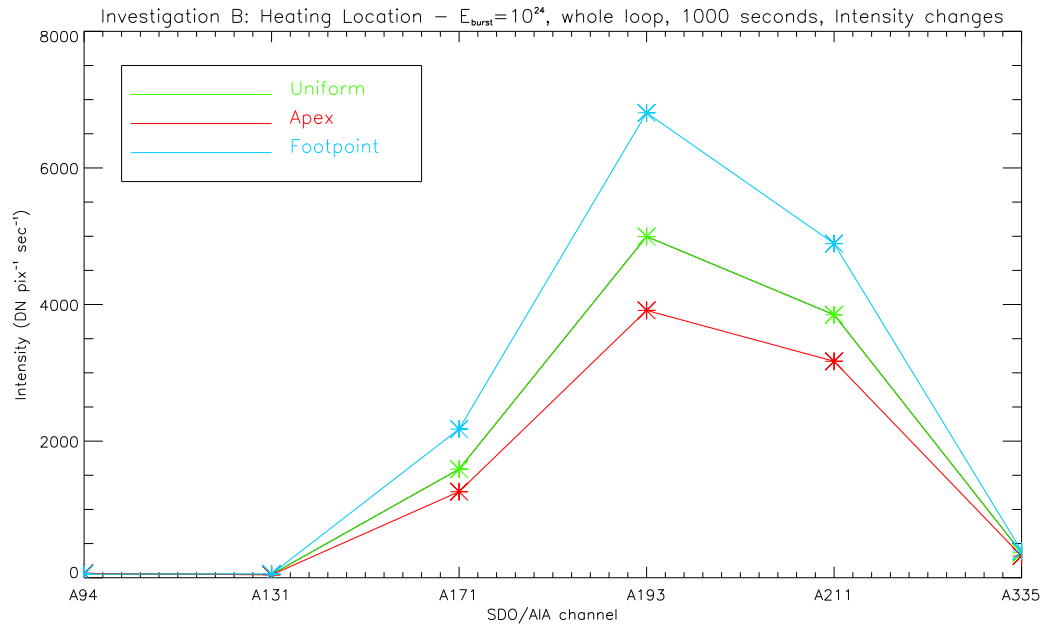

Figure 4.25: Synthetic SDO/AIA intensity changes calculated from each simulation. Note: the intensity values are not continuous and are marked with a $*$ symbol. The lines are to show the changing intensity value trend between simulations.

In summary, changing the spatial distribution of the nanoflares causes a shift in the subsequent DEM. This difference is more obvious when intensity values are considered. In order to detect any obvious trend in the DEMs, long timescales (1000s) had to be considered in order to average over the temporal and spatial fluctuations. This suggests that this effect would not be measurable in real SDO/AIA data unless a long time series was considered. However, this would pose certain difficulties as real observations of coronal loops are generally not stable for this length of time.

The very slight shift in the DEMs is perhaps too subtle to be considered a unique signature as such shifts could easily be caused by general changes in the plasma properties of the loop.

4.2.3 Investigation Ci: Changing the E_{tot} of the system by increasing the E_{burst}

An important check to perform is making sure that changing the total energy of the system shows a clear effect in the corresponding DEM. This has been investigated by running simulations 4, 7 and 8 from Table 4.2 where the average size of each nanoflare increases by an order of magnitude. Table 4.6 provides further details of the differences between these three simulations. In each case the loop length is the same (100 Mm), there are 128 strands with 64 nanoflares per strand, and these nanoflares are distributed evenly along the loop length and throughout the simulation time (see Figures 4.26 and 4.27).

Strand No.	Total Energy	Ave. Burst Energy	Power Law	Average EMT[a]	EMT[a] range
128	5.14×10^{27}	6.28×10^{23}	2.57	6.276	6.252–6.318
128	5.14×10^{28}	6.28×10^{24}	2.57	6.562	6.537–6.628
128	5.14×10^{29}	6.28×10^{25}	2.57	6.849	6.820–6.895

Table 4.6: Model Parameters for changing total energy input. EMT strands for the emission measure weighted temperature (see Equation 4.2.0.1).[a] data taken at loop apex.

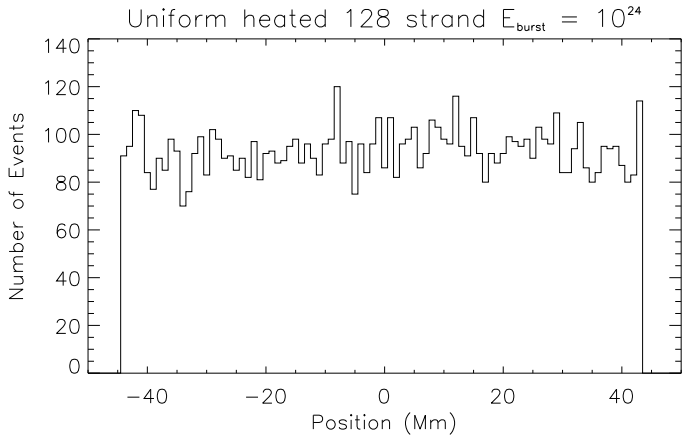

Figure 4.26: Figure showing the spatial distribution of the nanoflares over the length of the 100 Mm loop. This plot shows the distribution over the length of the loop for the E_{burst}=10^{24} erg case but is identical of the distribution seen in the other two energy cases.

Figure 4.28 shows the relationship between the number of nanoflares in each simulation

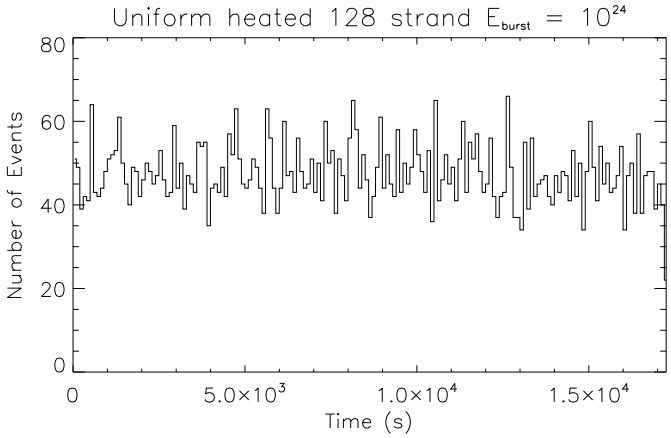

Figure 4.27: Figure showing the temporal distribution of the nanoflares over the time-length of the simulation. Again, this plot shows the nanoflare distribution over time for the $E_{burst}=10^{24}$ erg case but is identical of the distribution seen in the other two energy cases.

(8192 in each case) and the size of each nanoflare energy. The slope of this power law is exactly the same in each case as the nanoflare energy has been increased by a factor of ten in each case, resulting in the power law merely shifting to higher energies.

Once again the temperature and density outputs of the MSHD model can be combined into an average emission measure weighted temperature (EMT) using Equation 4.2.0.1 in order to quickly assess the plasma behaviour over time in each simulation. A measure of this EMT at the loop apex over the entire simulation time is shown in Figure 4.29 where it can be seen that changing the average nanoflare energy (and hence the total energy going into each simulation) has a dramatic effect on the loop plasma with the average EMT doubling each time the total energy is increased.

Making further use of the raw temperature and density values allows various DEM plots to be constructed. Figure 4.30 shows a selection of DEM plots from the three simulations based on various cuts of the model data. The top and middle DEMs are based on cuts of the data taken at the loop apex and leg respectively and show the same overall pattern. The only difference is a slight shift to lower temperatures seen in the leg DEM which is to be expected as the lower portion of the loop does not reach as high a temperature as the apex section. The bottom set of DEMs are based on data averaged over the

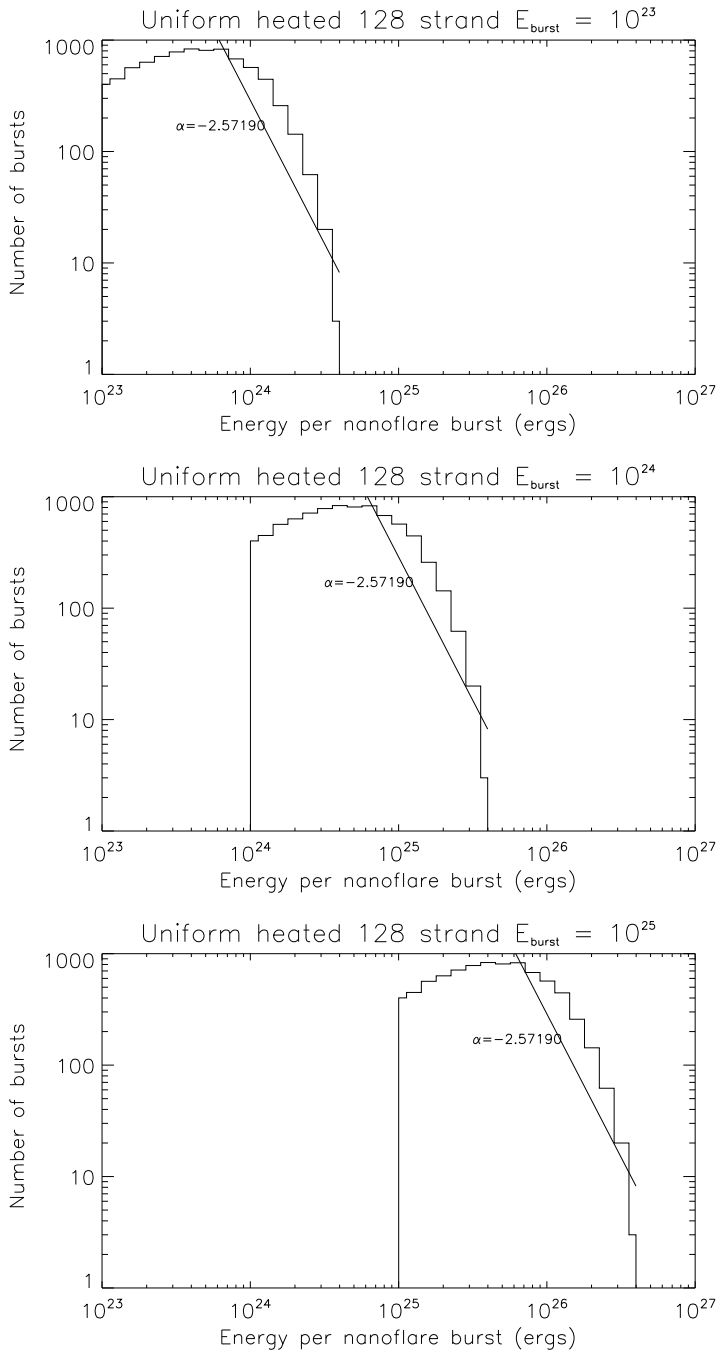

Figure 4.28: Figures showing the relationship between the number of nanoflares and the nanoflare energy in each simulation as a power law.

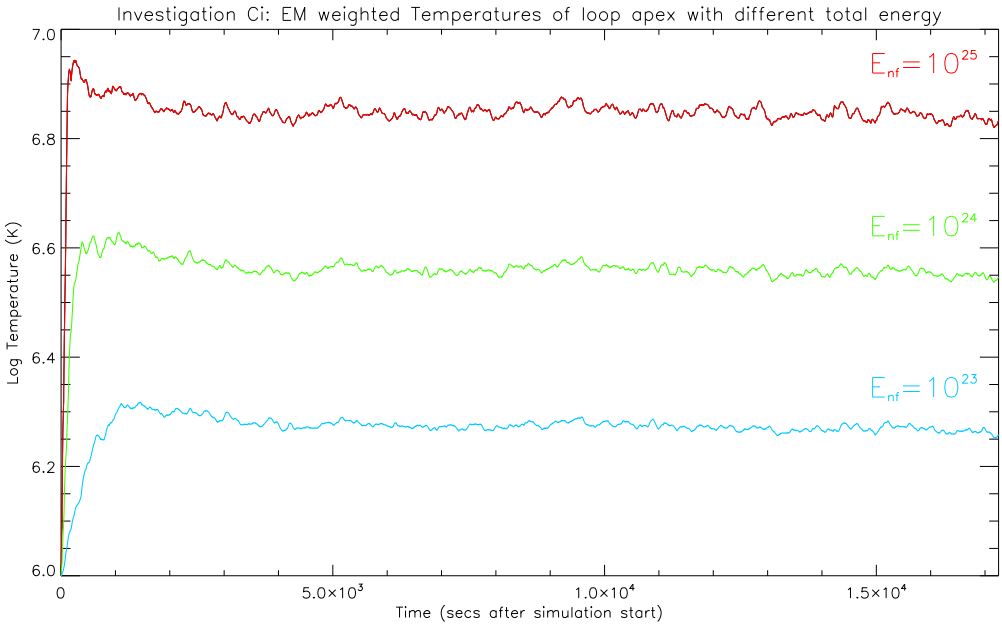

Figure 4.29: The emission measure weighted temperature of each simulation of increasing nanoflare energy.

whole coronal loop length for 100 seconds and shows a much more even distribution of plasma over the temperature bins. Each DEM plot shows the same clear trend with the higher energy simulation (red) being shifted towards higher temperatures compared to the 'standard' energy simulation (green) and the lower energy simulation (blue) being shifted towards lower temperatures. This is an obvious result but serves as both a check that the simulation is performing as expected, and also as a gauge to see how far the DEMs shift when the total energy is changed. This allows restrictions on the total energy going into the simulation to be made as energies that give unphysical results (e.g., the majority of the plasma over Log T = 7.0) can be adjusted to sensible levels.

Once again the DEMs with a smaller size of temperature bin (right column of Figure 4.30) highlight various instances where the spread of the DEM is less uniform (i.e., the variation from temperature bin to bin is not an even progression). This is seen most clearly in the $E_{burst}=10^{25}$erg case (red) at around Log T = 6.4. These variations are the same as those seen in Investigation B where the evolution of one or two strands happens to be further away from the strand average in terms of temperature and density distribution. These variations have mostly evened out in the lower plots of Figure 4.30

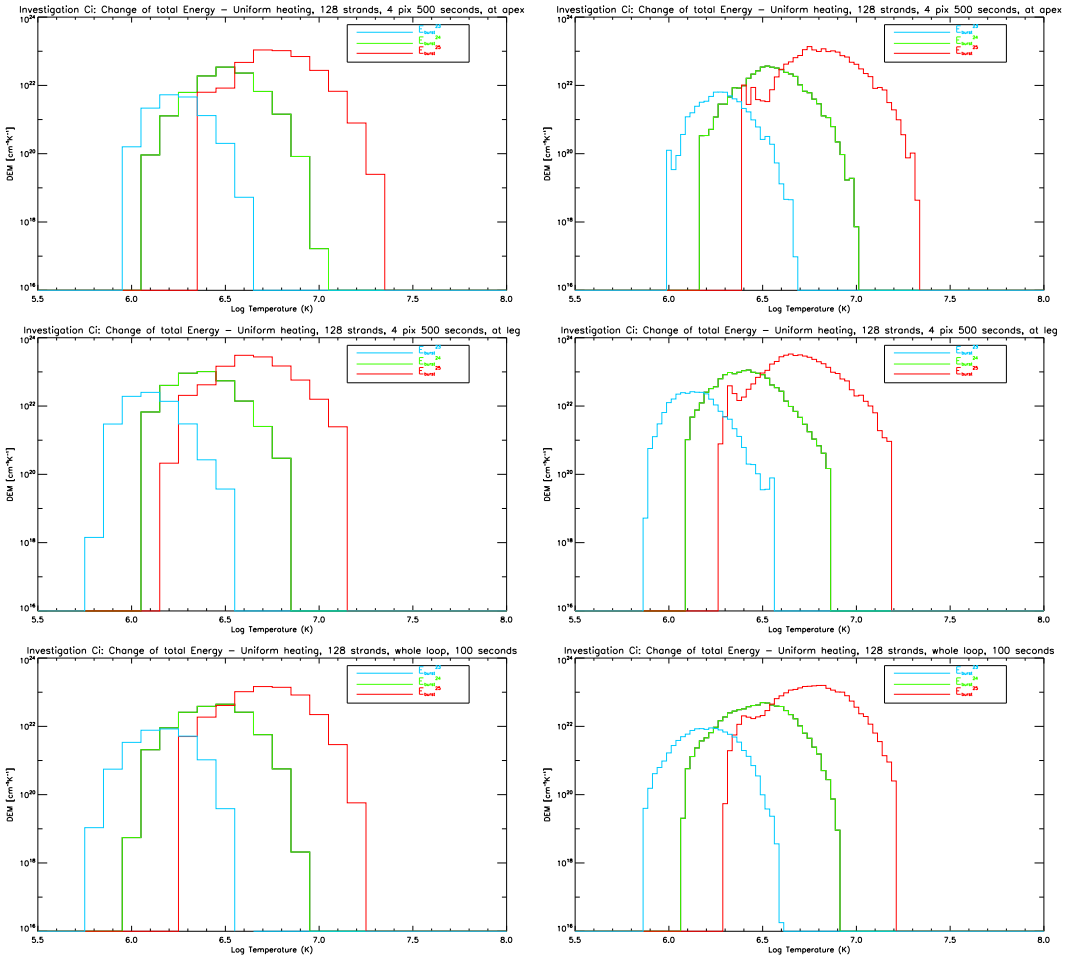

Figure 4.30: Various DEM plots of the three simulations taken at different cuts in space and time and with two temperature bin sizes. *Top:* DEMs based on data from the loop apex averaged over 500 seconds. *Middle:* DEMs based on the same 500 seconds but taken lower on the loop towards the footpoints. *Bottom:* DEMs based on data averaged over the whole loop length for 100 seconds. In each case the left column shows DEMs with temperature bins of Log $\Delta T/K = 0.1$ while the right column shows a more detailed view with Log $\Delta T/K = 0.025$.

as this is based on the whole loop rather than just a small section.

An interesting difference between the simulations can be seen by computing the synthesised SDO/AIA intensities by folding the lower DEM in Figure 4.30 through the instrument response function. The intensity seen in each AIA filter by each simulation is shown in the top plot of Figure 4.31. Unlike investigations A and B where the resulting intensity values were simply scaled differently between simulations, here there is actually a change in which is the dominant highest intensity channel in each case. This is due to the shifting to higher temperatures as the total energy in the simulation is increased by a factor of ten.

The middle panel of Figure 4.31 re-plots the DEM created from data over the whole loop length over 100 seconds and is plotted above the normalised temperature response functions of SDO/AIA (bottom panel). The position of the DEM peaks in conjunction with the sensitivity peaks of AIA can be used to help interpret the different intensity values seen. In each channel the highest intensity seen is from the simulation whose DEM peak is closest to that channel's maximum sensitivity.

As total energy increases, the DEMs are seen to rise in height and also widen across the temperature range covered. The increase in DEM height is due to the density increasing in each case as more plasma is evaporated up into the loop as the total energy increases. The change in width of the DEM can be attributed to the differences between the plasma properties in each case seen in Figure 4.29 where the EMT of the $E_{burst}=10^{25}$ is seen to be the highest and most varied. The increase in DEM height also affects the synthetic intensity values as intensity values will be higher when the corresponding response curve peaks within one of these larger DEMs.

This investigation has shown that changing the energy input by an order of magnitude creates a large variation in the corresponding DEM and intensity values. These simulated observables allow the validity of each input energy to be tested (i.e., is it physically realistic?) and could set higher and lower bounds on what could possibly be observed

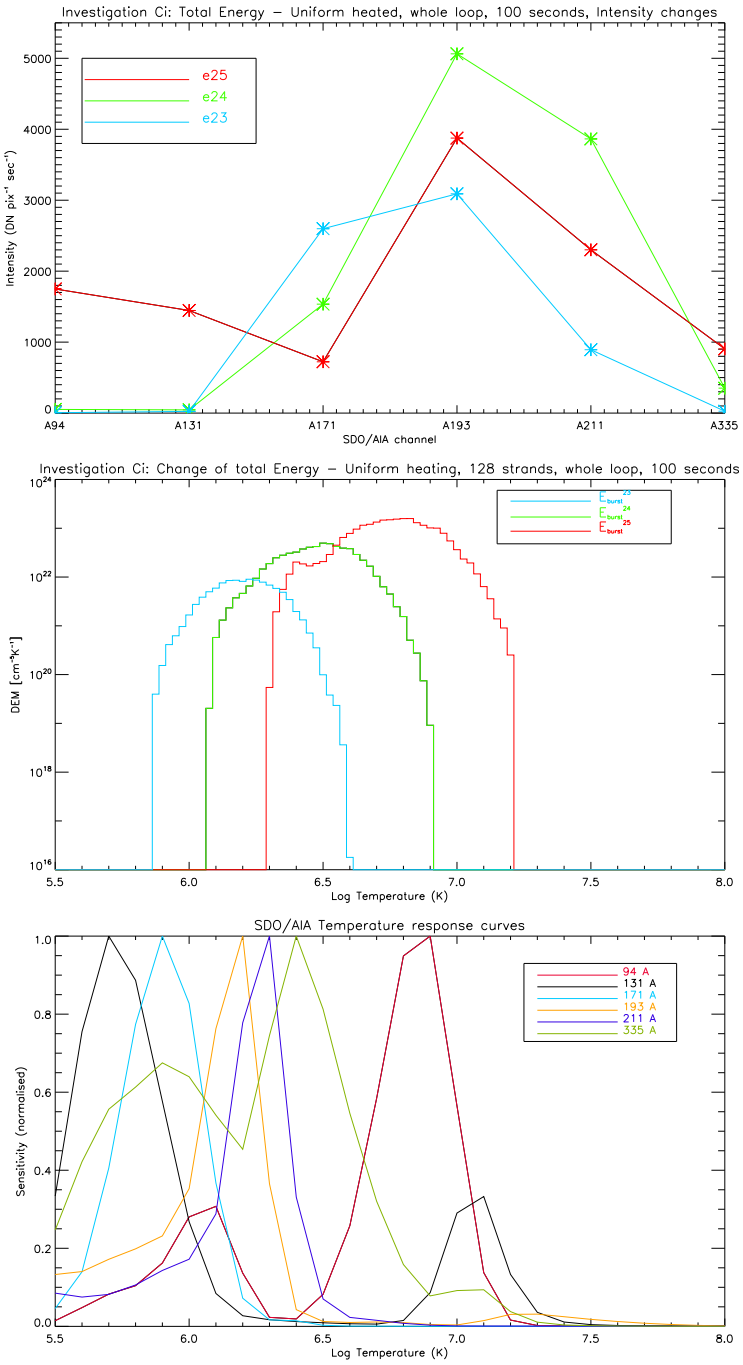

Figure 4.31: Synthetic intensity changes seen by SDO/AIA as total simulation energy changes. Note: the intensity values are not continuous and are marked with a $*$ symbol. The lines are to show the changing intensity value trend between simulations. DEM position (middle) compared to SDO/AIA instrument response function (bottom) in order to quantify changes in intensity seen.

in real coronal loops.

4.2.4 Investigation Cii: changing the number of nanoflares per strand

The energy balance within each simulation is based on the number of nanoflares per strand ($N_{nanoflares}$) and the individual energy in each of these nanoflares ($E_{nanoflare}$). The total energy in the simulation will be equal to the sum of all these individual nanoflares. Investigation Ci has shown that large differences are observed between simulations where the $E_{nanoflare}$ has been increased whilst keeping the $N_{nanoflares}$ per strand the same. This had the effect of changing the total energy going into the loop and had a clear signature in the DEM.

A more subtle change to the energy equation can be investigated by keeping the total energy going into the system the same but changing its constitution. This section investigates the effect of changing the number of nanoflares per strand (and subsequently changing the energy per nanoflare) and the effect that this has on the MSHD model outputs and synthetic DEM and intensity values.

General simulation traits

Table 4.7 lists some of the important parameters of the three simulations designed to test the effect of changing the number of nanoflares per strand. Each one is a 100 Mm loop consisting of 128 strands with the heating distributed primarily towards the footpoints. The total energy of each simulation is kept around the same value of 5 x 10^{28} ergs but there is a little variation around this figure due to the random elements in the simulation. The nanoflare distribution along the loop is concentrated at the footpoints as shown in Figure 4.32 and their distribution over the simulation time is seen in Figure 4.33 to be evenly spaced.

Strand No.	Heating Location	No. Bursts per strand	Total Energy	Ave. Burst Energy	Power Law	Average EMT[a]	EMT[a] range
128	FP	16	5.10×10^{28}	2.49×10^{25}	2.97	6.522	6.456–6.645
128	FP	64	5.13×10^{28}	6.26×10^{24}	2.87	6.522	6.492–6.591
128	FP	640	5.17×10^{28}	6.32×10^{23}	3.03	6.510	6.488–6.558

Table 4.7: Model Parameters for changing nanoflare number per strand. EMT strands for the emission measure weighted temperature (see Equation 4.2.0.1).[a] calculation based on data from the loop apex.

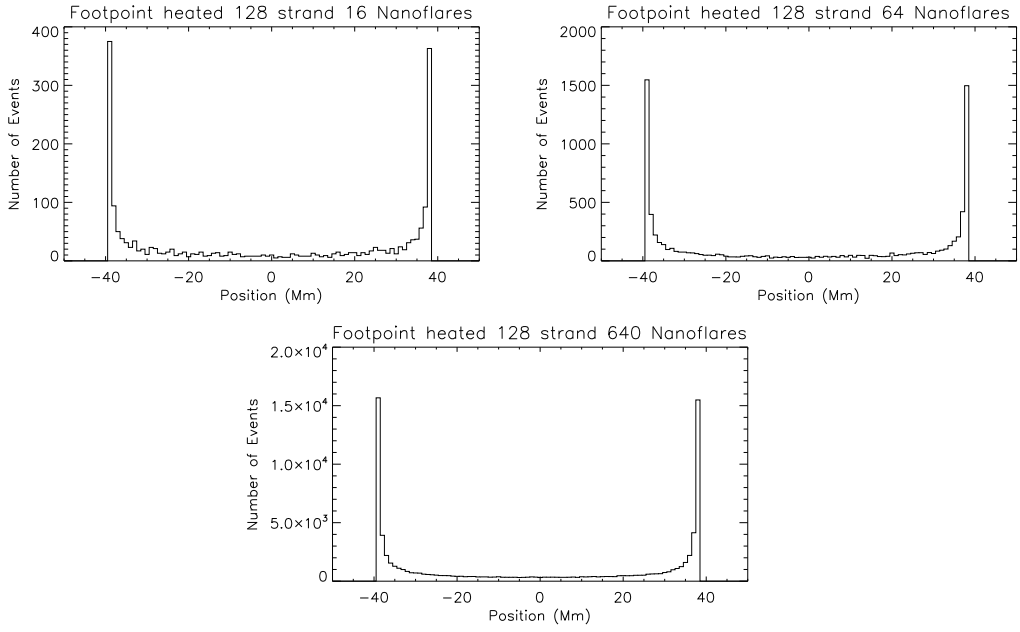

Figure 4.32: Figures showing the spatial distribution of the nanoflares over the length of the 100 Mm loop.

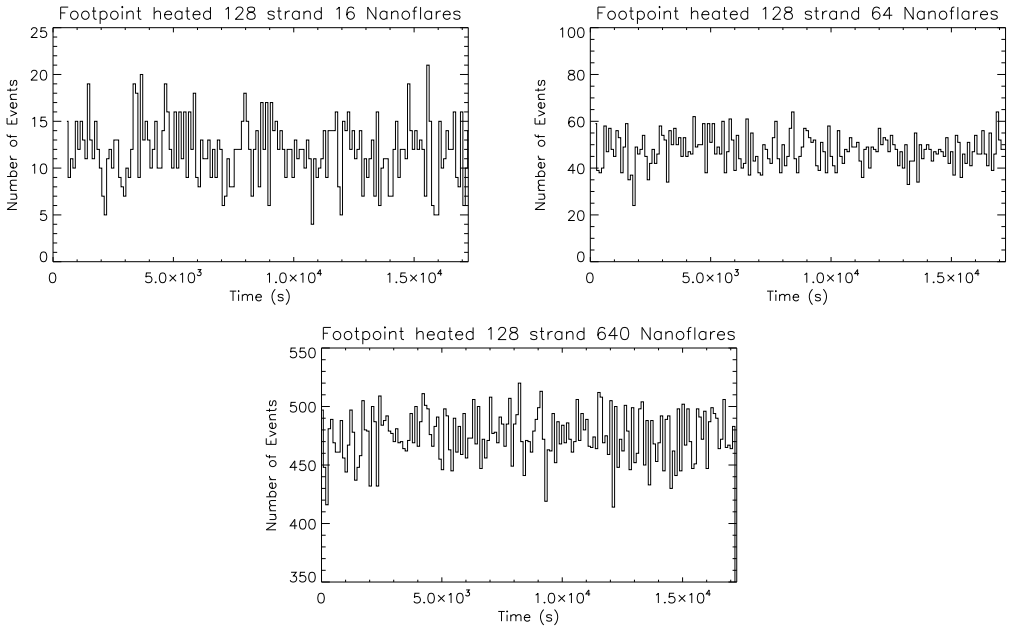

Figure 4.33: Figures showing the temporal distribution of the nanoflares over the time-length of the simulation.

The power law of each simulation is seen to have a slightly different slope in each case (Figure 4.34) but this is just an effect of changing the number of nanoflares per strand and the corresponding average nanoflare energy. This variation of ~0.1 does not greatly influence the outcomes of each simulation.

The behaviour of the loop plasma in each case can be more accurately characterised by plotting the average emission measure weighted temperature from Equation 4.2.0.1 of each simulation over time. This gives a more realistic view of the plasma behaviour as it considers both temperature and density values. This EMT for the three simulations is shown in Figure 4.35. It is clear the 16 burst/strand simulation (green) shows the greatest temperature variation with the 64 burst/strand (red) and the 640 burst/strand (blue) smoothing out as burst number increases.

The large variation in EMT of the 16 burst per strand simulation is due to the associated increase in each nanoflare's energy. Large, infrequent bursts heat the plasma up to more extreme values and the long time between heating episodes allows the strand plasma to cool creating the variation seen in Figure 4.35. The average value of EMT for the 16

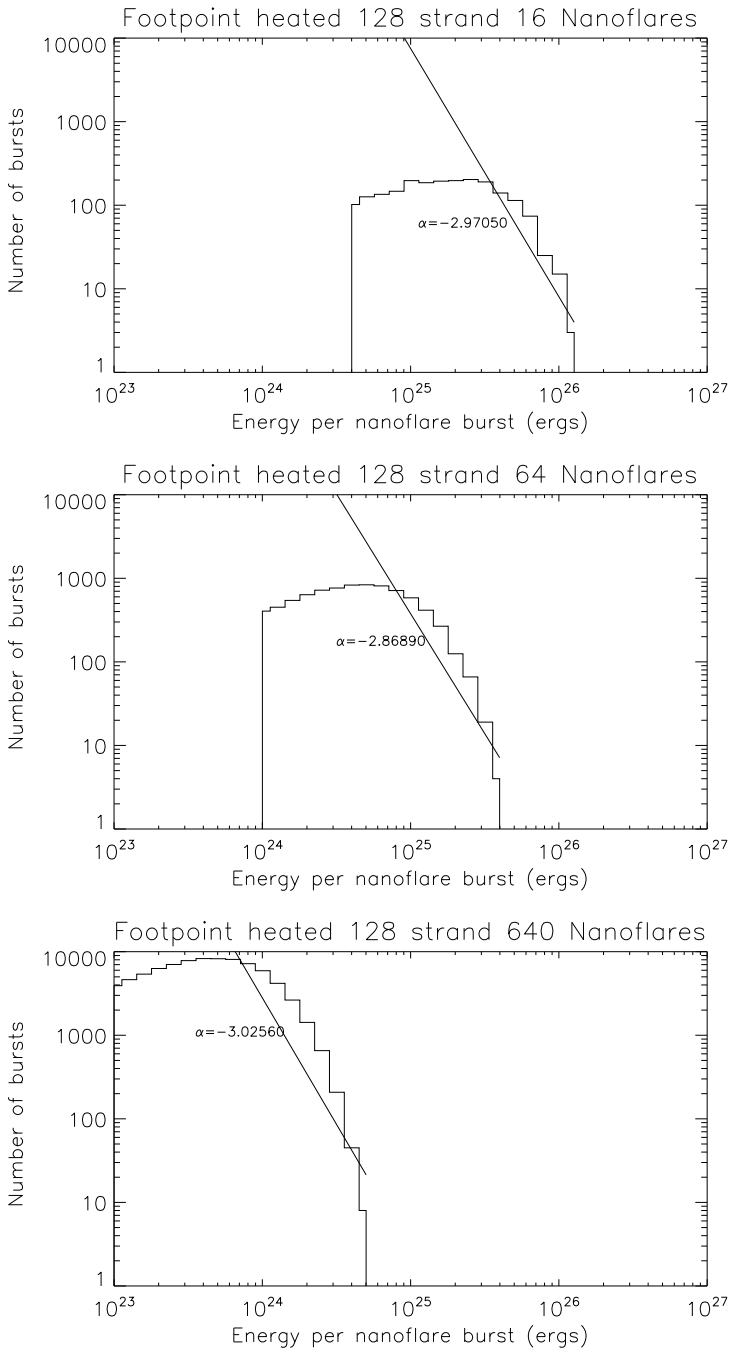

Figure 4.34: Figures showing the relationship between the number of nanoflares and the nanoflare energy in each simulation as a power law.

and 64 burst simulations is very similar at around Log T/K=6.522 but the value for the 640 burst simulation is slightly lower at Log T/K=6.510 as this simulation can simply not reach this temperature with its frequent small bursts.

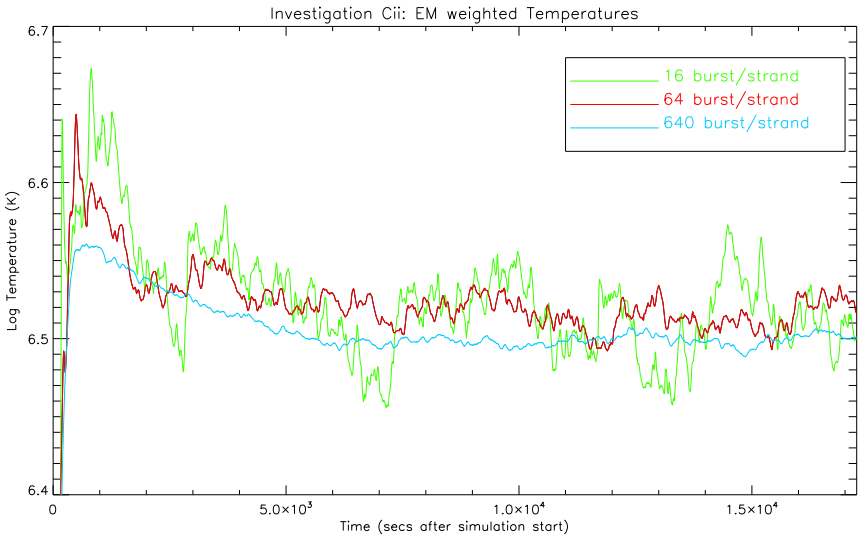

Figure 4.35: Average emission measure weighted temperature profile of the simulations over time based on data from the apex of the loop.

Impact on DEM

Figure 4.36 shows a selection of DEM plots made from different cuts of the three simulations examining the effect of changing nanoflare number. It can be seen that a similar trend is present in all three time/space cuts. The DEM based on the simulation with 16 flares/strand is very wide in each case while the DEM becomes narrower as nanoflare number per strand increases (i.e., also as average nanoflare energy decreases). This can be traced back to the results from the EMT plots in Figure 4.35 which show that a much wider variation in temperature is reached when there are fewer, larger bursts than if there are many small bursts going off in the loop. This accounts for the difference in the spread of the DEMs.

Once again the DEM with smaller temperature bins highlights some non-uniform features in the distribution. The 64 burst/strand simulation (red) is the same one that was

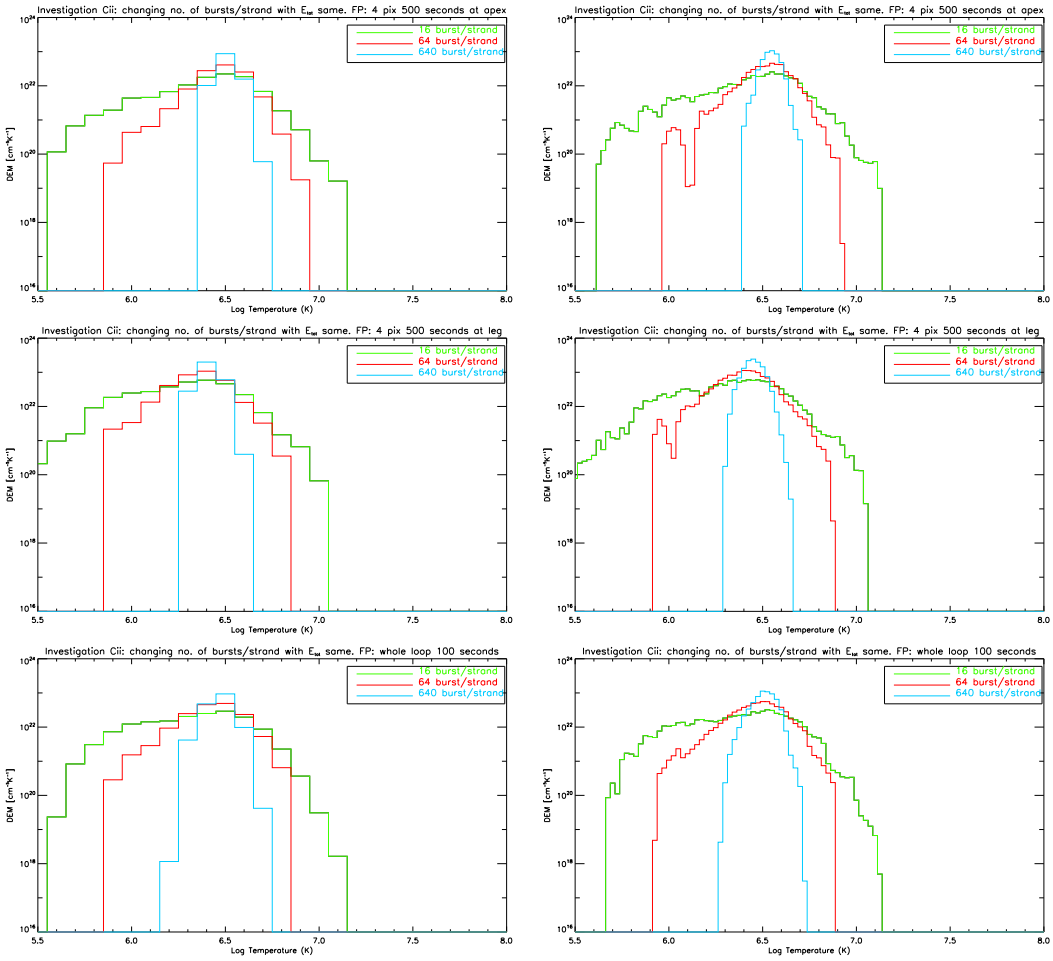

Figure 4.36: DEM plots based on different cuts of the data for changing nanoflare number. Top: DEM plots (at different temperature bin size) based on data from the apex of the loop averaged over 500 seconds. Middle: DEMs based on the same 500 seconds but taken from the leg of the loop model. Bottom: DEMs based on data from the whole coronal section of the loop averaged over 100 seconds.

studied in Investigation B where this footpoint heated model was compared to apex and uniform heating distributions. As was shown previously, the peak at Log T = 6.0 can be traced back to the behaviour of one particular strand as shown in Figure 4.23.

Factors affecting DEM width

The extreme width of the 16 burst/strand simulation DEM seen in Figure 4.36 justified further investigation. It was previously assumed that the main factor determining the width of a DEM from these simulations was the size of the average nanoflare energy. However, in Investigation A the four DEMs made from simulations of increasing strand number did not show a significant change in width despite the fact that the burst size covered a number of values as strand number changed. The only small change in width observed was due to the increasing strand number increasing the number of temperature and density elements being used to calculated the DEM.

No. of strands	Cross sec. strand area (cm^2)	No. of bursts per strand	Total bursts per loop	Ave. nanoflare energy (ergs)	Reheating Timescale (sec)
16	$8.00x10^{15}$	64	1024	$5.20x10^{25}$	649.41
32	$\mathbf{4.00x10^{15}}$	**64**	**2048**	$\mathbf{2.58x10^{25}}$	**644.53**
64	$2.00x10^{15}$	64	4096	$1.25x10^{25}$	626.22
128	$1.00x10^{15}$	64	8192	$6.27x10^{24}$	627.44
128	$\mathbf{1.00x10^{15}}$	**16**	**2048**	$\mathbf{2.49x10^{25}}$	**2490.23**
128	$1.00x10^{15}$	64	8192	$6.26x10^{24}$	626.22
128	$1.00x10^{15}$	640	81920	$6.31x10^{23}$	63.11

Table 4.8: Comparison between simulations undertaken to investigate changing strand number and changing nanoflare number. The first four rows show details of the Investigation A simulations in comparison to the three simulations run for Investigation Ci. The two entries in bold show two simulations where the total number of bursts in the loop are the same as is the average nanoflare energy. The main difference between these two is the strand number and hence the strand volume. The reheating timescale refers to the required time between nanoflares if this heating mechanism is to power the corona.

Table 4.8 lists some details of the four simulations from Investigation A as well as the three simulations from Investigation Cii. To investigate the large width of the 16

burst/strand simulation seen in Figure 4.36 the 32 strand simulation from Investigation A was chosen for comparison. Each of these simulations has the same total number of bursts within the loop, the same average energy per burst, and the same total energy going into the simulation. The heating distribution of each simulation is different with the 16 burst/strand simulation being footpoint heated while the 32 strand simulation is uniformly heated. This difference can be overlooked as Investigation B showed that these two heating profiles lead to a very slight shift in the resulting DEMs. As long as this is kept in mind other, more significant changes can be studied.

The other differences between the two simulations are the number of bursts per strand and the number of strands within the loop. Since the average energy of each nanoflare is the same, the emission measure weighted temperature evolution of each simulation is expected to be similar. This is indeed the case as is shown in the top panel of Figure 4.37 where the variation of the EMT is similar in each case. As was shown in Investigation B, the footpoint heated simulation (16 burst/strand) has a lower average EMT than the uniform heated one (32 strands) but the variation in both cases is of a similar magnitude. The 16 burst/strand EMT variation is 10% larger than that exhibited by the 32 strand one. This is quite a small difference as other simulation EMTs vary by much larger values e.g., the temperature variation of the 640 burst/strand EMT is 6 times smaller than the variation of the 16 burst/strand EMT (Figure 4.35).

Despite this similarity in EMT variation, the DEMs produced from these two simulations are very different as is seen in the lower panel of Figure 4.37. The reason for this can be traced back to the different strand number in each simulated loop which results in different strand volumes in each case. The cross-sectional area of a strand in the 32 strand loop (with 64 bursts/strand) is four times larger than that of a strand from the 16 burst/strand simulation (due to it having 128 strands in total). Since the burst size remains the same it is this change in area/volume that causes the large difference in the distribution of the plasma temperatures. Considering one strand in each simulation:

- **16 burst/strand sim.:** this strand has 16 bursts of energy E going into a volume V.
- **32 strand sim.:** this strand has 64 bursts of energy E going into a volume 4V.

Even though the 32 strand simulation has more energy bursts per strand, the higher volume the energy is being deposited into means that the plasma will not reach as high temperatures as the 16 burst/strand simulation. The higher number of bursts also means that the time between heating events is less which constrains the plasma to a narrower temperature range as opposed to the 16 burst/strand case where the plasma has much longer to cool in between heating episodes leading to the very wide temperature distribution seen in the DEM.

Now that the reason for the different widths of these DEMs is known, the other synthetic observables relating to the three simulations exploring nanoflare number per strand can be investigated.

Impact on intensity values

The synthetic observations of these three simulations exploring nanoflare number per strand can be further investigated by taking the DEM from the bottom-right of Figure 4.36 and folding it through the SDO/AIA temperature response function to get out synthetic intensity values. Figure 4.38 shows the variation in these intensity values as well as accounting for the differences seen in each case.

The top plot in Figure 4.38 shows how the values of intensity rise and fall from channel to channel for each simulation (NB the intensity values are not continuous and are marked by the asterisks). In the 131Å, 171Å, 193Å and 94Å channels the same pattern persists with the 16 burst/strand simulation having the highest intensity followed by the 64 and then the 640 burst/strand ones. The reason for this can be seen in the middle

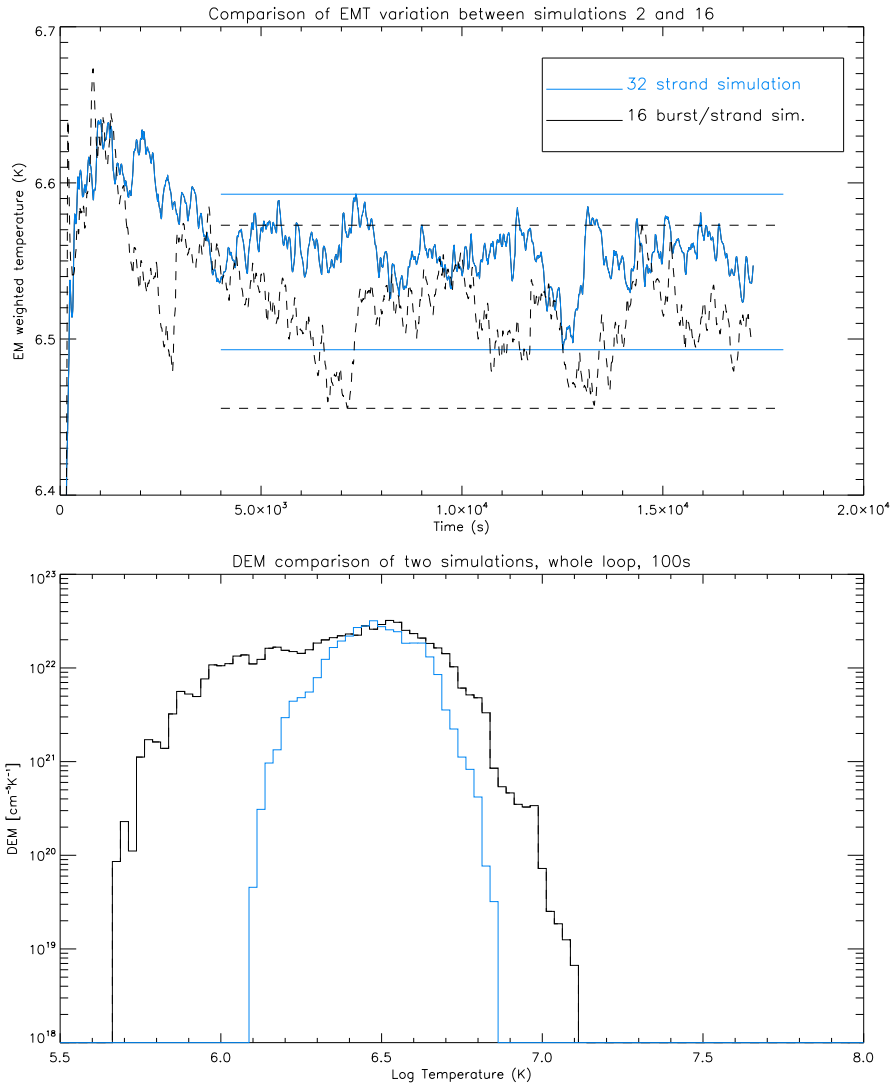

Figure 4.37: *Top:* plot showing that the variation in the two simulations' EMT is around the same size. The horizontal lines mark the maximum and minimum EMT's of each simulation with the 16 burst/strand variation being 10% larger that the one seen in the 32 strand simulation. The 16 burst/strand simulation has a lower average EMT as this simulation is footpoint heated compared to the uniformly heated 32 strand simulation. This shift was observed in Investigation B but only caused a slight shift in the corresponding DEM. *Bottom:* the DEMs calculated for each simulation have very different widths despite the similarities highlighted in Table 4.8.

plot which shows the DEM the intensities were calculated from plotted with a non-log y-axis. Overplotted on this figure are the approximate temperature peaks of the AIA response curves seen in the bottom plot. These peak positions are plotted as different coloured asterisks (at an arbitrary y-axis value) in order to explain the intensity values seen in the top plot. The 640 burst/strand DEM (blue) is much higher than the other two as all the plasma in this simulation is constrained to a narrow temperature region meaning it will have a high density within these temperature bins.

The 16 bursts/strand (green) intensity is higher than the other two in most channels as the DEM values where these channels have their peak sensitivity is simply higher than the other two. In the 211Å channel the order changes with the 64 burst/strand (red) intensity being the highest followed by the 16 and 640 burst/strand values respectively. This is due to the red DEM in the middle panel beginning to rise within the 211Å temperature response curve.

A similar result is seen in the 335Å channel where for the first time the 640 burst/strand simulation has the highest intensity value. This is due to the 640 burst/strand DEM (blue) rising within the temperature range of the 335Å response peak. The narrowness of the 640 burst/strand DEM is the reason why it has such low intensity values in most channels. There is simply less sensitivity in AIA at the temperature the DEM peaks around (Log T ~ 6.5). If the total energy going into this simulation was higher or lower this would cause the DEM to slide up/down the temperature range and its corresponding values in intensity would drastically change.

4.2.5 Investigation D: Investigating the impact of allowing the loop simulation to heat then cool

It is possible that coronal loops undergo many instances of heating and cooling over their lifetimes so it is important to be able to identify signatures of such processes in

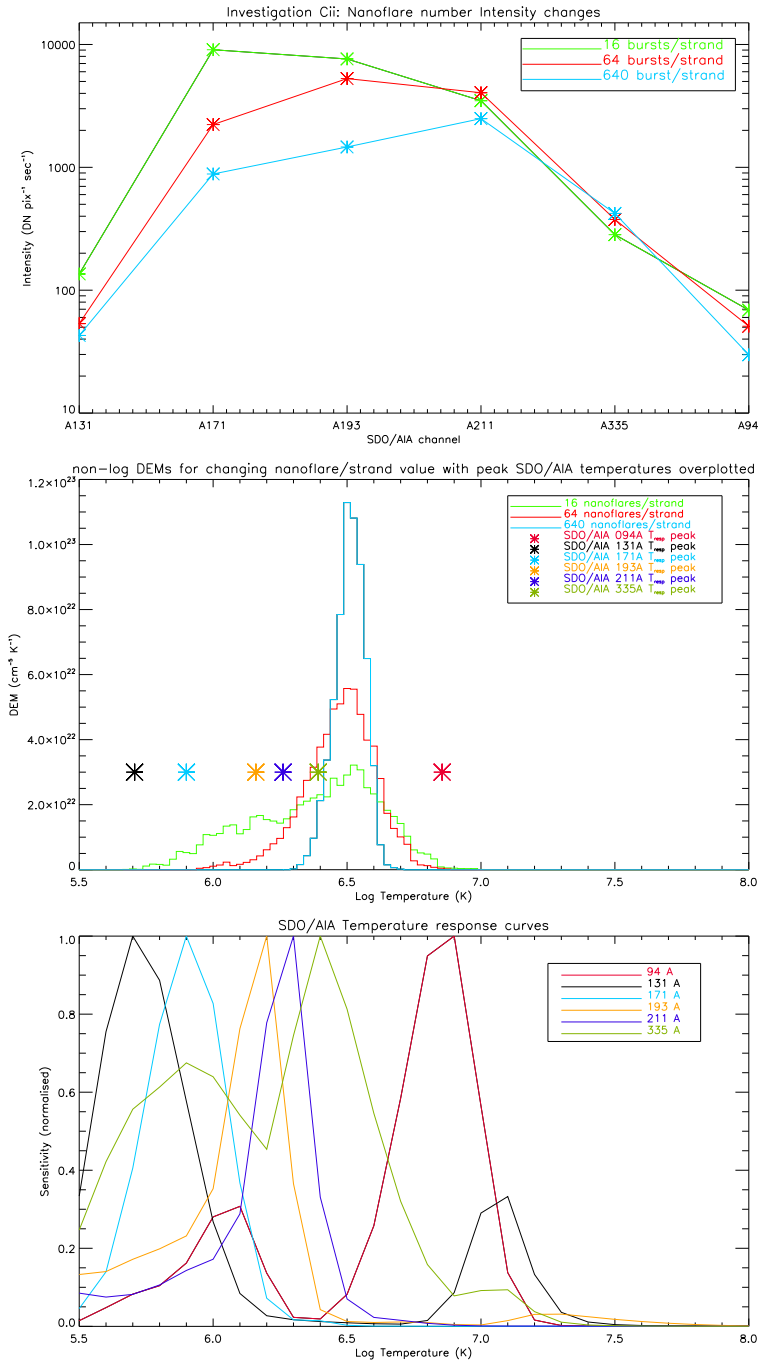

Figure 4.38: *Top:* change in intensity seen in each AIA channel in each simulation. The ordering of these values is explained in the middle and bottom plots. *Middle:* DEM values from the three simulations plotted on a non-log scale. The large asterisks symbols indicate at what approximate temperature each AIA channel has its main peak at. *Bottom:* SDO/AIA normalised temperature response curves.

any model. By understanding what a cooling loop looks like in terms of its DEM and intensity measurements, real instances of these cooling processes may be detected and related back to the physical mechanisms explained by the model. In order to study the various effects of cooling on the MSHD loop simulation, three runs were undertaken where all the nanoflare energy release was confined to the first quarter of the simulation. Table 4.2 lists these simulations as numbers 13, 14 and 15 where it can be seen the only difference is the total energy going into the loop (see also Table 4.9). In each case this total energy has been increased by an order of magnitude. This means that the cooling profile can be looked at in three different energy scenarios.

General traits of different cooling simulations

Table 4.9 lists the general traits of the three simulations undertaken to explore loop cooling. In each simulation the loop length was 100 Mm, the strand number was 128 and the number of bursts per strand was 64. The total energy going into the loop was increased by an order of magnitude each time to see what effect this had on the cooling process. Table 4.9 shows this energy change, note that the resulting power law has the same slope in each case (Figure 4.40). The average emission weighted temperature (EMT) of each simulation before the cooling starts is also noted as well as the time taken for each simulation's EMT to drop to its minimum value. This will be discussed further in the following sections.

Figure 4.39 shows the nanoflare distribution along the loop length (left) and over the 17250 second time length of the simulation (right). The figures plotted are for the $E_{burst} \sim 10^{24}$ case (i.e., the middle entry in Table 4.9) but are identical to the other distributions. The right plot of Figure 4.39 illustrates how these simulations can be used to study loop cooling. All the nanoflares have been constrained to the first quarter (i.e., between t=0 and t=4312 seconds) of the simulation after which there is no source of

Strand No.	Total Energy (ergs)	Ave. Burst Energy (ergs)	Power Law	Average EMT[a] (K)	Cooling Time (s)
128	5.14×10^{27}	6.28×10^{23}	2.57	6.46	3728
128	5.14×10^{28}	6.28×10^{24}	2.57	6.75	4205
128	5.14×10^{29}	6.28×10^{25}	2.57	7.04	4706

Table 4.9: Model Parameters for changing total energy input in a cooling loop i.e., one in which all the nanoflares occur in the first quarter of the simulation. EMT strands for the emission measure weighted temperature (see Equation 4.2.0.1).[a] data taken at loop apex and refers to average EMT before the heating was stopped. The cooling time is the approximate time taken for the simulation to reach its temperature minimum once the heating was stopped.

heating within any of the strands. Naturally the loop will begin to cool over the remaining simulation time and the MSHD model will continue to track the corresponding temperature and density values. This will allow the evolution of the strands after the heating has stopped to be examined.

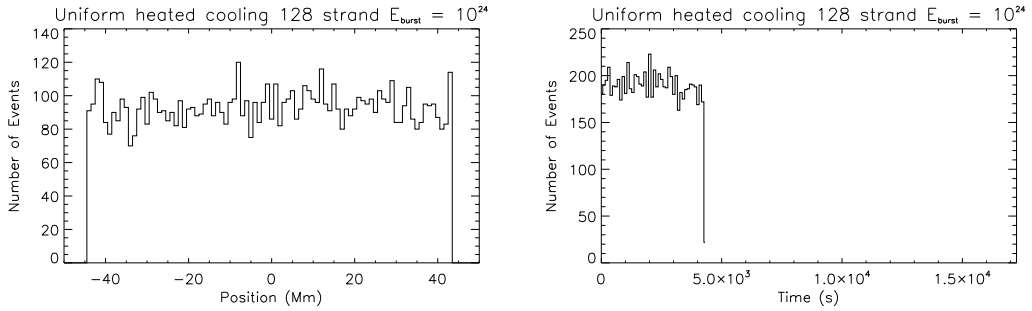

Figure 4.39: Left: spatial distribution of the nanoflares over the loop length showing that they are uniformly distributed. Right: temporal distribution of the nanoflares over the entire simulation time showing that they are all confined to the first quarter of the simulation in order to investigate loop cooling. These two plots are for the $E_{burst} \sim 10^{24}$ case but are identical to the two other energy scenarios investigated.

Figure 4.40 shows the changing power law associated with the three simulations examined in this section. The slope of each plot is the same (as total nanoflare number remains the same) but the peak of the plot moves to higher energies as the energy per nanoflare is increased. This is the same movement that was observed in Investigation Ci where the energy was also increased by a power of ten in each case.

The temperature and density evolution of each multi-stranded loop can be summarised

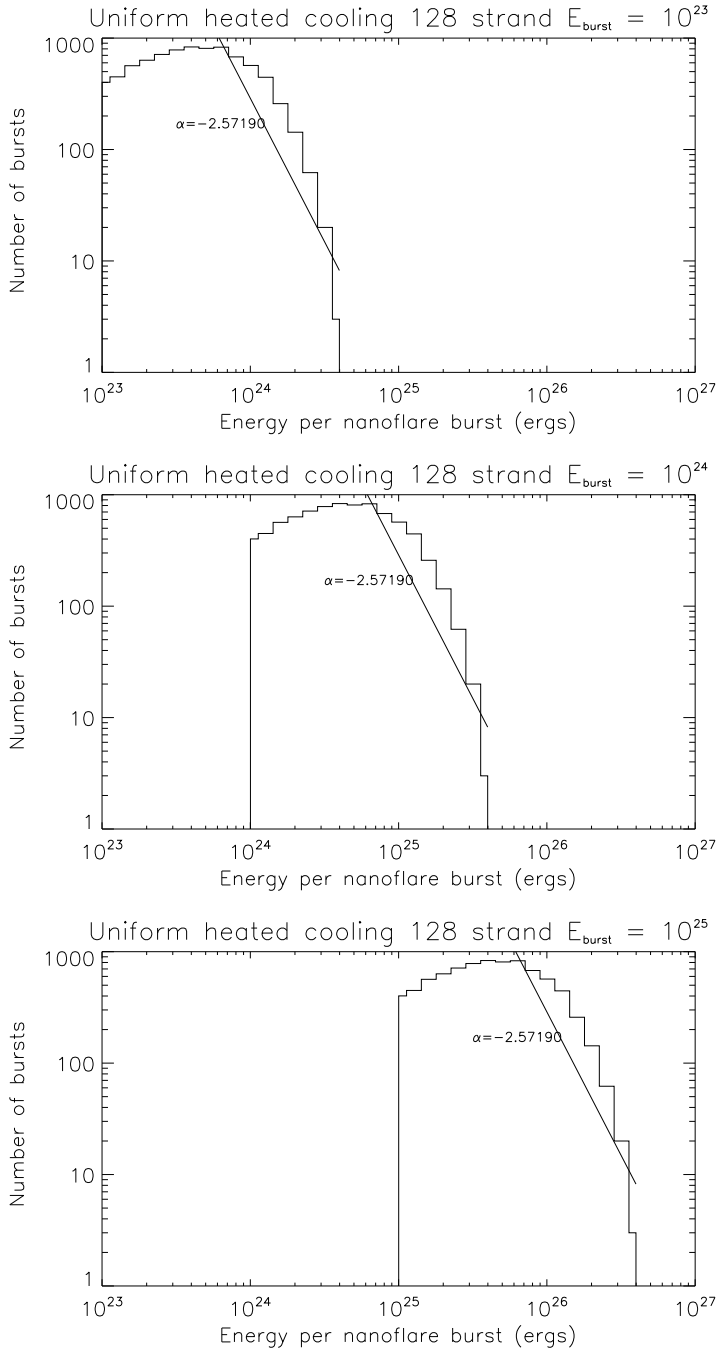

Figure 4.40: Figures showing the relationship between the number of nanoflares and the average nanoflare energy in each simulation as a power law.

by plotting the average emission measure weighted temperature (Equation 4.2.0.1) as it changes over the simulation timescale. Figure 4.41 shows two versions of this plot: one with a Log temperature scale and one without. It can be seen that from t=0 until t=4312 seconds the EMT remains more or less stable for each energy scenario. In this time range the three simulations are clearly defined by their average EMT which is stratified according to the total energy input in each case. Each plot shows that after this time period (represented as a vertical dashed line), the average EMT starts to decline due to the absence of nanoflare heating.

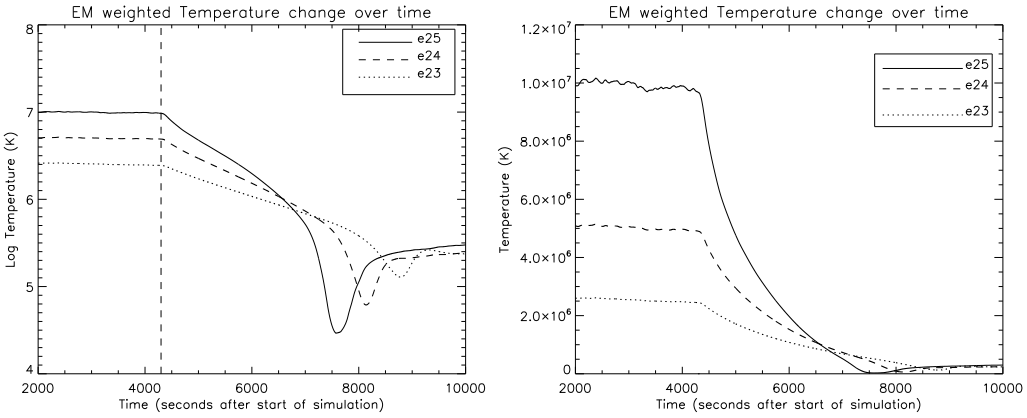

Figure 4.41: Left: plot showing the evolution of the emission measure weighted temperature (Log EMT) from a stable value for each energy case which starts to decline at ~4312 seconds (vertical dashed line) after the nanoflares have ended. Each energy scenario reaches a minimum value after which the simulation tries to adjust itself leading to the 'bounce' in values. This is just a computational effect and so values after this bounce will not be considered. The effect is also exaggerated in this plot due to the log scale. Right: the same plot but plotted in MK units (i.e., not on a log-scale) to show that this 'bounce' is really a tiny perturbation.

In the left-hand plot it can be seen that the EMT declines in each case until it reaches a minimum value after which each plot is seen to 'bounce'. This is a numerical overshoot by the simulation as it tries to reach an equilibrium temperature and does not necessarily reflect a physically accurate interpretation of how the plasma would behave. The right-hand-side plot shows the same values but plotted on a non-log temperature scale. The point of this is to show that the size of this 'bounce' is exaggerated in the log plot and is in fact only a small perturbation.

The slope of the decline in each energy scenario's EMT is an interesting feature to note. It is clear that the higher energy simulation (E_{burst}~10^{25}) declines much more steeply than the E_{burst}~10^{24} case which is turn is also steeper than the lower energy (E_{burst}~10^{23}) case. The relationship between the emission measure weighted temperatures and the unweighted temperature values is shown in Figure 4.42 where it can be seen the two quantities are very closely related.

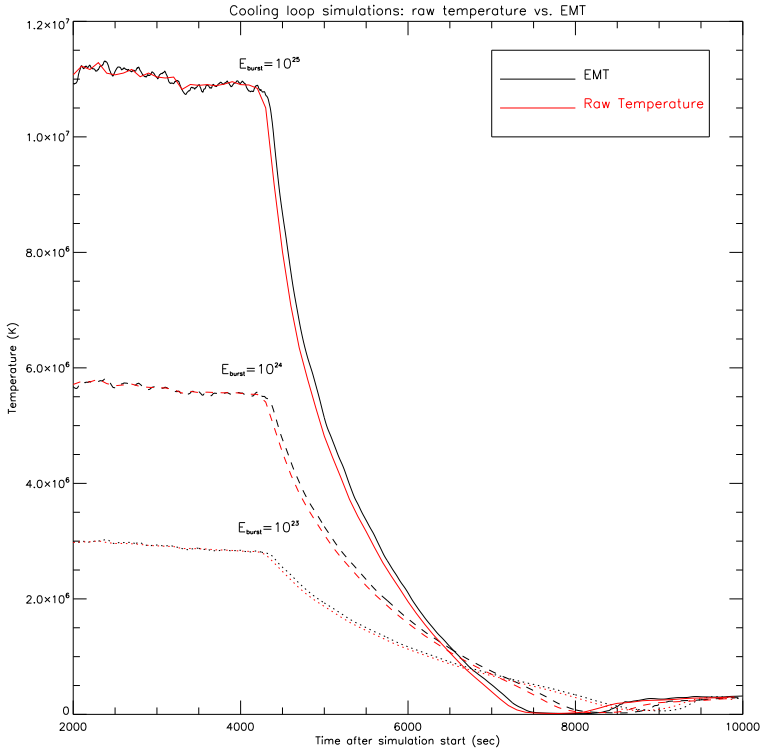

Figure 4.42: Plot showing the relation between the emission measure weighted temperatures and the unweighted temperature values (red) over the course of the loop cooling. It can be seen the two values are very closely related.

Figure 4.43 shows how the temperature evolution of the cooling simulations corresponds to the changing density values in each case. The three vertical dashed red lines indicate the times at which the temperature of one simulation equals another. Even though at these points the simulations have equal temperatures, the EMT of each simulation continues to decline at a unique slope as the density values are very different (i.e., an order of magnitude different). After the strands have stopped being heated, they will cool by radiation. The rate of the radiative cooling is heavily density dependant (i.e., $\tau_{rad} \propto \rho^2$) which is why each simulations cool at a different rate.

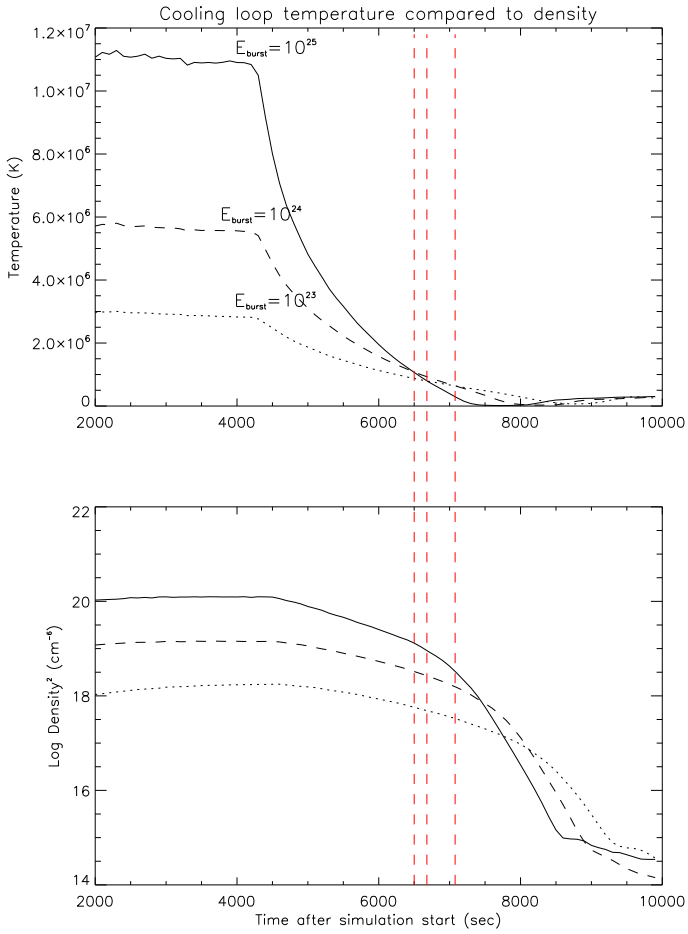

Figure 4.43: Plot showing that even when the three cooling simulations reach a common temperature (denoted by the vertical dashed red lines), they still have widely different log density values (around an order of magnitude different) leading to the different progression of the EMT values.

Impact on DEM as loop cools

In order to relate the MSHD model outputs to possible 'real' observations, the temperature and density values over the entire simulation (for each energy case) can be used to calculate synthetic DEMs. Although the entire simulations is 17250 seconds in duration, Figure 4.41 considers the loop evolution between t=2000s and t=10000s. These 8000 seconds include the point at which the heating is removed (t = 4312s) and follows the resulting cooling until a minimum value of EMT is reached in each case. By dividing this 8000s into sections of 100 seconds, 80 DEM plots can be made which follow the behaviour of the simulation. The change in these DEMs over time can be seen in the movies listed in Table 4.10.

Movie name	Energy case (ergs)	Loop position examined
DEM_e23_c4.mov	E_{burst}~10^{23}	whole coronal loop
DEM_e23_legapex.mov	E_{burst}~10^{23}	leg vs. apex
DEM_e24_c4.mov	E_{burst}~10^{24}	whole coronal loop
DEM_e24_legapex.mov	E_{burst}~10^{24}	leg vs. apex
DEM_e25_c4.mov	E_{burst}~10^{25}	whole coronal loop
DEM_e25_legapex.mov	E_{burst}~10^{25}	leg vs. apex

Table 4.10: List of movie names and the energy scenario they refer to. A distinction is also made between the behaviour of the DEM based on the entire coronal part, and ones made from data concentrated at the loop apex and leg to see if these areas evolve differently.

For simplicity, these 80 DEMs have been averaged and condensed into the eight plots seen in Figures 4.44, 4.45, and 4.46. In each figure, two versions of the DEM progress have been plotted. The left-hand plots in each case show how the DEM evolves based on the entire coronal portion of the loop (black) while the right-hand plots show this same progression but distinguish between the DEMs based on data from the loop apex (green) and leg (red) in order to see if they evolve differently.

Each energy scenario shows the same effect seen in Investigation Ci where the DEM

shifts to higher temperatures as the total energy deposited within the simulation increases. The first plot (t=2500s) of each figure illustrates this point with all the DEMs moving up the temperature scale from one energy scenario to the next. A widening of the DEMs as energy increases is also observed and is due to the variation in the EMT becoming larger as the average nanoflare energy increases. After the heating stops (at t=4312s), the DEMs in every case are observed to move to lower temperatures and eventually disappear as the plasma goes below Log T = 5.5. This is due to the combination of the plasma temperature reducing as well as the loop plasma draining back down into the model chromosphere causing the density to reduce.

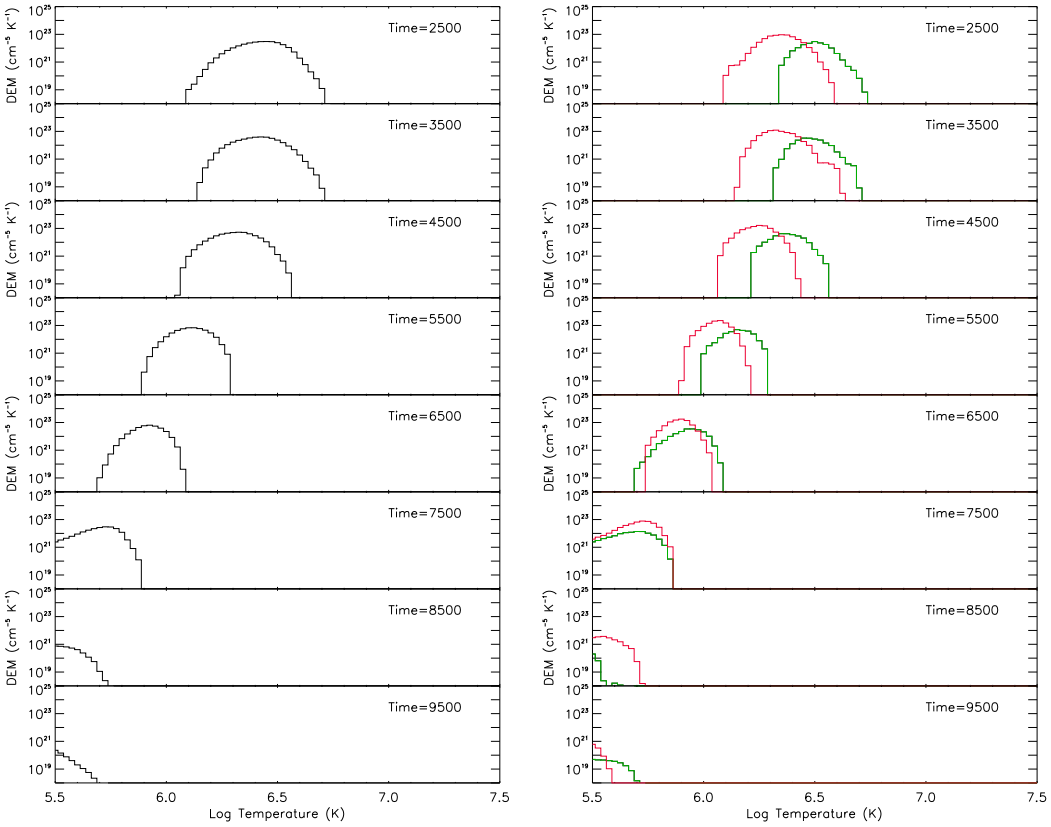

Figure 4.44: DEM changes observed in cooling loop with average E_{burst}~10^{23}. Left: DEMs over time for whole coronal loop. Right: DEMs over time for areas based on loop apex position (green) and loop leg (red). Time increased from top to bottom.

An interesting feature to note is seen in the right-hand plots in each figure which examines how the DEMs based on the loop leg and loop apex differ. Initially the leg DEM (red) is observed to be peaked at a lower temperature compared to the apex DEM (green)

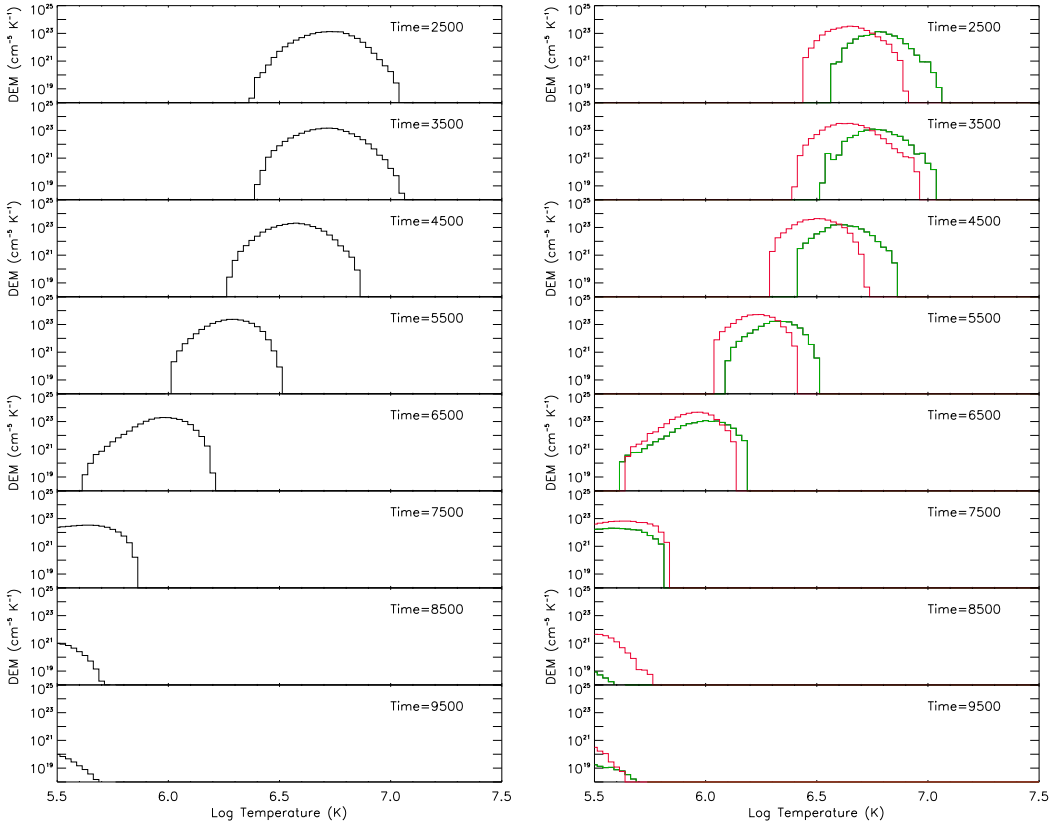

Figure 4.45: DEM changes observed in cooling loop with average E_{burst}~10^{24}. Left: DEMs over time for whole coronal loop. Right: DEMs over time for areas based on loop apex position (green) and loop leg (red). Time increased from top to bottom.

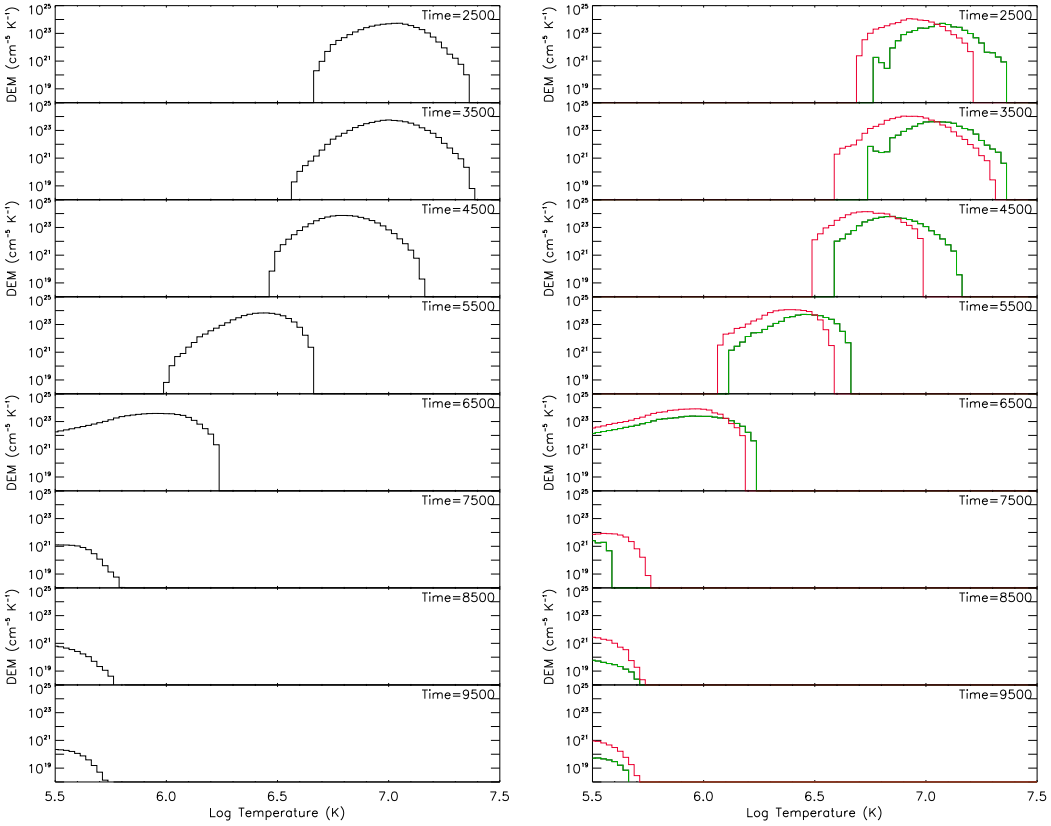

Figure 4.46: DEM changes observed in cooling loop with average E_{burst}~10^{25}. Left: DEMs over time for whole coronal loop. Right: DEMs over time for areas based on loop apex position (green) and loop leg (red). Time increased from top to bottom.

due to the loop legs being denser and having a lower average temperature. Over time however, the apex DEMs are seen to move to lower temperatures and disappear faster than the leg DEMs. By t=7500s in each case the leg DEMs (red) have swapped places with the apex DEMs and persist for longer.

This is because the cooling of the loop represents a 'draining' of plasma from the coronal part of the loop back into the chromospheric section and naturally the last section of the loop to retain plasma dense enough to contribute to the DEM will be in the legs.

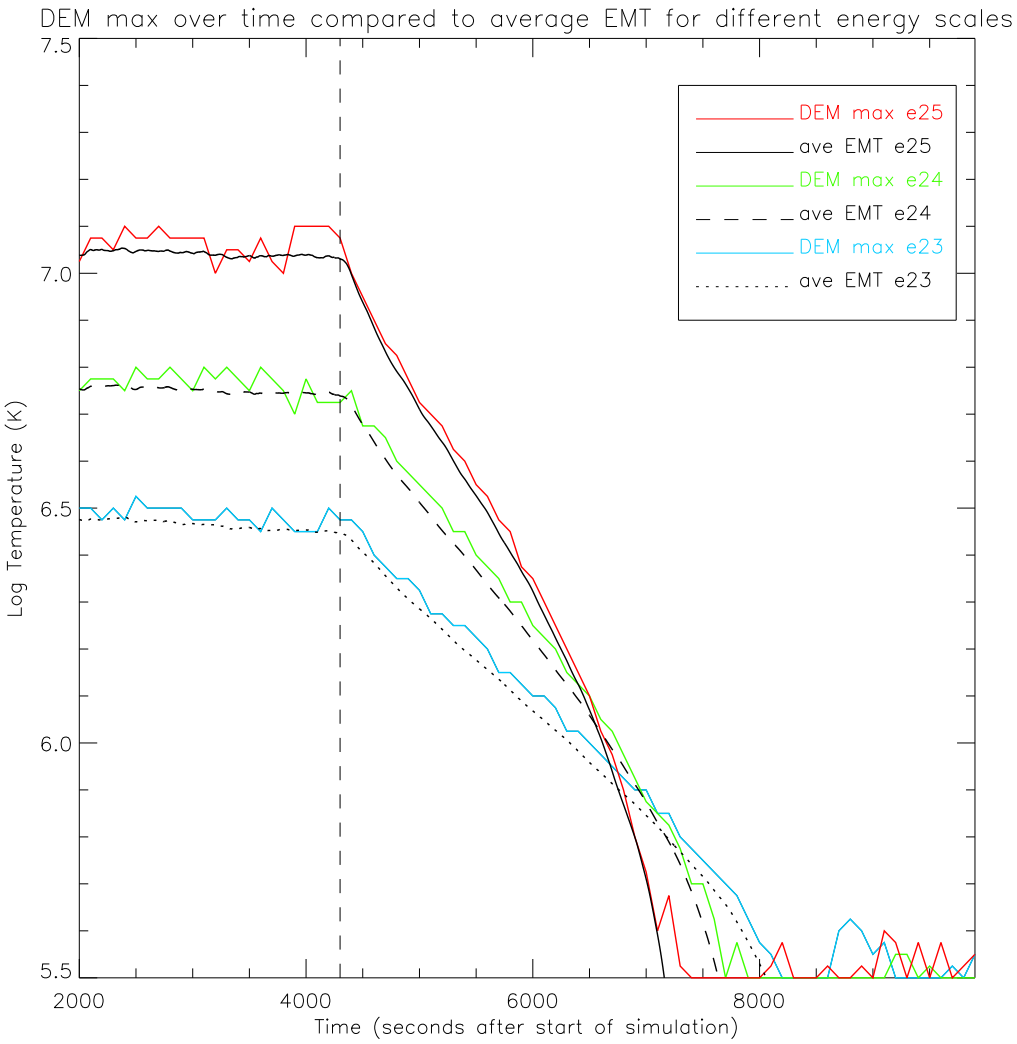

Figure 4.47: Plot showing the peak temperature of the DEM for each energy case as it cools over time (coloured lines) compared to the average emission measure weighted temperature values for each simulation over time. It can be seen that the peak DEM temperature follows very closely the EMT values in each case.

The way in which the DEMs change as the cooling takes place is explored further in Figure 4.47. The temperature at which each of the 80 DEMs (calculated for each simulation) peaks at is plotted as it changes over time. It can be seen that before the heating stops each DEM has its peak temperature at a value similar to the calculated EMT for that energy scenario. As the cooling begins, each simulation shows a very good agreement between the peak temperature of the DEM (coloured lines) and the corresponding EMT values from Figure 4.41 which are overplotted.

This suggests a very interesting observational advantage i.e., that by observing how a loop cools and computing its DEM changing over time, the physical temperature and density values of the plasma can be inferred even when the DEM is quite broad. The simulation results show that based on the steepness of the falling EMT/peak DEM temperature over time, estimates on the average nanoflare energy can be made.

It is likely this result is tied into the multi-stranded nature of the simulation as a monolithic loop (i.e., one that is essentially one large strand) would show a much larger variation in EMT that the DEM may not follow the same trend. This is a topic that will be explored in future work (see Section 7). The trend seen here for different total energy input could be used as a basis for comparison with real observational data. The rate of the decline in the peak DEM temperature could be used to see which of the energy scenarios it is most similar to. If the cooling behaviour of all the simulations was studied (i.e., cooling loops with different strand numbers and heating location etc.) more robust conclusions could be drawn about the real observation's similarity/dissimilarity to the MSHD model.

Impact on synthetic intensity values

Using the DEMs calculated over the timescale of the simulation, the possible intensity that would be observed by SDO/AIA as the loop cools can be measured. By folding each DEM through the instrument's temperature response functions the intensity in each

channel over time for each energy scenario can be generated. These response curves are shown in Figure 4.48 where each curve has been normalised relative to its maximum value. This allows easy identification of where each channel has its peak temperature sensitivity and in what order these peaks occur in as temperature is increased.

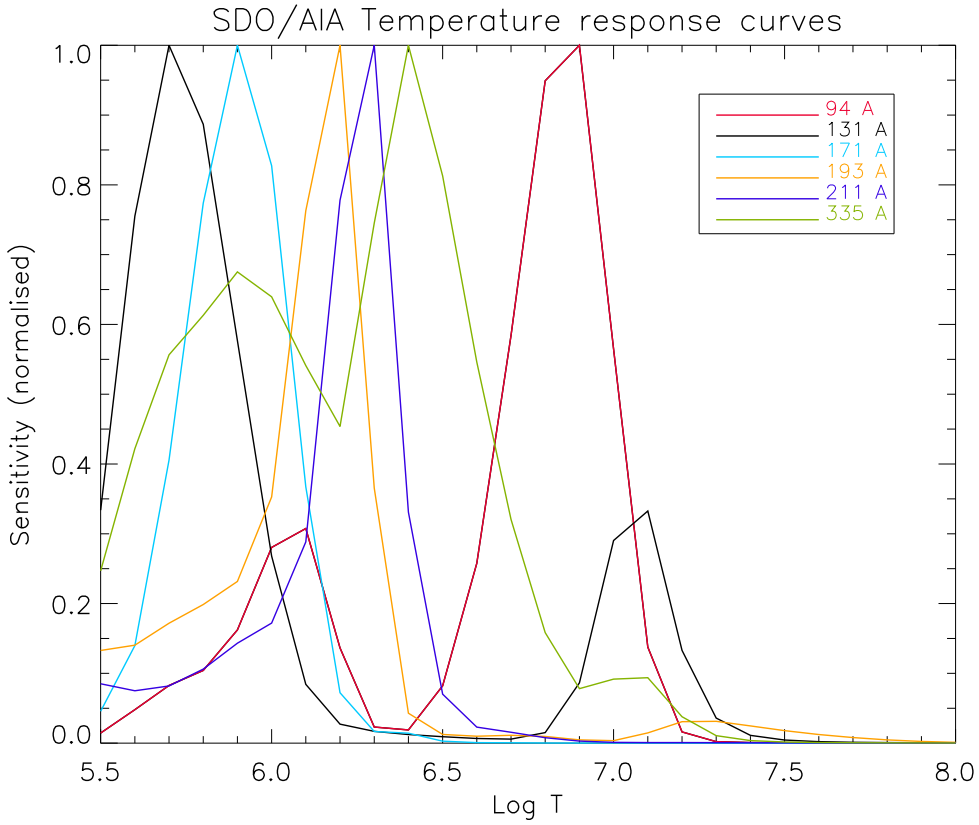

Figure 4.48: SDO/AIA temperature response curves from the AIA_get_response.pro.

Figure 4.49 shows how the intensity of the loop changes within each AIA channel as the cooling progresses for the three simulations. These plots represent intensity values calculated from looking at a section at the apex the loop. Similar plots were made for the whole coronal part of the loop and just the leg but very similar results were achieved and thus are not included here. It is quickly seen that by changing the total energy going into each simulation, observable changes in the resulting intensity are created.

Each channel's intensity peaks at a different time and displays different rise and fall profiles leading to some channel peaks looking 'wider' than others. In each case these patterns can be explained by referring to each simulation's EMT over time as well as

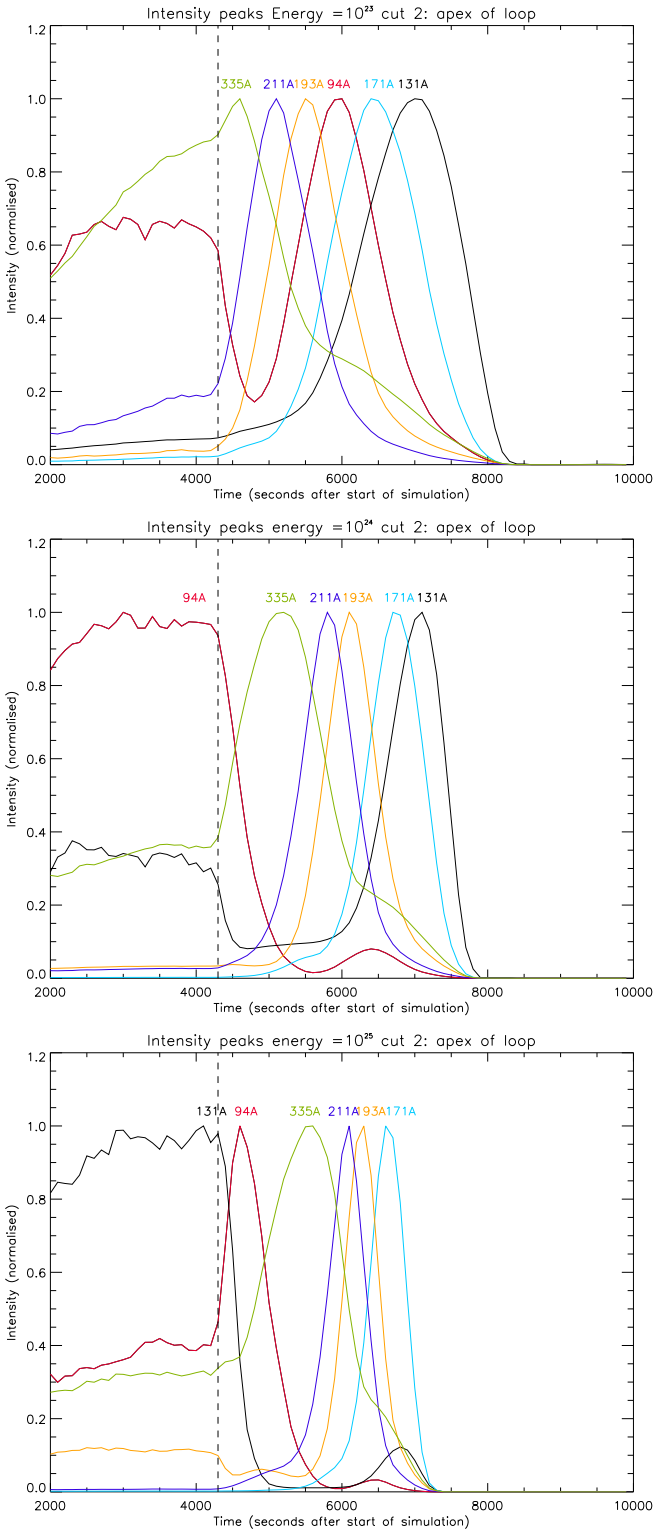

Figure 4.49: Graphs of intensity change over time. The dashed line indicates when the heating stopped. Each plot is made from simulated data from the apex part of the loop where the total energy deposited in the loop increases by a factor of ten from top to bottom.

looking at the instrument response functions. In order to make sure the intensity changes observed are fully understood, each channel shall be looked at in turn. The intensity changes seen in the AIA 94Å, 131Å, and 171Å channels are seen in the left column of Figure 4.50 while Figure 4.51 investigates channels 193Å, 211Å, and 335Å.

For each channel the left plot shows how the intensity in this channel varies between the three different simulations of increasing total energy over time. The right-hand plot for each channel tries to explain these different intensities by plotting two quantities. Firstly, the average emission measure weighted temperature for each energy scenario is plotted as it changes over time (black solid, dashed and dotted lines). This allows the combined effect of the temperature and density changes in the plasma to be seen. In addition to this, the normalised instrument temperature response curve for each channel is overplotted. This coloured curve (filled area) has nothing to do with the lower x-axis (time) but shows where the peaks of the sensitivity in this channel are along the y-axis (temperature). This allows the two factors to be directly compared and results in the differing intensity values being easily explained.

94Å intensity changes:

The topmost two plots in Figure 4.50 show both the changes in the intensity values seen in the 94Å channel by each simulation (red lines in left plot), and also a plot to explain the differences in these intensity values (right plot). Before the heating stops (at t=4312s where the vertical dashed line indicates) it can be seen that the dashed red line (E_{burst}~10^{23}) has the highest intensity followed by the e24 and e25 cases (henceforth the notation of 'e24' will refer to the simulation with the average nanoflare energy of E_{burst}~10^{24} etc.). By looking over at the right plot, this pattern can be understood. The red filled plot shows the normalised AIA 94Å temperature response curve overplotted with each energy scenario's EMT profile. It can be seen that before the heating stops, the dashed line (i.e., the e24 case) lies closest to the peak of the channel sensitivity at

around Log T=6.8. As the cooling begins, the intensity plots show that the e25 case has a sudden peak at t=4500s. This is because the corresponding EMT line in the right plot (solid line) has crossed the peak of the channel's sensitivity. The intensity peaks occurring at around t=6000s are the result of the EMT lines crossing the 94Å secondary sensitivity peak at LogT=6.0. Although the e25 and e24 intensity peaks look relatively small compared to the e23 one at this time, it is important to remember that these intensity values have been normalised with respect to their maximum values.

131Å intensity changes:

The intensity changes seen in the three simulations in the 131Å channel can also be explained by looking at the EMT behaviour in relation to the instrument's response function for this channel. The e25 intensity is much higher than the other two while the heating is still in progress as the EMT for this energy is right in the middle of the high energy sensitivity peak for this channel. All the intensity values then fall as the EMT values cross a temperature range in which this channel has low sensitivity. At around t=7000s all three simulations peak as at this time the EMT values have fallen to a temperature range in which the 131Å channel has its main sensitivity. It can be seen that the e23 case has the widest intensity peak at this time. This is due to the EMT for this simulation having a less steep decline compared to the other two and so this simulation spends a longer time within the temperature range the 131Å channel is sensitive to.

171Å intensity changes:

This AIA channel has only one main sensitivity peak at around LogT=5.8 so the intensity changes over time in each simulation also peak at one particular time. The timing of these intensity peaks is determined by the time the corresponding EMT values reach the temperature range that this channel is sensitive to. This occurs at around t=6500s

but the exact time of the peak and also the width of the peak differs for each energy case. The effect of the different gradients in the decline of the EMT in each energy case (i.e., the gradient of the EMT decline increases with higher energy) can also be seen more clearly here. The order in which each EMT line reaches the peak of the channel sensitivity is reflected in the timings of the intensity peaks (i.e., e23, followed by e25 and e24). The width of each intensity peak is also clearly different. As energy increases the width of each intensity peak is narrower due to the corresponding increase in the gradient of the EMT decline. The high energy case (e25) simply spends less time within the temperature range the channel is sensitive to resulting in the intensity rising and falling over a shorter time span.

193Å intensity changes:

Figure 4.51 shows that the intensity values seen in the 193Å channel show a similar pattern to that seen in 171Å as the temperature response curve is peaked around one main temperature value. In this channel that peak occurs at around LogT=6.2 (slightly higher than the 171Å peak) so the calculated intensity values will peak sooner. The intensity changes for the three simulations are seen to peak at around t=6000s with the order of the peaks corresponding to the order the EMT values reach the temperature the channel is most sensitive to. Again the width of the intensity peaks is affected by the gradient of the EMT changes in each case.

211Å intensity changes:

Again a similar pattern is seen in the intensity changes over time for each simulation. The peak of the 211Å sensitivity is at around LogT=6.3 so the peaks in intensity occur slightly sooner than in the last two channels. Once again the ordering of the intensity peaks and the widths of the rises can be explained by seeing how the EMT values move through the response curve temperature range.

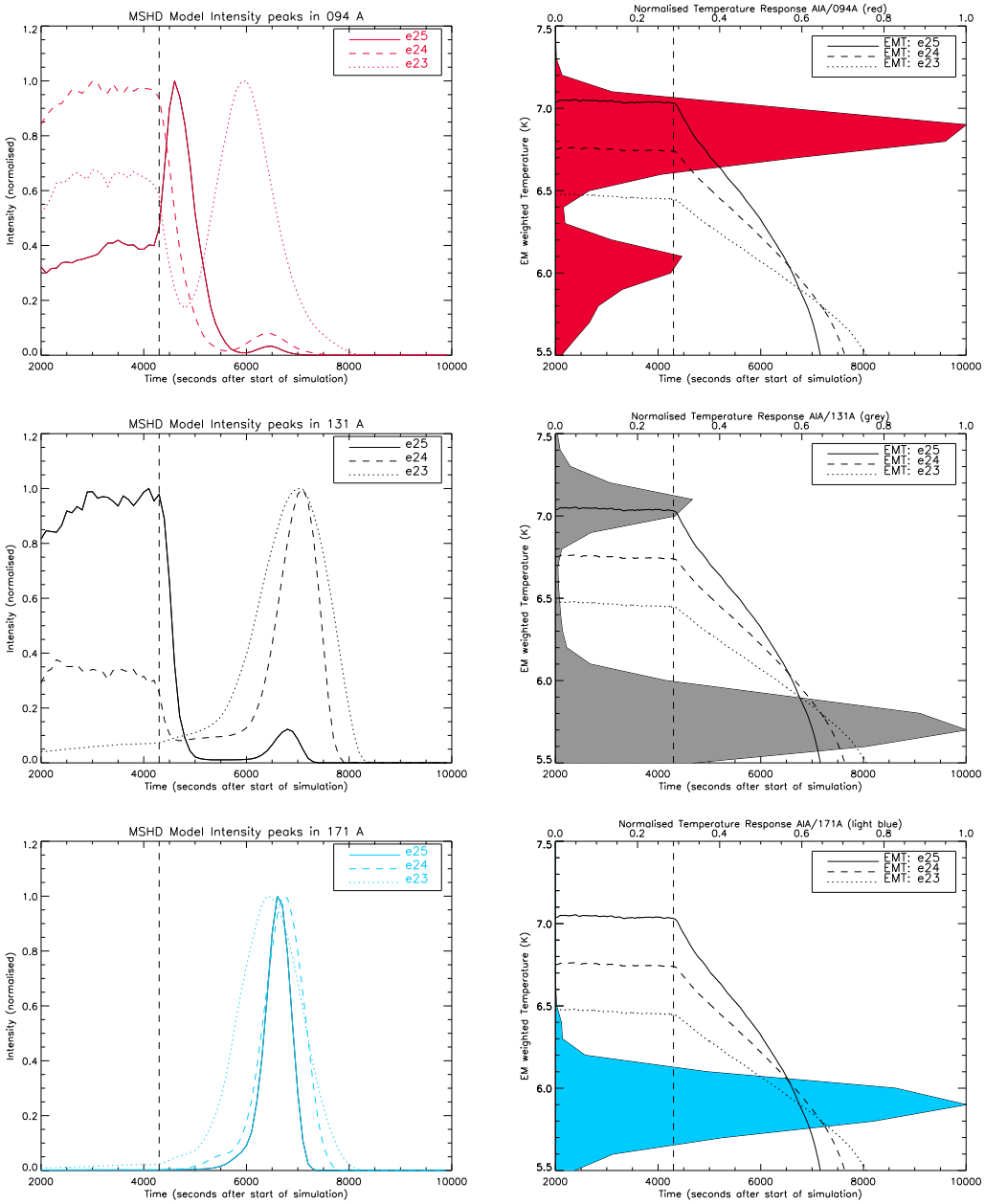

Figure 4.50: Plots showing both the intensity behaviour of the cooling loops in channels 94Å, 131Å, and 171Å (left column) and the corresponding EMT evolution over time (black lines) in relation to each channels temperature response function (filled coloured section).

335Å intensity changes:

The 335Å channel is not as simple as some of the others as it has contributions from a wider range of temperatures. This is seen in the bottom-right plot of Figure 4.51 where the filled green area represents the normalised temperature response curve in this channel. The fact that this response curve covers a wider range of temperatures is the reason why the corresponding intensity curves are wider and show more variation in their declining phase as the EMT values move from one sensitive temperature range to the next.

The main thing to take away from this analysis is that the calculated intensity values in each channel and how they change over time can be precisely explained by referring to the behaviour of the emission measure weighted temperature of each simulation in relation to the instrument response functions. This has allowed the MSHD model to explore a cooling loop but in terms of real observations these results can also be useful. When observing a real coronal loop with SDO/AIA the intensity of that loop in each channel can be recording over time. If a cooling pattern is observed (i.e., the intensity rising and falling in a certain order) then by using the temperature response curves some conclusions about the loop (in terms of its energy, density and temperature) can be made. For example, the rate at which the intensity rises and falls (i.e., the width of the intensity profiles) is an indication of the gradient of the decline in the EMT which is in itself an indication of the average nanoflare energy in each case.

A similar study was conducted by Viall & Klimchuk (2011) who used the EBTEL 0D model to see how their simulated loop cooled through the AIA channels over time and compared these results to real observations. In terms of the model results, they found a very similar pattern of intensity peaks. Figure 4.52 shows their results for two energy cases. The left-hand plot shows the resulting intensity changes after a heating event of size E while the right-hand plot shows the intensity changes occurring after a heating event ten times greater i.e., 10E.

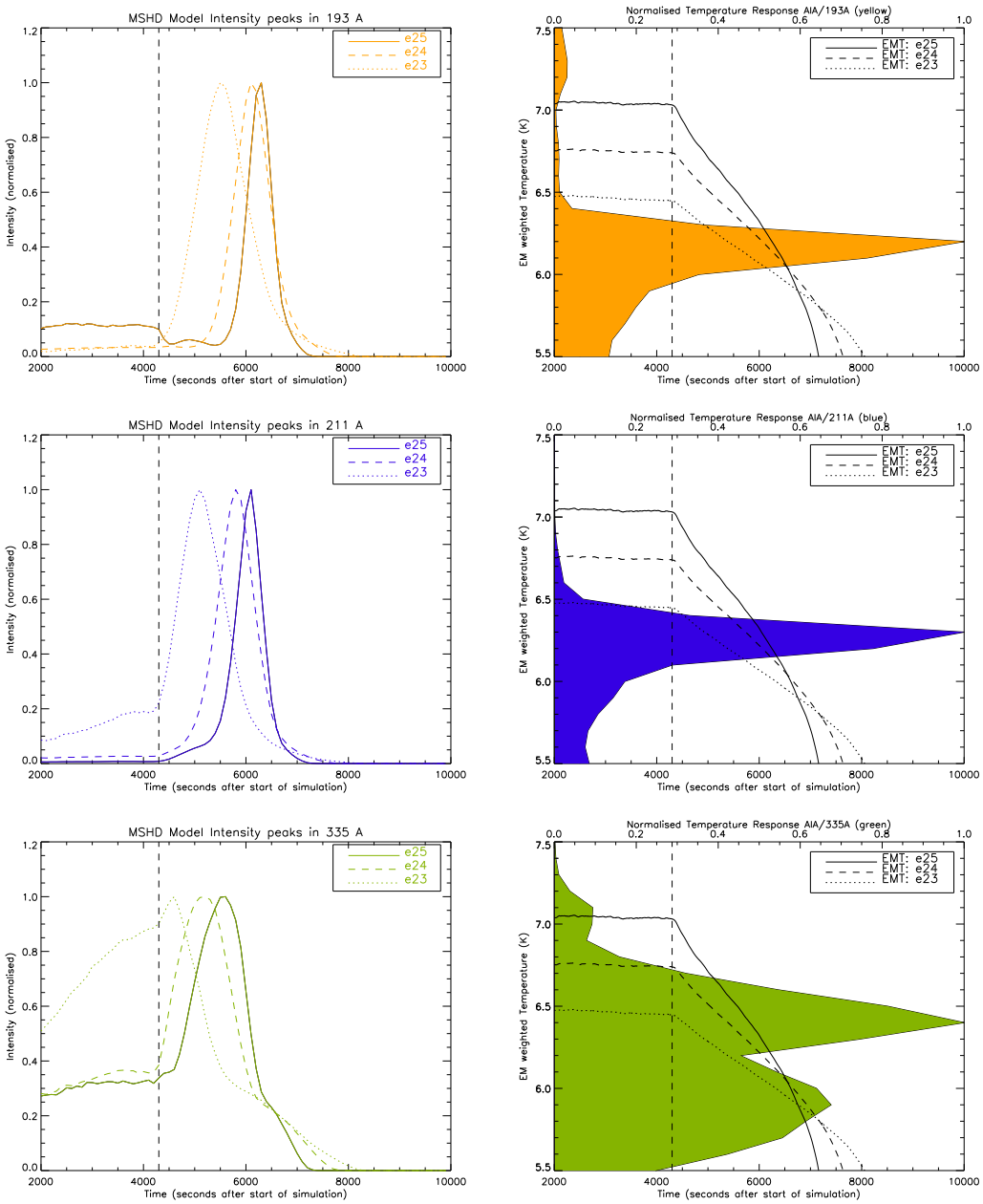

Figure 4.51: Plots showing both the intensity behaviour of the cooling loops in channels 193Å, 211Å, and 335Å (left column) and the corresponding EMT evolution over time (black lines) in relation to each channels temperature response function (filled coloured section).

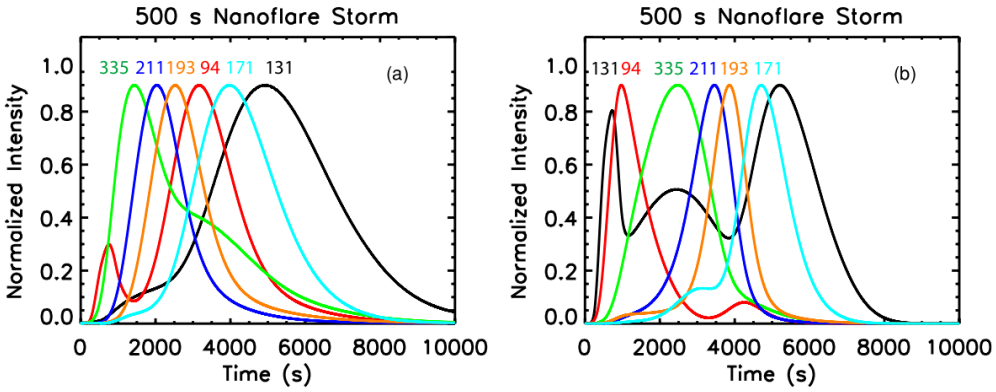

Figure 4.52: Figure from Viall & Klimchuk (2011) showing the intensity peaks seen in a cooling loop simulated with the EBTEL code. The right graph (a) shows the cooling after a 500s heating of energy E while the left graph (b) shows a cooling after a 500s heating event of energy 10E.

In the first case (a) the results from their study are almost identical to the intensity values found for the e23 case from the MSHD model (top plot of Figure 4.49) suggesting that the total energy going into each simulation is around the same value. However, when looking at their results for the order of magnitude higher energy case (b) a different set of results is seen. The clustering of the 335, 211, 193 and 171Å peaks is very similar to the MSHD e24 case (middle plot of Figure 4.49) but the 131Å peak occurs at both the start and the end of the cooling whereas it is only observed in the latter stages of the MSHD cooling. This suggests that their higher energy scenario is halfway between the e24 and e25 energy levels explored in this chapter. By looking at the middle-right plot of Figure 4.50 it can be seen that in order for the 131Å intensity values to show two equal rises, the EMT has to be higher than the e24 case but not as high as the e25 case or the resulting plot would be too similar to the lower plot of Figure 4.49.

It is also not clear how the 131Å intensity changes seen in their higher energy case (Figure 4.52 (b)) manages to get three intensity rises over the course of the cooling. The sensitivity of 131Å only peaks at two temperatures (LogT~5.7 and 7.0) as seen in Figure 4.48, so in order for three rises to be observed the plasma must undergo some additional heating i.e., causing it to dip back into the peak sensitivity of the channel after cooling through it once already. Additional work on this issue and details of further

examination of the cooling MSHD simulation is detailed in Chapter 7 in the Future Work section.

4.2.6 Summary

The MSHD model has proved to be a reliable and flexible tool for simulating a coronal loop. As the parameter space of the model has been explored it is clear that the model responds as it should in a physically realistic way. Each investigation of the parameter space (A-D) has shown a unique result with the resulting DEM changing in a way that can be explained by the particular model outputs. A summary of the main results from each investigation is given in Table 4.11 where the unique DEM and intensity changes observed are noted.

The changes observed in each case could be used to explain similar signatures observed in the DEMs of real data. However, care should be taken when applying the model results to real data as in most cases, the changes observed in the DEMs as the parameter space is altered are very small. Therefore these signatures are not unique in that there could be multiple reasons for the changes seen.

The results from the cooling simulation do show a unique signature in that the total energy of the system can be determined by looking at the pattern of the intensity values and DEM peak temperature as they change over time. The intensity values in each channel were observed to peak in a particular order depending on the total energy of the simulation. Additionally, the rise/fall time of each peak was found to be related to the energy with the higher energy simulation having much shorter rise/peak timescales than the low energy simulation. The temperature that the maximum of the DEM occurs in was also found to follow a particular pattern based on the total energy of the simulation. As the cooling progressed, the temperature bin where the DEM peaks was found to follow the evolution of the emission measure weighted temperature very closely.

Investigation	Unique signatures/key results
A (strand no.)	$\sqrt{2}$ scaling observed in DEM and intensity values. This is due to the line-of-sight element changing (i.e., the strand diameter). → This will not be taken further as this result is not a true unique signature and is just a result of the LOS assumption.
B (heat loc.)	Slight shift between DEMs observed. This is explained by the temperature and density profiles of each simulation. → This shift is clear but not large enough to be thought of as a unique signature.
Ci (tot. energy)	Large shift to higher temperatures observed in the DEM as total energy is increased. Each simulation is observed to have a different channel of peak intensity as the DEM moves up the temperature range to other channel sensitivities. → This result was expected but is useful to show that the model is behaving in a physically realistic way and serves to put reasonable limits on the model energy inputs.
Cii (nanoflare no.)	Large change observed in the width of the DEMs. → This study showed that the width of a DEM is determined by a combination of factors such as the energy of each nanoflare, the time between subsequent nanoflares, and the volume in which the nanoflares are deposited. This means an observed change in DEM width is not a unique signature as it can be caused by more than one parameter.
D (cooling loop)	DEMs are observed to cool and drain over time once nanoflare heating has stopped. DEM peak temperature change over time is consistent with the change in the emission measure weighted temperature. This decline has a unique slope which is related to the total energy of the simulation. The intensity in each AIA channel over time (for each of the three cooling simulations with different total energy) also show a unique pattern. The order and rise/fall times of the intensities can be directly linked to the decline rate of the EMT and how it relates to the instrument response functions. → The DEM result is unique and could potentially be used to infer the temperature and total energy of observations of real coronal loops. The intensity changes can also compared with real data to infer the energy of the loop system based on the order in which the AIA channels peak.

Table 4.11: Summary of the main results of the parameter space investigation of the MSHD model. The unique results in each case (or lack thereof) are also noted for each investigation.

The results of the exploration of the MSHD model are intriguing and will be looked at in more detail in future work. It would be interesting to compare the model results with real AIA data but before doing that, the ability of a particular DEM solver code to reconstruct the model DEM is explored. This will allow real data to be interpreted by the solver with a greater degree of confidence.

Chapter 5

Testing DEM Solvers

Now that the parameter space of the MSHD model has been explored, and the reaction of the synthetic DEMs and intensities to various changes has been understood, the next step is to try and relate the MSHD model to real coronal loop observations. However, before this can be done, the method by which real observations are interpreted in terms of their differential emission measure distribution has to be examined.

The MSHD model allows the exact plasma temperatures and densities used to construct a particular DEM to be known and can track how these values change in time. Using the model as a 'synthetic' observation is an ideal way in which to test various DEM solver codes. By providing the solver code with the six values of intensity 'observed' by AIA when interpreting the model, the similarity between the DEM the solver has fitted and the true DEM built by the temperature and density elements of the model can be compared.

Figure 5.1 shows a flowchart describing the steps involved in this comparison. If the solver code can reconstruct a DEM representing the physical distribution of plasma temperatures and densities based only on the six MSHD intensity values it is provided with, a greater level of confidence can be applied to the solver results concerning real

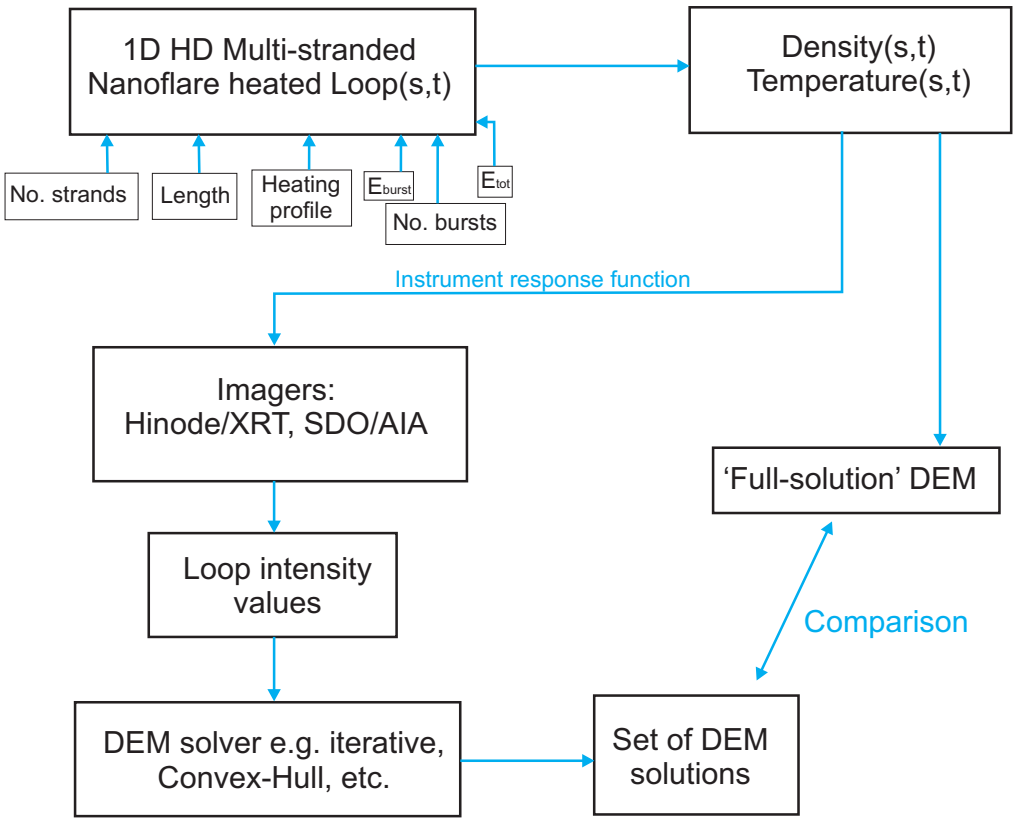

Figure 5.1: Flowchart of process involved in comparing the MSHD model outputted DEM to one reconstructed from a DEM solver code.

observations. The solver code tested in this section is named XRT_DEM_iterative2.pro (Weber et al. 2004; Golub et al. 2004) and although it was written to deal with Hinode/XRT data, it can be adapted to take in SDO/AIA data values.

There are a wide variety of other solver codes available, each with their own advantages and disadvantages. Two particular types of code will be described here (with more information found within given references) but the analysis will be confined to the results from XRT_DEM_iterative2.pro.

5.1 How the solver codes work

A DEM solver code is designed to take in values of plasma intensity counts (measured by an imager or spectrometer) and find a DEM solution which gives the minimum error for these values i.e., a DEM solution which when folded back through the appropriate instrument response function will give out values of intensity with a minimum χ^2 value compared to the original values.

$$I_\lambda = \int DEM(T)\, R_\lambda(T)\, dT \tag{5.1.0.1}$$

Equation 5.1.0.1 shows how the intensity seen in a certain channel (I_λ) is related to the DEM and the temperature response function of that channel (R_λ(T)) in a particular instrument. In principle, the DEM could be found by inverting this equation but problems arise as the response functions overlap at certain temperatures (Weber et al. 2004). There are two main methods (and two types of solver code) that are used to solve this inversion problem: iterative methods and direct inversion methods.

5.1.1 Iterative methods:

An iterative solver starts with an initial guess (based on the intensity values provided) and performs a least-squares fit which is represented by a spline with evenly spaced knots in logT space. These knots are adjusted at each iteration in order to reduce the χ^2 fit of the real observations to the predicted observations. At each iteration the real observations given to the solver are randomly adjusted to a value within the errors given. This allows the local minimum solution to be found. This method is described in further detail in Weber et al. (2004) and Golub et al. (2004).

Schmelz et al. (2007) used an MCMC (Markov-chain Monte-Carlo; Kashyap & Drake 1998) based DEM reconstruction available in the PINTofALE analysis software to study the temperature distribution of coronal loops seen in three TRACE channels. They noted that the MCMC iterative method draws its fits from the posterior probability distribution function which gives a more accurate measure of the statistical uncertainty. However, this method (as with most solvers) does not include an estimate of the errors due to the choice of emissivity, elemental abundances or assumptions of non-equilibrium ionization that the DEM reconstruction makes. This is a point to keep in mind if conclusions are to be drawn from any DEM solver. They further caution against relying on data which does not adequately constrain the DEM distribution at high and low temperatures i.e., by using a low number of filters.

Warren et al. (2011) also used the MCMC emission measure algorithm from PINTofALE to determine the distribution of temperatures in the short, hot loops observed at the core of an active region. They used intensities taken with Hinode EIS and XRT and found that the DEM solver returned values of intensity that were mostly consistent (to within 25%) with the observations. They note that the thicker filters of XRT help to constrain the high temperature end of the DEM but that the broad nature of the corresponding response functions means that there is still some uncertainty regarding the high temperature slope of the DEM. The low temperature end of the distribution is

less constrained so the authors note that the values here should be considered an upper bound on the emission measure.

Schmelz et al. (2009b) used two types of iterative solver, XRT_DEM_iterative2.pro and MCMC, to study the emission from active region cores. They found that the two solvers showed excellent agreement with the results falling within 1-2σ of each other. They also noted that better fits were achieved when more XRT filters were utilised and that the solvers performed better when reconstructing multi-thermal distributions as opposed to spiked isothermal ones. This is because jagged or more isothermal DEMs are not reconstructed well by the spline fitting of the iterative code.

One of the disadvantages of using an iterative solver compared to a direct inversion method is that iterative solvers tend to be slower. This was discussed by Weber et al. (2004) and is something to keep in mind if a large number of calculations have to be made.

5.1.2 Direct Inversion methods:

Inversion algorithms use the inverted form of Equation 5.1.0.1 written in matrix form:

$$DEM_T \; R_{\lambda,T} = \; I_\lambda \tag{5.1.2.1}$$

in order to solve them as a set of linear equations. However, this can lead to some unphysical solutions with negative DEM values in some temperature bins. Additional assumptions can be applied to the solutions in order to get out the most physically realistic values e.g., by disregarding negative solutions or only allowing smooth distributions over the logT space. Singular value decomposition (SVD) can also be used to solve Equation 5.1.2.1 and reduce the inversion problem to a square system of equations with a principle solution. A more detailed explanation of these calculations is given in Weber

et al. (2004) and Plowman et al. (2012).

The SDO/AIA instrument has provided scientists with a previously unknown level of spatial and temporal resolution. In order to carry out analysis on a large area (e.g., an entire active region or the whole solar disc), codes to reconstruct the DEM must be very fast in order to process the vast amount of data generated by the instrument every few seconds. Weber et al. (2004) compared the run-times and accuracy of three types of solver: one iterative, and two types of direct inversion. They found that run-times were reduced by 2-4 orders of magnitude when using a direct inversion method as opposed to an iterative one.

The Convex-hull solver is a new form of SVD direct inversion method written by Dr Mark Weber. This code solves an intensity vector and finds a series of χ^2=0 solutions, which are each composed of six isothermal components (i.e. each solution has six non-zero temperature bins).

The Convex-hull method allows all of the globally best solutions to be found so one must apply some a priori knowledge or judgement to reduce the set of solutions down to a single representative solution. This is in contrast to iterative solvers which can only find the locally best solution. Some initial work using this solver in conjunction with the MSHD model is presented in the future work chapter.

Now that some of the basics behind various DEM solvers have been discussed, a fuller exploration of the iterative solver code can be made. In order to examine the ability of this solver to reproduce plasma parameters, comparisons can be made between the DEMs already constructed from MSHD model and the various solutions from this solver.

MSHD model data for various time/space cuts of each of the 17 simulations listed in Table 4.2 are available for reconstruction and subsequent comparison. In order to detail the various issues involved in using this DEM solver, particular attention is paid to one

example which is used as a case study. After all the intricacies of comparing the solver solution to the real solution have been highlighted, the success/failure of the solver to reconstruct the other variations of the MSHD model is investigated. Subsequently it can be investigated whether the solver is able to distinguish between the results outlined in Section 4.2 where changes in the parameter space of the model resulted in specific differences in the DEMs.

5.2 Testing the iterative solver: example case study

The XRT_DEM_iterative2 solver can be used as a 'black box' i.e., one can put in values of intensity and get out a DEM reconstruction, without having to know exactly how the fit was achieved. However, there are various keywords which allow the user to gain a better understanding of how 'good' the fit is. This section aims to quantify the goodness-of-fit of the solver's DEM to the original model DEM and describe what factors go into determining this.

The case study in this section focuses on one of the time/space cuts of one of the MSHD simulations which was chosen to showcase the details and considerations of applying the solver to a modelled dataset. The dataset chosen is made from information from the apex of the 16 strand loop simulation where the DEM and intensity values were shown in Investigation A of the previous section. This particular dataset was chosen as the modelled plasma had an even spread over temperature which resulted in a uniformly smooth DEM distribution.

As the name suggests, the XRT_DEM_iterative2 solver was designed to reconstruct DEMs based on Hinode/XRT data. It can be adapted to work for AIA intensities by defining the instrument temperature response using the AIA_get_response procedure rather than the corresponding XRT one. Once this has been implemented, values of intensity the six Fe AIA channels (94Å, 131Å, 171Å, 193Å, 211Å, and 335Å) calculated

from the MSHD model are passed to the solver along with an estimate of the error on these intensity values.

For this study an error of 10% in the intensity values was employed in each case; note however that other authors (e.g., Schmelz et al. 2009b) have used a much lower value (3%). The error value chosen here was set at this higher level to reflect the various sources of uncertainty and noise that are present in any dataset. It also serves as a cautious first estimate that can be revised if the solver DEM solutions are found to be too widely spread.

After inputting (i) the model intensity values (referred to as $\mathbf{I}_{orig}$ in the rest of this section), (ii) the error on these values, and (iii) the appropriate instrument temperature response in the solver code, the programme will run for a specified number of iterations (N=100 in this case) before outputting the following:-

- $\mathbf{I}_{obs}$: 101 sets of intensity values for each channel. The first value is that of I_{orig} with the next 100 being values based on the original that has been perturbed within the allowed errors. These form the starting point that the 101 DEM solutions are based on i.e., they are treated as a series of 'observations'.
- **DEM_out**: 101 DEMs over 26 temperature bins each fitted from the corresponding iteration of I_{obs} according to the reconstruction technique of the solver.
- $\mathbf{I}_{gen}$: 101 sets of 'generated' intensity values which come from putting the DEM_out solutions back through the temperature response. These values are the closest match the solver can get to the I_{obs} values for each iteration.
- **Chisq**: 101 measurements of how close I_{gen} gets to I_{obs} for each iteration. This χ^2 value, as well as an alternative, are discussed further in the following section.

A visual representation of the input and output values of the solver is shown in Figure 5.2. The I_{obs} and I_{gen} values outputted by the solver serve to explain how the DEM

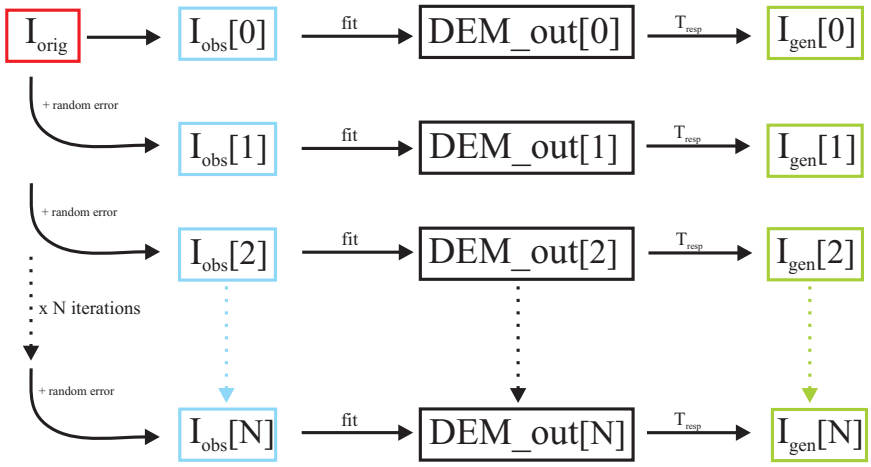

Figure 5.2: Representation of the way the input and output values of the solver are tied together. The initial input intensity from the MSHD model (I_{orig}) is used alongside the given errors to create a set of input intensities (I_{obs}) from which each DEM solution is generated. Putting each DEM solution back through the instrument temperature response gives a series of generated intensities (I_{gen}). These outputted intensity values do not exactly match the ones the DEM was reconstructed from and the solver keyword CHISQ measures on how close the values are.

solutions are obtained and also how the solver χ^2 value is calculated (see below).

5.2.1 Selecting the best iterative solution based on intensity reconstruction

The intensity values of I_{obs} and I_{gen} do not need to be examined in order to use the solver DEM solutions, but they can provide an interesting perspective on how the given error is interpreted by the solver and can also potentially indicate which solution is the best i.e., which iteration's DEM is the closest match to the real DEM produced by the model. In this case study the MSHD model values of intensity and DEM are used in conjunction with the outputs of the solver listed above in order to try and quantify how well each solver DEM matches up to the real DEM.

As discussed above, the solver outputs a value of Chi-square which indicates how well the I_{gen} matches the I_{obs} values. This section aims to quantify if this measure alone is

enough to determine which solver solution should be used concentrated on and designated the ‘best’ fit.

The reason for this extra analysis can be explained by considering using the solver to analyse real observational data. In that scenario the intensity values measured are the only information available so it would be reassuring to know that a good solution can be found (i.e., one with a DEM that accurately represents the distribution of plasma temperature) by relying on some type of Chi-square fit of the I_{gen} to the I_{obs} values. In the case of real data, there is no full-solution ‘real’ DEM to compare the solver solutions to whereas in this case study this information is available. This means the solution(s) with the highest goodness-of-fit measure can be compared to the real temperature distribution of the model DEM.

Before examining the Chi-square that the solver outputs, the spread of the various values of intensity is examined. Figure 5.3 shows the original intensity values plotted as a red solid line with the 10% error indicated. This figure also has the 100 values of I_{obs} overplotted as blue dotted lines. As with other intensity plots in this chapter, the continuous lines are meant to illustrate the overall pattern between channels and are not a suggestion that the intensity values are anything other than discrete.

It can be seen that many of the I_{obs} values lie outside the error bars of the original intensity values. This is because the solver uses the specified error to construct a Gaussian distribution of intensity values where the mean is the I_{orig} and the σ is the error value given. Each value of I_{obs} will fall within the Gaussian but not all within 1σ of the mean. This is shown in Figure 5.4 where the distribution of the I_{obs} and I_{gen} values in each channel have been plotted. It can be seen that in a lot of cases the values of I_{obs} and I_{gen} fall within 1σ but there are many values that do not. In some cases values even fall in the extreme wings of the distribution (e.g., see the 335Å case).

This is another factor that needs to be considered when evaluating the various solver solutions. Only iterations where the I_{obs} and I_{gen} both fall within 1σ of the mean will

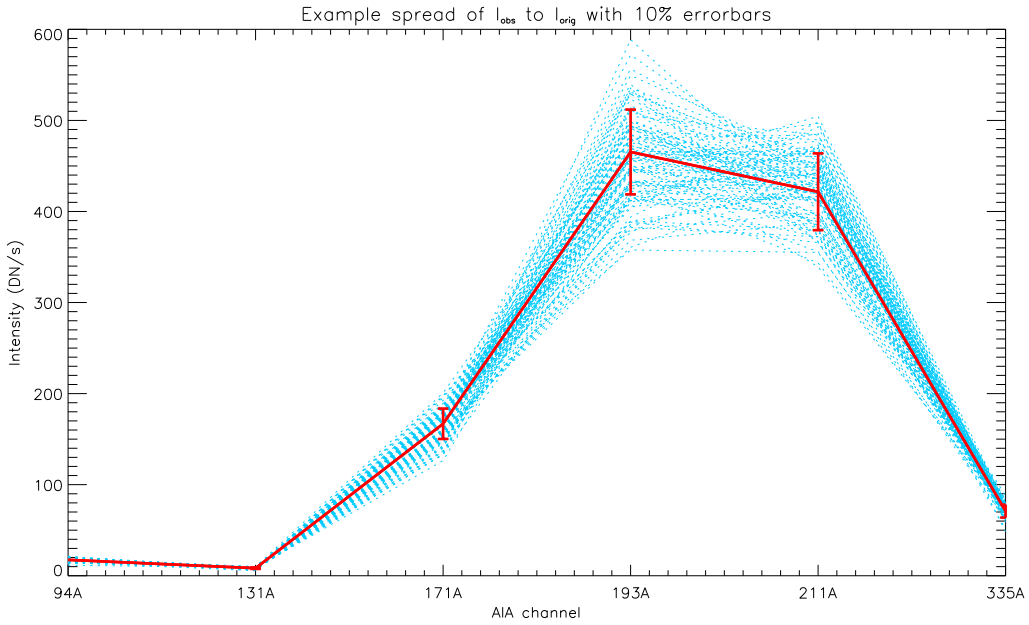

Figure 5.3: Spread of I_{obs} values (blue) around the I_{orig} values (red) with 10% errorbars added. All 101 values of I_{obs} are overplotted. Values of intensity are plotted with lines rather than symbols to show the general trend, not to suggest that these values are continuous. This spread is due to the solver taking the inputted error values as the sigma of a Gaussian distribution with mean=I_{orig} in order to calculate the values of the perturbed I_{obs} values.

be considered further. In this case study only 11 out of the 101 iterations fulfilled this criteria. This set of solutions can be further cut down by examining the Chi-square more closely.

The solver outputs a value of χ^2 for each of the solutions (of which there are 101 in this example) which is hereafter designated as $\chi^2{}_{obs2gen}$ and is calculated from the equation:

$$\chi^2_{obs2gen}[N] = \sum_{\lambda=0}^{5} \frac{(I_{obs,\lambda}[N] - I_{gen,\lambda}[N])^2}{\sigma^2} \qquad (5.2.1.1)$$

where N is the number of iterations performed (i.e., number of DEM solutions calculated), λ refers to which of the six EUV Fe channels the intensity (I) is measured in. This value is a measure of how well the I_{gen} matches the I_{obs} value for each iteration. It is a measure of how close the intensity being fitted (i.e., I going in) is to the solution

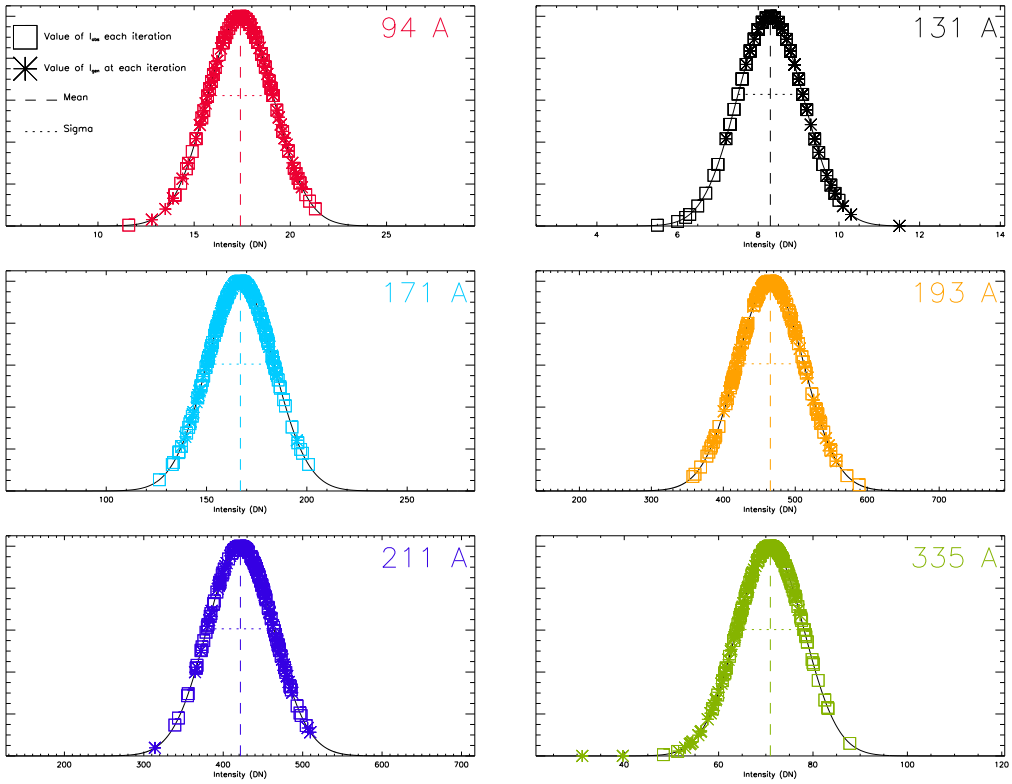

Figure 5.4: Gaussian distribution of I_{obs} (□) and I_{gen} (∗) values where the distribution mean is I_{orig} and the σ is 10% of the I_{orig}. It can be seen that although lots of values are within 1σ of the mean, many are not. The values plotted are to show the overall trend of the I_{obs} and I_{gen} values and do not indicate the relationship between the two values in each iteration. This is addressed later on.

intensity (i.e., I going out).

The solutions can be sorted according to this measure with the minimum value representing the iteration where the I_{obs} and I_{gen} are closest in value and where the maximum indicates that the values are very far apart and therefore the fit has not been ideal. However, using only the $\chi^2_{obs2gen}$ value as a measure of the goodness-of-fit neglects the earlier point made that some values are outside the 1σ of the distribution. An iteration that has the minimum $\chi^2_{obs2gen}$ value only shows that the I_{obs} and I_{gen} are a good match to each other but does not indicate how close to I_{orig} the values are i.e., the I_{obs} and I_{gen} could be out at the wings of the distribution.

Another version of the Chi-square is given in the equation:

$$\chi^2_{gen2orig}[N] = \sum_{\lambda=0}^{5} \frac{(I_{orig,\lambda}[N] - I_{gen,\lambda}[N])^2}{\sigma^2} \qquad (5.2.1.2)$$

which is the same as the previous calculation except the comparison is between the original values of intensity and the outputted I_{gen} values (designated as $\chi^2_{gen2orig}$). This test shows how well each iteration's solution intensity value (I_{gen}) matches the original intensities (I_{orig}). This is a useful second test as an ideal solution would have a DEM which, when folded back through the instrument temperature response, would produce intensities as close as possible to the original values the solver was given.

Each Chi-square calculation gives a measure of the goodness-of-fit of each iteration where the best fit is the one with the lowest value of χ^2. The two Chi-square measurements can be used together to indicate (i) which solutions have the best fit of I_{obs} to I_{gen} values, (ii) and also lie as close as possible to the mean of the distribution.

Figure 5.5 shows the range of values of $\chi^2_{gen2orig}$ ($\diamond$ symbols) and $\chi^2_{obs2gen}$ ($*$ symbols) for the 101 iterations of the solver. It can be seen that most values lie under 20 but a few values exceed this with a clear outlier at iteration 77.

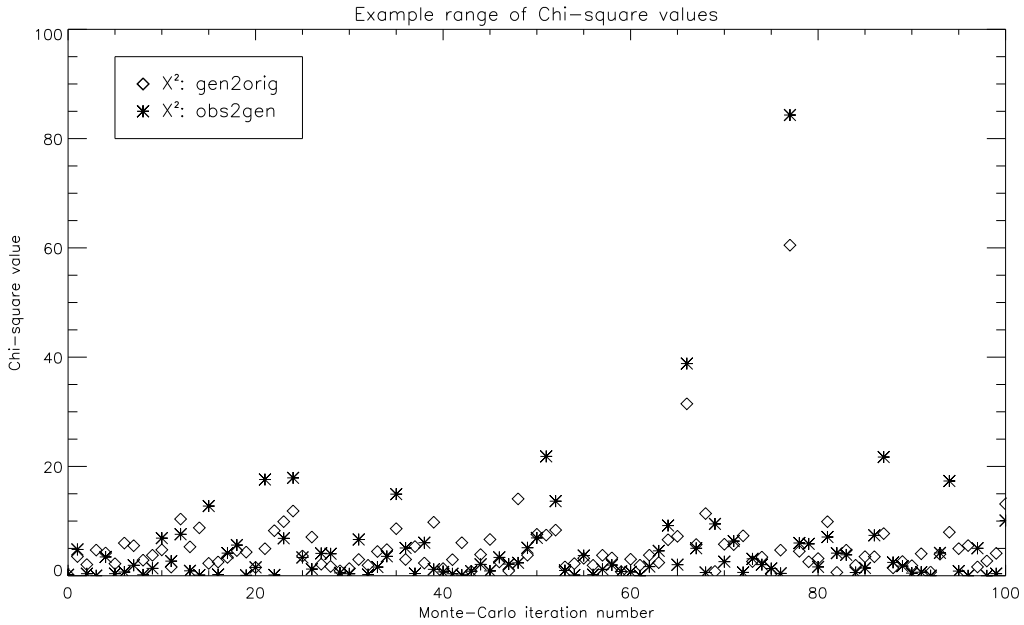

Figure 5.5: Plot showing the distribution of Chi-square for each iteration of the solver. For each iteration two values are plotted based upon the goodness-of-fit between the outputted solver intensities (I_{gen}) and (i) I_{obs} ($*$ symbols) and (ii) I_{orig}, the original MSHD model intensities ($\diamond$ symbols).

Looking more closely at the solutions with the minimum and maximum values of the two Chi-square measurements can help to illustrate exactly what they represent. The maximum value of each χ^2 calculation occurs in the 77^{th} iteration where it can be seen the $\chi^2_{gen2orig}$=60 and $\chi^2_{obs2gen}$=85 (Figure 5.5). This case is examined further in Table 5.1 where the differences in the intensity values are listed. Figure 5.6 shows these differences more clearly where the the Gaussian distribution of the intensities around the original values are shown.

This figure illustrates why the ratio values listed in Table 5.1 are so bad (i.e., not close to unity in many cases), particularly in channel 335Å where the I_{gen} value is at the very limit of what the errors allow. The values of I_{gen} and I_{obs} are not close in any channel except 193Å which is where the best ratio values therefore occur.

Now that the worst intensity fit has been examined, solutions with the minimum Chi-square values from Equations 5.2.1.1 and 5.2.1.2 can be looked at. The solution with the best fit between values of I_{obs} and I_{gen} is at iteration 98 (in this example), while the

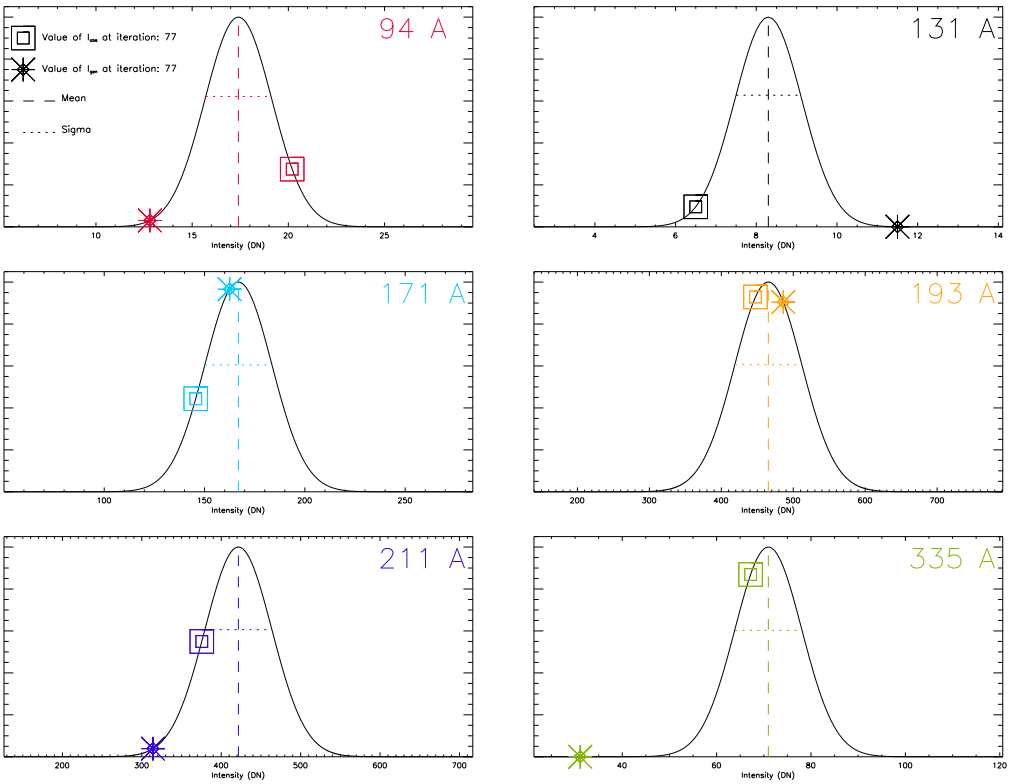

Figure 5.6: Examination of the I_{obs} (□) and I_{gen} (∗) values for iteration number 77 compared to the Gaussian distribution around the mean value of I_{orig} in each channel. This iteration has the maximum value of Chi-square in both methods and is therefore the worst fit. This is clear as the I_{gen} values are neither at the peak or near the I_{obs} values. The x-axis of the plot is 7σ to either side of the mean.

Channel	I_{orig}	I_{obs}	I_{gen}	Ratio (I_{gen}/I_{obs})	Ratio (I_{gen}/I_{orig})
94Å	17.40	20.24	12.75	0.630	0.733
131Å	8.30	6.53	11.52	1.763	1.388
171Å	166.87	145.58	162.49	1.116	0.974
193Å	465.35	447.49	486.21	1.087	1.045
211Å	421.61	375.52	314.04	0.836	0.745
335Å	70.96	67.21	31.12	0.463	0.439

Table 5.1: Table showing the intensity values relating to iteration number 77 which yields the highest Chi-square value. The two calculations of ratio show that both comparisons are poor in this case.

solution whose I_{gen} most closely matches the I_{orig} is iteration 0. The intensity distribution for each of these cases is shown in Figures 5.7 and 5.8.

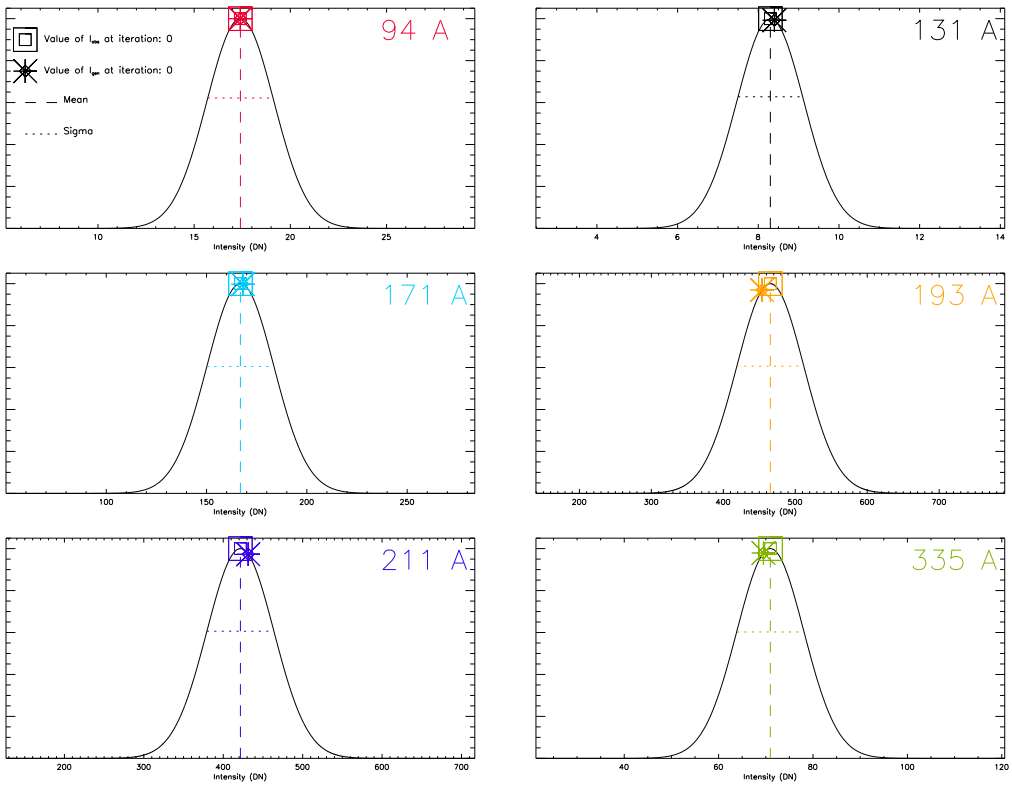

Figure 5.7: Gaussian distribution around the original intensity values for each AIA channel in the 0^{th} iteration. In this example $I_{obs} = I_{orig}$ so these values lie at the peak of the distribution. The intensity values from the generated DEM solution I_{gen} are also plotted to show how close these are to the original.

It can be seen that in both iterations (0 and 98) that the values of I_{obs} and I_{gen} fulfill both criteria of being (i) close to each other in value and (ii) both occurring within 1σ of the I_{orig} mean. Table 5.2 gives more details about these two solutions. The 'gen2orig' columns show the values of intensity in each channel from the original MSHD model values (I_{orig}) compared to the solver's modelled intensity values (I_{gen}) and the ratio of these two values. The 'It.' value refers to the number of the iteration where the minimum Chi-square value occurred.

Below these rows is the Chi-square value of each solution as well as a measure of the standard deviation and average of the ratio values. The 'obs2gen' column shows the same set of numbers for the iteration where there is a minimum Chi-square value

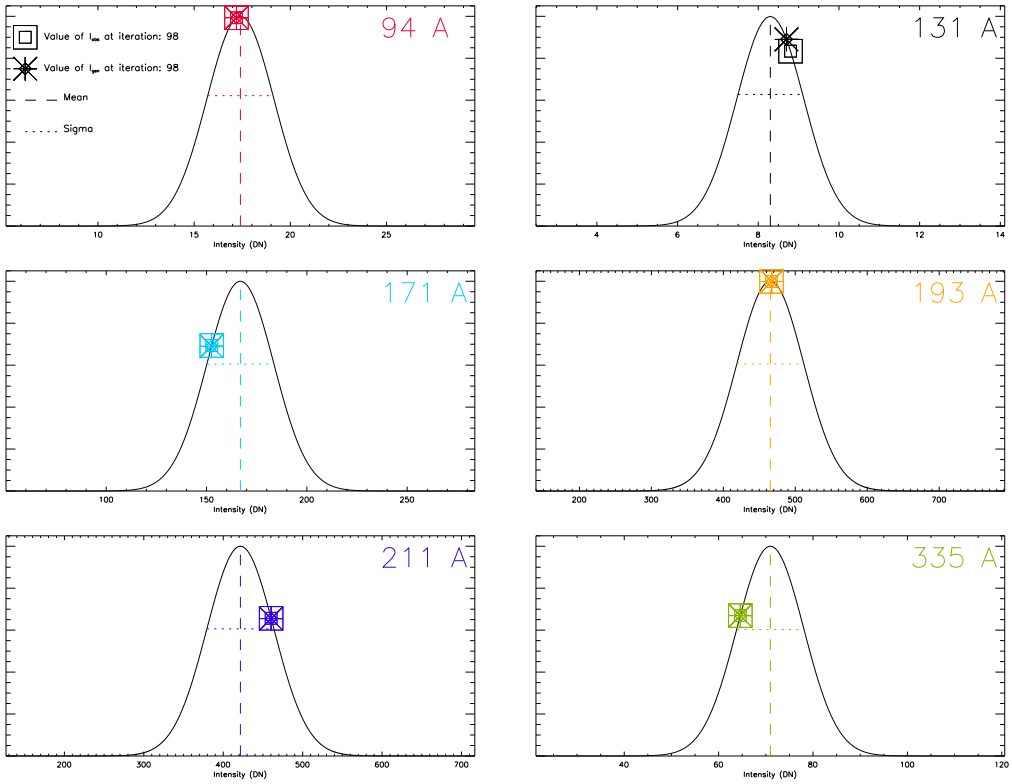

Figure 5.8: Gaussian distribution around the original intensity values for each AIA channel in the 98th iteration. In this example I_{obs} = I_{orig} plus some random error. The intensity values from the generated DEM solution I_{gen} are also plotted to show how close these are. This solution has the closest match of I_{obs} to I_{gen}.

comparing the input intensities (I_{obs}) to the outputted solver intensities (I_{gen}). It is clear that the ${\chi^2}_{obs2gen}$ is more successful that the ${\chi^2}_{gen2orig}$ as the value is much lower (i.e., 3 orders of magnitude smaller) and the intensity ratio is closer to unity. Again the only point to note is the differences between the original intensity values and the ones calculated from the solver. These values are within the error chosen so if they look like too large a departure it is an indication to reduce the σ value given to the solver to less than 10% of I_{orig}.

AIA Channel	gen2orig, It.=0			obs2gen, It.=98		
	I_{orig}	I_{gen}	Ratio	I_{obs}	I_{gen}	Ratio
94Å	17.40	17.45	1.0024	17.16	17.16	1.0001
131Å	8.30	8.39	1.0118	8.75	8.75	0.9997
171Å	166.87	168.05	1.0071	152.65	152.51	0.9991
193Å	465.35	453.82	0.9752	466.95	467.17	1.0005
211Å	421.61	431.38	1.0232	460.28	460.41	1.0003
335Å	70.96	69.46	0.9788	64.60	64.61	1.0002
		χ^2	0.1794		χ^2	0.0001
		Std. Dev(R)	0.0189		Std. Dev(R)	0.0005
		Average(R)	0.9997		Average(R)	0.9999

Table 5.2: Values relating to the two cases where the Chi-square is minimised in each variation of the χ^2 from Equations 5.2.1.1 and 5.2.1.2. The two solutions are named 'gen2orig' - where the comparison is between the best fit of the outputted intensity values (I_{gen}) and the original MSHD model intensities (I_{orig}); and 'obs2gen' where the best fit between one of the variations in input intensity (I_{obs}) and the corresponding solver output intensity (I_{gen}) is found. 'It.' refers to the iteration number of the particular solution.

As mentioned previously, having a minimum Chi-square value in either calculation does not necessarily mean that that solution is the best. For example, a solution with a minimum value of ${\chi^2}_{gen2orig}$ would be close to the original intensity values (i.e., within 1σ) but does not necessarily reflect a good fit as the I_{gen} value may be far from the value the solver was given to fit (I_{obs}). Also, a solution with a minimum ${\chi^2}_{obs2gen}$ value suggests a good fit between I_{obs} and I_{gen} but does not mean it occurs within 1σ of the mean.

This is shown clearly in the solution from iteration 96 which has the second lowest value of ${\chi^2}_{obs2gen}$ but is in the worst 30% of the ${\chi^2}_{gen2orig}$ values. Figure 5.9 illustrates

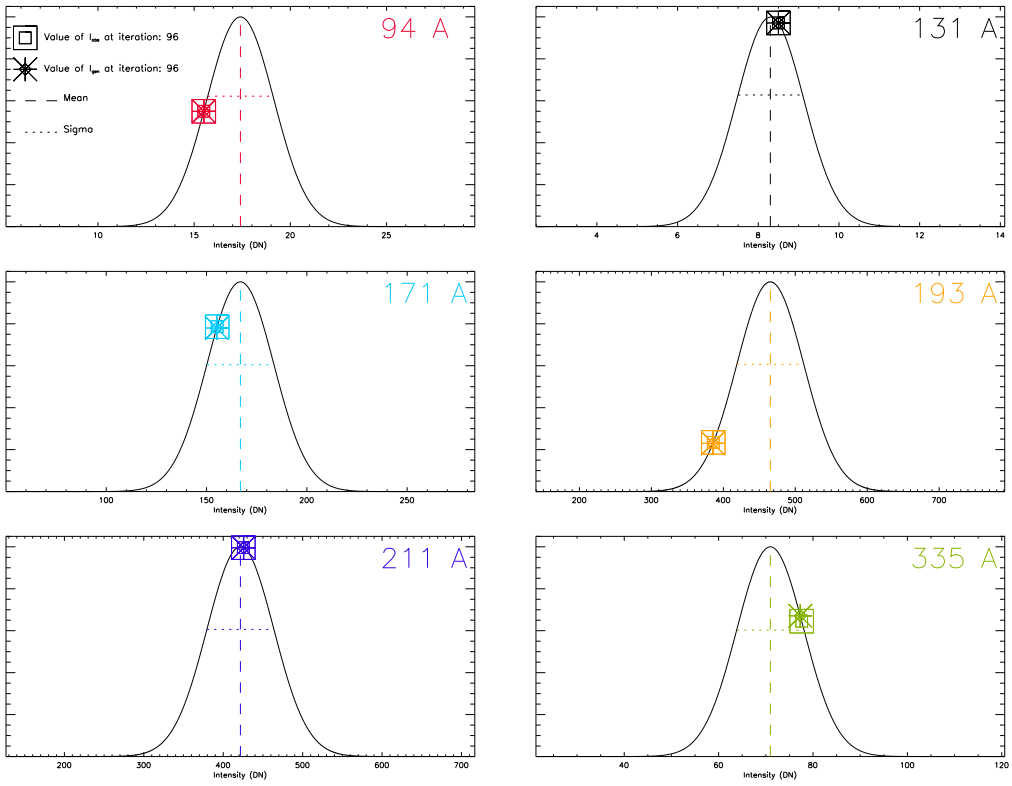

Figure 5.9: Gaussian distribution around the original intensity values for each AIA channel in the 96th iteration. This solution has the second best measure of I_{obs} to I_{gen} values but only the 72nd (out of 101) best value of I_{gen} to I_{orig}. The reason for this is that the 94Å and the 193Å values are not within 1σ of the mean. This shows that although the $\chi^2_{obs2gen}$ test gives this solution a good rating, the $\chi^2_{gen2orig}$ test highlights it is not as good a solution as it first seemed.

this where it can be seen that although there is a very good match between the I_{obs} and I_{gen} values, they occur more than 1σ from the original values in channel 94Å and 193Å. The point of this is to show that relying on the solver output value of Chi-square does not necessarily give a true indication of the best solution if the user explicitly wants the values within 1σ. However, if they are happy with any solution DEM which reproduces intensity values that lie anywhere within the Gaussian distribution then each solution can be considered equally good. If the distribution is considered too wide this can easily be altered by the user choosing a smaller error to give to the solver.

As previously mentioned, the solutions with the 'best' fits of intensity can be found by calculating the two Chi-square measurements and deciding on a way to use information from both to cut down the number of solutions. However, picking only the minimum value from each calculation means that some potentially good solutions are thrown away. For example, when the values of $\chi^2_{obs2gen}$ and $\chi^2_{gen2orig}$ are sorted according to their value, it is not clear if the iteration with the minimum value is the best by a long way or if there are other solutions that also have a very similar values and would therefore be just as valid a choice.

Figure 5.10 shows the Chi-square values from each calculation plotted with the solutions ordered according to their value. In each case the solid line shows that there are a couple of values at the minimum end, then the values increase and to a long series of values which get incrementally larger. At the end of each series the values jump up again for the few values with the maximum Chi-square. Overplotted on each graph is the position in the ranking (i.e., out of 101) of the iterations with the minimum Chi-square in each case (i.e., iterations 0 ($*$) and 98 ($\Diamond$)). Also overplotted with $\triangle$ symbols are the eleven previously mentioned solutions which have both I_{obs} and I_{gen} within 1σ of I_{orig}. Using these eleven solutions as a set of 'best' solutions and then ranking them according to how well they do in each of the two Chi-square tests can help to show where the best solutions are.

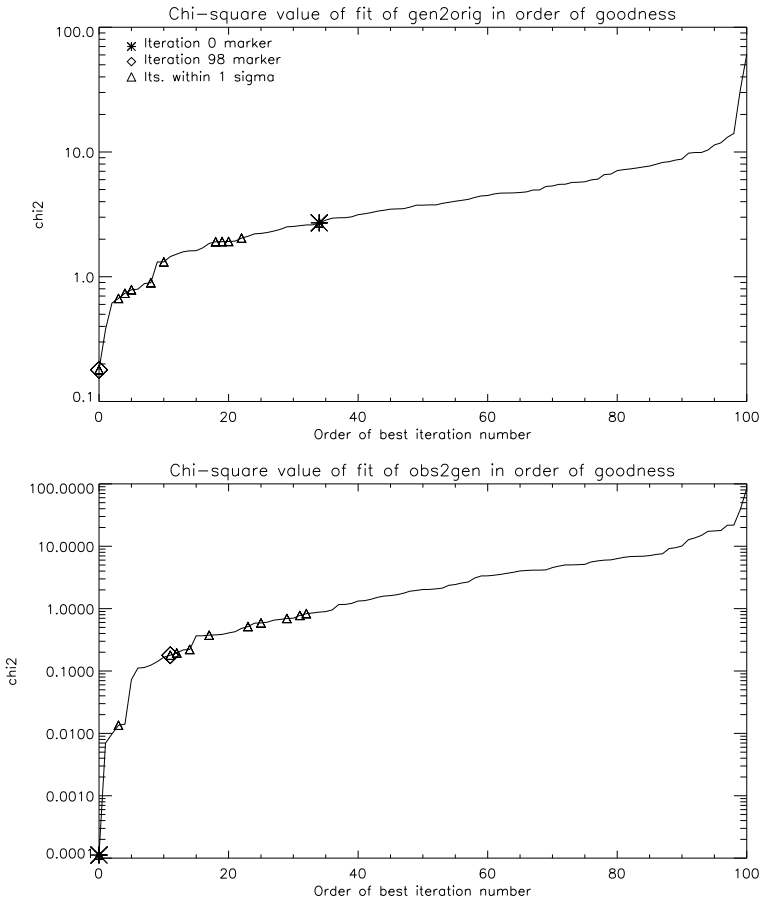

Figure 5.10: Comparison between the two Chi-square measurements ranked according to their value. The overplotted symbols show where certain solutions lie in the ranking.

Table 5.3 shows the details of this ranking. The first and third columns list the iteration numbers which have values within 1σ of I_{orig} ranked according to their Chi-square value in each method. As was already known, iteration 0 and 98 come out at the top solution in each method but what is also seen is that iteration 98 is last in the ranking based on the $\chi^2_{gen2orig}$ values i.e., out of the 11 best solutions, its value of I_{gen} is the furthest from the mean in the distribution. This suggests that it is best to focus only on iteration number 0 which ranks highly in the $\chi^2_{obs2gen}$ test too. Iteration number 92 also ranks highly in both tests and can be considered the second best intensity solution.

Iteration # ranked by $\chi^2_{gen2orig}$	χ^2	Iteration # ranked by $\chi^2_{obs2gen}$	χ^2
0	0.179414	98	0.000112200
92	0.669801	92	0.0135059
59	0.736685	0	0.179414
43	0.786560	56	0.194839
29	0.894557	32	0.221115
40	1.31491	2	0.375522
56	1.90670	29	0.515670
32	1.91065	84	0.589432
84	1.91629	40	0.695767
2	2.04058	59	0.777968
98	2.70281	43	0.830463

Table 5.3: Details of the iteration numbers of the eleven best intensity solutions and their ranking according to the different Chi-square tests. It can be seen that the 0^{th} iteration rates highly on both rankings whereas the 98^{th} iteration is first in $\chi^2_{obs2gen}$ but last in $\chi^2_{gen2orig}$. The values of each iteration's Chi-square is also given to show the magnitude of the differences between subsequent iterations.

Based on this ranking, the best intensity solution for this example is the one from iteration number 0. This solution will now be used to look for further goodness-of-fit measurements calculated between the DEM from the model and all 101 DEM solutions from the solver.

It will be interesting to note if the iterations with the best DEM solutions are the same, or at least similar to, those identified in Table 5.3. This would show that intensity matching alone is indicative of a good DEM match.

The ranking in Table 5.3 is a good starting point for finding the best solutions, but only indicates that there is a good match between the simulation and solver intensity values. Figure 5.11 shows that the various iterations of I_{obs} (which are all technically within the allowed intensity errors) can produce DEM distributions that have widely different shapes. It is clear that making a good match between the intensity values is not enough to conclude that the solver can interpret the spread of plasma properties that is actually there. A measure of the goodness-of-fit between the various solver DEM and the 'real' DEM from the simulation also has to be quantified. Henceforth the DEM built from the MSHD simulation will be referred to as the DEM_sim.

5.2.2 Selecting the best iterative solution based on the DEM goodness-of-fit

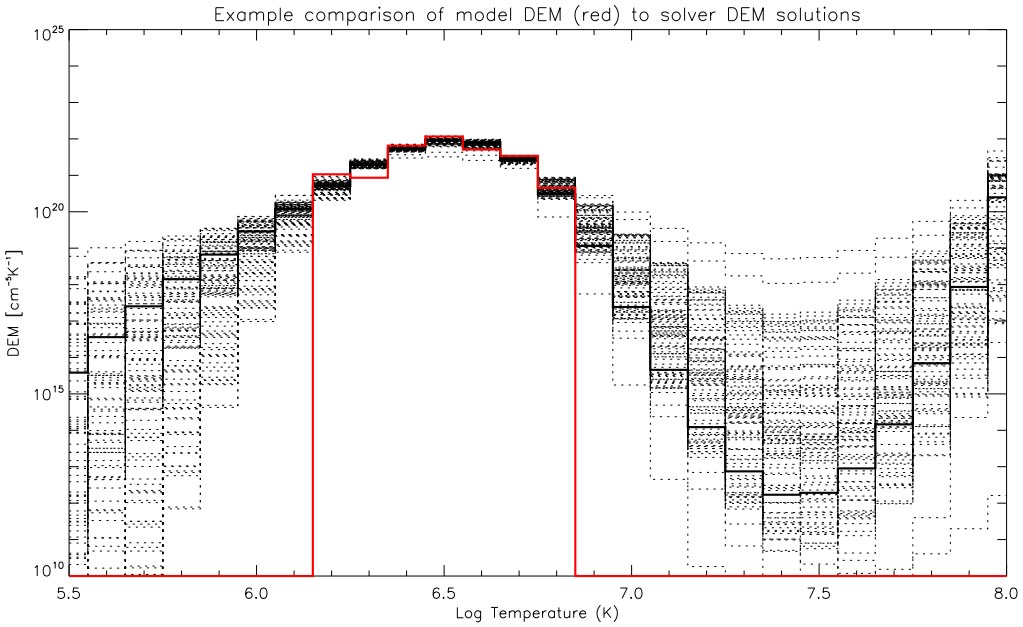

Figure 5.11: MSHD model DEM (red) overplotted with the 101 DEM solutions from the solver (black dotted lines). The black solid line is the DEM solver solution from iteration 0.

Now that the origin of the DEM solver solutions has been established, the 101 DEM reconstructions can be compared to the DEM made directly from the MSHD model outputs. This comparison is shown in Figure 5.11 where the DEM_sim is overplotted as

a thick red line over the solver solutions. The thick black line shows the first value of DEM_out and relates to the solution which has the lowest χ^2 value of I_{obs} compared to I_{orig} (i.e., iteration number 0 in this example, as discussed above).

At first glance it can be seen that the various solver solutions fit around the DEM_sim well, but that they each have components in temperature bins not occupied by the original. The spread of the solutions seen in these lower and higher temperature bins (i.e., 5.50<LogT<6.15 and 6.85<LogT<8.00) can be considered a measure of the uncertainty that the solver has at these temperatures. This is a reflection of the DEM solution being under-constrained and could be improved by the addition of other data (e.g., Hinode/EIS, XRT) which has more sensitivity at these temperatures.

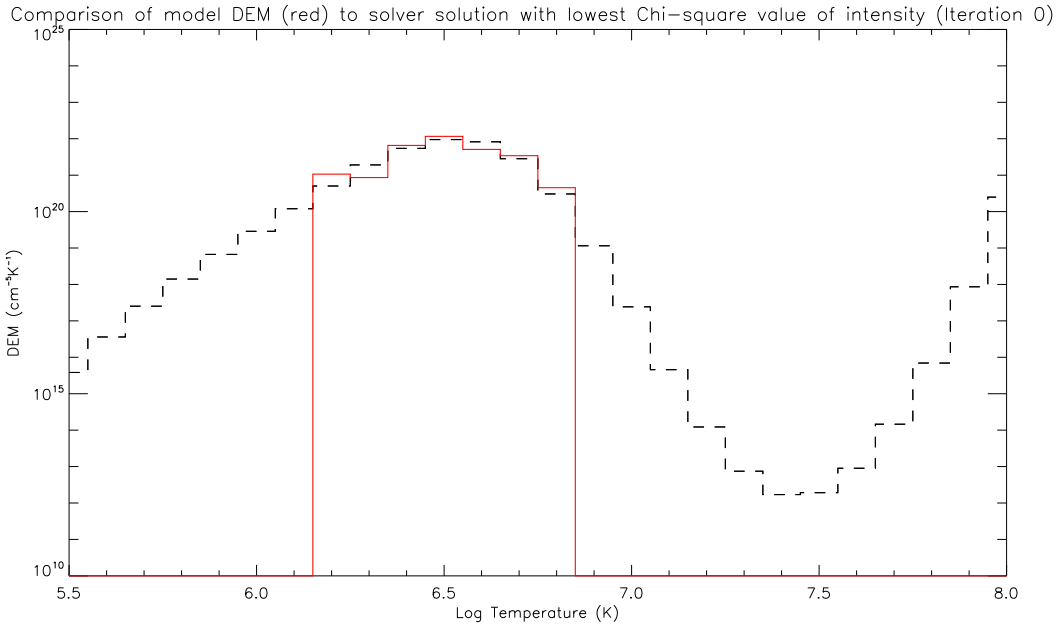

Figure 5.12: DEM plot showing the original DEM from the MSHD model outputs (red) compared to the DEM solution from the solver at iteration 0 (where the Chi-square of the I_{gen} compared to the original intensity values is minimised). The y-axis range is 15 orders of magnitude so to accurately compare the fit a closer look has to be taken.

Figure 5.12 shows the DEM_sim (red) compared to the solver DEM_out solution from the 0^{th} iteration which was the best solution for reconstructing the intensity values. It can be seen that both DEMs have a different shape overall, but that the solver solution seem to follow the shape of the DEM_sim in the temperature bins that it occupies. The

y-axis extends over 15 orders of magnitude and was picked to show the overall pattern of the DEM solution. In order to quantify the goodness-of-fit between the DEM_sim and this solution (as well as the fit of all the other solver solutions), a closer look is necessary.

5.2.3 Determining an importance rating for temperature bins to focus DEM goodness-of-fit investigation

Before examining how well the DEM_sim is reconstructed in the seven temperature bins it is distributed over, the importance of each temperature bin can be quantified. In the MSHD model, the intensity in each channel is worked out per temperature bin before being summed to get one value of intensity per channel. This means the distribution of each channel's total intensity can be examined to see which temperature bins contribute the most. This is important as when comparing DEMs, the focus should be on where the match is successful in bins that 'matter' rather than in bins that aren't important to any of the channels i.e., bins that don't significantly contribute to the intensity.

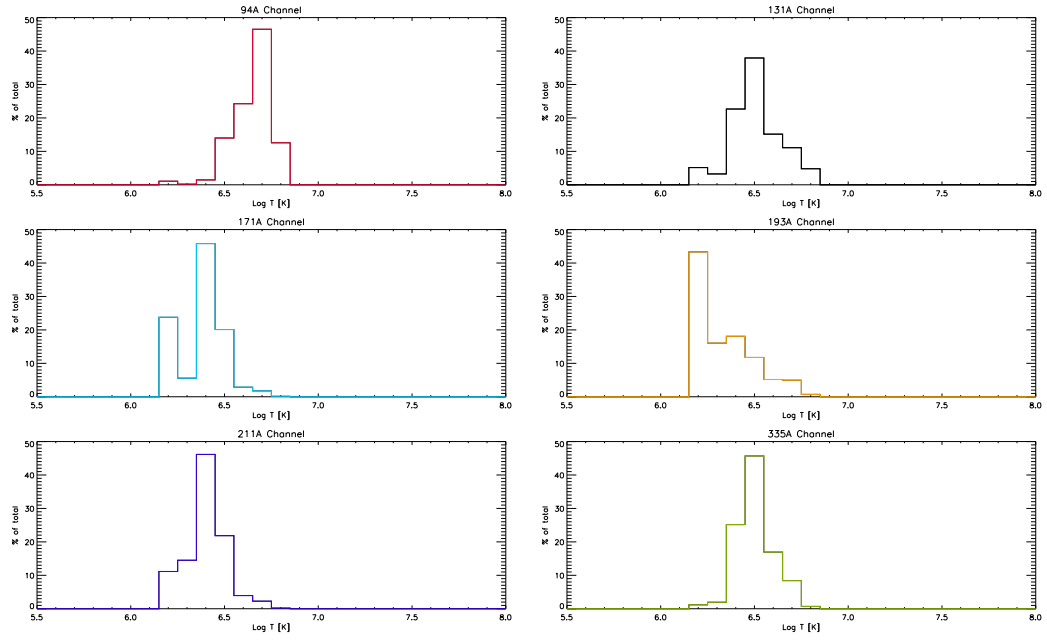

Figure 5.13: Contribution of each temperature bin to the total intensity seen in each channel for this particular model dataset.

Figure 5.13 shows the breakdown of each channel's total intensity across the different temperature bins. The values are plotted as a percentage of the total intensity seen in that channel. This means that equal consideration is given to channels that have much lower counts (DN s^{-1}) compared to others.

An important choice to make is how to combine this information to allow for the extraction of one importance rating per temperature bin. It is important to note that although each channel has one particular temperature bin that contributes the maximum of the intensity, in most cases there are other bins that should also be considered 'important' i.e., bins that contribute above 10% for example.

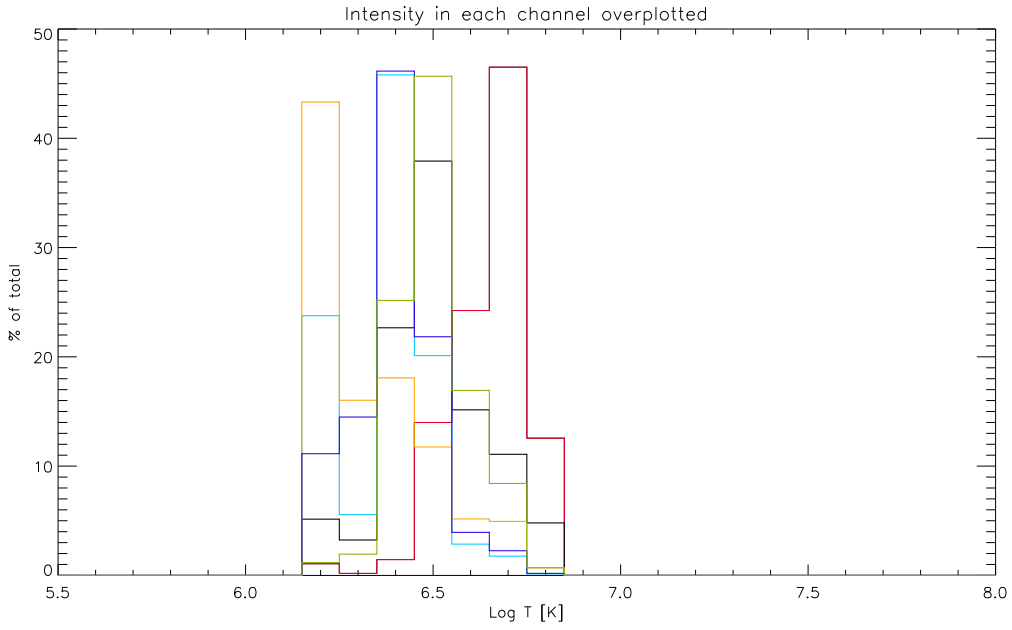

Figure 5.14: Summary plot showing the distribution of all the channel intensities over temperature overplotted on one another. This allows a clear view of the spread of temperatures important to the channels as well as showing which channel is the most important to each bin.

Figure 5.14 shows a plot where all the individual intensity distributions from Figure 5.13 have been overplotted in order to show which bins contribute the most to the intensity. The purpose of plotting it this way (as opposed to taking an average in each bin) is to demonstrate that if a temperature bin is important to one channel, it should be considered important overall i.e., not 1/6 as important if it happens to not be crucial to the other

channels.

Another way to interpret Figure 5.14 is that although some bins are only important to one channel (i.e., LogT=6.7 is primarily important to 94Å (red)) and should thus given a high importance rating, some temperature bins are very important to more than one channel. This is seen in LogT=6.4 and 6.5 where multiple channels have 20-50% of their total intensity.

These two ways of assigning temperature bin importance can be summarised as:

- **Method 1:** the importance of each temperature bin relies on a combination between how important each bin is for all the channels i.e., the contribution in each bin is summed then normalised (not averaged) to weigh the importance according to how many bins rely on it.
- **Method 2:** the importance of each temperature bin relies only on whether that bin is important to any one channel i.e., the importance weighting is based on the normalised shape of Figure 5.14 and does not take into account contributions from multiple bins.

Each method gives a different importance weighting to the various temperature bins as can be seen in Figure 5.15. The left hand plots show the overall shape and importance rating per bin while the corresponding right-hand plots have had each bin coloured according to this importance. It can be seen that in Method 1, the rating of two of the temperature bins that are designated very important in Method 2 have been significantly reduced.

This case study has considered two methods of determining the importance of each temperature bin. For the rest of this section, Method 2 will be used to determine this weighting. This method was chosen because it gives more weight to a temperature bin which is important even for only one channel which should be adequate for it to be

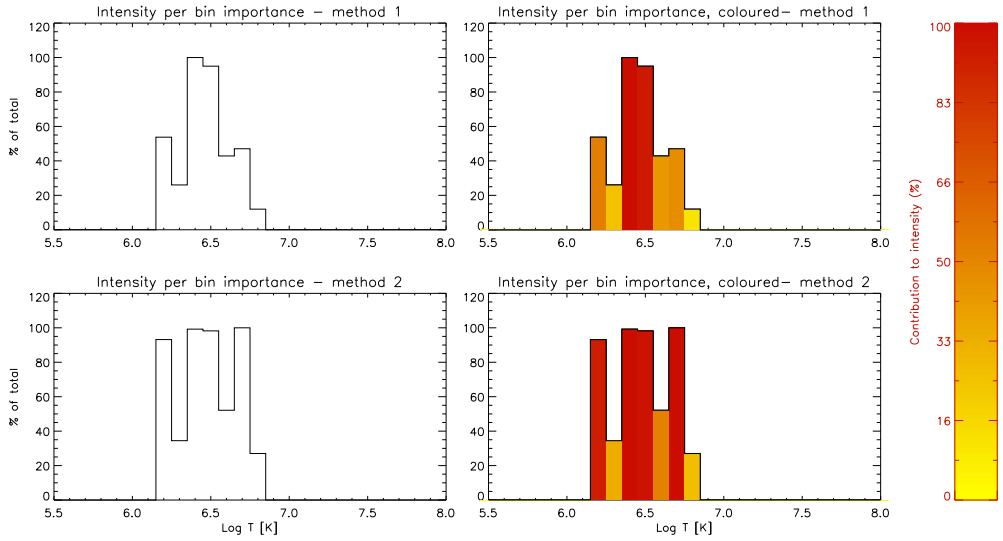

Figure 5.15: Comparison of two different ways investigated to assign an importance rating to each temperature bin. *Top:* Method 1 shape and values (left) and the same shape with bins coloured according to their importance rating (right). *Bottom:* same plots using Method 2. Note these plots are not DEMs - they only show the importance rating of each temperature bin.

considered important overall.

5.2.4 DEM goodness-of-fit considerations

This weighting of temperature bin importance can be applied to the DEM comparison, thus indicating where it is more important for bins to have a 'good' match between DEM values. Figure 5.16 shows the goodness-of-fit between the DEM_sim and the selected 0th iterative solution which was found to be the best solution for reconstructing the intensity values. The top plot shows the DEM_sim (black solid line) plotted with the important temperature bins coloured according to Method 2 as described above, overplotted with the solver solution DEM_out[0]. The range of the plot has also been decreased from 15 orders of magnitude (as shown in Figure 5.12) to two in order to take a closer look at the comparison. However, this plot is on a log y-scale which means

comparisons between the value of the DEMs in each temperature bin can be misleading. For example, the difference between the DEM_sim and the solution DEM_out[0] at LogT=6.5 looks less than the difference at LogT=6.2 but this is not a real result. Looking at the middle plot of Figure 5.16, the same DEM comparison is made but plotted on a non-log y-scale. This shows that the comparison in some of the temperature bins is not actually as close a fit as it appears in the top plot. The lower plot shows the residual values between the solver solution and the DEM_sim in each temperature bin. This has been plotted to show what percentage of the DEM_sim is represented by the residual value.

This figure gives a first look at the goodness-of-fit between the solver solution at iteration=0 and the DEM_sim. It can be seen that the largest residual value (123% difference) occurs at logT=6.3. This particular bin has only a 35% importance rating so this large deviation is not an issue. The fit in the four most important temperature bins (i.e., those coloured in red) have much lower residual values which is an encouraging sign.

This example only showcases the difference between the 0^{th} solver solution and the DEM_sim but it is possible that a better solution exists. By quantifying the goodness-of-fit between all 101 DEM solver solutions to the original model DEM, the best matches can be found. These can then be compared to the best solutions outlined above (see Table 5.3) which most accurately reproduce the intensity values. If the same iterations that give accurate intensity values also accurately reproduce the DEM distribution, this would be encouraging for using the solver with real observations where there is no 'real' DEM to compare the solutions with.

There are many ways in which the goodness-of-fit between the solver DEM solutions and the original DEM_sim can be quantified. The four options explored in this section involve calculating:-

- The **difference** between the DEM values of the DEM_sim and each DEM_out[N]

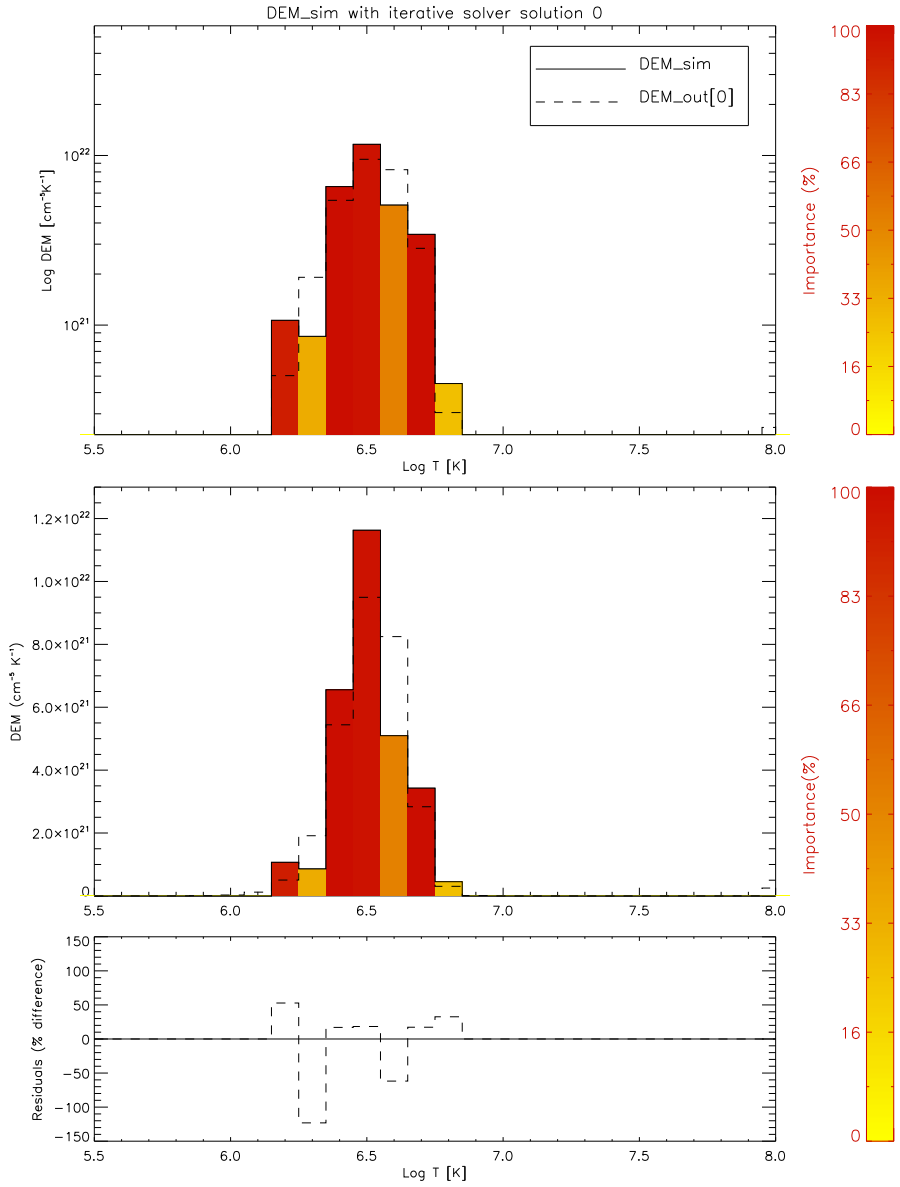

Figure 5.16: Plots showing the first goodness-of-fit analysis between the DEM_sim and the two selected iterative solutions. *Top:* misleading plot of DEM_sim (coloured by bin importance) overplotted with the selected solver solution. The comparison between this solution and the DEM_sim looks better in some bins that others but this is misleading as this plot is on a log-scale. *Middle:* same DEM comparison but on a non-log scale to highlight the difference between the two DEMs. *Bottom:* Plot of residual values between the two solutions. It can be seen that the 'important' temperature bins (i.e., those coloured red) have residual values of less than 20% in 3/4 bins which is interpreted as indicating a good fit in this case.

in the four important bins. The value in each bin is then summed to get a value per iteration. N refers to the number of the iteration.

- The **ratio** i.e., DEM_sim[T_i]/DEM_out[N,T_i]. For each iteration (N), the amount that the ratio in each of the important temperature bins (T_i) deviates from unity is measured and summed to get a value per iteration.

- A measure of the **Chi-square** fit of the DEMs (χ^2_{DEM}) is also made which is outlined in Equation 5.2.4.1. The σ value in this case is taken as 30% of the DEM_sim values but this value is somewhat arbitrary in this study as it is the ranking of the solutions (from minimum to maximum χ^2_{DEM}) that is sought after. This remains the same regardless of the error given. The only difference is the scaling up and down of the χ^2_{DEM} values when the error is decreased and increased respectively. In this equation N refers to the number of DEM solutions produced by the solver (i.e., the iteration/run number) and T_i refers to the particular temperature bins that have been designated as 'important' in this example.

$$\chi^2_{DEM}[N] = \sum_{i=0}^{T_i} \frac{(DEM\_out[N, T_i] - DEM\_sim[T_i])^2}{\sigma^2} \qquad (5.2.4.1)$$

- A measure of the DEM_out values in the **null** temperature bins is also made where the term 'null' refers to the bins not covered by the DEM_sim that have contributions in each of the DEM solver solutions. The ideal solver solution would have a minimum contribution in these bins as that brings it closer to the DEM_sim distribution. The effect of a large contribution in these null bins is also looked at i.e., at what point does the contribution from these null bins significantly affect the corresponding intensity values when the DEM is folded back through the temperature response?

The first three of these calculations (i.e., difference, ratio, and χ^2_{DEM}) should give very similar results for the ranking of the iterations by best value in each case. This is because

they are all based around the comparison between the solver and 'real' DEM values in each important temperature bin. These three calculations are performed only for the four temperature bins determined to be 'important' as it is the fit in these bins that it is most important to quantify.

The iterations that rank in the top eleven values of these three goodness-of-fit measures are listed in Table 5.4 alongside the ranking of the fourth goodness-of-fit measure (null bin contribution) and the order of the 'best' iterations based on the intensity fit discussed earlier. The two rankings (of iteration with best intensity fit) from Table 5.3 were combined into one ranking of the best iterations by evenly weighing each of the eleven solutions by where each one occurred in the ranking of each criteria i.e., ordered by position in $\chi^2_{gen2orig}$ and $\chi^2_{obs2gen}$.

It can be seen that the order of the goodness-of-fit in the three similar DEM criteria (i.e., difference, ratio, and χ^2_{DEM}), have a similar ranking. However, the solutions ordered by the iterations with the minimum contribution in the null temperature bins show a very different pattern. Also, the iterations identified as 'good' fits for intensity (2^{nd} column) don't seem to feature heavily at the top of the various DEM rankings.

Table 5.4 also shows the five lowest rankings for the DEM goodness-of-fit tests. It can be seen that iteration 77 does the worst at fitting the DEM as it did with fitting the I_{gen} values to the I_{obs} and I_{orig}.

The solution with the highest amount of material in the null temperature bins occurs in iteration 14 with the lowest value occurring in iteration 37. The importance of each temperature bin has already been discussed but if a significant proportion of a solution's intensity value comes from plasma in the null bins this suggests the solution is not ideal. Figure 5.17 explores this idea by plotting the DEM solution for the best and worst iteration (top row) with the 'null' temperature bins coloured in green.

Below each plot is the corresponding breakdown of intensity values where the black

Order No.	Sols ordered by intensity fit	Sols ordered by difference	Sols ordered by ratio	Sols ordered by Chi-square	Sols ordered by null bins
0	0	9	9	9	37
1	92	4	48	48	26
2	56	80	4	4	7
3	29	56	23	23	54
4	98	20	11	11	83
5	32	48	40	56	55
6	59	40	56	40	96
7	40	15	30	30	57
8	43	11	80	82	90
9	2	23	93	27	46
10	84	41	82	93	5
.		.	.	.	.
.		.	.	.	.
.		.	.	.	.
.		.	.	.	.
↓		↓	↓	↓	↓
95		42	83	37	77
96		14	14	96	25
97		12	7	45	45
98		39	45	66	100
99		66	37	14	22
100		77	77	77	14

Table 5.4: Table showing the top eleven and bottom five iteration numbers ranked according to how well they do in each of the four goodness-of-fit tests.

line shows the ‘full’ intensity values (i.e., that are calculated by folding the entire DEM solution back through the temperature response), the red line shows the intensity calculated by using just the ‘main’ temperature bins (i.e., those covered by the DEM_sim), and the green line which shows the intensity values calculated when the DEM using only the null temperature bins is used.

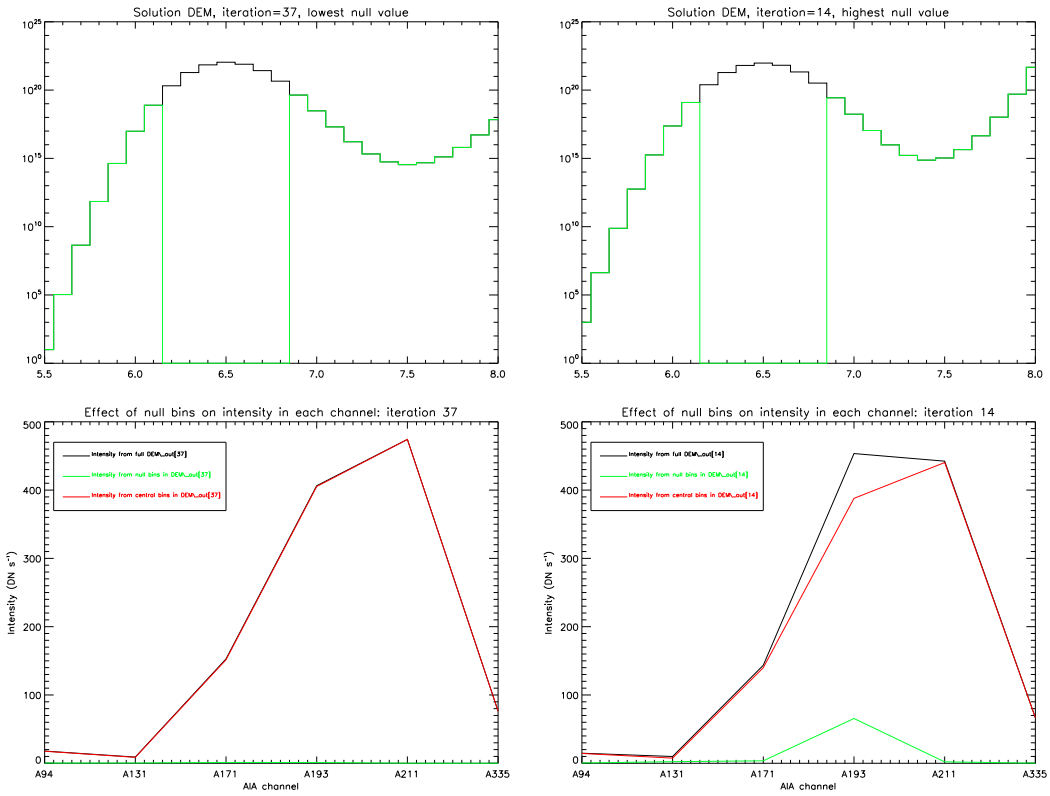

Figure 5.17: The two iterations with the best and worst (i.e., lowest and highest) contributions in null temperature bins to the DEM solver solution. The top plots show the DEM solver distribution for the best (left) and worst (right) results. The null temperature bins are coloured green in each case. The lower plots show the corresponding breakdown of intensity values which occur when the DEM solution is (i) kept whole (black line) (ii) cut to only the bins the DEM_sim occupies (red line) and (iii) cut to only the null bins (green line). In the left-hand plots, it is clear that the null bins contribute a very small percentage of the total intensity whereas in the right-hand plots, the contribution from the null bins is clearer.

The left-hand plots (iteration=37) show that the null bins contribute a very small percentage of the total intensity i.e., most of the intensity is generated from temperature bins 6.2<LogT<6.8. However, in the right-hand plots (iteration=14) it can be seen that the higher contribution in the null bins has resulted in an increase in the intensity that

these bins produce. The intensity values of the 'main' and 'null' bins as a percentage of the total intensity are given in Table 5.5. This table shows the results for the best and worst examples of null bin contributions, but also for the 0^{th} iteration as this solution was found to be the best fit of intensity.

AIA Channel	94Å	131Å	171Å	193Å	211Å	335Å
Iteration=37: lowest null contribution						
% of I_{gen}[37] from main part	98.36	95.89	99.21	99.73	99.97	99.95
% of I_{gen}[37] from null part	1.64	4.11	0.79	0.27	0.03	0.05
Iteration=14: highest null contribution						
% of I_{gen}[14] from main part	97.48	76.41	97.49	85.55	99.54	99.77
% of I_{gen}[14] from null part	2.52	**23.59**	2.51	**14.45**	0.46	0.23
Iteration=0:						
% of I_{gen}[0] from main part	99.26	95.03	83.48	95.92	99.57	99.82
% of I_{gen}[0] from null part	0.74	4.97	**16.52**	4.08	0.43	0.18

Table 5.5: Information on the null temperature bin contributions to intensity for three solutions (i) iteration=37 which is the best solution in terms of null contributions, (ii) iteration=14 which is the worst, and (iii) iteration=0. This last solution is also examined to see where it lies in relation to the best and worst case. The I_{gen} values for the three cases looked at are plotted as a percentage of the total. Values of percentage contribution in bold are those found to be too high.

As expected, the contribution of the null bins in iteration=37 to the intensity is minimal with all values contributing under 5%. Iteration=14 also has some good results but the intensity is much higher in the 131Å (~24%) and 193Å (~14%) channels due to the higher contribution from the null bins at high temperature values. Iteration=0 shows a low contribution in most channels from the null bins except in the 171Å channel where the contribution to the total is ~17%. This is within 2σ of the I_{gen} value so does not mean that the 0^{th} iteration is dominated by plasma in the null bins.

Examining the null temperature bin contributions has shown that even the solution with the highest contribution (i.e., the 'worst' iteration in this ranking) does not significantly affect the resulting intensity measurements. Table 5.5 has illustrated that the intensity values generated from the null bins in iteration=14 contribute a maximum of ~24% in the 131Å channel which means the intensity from the main bins is still within 3σ of

the total. Therefore, in this case study the contribution from null temperature bins will not influence the choice of best solver solution. For other cases (i.e., other time/space cuts of other runs of the MSHD simulation) this calculation may be more important so it will still remain a test of goodness-of-fit. In this case a lower contribution from the null bins is still considered 'better' as solutions with less plasma at temperatures not represented by the DEM_sim give a truer indication of the real temperature distribution of the plasma.

Figure 5.18 groups the four goodness-of-fit tests for the DEM solver solutions together to show how each one differs over the number of iterations. This gives an indication of whether there a few 'good' iterations in each case followed by a series of less good ones, or if all the iterations have a similar value suggesting that any of them could be classed as a good fit. As suspected, the pattern in the difference, ratio, and Chi-square tests for the DEM (plots (a), (b) and (c)) have the same shape. The position of the 0^{th} iteration is also very similar in each case as well as where the eleven best intensity solutions lie.

The fourth plot shows the iterations ordered according the DEM_out values in the null bins follow a gentle increase for the best ~55 solutions but then the values increase sharply. Two of the eleven best values (iterations 92 and 32) fall in this second region but since it has been shown that even the worst iteration is within what is considered a reasonable solution, this is not a problem.

By combining the ranking of the best DEM_out solutions for the difference, ratio, and Chi-square test (which are very similar anyway) a final goodness-of-fit ranking can be calculated. Focusing on the eleven solutions which fit the intensity the best, the position that these iterations lie in the best DEM fit ranking can be checked. Table 5.6 shows the ranking of these solutions according to their goodness-of-fit to the intensity values, and also their goodness-of-fit to the original DEM_sim. For example, iteration=0 is the best choice for reconstructing the original intensity values and is the 26^{th} best choice of DEM solution.

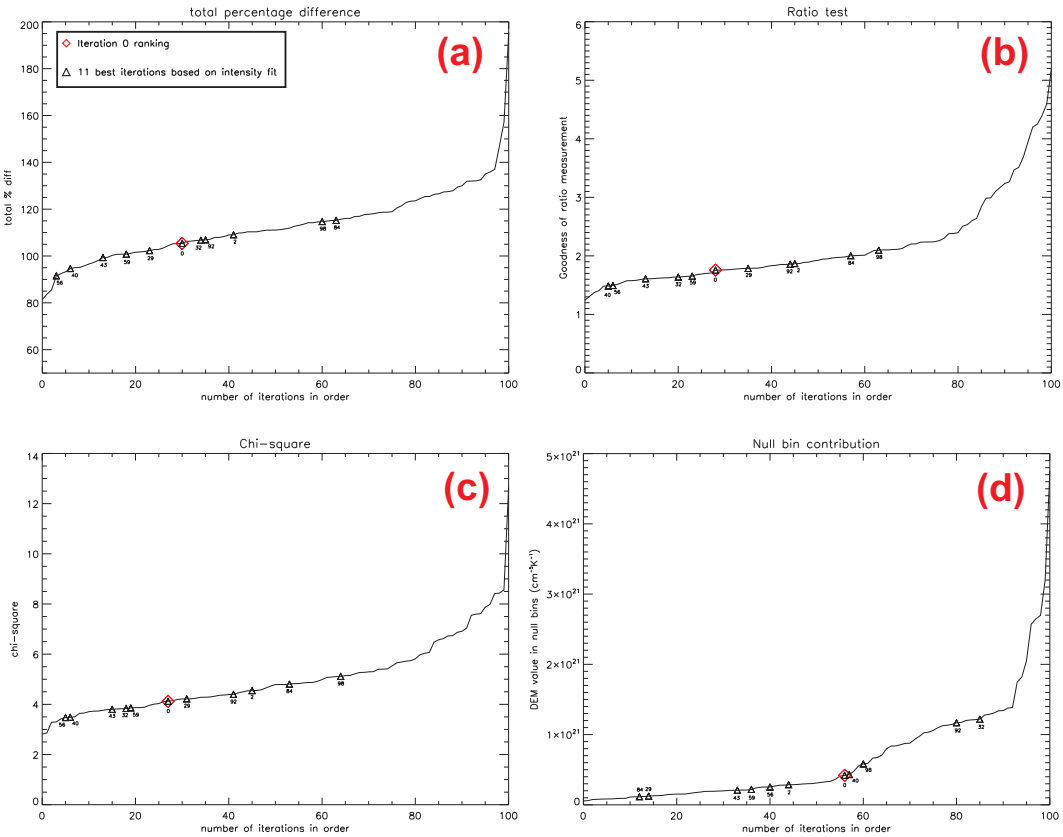

Figure 5.18: DEM solver solution goodness-of-fit tests. Each plot shows the calculated value of each test plotted according to its ranking i.e., the iteration ranking from the full version of Table 5.4 is used to order the values of difference, ratio, Chi-square, and null tests. Overplotted on each test is the location of where the 0^{th} iteration occurs in the ranking (◊) as well as the positions of the eleven best solutions for intensity (△). These have been annotated with their iteration number to identify which solutions do best in each case. It can be seen that the ordering in the difference, ratio, and Chi-square plots is very similar.

Iteration number (N)	Ranking of iteration in fit to intensity	Ranking of iteration in fit to DEM
0	1	26
2	2	42
29	3	27
32	4	21
40	5	6
43	6	10
56	7	3
59	8	16
84	9	56
92	10	37
98	11	62

Table 5.6: Ranking of best eleven solutions in terms of how well they fit the original intensity and DEM values e.g., iteration 0 produces a DEM solution which is the best at accurately reconstructing the original intensity values and is the 26^{th} best solution at matching the MSHD DEM.

The ranking of these eleven solutions in terms of how the corresponding DEM_out solution matches the DEM_sim (column 3) shows quite a spread of values. There are six values that fall within the first quarter of the best solutions while there are also some that less ideal e.g., the 98^{th} iteration being only the 62^{nd} best DEM fit. In this example, the choice of iteration 0 as the solution which best reconstructs both the input intensities and the 'real' DEM distribution, is considered a good one.

The 0^{th} solution of the solver being ranked 26^{th} best in DEM goodness-of-fit doesn't sound ideal but when this position is checked in Figure 5.18 ($\Diamond$ symbol) it can be seen that in each test it lies in a region where the values have only increased slightly from their lowest value. Iteration 56 and 40 would perhaps be better choices as they rank highly on both measures in Table 5.6 but since their values in the various DEM goodness-of-fit tests are in a similar range to the 0^{th} one, iteration 0 is considered to be a good choice. If real observations were being used, the secondary test of measuring the goodness-of-fit of the DEM solutions against the 'real' DEM could not be measured so there would be no way to know which of the eleven solutions identified earlier is best. It is reassuring to know that picking the best solution for intensity reconstruction is also a good solution

for reconstructing the original DEM distribution.

In this case study, care has been taken to try and address the various goodness-of-fit issues that exist when trying to compare a model DEM with possible solutions. By firstly calculating which solutions best reproduce the intensity values given to the solver, the solutions which then best fit the model DEM distribution can also be found and compared. In this example, the eleven solutions of good intensity fit do a good job of identifying solutions which also describe the DEM distribution well.

Now that the various issues in determining whether or not the solver can accurately reconstruct the MSHD model DEM have been looked at, other time/space cuts of the various simulations can be looked at to see (i) where the solver does well/badly, and (ii) if the best solver solutions can follow the various changes that were observed in the model DEMs when specific changes were made to the model parameter space.

5.3 Testing the iterative solver: solver strengths/weaknesses

Now that the intricacies of comparing the MSHD model DEM to the various iterative solver solutions have been thoroughly discussed, the various calculations to measure goodness-of-fit can be applied to the other data-sets. Table 4.2 in Section 4.2 listed all the simulations of the MSHD model that were run, each with different model parameters (e.g., strand number, total energy etc.). Using the same methods as in the case study described above, a selection of these simulation cuts were then used alongside the iterative solver in order to:-

1. see how well the solver solutions fit the original intensity values,
2. see if the 'best' solution(s) for reconstructing the original intensity values are also good at reconstructing the original DEM distribution,
3. see if the 'best' solution overall is clearly identifiable early on i.e., is it iteration 0 or one with a minimum Chi-square value?
4. if the best solution is *not* identifiable without the real DEM for comparison (i.e., treating this like a real observation), how different is this solution to the one identified as best for intensity reconstruction? Are both solutions equally good or totally different?

The goodness-of-fit of the iterative solver DEM solutions were measured for simulations that cover all the investigations described above in Section 4.2 i.e., investigations A-D. In most cases the solver did very well and produced a DEM solution that accurately matched the original model DEM distribution as well as the original intensity values. This section describes the comparisons between the original DEMs and the corresponding solver DEMs in more detail.

5.3.1 DEM smoothness investigation:

Figure 4.10 back in Section 4.2.1 showed the large variation in DEM shape that could occur when the simulation dataset the DEM was based on was very small. By increasing the size of this dataset the DEM became more smoothed out i.e., distributed more evenly across the temperature bins. This increase in smoothness is shown in the top four plots of Figure 5.19 where the top two plots (cut 1a and 1b) are based on model outputs (temperature and density) from an area representing 1 AIA pixel that has been exposed for 3 seconds. 1 AIA pixel is approximately 4 grid spaces in the model so the number of temperature and density elements involved in calculating these DEMs for the 16 strand loop is 4 x 3 x 16 =192.

The next plot is based on 'cut 3' which involves data from a larger area (4 AIA pixels) and a longer time duration (500 seconds) so this DEM is based on 128,000 temperature and density elements. It can be seen the DEM has a much more uniform shape than the top two. Lastly, data from a 'cut 6' of the model (4 AIA pixels over 2000 seconds) is shown as a DEM in the lower right panel. This DEM is made from 512,000 temperature and density elements and it can be seen it has an even more uniform shape. The intensity values based on these four DEMs were then passed to the iterative solver to see if increasing the size of the dataset each DEM is based on would result in an increase in the goodness-of-fit of the solver solution.

The lower four plots of Figure 5.19 show the same four model DEMs (this time in red) overplotted with their corresponding iterative solver DEM solutions with the 'best' iteration represented as a solid black line. It can be seen that the fit of the solver DEMs to the original DEM becomes closer as the model dataset size increases. This is quantified in Table 5.7 which shows details of the fit in the four data cuts in terms of the various measures of the Chi-square. The best solver solution identified in each case is iteration 0 apart from cut 1b where iteration 12 is found to be better at reconstructing both the intensity values and DEM distribution of the original. The Chi-square values of the

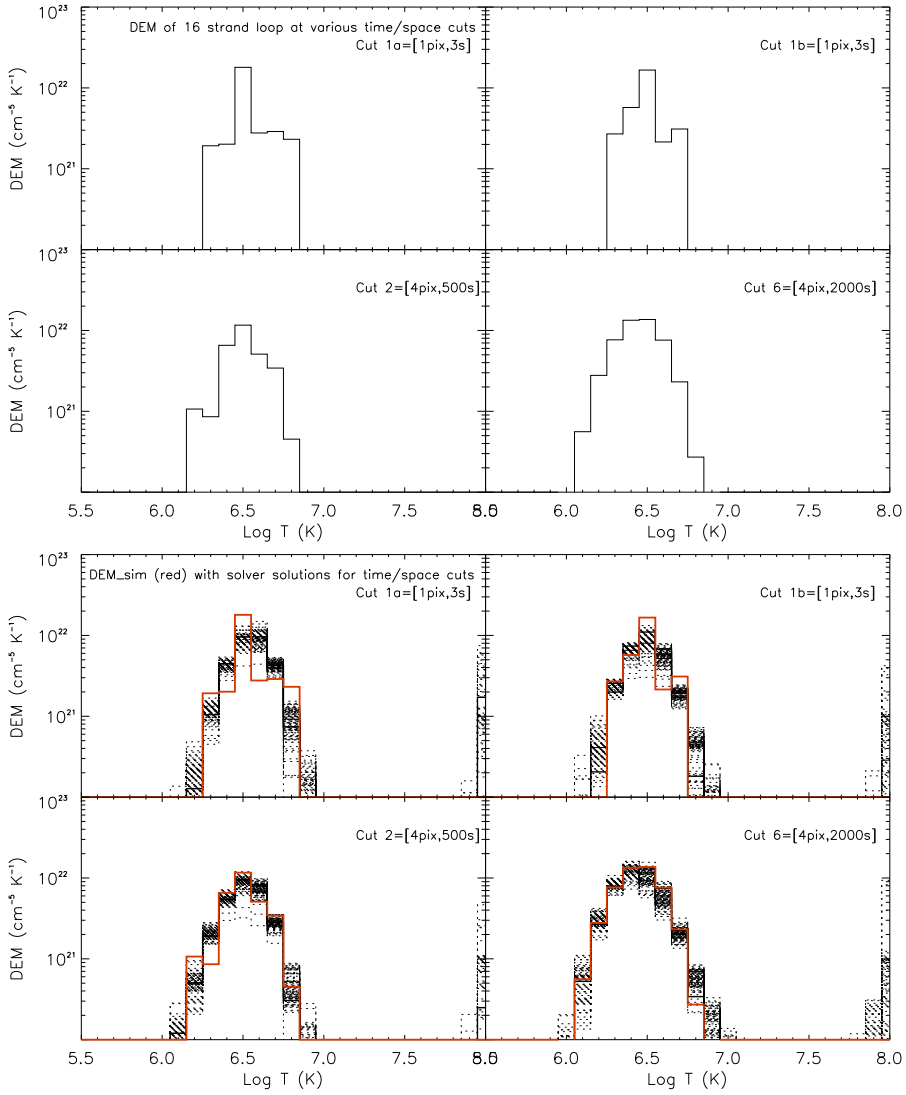

Figure 5.19: Top four plots show the model original DEM from cuts of the 16 strand loop. The dataset each DEM is based on increases from a minimum in the top two plots (cuts 1a and 1b) to a maximum in the lower right plot (cut 6). The set of four plots at the bottom of the figure show these same DEMs (red) with the iterative solver solutions overplotted. The thick black line in each case represents the solution that was found to be the best fit overall to matching the model intensity and DEM distribution.

'best' solution to the original model values in terms of intensity (both to the I_{orig} and I_{obs}) and DEM are also noted. It can be seen that these Chi-square values reduce significantly as the dataset size increases.

	cut 1a	cut 1b	cut 2	cut 6
Best sol.	0	12	0	0
$\chi^2_{gen2orig}$	1.285	0.953	0.179	0.023
$\chi^2_{obs2gen}$	1.285	0.954	0.179	0.023
χ^2_{DEM}	9.88	5.14	4.12	0.053

Table 5.7: Comparison of the goodness-of-fit improvement measured with different chi-square values for DEM reconstructions where the MSHD model data-set size has increased in size as the cut number increases.

The iterative solver does very well at reconstructing the original model DEM in most cases. The goodness-of-fit between the solution determined as the 'best' and the original DEM is found to be best in cases where the DEM_sim has a more uniform distribution over several temperature bins. The solver does less well in the case where the DEM_sim has a significant contribution in one particular temperature bin (such as in the top-left plot of Figure 5.19) or if the DEM_sim is very narrow. This suggests that care should be taken when using this solver to interpret AIA data based only on one exposure. Ideally, a number of files should be averaged in time and over more than one pixel in order to smooth out small-scale variations. Although the solver is good at reconstructing intensity values, for the true shape of the original DEM to be most accurately recovered a smoother dataset needs to be supplied.

5.4 Testing the iterative solver: tracking the changes of different simulations

The different simulations run to explore the model parameter space displayed certain signatures as each particular parameter was changed:-

- Investigation A:- the $\sqrt{2}$ rise in the DEM as strand number doubled,
- Investigation B:- the slight shift between DEMs of different heating locations,
- Investigation Ci:- the large shift between DEMs as total energy was increased
- Investigation Cii:- the narrowing of the DEM observed as nanoflare number per strand increased,
- Investigation D:- the order and timescale of intensity peaks in each AIA channel, as well as the change in the DEM position as loops of different total energy were allowed to cool after a period of nanoflare heating.

The solver solutions should also display these signatures if the fit in each case has been successful. The ability of the best solver solutions in each case to reproduce these results are examined to see where the solver does well and where it does not.

5.4.1 Following Investigation A changes: increasing strand number

Figure 5.20 shows the original DEM_sim (red line) for the four cases of increasing strand number overplotted with their corresponding iterative solver solutions. In each case the solution determined to be the 'best' (using the analysis described in the case study above) is highlighted (solid black line). As in the case study it can be seen that the cloud of solutions seems to match the original DEM_sim well although the values diverge at lower and higher temperatures due to a lack of constraints.

A closer examination of the solver fit to the original DEM can be seen in Figure 5.21 where the range of the y-axis has been reduced to three orders of magnitude. This zoomed in view shows that the solver solution in each case (black dashed line) matches the original DEM solution (red line) very well. The Chi-square value of the chosen solver solution in matching the original intensity and DEM_sim values is also given in

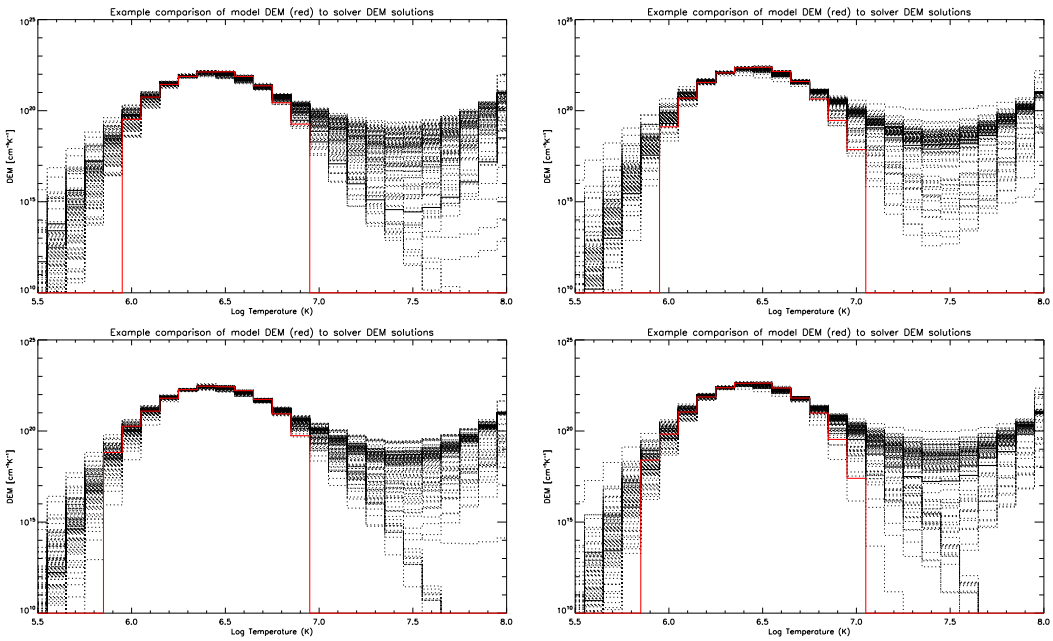

Figure 5.20: Plots showing the model DEM_sim (red) overplotted with the 101 iterative solutions (black) for increasing strand number. Top-left plot shows the 16 strand number case, followed by 32 strand (top-right), the 64 strand case (bottom-left) and the 128 strand case (bottom-right).

each plot. These values in each case are very low (i.e., between 0-3) which shows the fit to both intensity and DEM distribution is good.

The next step is to see if the best iterative solutions for fitting the DEMs of increasing strand number also show the $\sqrt{2}$ increase observed in the model data. Since Figure 5.21 shows that the solutions do a very good job of fitting the original DEMs (especially in terms of their peak position), it is very likely the DEM solutions will also show this trait. Figure 5.22 shows the DEM_out solutions (black) for each strand number compared to data from the 128 strand case which has been scaled by $\sqrt{2}$ in order to see if the solutions follow this pattern. It can be seen that the solution DEMs also show the $\sqrt{2}$ scaling displayed by the original data in Figure 4.15.

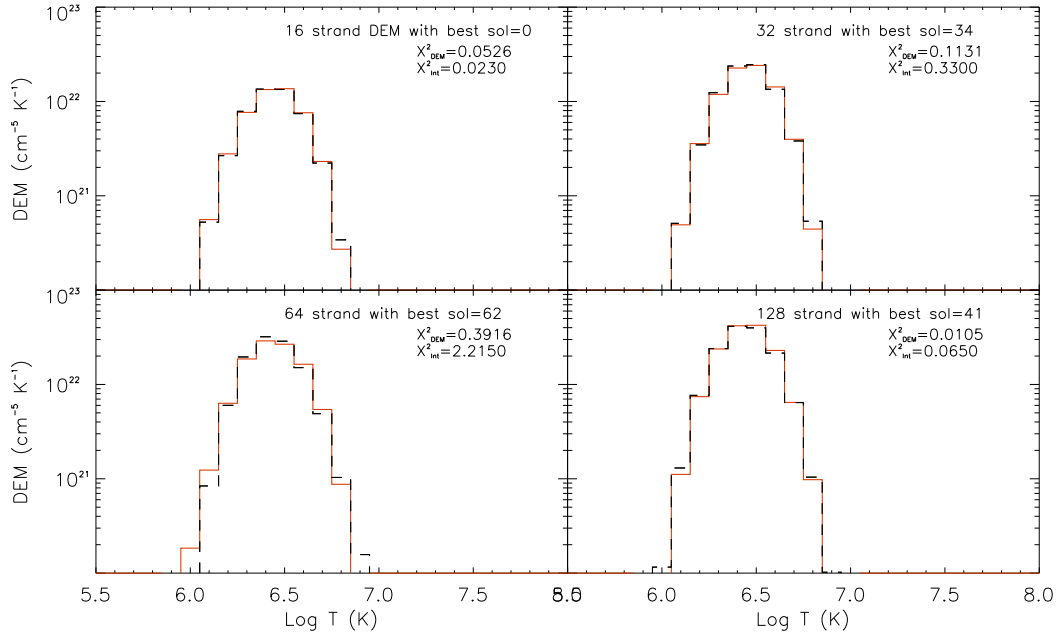

Figure 5.21: Plots showing the fit between the original DEM for increasing strand number (red line) and the best iterative solution in each case (dashed black line). Each plot also notes the Chi-square values of the fit to the DEM and the original intensity values. The fit in each case is considered to be very good.

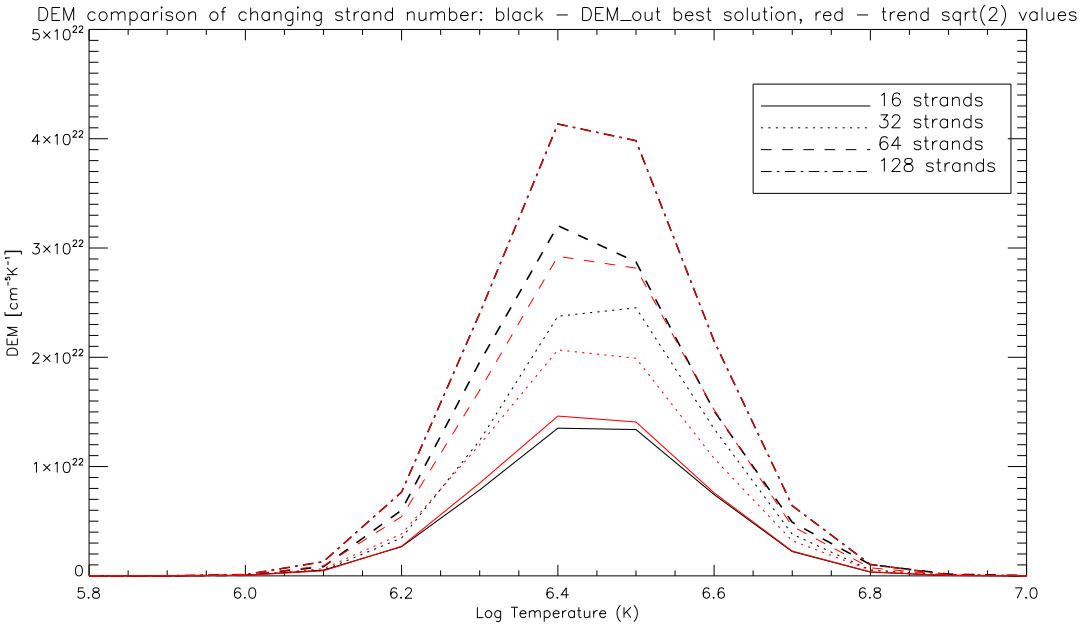

Figure 5.22: DEM_out solutions plotted on a non-log scale in black with the 128 strand values scaled down by $\sqrt{2}$ overplotted in red. It is a close visual fit showing that the solutions are able to match the observed scaling from the model.

5.4.2 Following Investigation B changes: changing location of heating

Changing the location of the nanoflare heating within the simulated 128 strand loop resulted in a small shift between the different DEMs. This was observed as a slight shift towards lower temperatures in the footpoint heating case compared to the uniform case, and the apex heated DEM being shifted towards higher temperatures. This shift was very small (~ 1 temperature bin either way) so it will be interesting to see if the solver solutions can pick it up. Particularly because the iterative solutions tend to have higher contributions at low and high temperatures which could cause the shift to be masked if it only occurs within the central temperature bins.

The results of the individual comparisons between the original DEM_sim and the solver solutions for each heating scenario are shown in Figure 5.23. It can be seen that the fit in each case looks good although at higher temperatures the difference between the two DEMs in each case becomes more apparent. The Chi-square for the DEM fit in each case is good (0.33, 1.34, 0.04 for apex, uniform and footpoint heating respectively) despite this difference at higher temperatures, as the fit is based on the important bins within the DEM_sim only.

Figure 5.24 shows the shift between the solver solution DEMs for the different heating locations. The slight shift between the DEMs is observed but is most clearly seen in the lower panel of the plot which shows the difference between the apex and uniform case, and the footpoint and uniform case very clearly. This match coupled with the low Chi-square values for the three fits shows that the solver has done very well at matching the model in this situation.

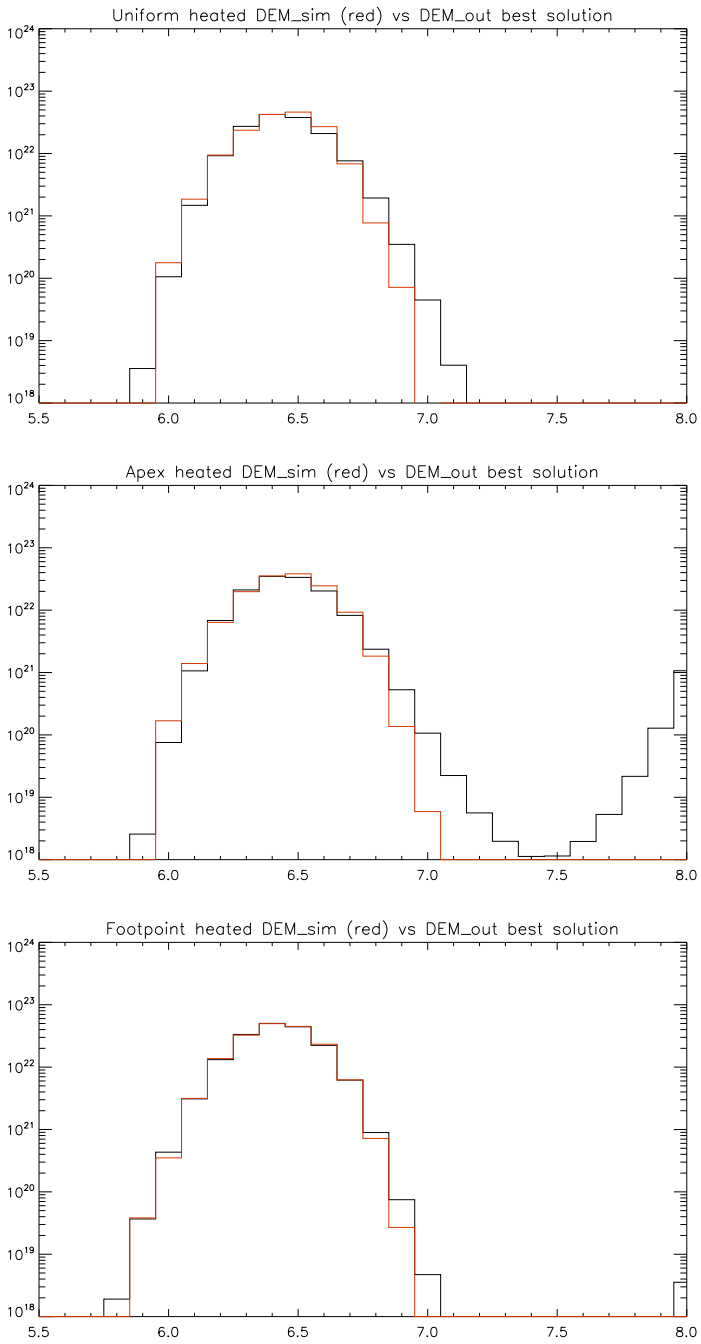

Figure 5.23: Plots showing the fit between the original (red) and solver DEM (black) for different heating locations.

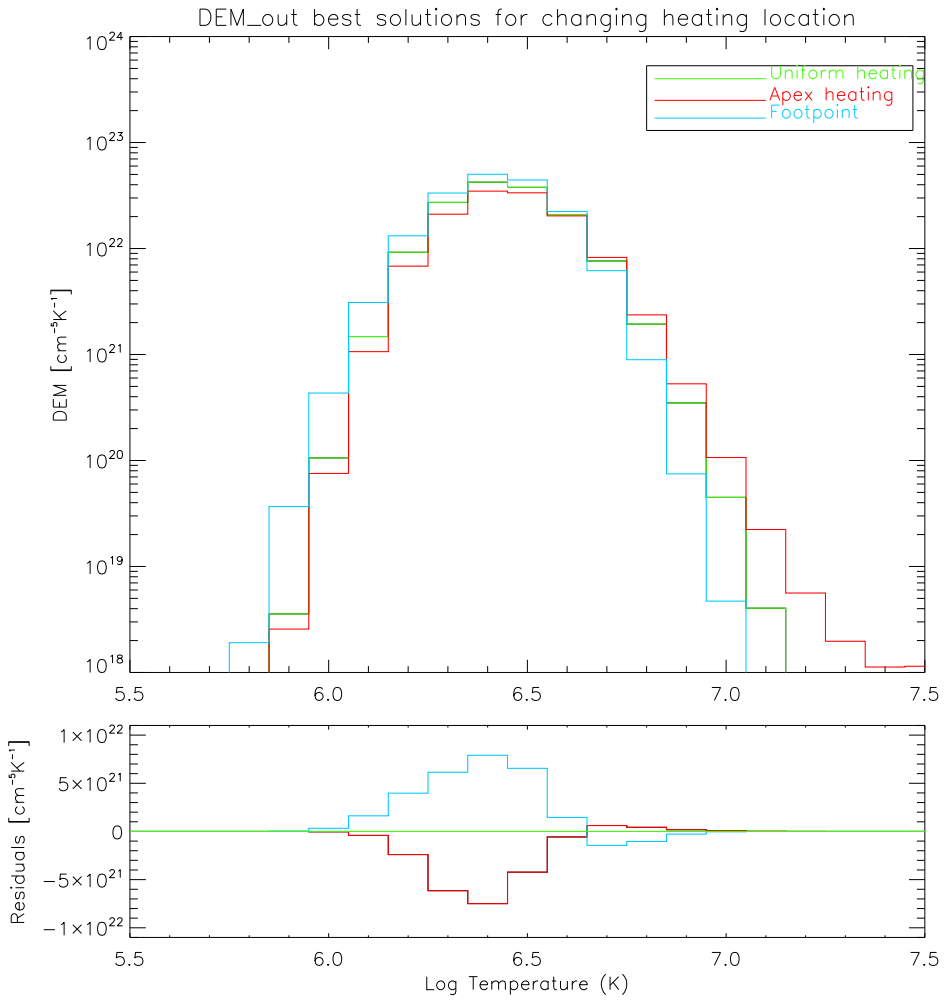

Figure 5.24: Plot showing the shift between the solution DEMs of different heating location. The top panel shows the three DEM_out solver solutions for the different heating locations while the lower plot shows the differences between the apex and footpoint case in comparison to the uniform case. The shift between the DEMs is clearly seen in the difference plot.

5.4.3 Following Investigation Ci changes: increasing total energy

Increasing the total energy of each simulation by an order of magnitude resulted in a very clear shift of the DEM_sim to higher temperatures. This result is also clearly observed in the solver solutions chosen as the best fit to the original DEMs.

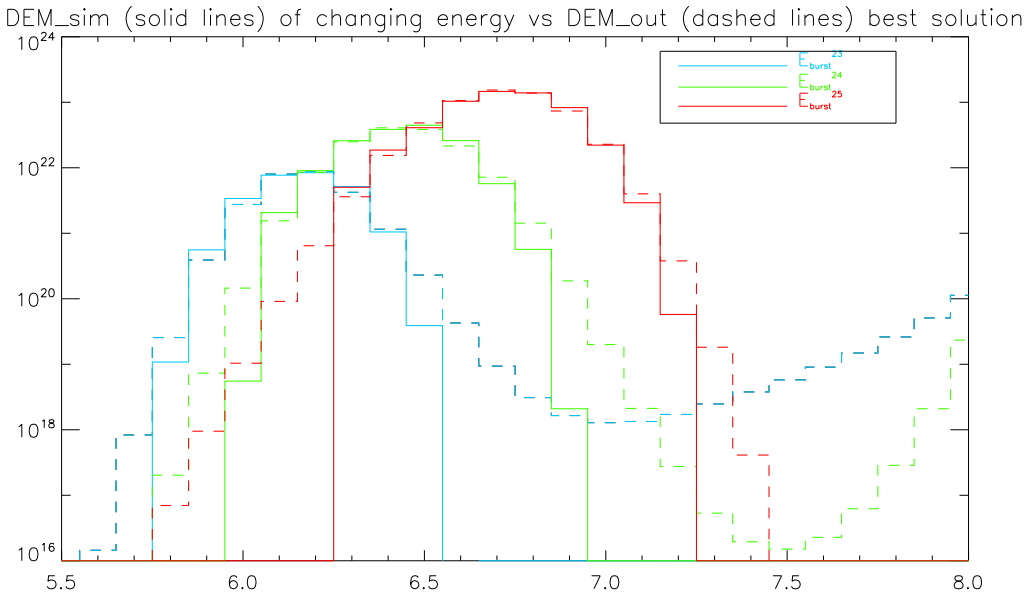

Figure 5.25: Plot showing the comparison between the original (solid lines) and solver solution (dashed lines) DEMs for increasing total energy.

Figure 5.25 shows the original DEMs for the three energy scenarios plotted (solid lines) with the corresponding solver solution DEMs overplotted (dashed lines). It can clearly be seen that the solver solutions match the peaks and widths of the original DEMs very well. The various Chi-square measurements of the fits are given in Table 5.8 where it can be seen that the values are all reasonably low and do not show any particular improvement either way as the total energy is changed.

This is due to the fact that the three original DEMs have the same level of smoothness and cover the same width in log(T) space meaning they are equally well reconstructed by the solver. The iterative solver does a very good job of reconstructing the DEM distribution and overall pattern in this case.

	E=10^{23}	E=10^{24}	E=10^{25}
Best sol.	1	70	0
$\chi^2_{gen2orig}$	0.4233	0.7358	0.3383
$\chi^2_{obs2gen}$	1.1388	3.4612	0.3383
χ^2_{DEM}	0.008627	0.9184	0.5199

Table 5.8: Comparison of goodness-of-fit improvement for DEM reconstruction of simulations of different total energy.

5.4.4 Following Investigation Cii changes: increasing number of nanoflares per strand

So far, the iterative solver has done an excellent job of following the various changes observed in the MSHD model DEMs as the parameter space is altered. In investigation Cii, changing the number of nanoflares per strand, whilst keeping the total energy of the simulation the same, resulted in the original DEM_sim significantly changing its width (see Figure 4.36). Many low-energy nanoflares per strand resulted in a very narrow DEM whilst a low number of high-energy nanoflares resulted in a very wide DEM.

Figure 5.26 shows the original DEM in each case overplotted with the best solver solution. It can be seen that the solver does quite well at matching the values of the 16 burst/strand and the 64 burst/strand scenarios although the Chi-square values are higher in the 16 b/s case than is ideal. However, for the 640 burst/strand case the solver solution DEM only matches the original DEM well in one bin. The original DEM is much taller and thinner than the solution DEM making it a poor match. This is also illustrated in the Chi-square values which are the highest values seen so far.

The extremely high Chi-square value of the fit between the original intensity and the solver intensity can be explained by looking at the I_{gen} values compared to the I_{obs} and I_{orig}. Figures 5.27 and 5.28 show the intensity distribution for the iterations which minimise the $\chi^2_{gen2orig}$ and $\chi^2_{obs2gen}$ value respectively. Even though these are the best solutions for intensity it can be seen that the values of I_{obs} and I_{gen} are far from each other and the mean in each case. This shows that this particular case has not been fitted well

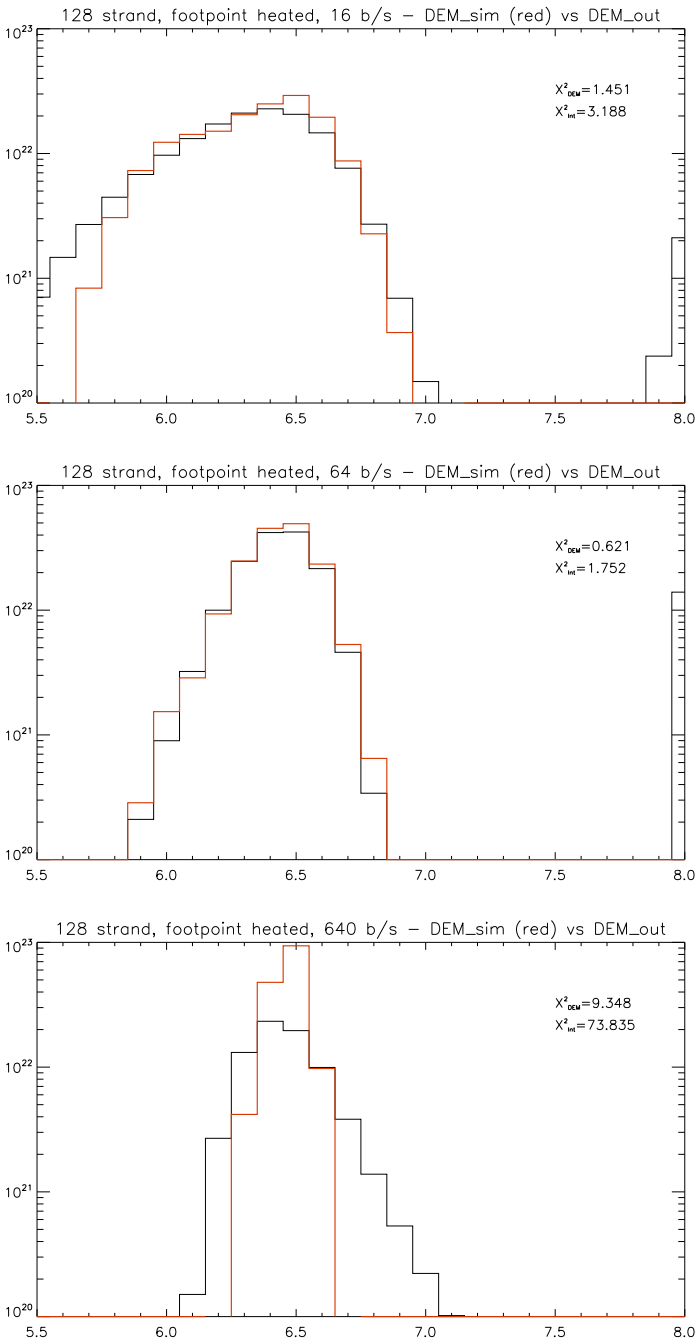

Figure 5.26: Plots showing the comparison between the original DEM (red) and the best solver solution (black) for increasing the number of nanoflares per strand.

as the value of I_{gen} is within 6σ rather than 1. This illustrates that the iterative solver doesn't perform as well when the DEM distribution being fitted only covers a few temperature bins. This is because there are less constraints available to shape the solver DEM and also because in this case the peak of the model DEM is at logT=6.5 which is a temperature where none of the AIA channels has a particularly strong sensitivity.

5.4.5 Following Investigation D changes: effect of heating loop then allowing to cool

Solver intensity values

By allowing the loop simulation to cool after a period of nanoflare heating, the intensity of the loop seen in each channel was seen to follow a specific pattern over time as the loop cooled through the various temperature sensitivities of the six AIA channels. By taking the I_{gen} values of the best solver solution at each timestep, the ability of the solver solutions to recreate this intensity pattern is investigated.

Figure 5.29 shows the results of this comparison where the intensities over time from the best solver solutions are plotted as dashed lines and compared to the original intensity values (solid lines). It can be seen that the solver solutions accurately match the peaks and rise/fall timescales for each channel.

Solver DEM distribution

As discussed in the case study, just because the intensity values match well does not mean that the DEMs will necessarily be a good match too. Figure 5.30 shows the match between the original model DEM (red line) and the best solution of the iterative solver (black line) at eight timesteps over the course of the loop cooling time. Note that the time the heating stops is t=4310s after which the DEMs are observed to move to lower temperatures as the plasma cools and drains. Movies of the evolution of the model DEM

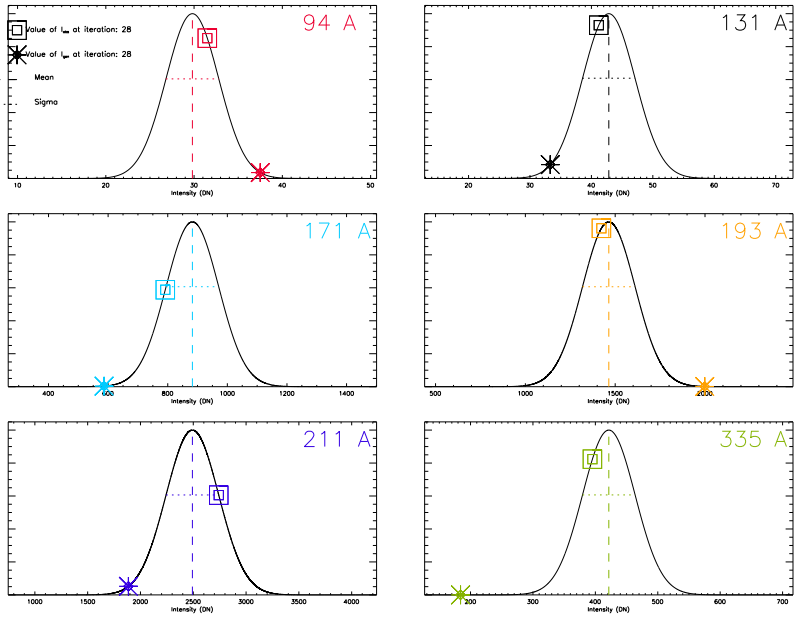

Figure 5.27: Gaussian distribution of intensity values for the 640 burst/strand scenario. Showing results for iteration 28 which has the minimum $\chi^2_{gen2orig}$ value. It can be seen that even though this is the example with the best fit of I_{gen} ($*$) to the original intensity values (peak of distribution), the values of I_{gen} do not fall within 1σ of this peak.

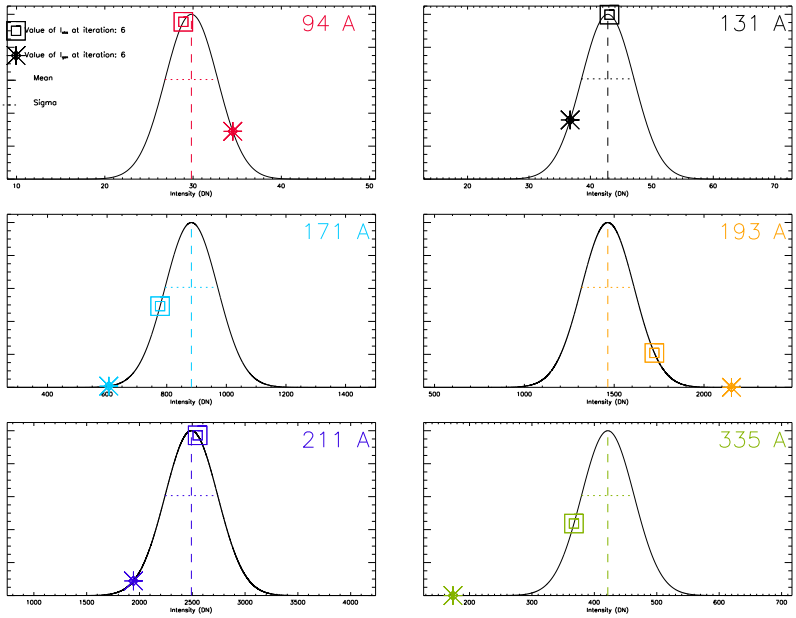

Figure 5.28: Gaussian distribution of intensity values for the 640 burst/strand scenario. Showing results for iteration 6 which has the minimum $\chi^2_{obs2gen}$ value. This iteration represents the case where the I_{obs} and I_{gen} values are the closest to each other. However, it can be seen that they do not match one another well.

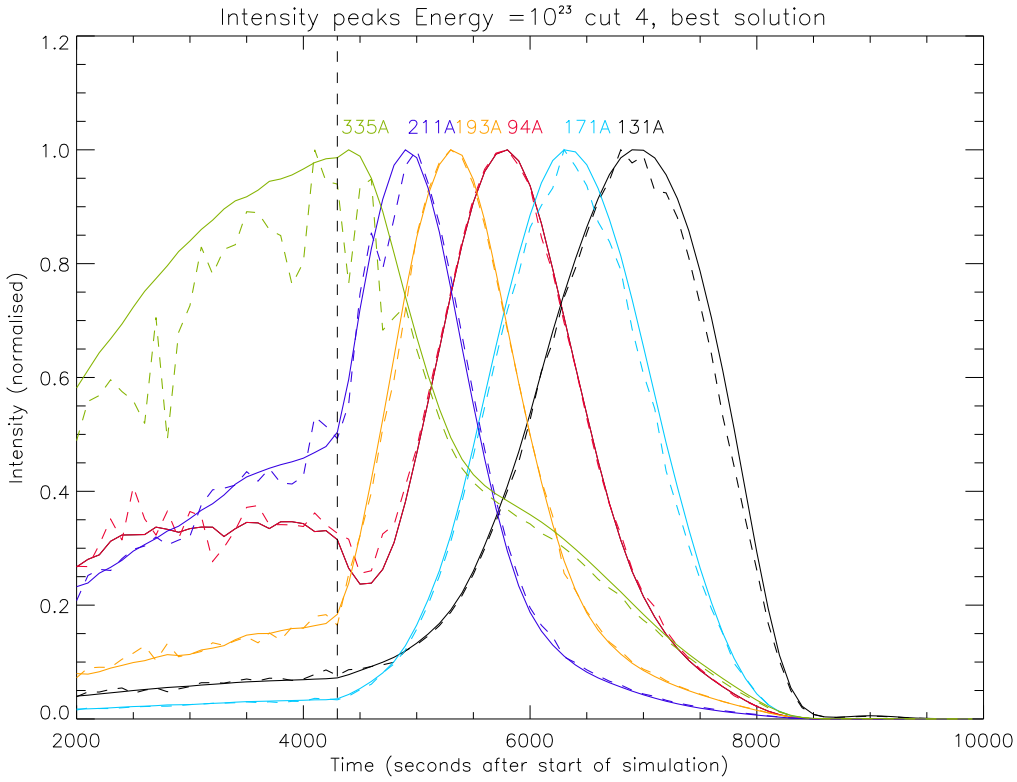

Figure 5.29: Figure showing the comparison between the original intensity values (solid lines) in each channel and how they change as the loop cools over time, and the intensity from the best solution of the solver (dashed lines). This plot is for the E=10^{23} ergs energy scenario but is representative of the other two energy cases which show a similar comparison.

compared to the corresponding set of solver solutions are listed in Table 5.9.

Movie name	Energy case (ergs)	Loop position examined
DEM_sol_e23.mov	E_{burst}~10^{23}	whole coronal loop
DEM_sol_e24.mov	E_{burst}~10^{24}	whole coronal loop
DEM_sol_e25.mov	E_{burst}~10^{25}	whole coronal loop

Table 5.9: List of movie names and the energy scenario they refer to. Each movie depicts how the MSHD model DEM compares to the calculated set of iterative solver solutions as the loop cools over time.

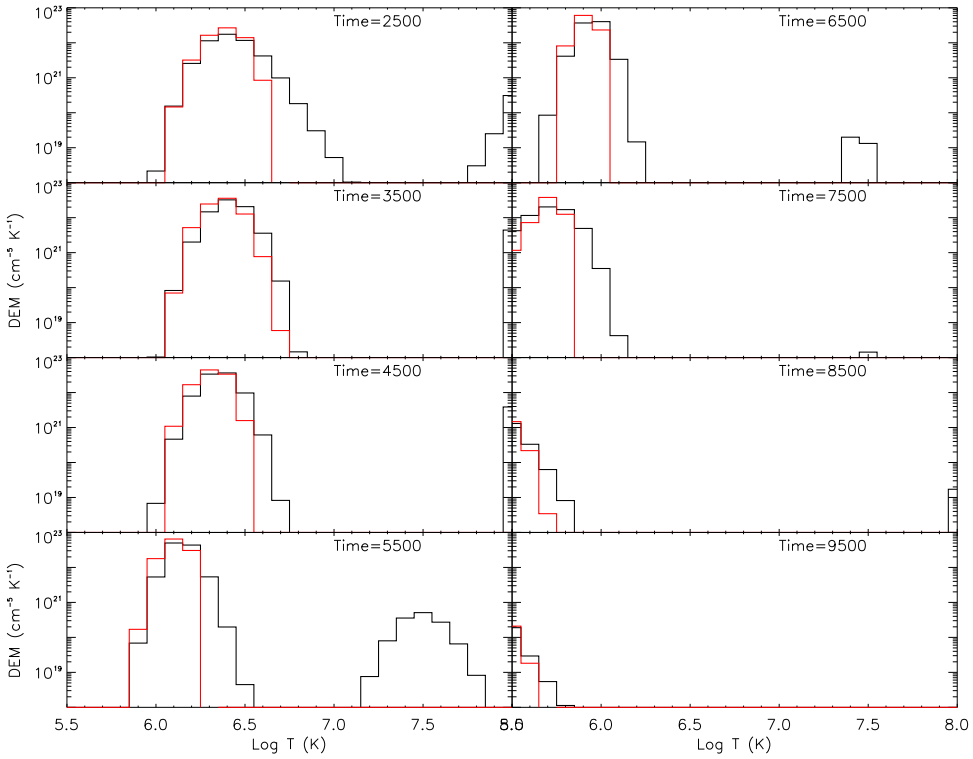

Figure 5.30: Figure showing the comparison between the original DEM (red) and the solver DEM (black) at eight timesteps as the loop cools over time.

It can be seen that the solver DEMs closely follow the movement of the original DEMs but that in some cases there are differences in the solver DEMs width and high temperature contribution. This peak is most apparent in the t=5500s plot in the bottom-left corner of Figure 5.30. It should be noted that this contribution is exaggerated due to the log plot on the DEM scale and is in fact two orders of magnitude lower than the DEM peak.

In Investigation D, the peak temperature position of the original DEMs was seen to closely match the emission measure weighted temperature as the plasma cooled (see Figure 4.47). This change is also seen when the peak temperature position of the solver solution is tracked over time as shown in Figure 5.31.

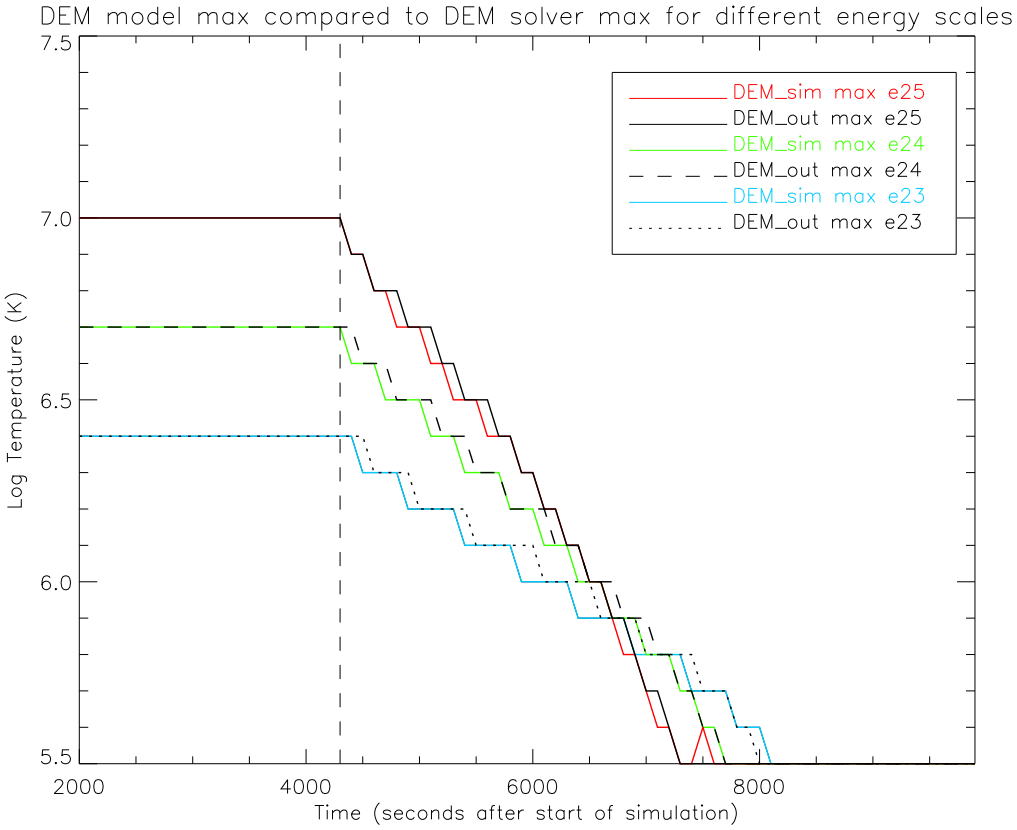

Figure 5.31: Temperature position of solver DEM_out peaks compared to the original DEM_sim. Both values are seen to closely match.

This plot shows the decline of the peak temperature position of the DEM over time for both the original DEM_sim (coloured lines for the three different energy scenarios), and the solver DEM_out (black lines with different styles for the different energy scenarios). It can be seen that the solver solutions match the original values very closely and would therefore also follow the emission measure weighted temperature decline. This shows that the solver DEMs can be trusted to accurately follow the declining temperature of the plasma in a cooling loop. The DEM_sim's in this case are based on cuts of the model data of 100 seconds (although over the entire length of the loop) which suggests that one need not necessarily have to average over 1000's of seconds of data in order to

get a good fit from the solver code.

5.5 Summary

This chapter has looked in detail at the issues involved in comparing simulation outputs (in terms of intensity and DEM distribution) with the solutions offered by an iterative DEM solver code.

The detailed case study performed has highlighted the various ways in which the goodness-of-fit can be defined and used to find the best solver solution. This is a step forward in terms of quantifying how good one DEM fits another and illustrates that simply plotting one over the other and looking at the visual fit is not good enough.

It has also showed that the 'best' solution in terms of intensity and DEM reconstruction was in general neither the first solution (i.e., iteration 0) or the iteration with the minimum value of Chi-square (as defined by the solver output keyword). This reinforces the importance of calculating the various goodness-of-fit measures described in the case study.

Using the different versions of the MSHD model as a series of synthetic observations, the effectiveness of the iterative solver was tested. In the majority of cases the solver was found to provide solutions which very closely reconstructed the original model intensity and DEM values. The best solution in most cases was also easily identifiable at an early stage i.e., when comparing the reconstructed intensity values. There were no examples where the best solutions for reproducing intensity did a poor job at reconstructing the DEM distribution. Each of the solutions identified as the best for intensity also did a good job at fitting the DEM.

This suggests that using the solver and picking the best solution based on the method described in the case study, will give an accurate reflection of the true DEM distribution.

The only case where the solver did not manage to accurately reconstruct the original intensity values or DEM distribution was the case where the model DEM was very narrow. This suggests that the solver is best suited to observations that are not isothermal i.e., have contributions from multiple wavelengths representing a range of temperature.

Chapter 6

Investigation of an Erupting Polar-Crown Prominence

This chapter explores a different type of coronal feature to other chapters - solar prominences. A case study of an eruptive polar-crown prominence observed by SDO and STEREO is analysed with particular focus paid to the possible eruption onset mechanisms. This chapter aims to investigate the structure and pre-eruptive rise of the prominence and its associated cavity by using observations from two points-of-view (SDO/AIA and STEREO-A/SECCHI/EUVI). Following this, the eruption itself is studied and various potential "trigger" mechanisms explored.

The first part of this work was done in collaboration with Stephane Régnier and was published in Régnier, Walsh & Alexander, 2011 (see Appendix for a copy of the paper). Réngnier was the lead on this paper and his work involved the initial observations with AIA where the structure of the prominence was studied, and a basic measure of the prominence eruption speed. This chapter takes this work further by including STEREO observations, a more accurate measure of the eruption velocity and an investigation of the eruption initiation methods. Any figures taken or adapted from the paper have been clearly identified as such.

6.1 Introduction to Solar Prominences

One of the most important areas of solar physics research today concerns the nature of solar eruptions. Observationally, these eruptions manifest as solar flares, prominence eruptions, and coronal mass ejections (CMEs) and are seen to differ in structure and duration (see Section 1.2.2). However, much work has been done to identify the association between these features as they are believed to be physically related. Munro et al. (1979) used the white-light coronagraph on Skylab to investigate 77 CMEs and their associated solar activity over the period 28 May 1973 - 3 Feb 1974 (during solar minimum). The associations of these CMEs with flares and eruptive prominences (EPs) is presented in Table 6.1. Out of the 77 CMEs observed, 34 could be associated with surface phenomena on the solar disc but the remaining 43 could not. Assuming that half (~38) of the observed CMEs originate from the far-side of the Sun, this suggests that a very high percentage of near-side CMEs are associated with surface phenomena (i.e., 34/38 = ~90%). The majority of these surface phenomena have an eruptive prominence component (~70%) which supports the idea that prominences are the pre-eruption component of CMEs and not a separate class of eruptive event.

Event	% of CMEs associated with event
EP only	~50
EP with flare	~20
Flare only	~20
No event	~10

Table 6.1: CME association with other solar activity. Based on results from Munro et al. (1979). EP - eruptive prominence.

Webb & Hundhausen (1987) followed up this work by observing 58 CMEs with the HAO Coronagraph on the Solar Maximum Mission satellite during the period between March - August 1980 (during solar maximum). This work studied the same associations at a different point in the solar cycle and confirmed the previous result. They noted that the high incidence of CMEs associated with EPs is most likely *underestimated* due to difficulties in observing eruptive prominences compared to flares. This underestimation

also comes from the inability of both studies to correct for 'backside' CME associations i.e., CMEs being released from the opposite side of the Sun will be included in the survey, but any prominence component present will not be observable whereas associated flares are more likely to be detected as unresolved X-ray emission. Webb & Hundhausen (1987) also disagreed with the idea that isolated CMEs i.e., those where no prominence or flare component is observed (such as the 10% in Table 6.1), are a separate class of CME as was suggested by Wagner (1984). Webb & Hundhausen (1987) propose that CMEs designated as "isolated" are either too low in energy for a clear association to be observed or are misplaced backside events.

CMEs are the main drivers of space weather so understanding their onset mechanisms and how to predict them by observing the pre-eruption corona is of great importance. Eruptive prominences have proved to be a vital component of most, if not all, CMEs and offer a clear view of the beginning of these eruptions. An understanding of the structure and dynamics of solar prominences is therefore necessary in order to gain a fuller understanding of solar eruptions.

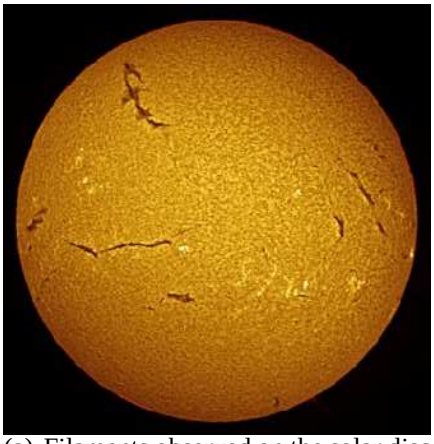

(a) Filaments observed on the solar disc

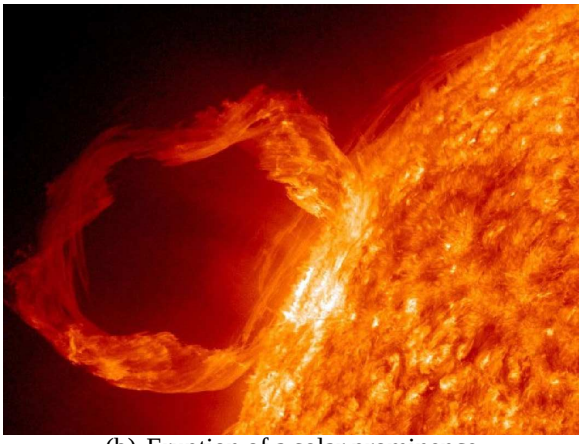

(b) Eruption of a solar prominence

Figure 6.1: Figure (a) shows an image of the solar disc taken with an Hα filter[1]. The dark lines on the disc indicate the locations of various filaments while Figure (b) shows one of SDO's 'firstlight' images of an erupting prominence taken with the AIA instrument in the 304 Å channel.

Solar prominences are long structures, suspended within the solar atmosphere, that are

[1] Amateur image taken with an Hα filter. Credit Jack Newton, Arizona Sky Village.

characterised by relatively cool, dense material which is held in place by the magnetic structure surrounding it. Some authors consider the material alone to be the "prominence" but here the term prominence refers to both the material and its surrounding magnetic field structure. They are an interesting coronal phenomenon as they are typically 100 times cooler and denser than the surrounding corona (Labrosse et al. 2010). The term "prominence" can be used interchangeably with the term "filament" as both refer to the same feature seen from different points of view. Filaments are observed projected against the solar disc where they are primarily seen in certain absorption lines such as Hα (see Figure 6.1(a)). Prominences, on the other hand, are the same feature when observed above the solar limb and can be observed in many wavelengths. In particular, the He II line at 304 Å allows us to examine prominences very well in EUV (as shown in Figure 6.1(b)) as it has a $LogT_{max}$(K) = 4.9 which is close to the characteristic prominence temperature of T = 10^4 K (Labrosse et al. 2010).

The term prominence is quite general and can be used to describe a range of different structures. As well as distinguishing between line-of-sight effects ("prominence" vs "filament"), the term prominence can be further constrained by the dynamics of the structure leading to the terms stable, eruptive, active, and a sub-type known as "disparation brusque" (sudden vanishing) which refers to a type of prominence eruption where the structure breaks up and is no longer identifiable. The different prominence classifications are discussed by Gilbert et al. (2000) who went on to clearly define the different between "active" and "eruptive" prominences. They make it clear that a prominence can be active without erupting and define an erupting prominence to be one in which all or some of the prominence material is observed to be ejected outwards and to escape the Sun's gravitational field. Active prominences, on the other hand, are described as having notable motions but do not result in any part of the prominence escaping the solar atmosphere.

A distinction is also made using the location of the prominence to describe them as either active-region or quiet-region prominences. A common trait that all prominences

share is that they are nearly always found over Polarity Inversion Lines (PIL). This is defined as a region where the magnetic field direction changes from one polarity to another i.e., between areas of neighbouring positive and negative polarity. Such areas are found in active regions, around Sunspots, and around the areas of open magnetic field at the polar regions. Quiescent prominences are long-lived (days to months) and tend to be found in quiet-Sun areas. These prominences are usually larger than ones seen around active regions and have typical dimensions of 60–600 Mm in length, 15–100 Mm in height above the chromosphere, and are 5–15 Mm thick (Tandberg-Hanssen 1995). Active region prominences tend to be smaller (of order 10Mm), are found lower in the atmosphere (<10Mm) and can usually be found threaded through or curved around an active region (Mackay et al. 2008). They are observed to have rapid flows along the structure and can change in structure dramatically over short periods of time (minutes-hours) compared to their quiescent counterparts.

6.1.1 Formation and Structure

It is safe to say that although these types of prominence differ in size, dynamics and location, they share a common composition. Material of chromospheric temperature and density being located at coronal heights has been a challenge to explain, particularly the structure of the magnetic field supporting these structures.

The basic structure of a prominence consists of a long spine structure which runs parallel to the solar surface. Protruding from this central structure are features called barbs which appear to link (or tether) the prominence to the chromosphere and are observed to be composed of multiple threads (see Figure 6.2). Some prominences, most commonly large quiescent prominences, are also observed with a coronal cavity component such as that seen in the right panel of Figure 6.3. Cavities can be defined as areas of depleted density in the corona and are also associated with CMEs in the classical three-part structure of core, cavity, and front, shown in the left panel of Figure 6.3. These cavities are

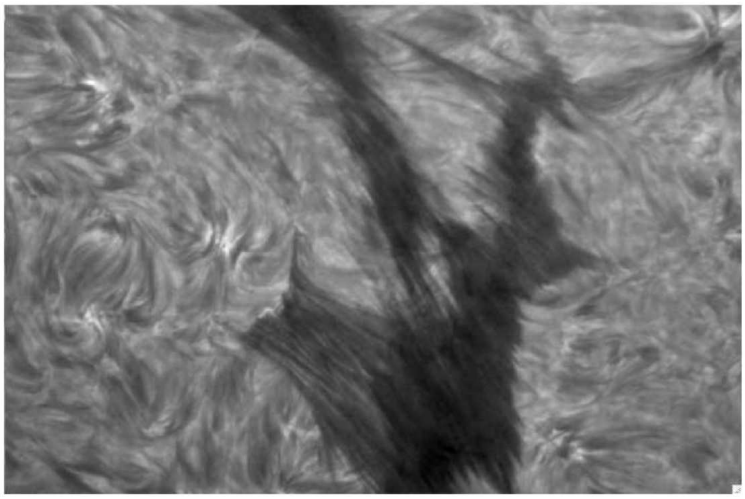

Figure 6.2: Prominence barbs seen in Swedish Solar Telescope high resolution Hα image (from Lin et al. 2005). The barbs are the thread-like dark structures seen in the middle of the image.

often modelled as the centre of a magnetic flux rope which is subject to some sort of instability causing it to rise up and be ejected. In CME models it is not clear if this flux rope exists in the pre-eruption corona or if it is formed during the eruption process. Quiescent flux ropes can be used to explain prominence and cavity observations from a theoretical point of view and are supported by observation.

The magnetic structure of prominences is a key question that both observers and theorists are trying to solve. Many models (such as Kuperus & Raadu 1974) represent the internal structure of the prominence as a flux rope which remains stable within an overlying magnetic field due to the balance between the upward acting magnetic tension (due to the curvature of the field lines) and the gravitational force acting downwards on the mass of the prominence material. This material is shown in Figure 6.4 where the prominence configuration can be seen from two points of view. The twisted magnetic flux rope seen in the lower panel of the figure, supports the prominence material in the dips of the field lines. The prominence should remain in equilibrium until some internal or external factor causes one force to win out over the other leading to the prominence

[2]Left image taken with High Altitude Observatory/Solar Maximum Mission coronagraph. Middle image taken at National Center for Atmospheric Research/High Altitude Observatory Newkirk White-Light Coronal Camera (WLCC) telescope.

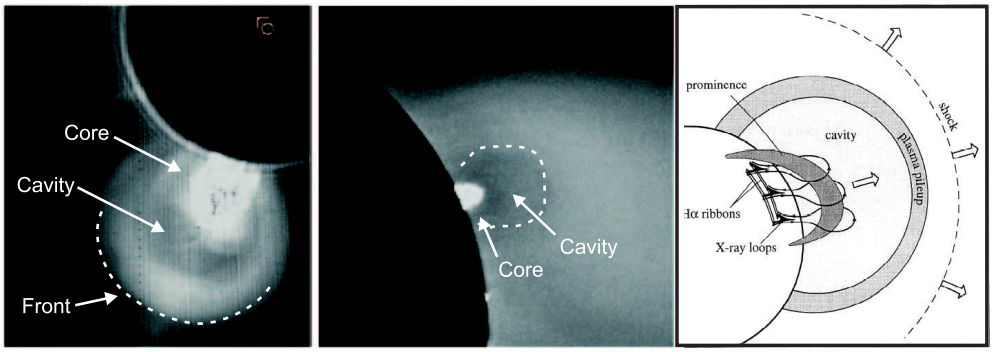

Figure 6.3: Image from Gibson et al. (2006) of two coronal cavities seen in white light coronographs[2]. The left image shows the three-part structure of an expanding CME with its bright core, dark cavity and bright front, while the middle image shows a quiescent prominence and its surrounding cavity. This structure is explained in the right panel which shows a cartoon of the prominence cavity structure (Forbes 2000).

erupting or draining back to the chromosphere.

The way in which prominences form is another issue currently still under debate (Mackay et al. 2010). It is generally accepted that there are two main ways in which prominence material can be found in the corona: either cool material is injected upwards or coronal material condenses towards the surface. Observations of flows from the chromosphere up to the corona are well established (see e.g., Chae et al. 2000, and references within) and thus find in favour of the idea that prominences are formed by mass injection driven by chromospheric evaporation. On the other hand, proponents of the coronal condensation theory interpret the existence of a cavity as evidence that this area is the now-evacuated location of the coronal material that has cooled and settled in the magnetic field dips. This debate is still ongoing and only observing the magnitude and direction of these mass flows using high-cadence, multi-wavelength observations will settle it either way.

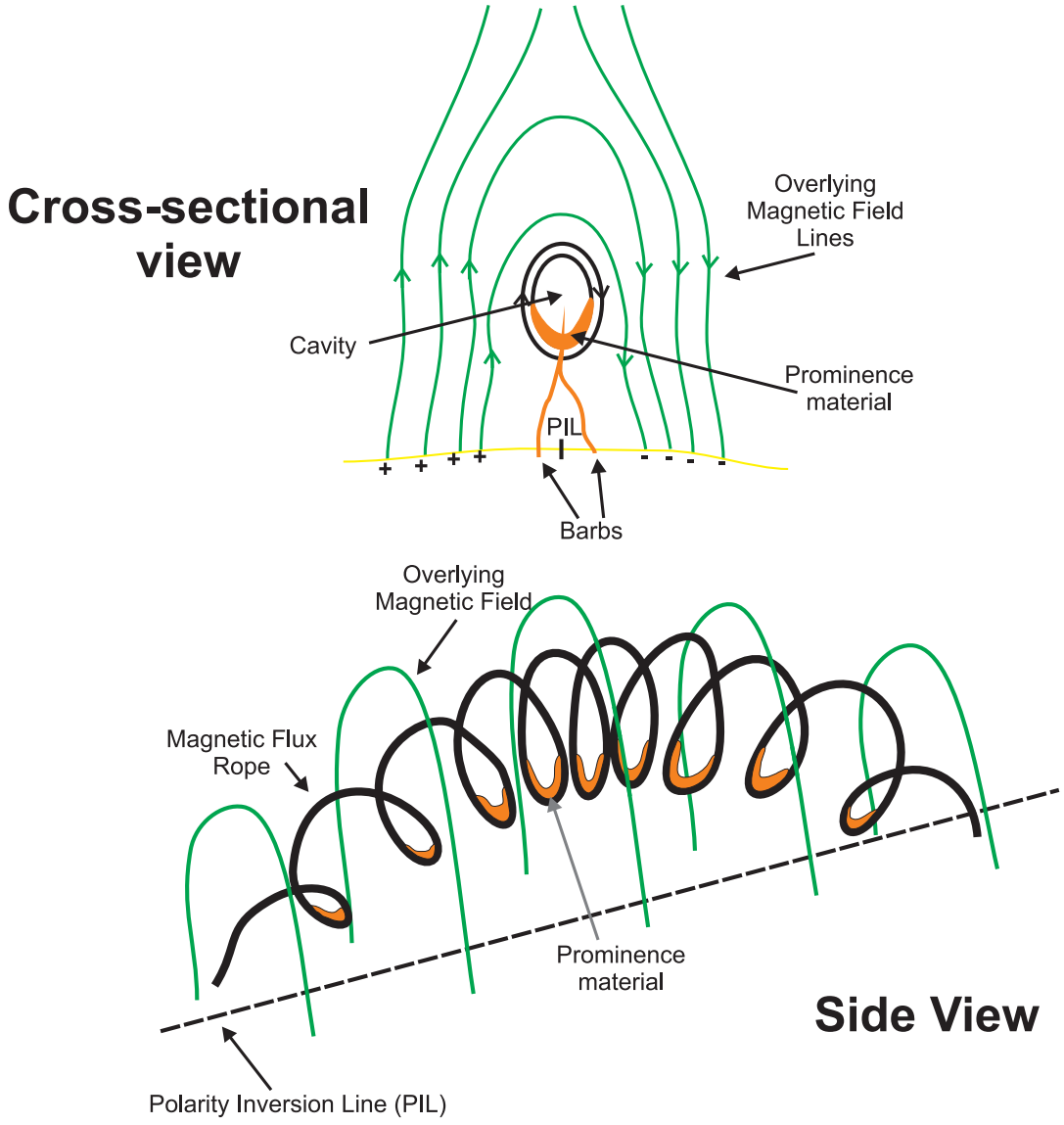

Figure 6.4: Sketch of prominence material and magnetic field line location. Top image shows cross-section through a prominence while bottom image shows the length of a prominence seen from the side.

6.2 Eruption of Prominences

Solar eruptions may be well observed, but their initiation processes and evolution are still not fully understood. Eruptions (in the form of CMEs, flares and prominences) can occur across the solar disc and are more numerous during times of increased magnetic activity i.e., around one CME every other day is observed at solar minimum compared with several per day at solar maximum (Gopalswamy 2006).

6.2.1 Energetics

A range of models exists to try and explain the varied set of observations there are of eruptive events. A leading model that encapsulates a lot of current ideas is named the CSHKP model (Carmichael 1964; Sturrock 1966; Hirayama 1974; Kopp & Pneuman 1976) after the authors that inspired it. The main components of this model are shown in Figure 6.5. This figure shows the magnetic consequences of a rising prominence at the start, maximum and end of an eruption. Figure 6.5(a) sets out the configuration of a rising prominence within an overlying magnetic field. The reason for the upward movement of the prominence (which is seen as a cross-section in this panel) is not vital to the model and can assumed to be due to one of the various trigger mechanisms described in Section 6.2.2. When the prominence comes into contact with the overlying field, magnetic reconnection will occur causing collapse from all sides. This reconnection occurs at the X-point marked on Figure 6.5b which is where the release of magnetic energy causes heating and particle acceleration to take place. This heat flows down to the chromosphere where it brightens and evaporates material. If the magnetic energies are high enough this process can cause a flare to be released. Otherwise the process will continue in the same way and the prominence will be accelerated upwards (Figure 6.5b' shows the side-view of the prominence eruption). Once the prominence is ejected the evaporated material can flow back down the loops legs as shown in Figure 6.5c. This

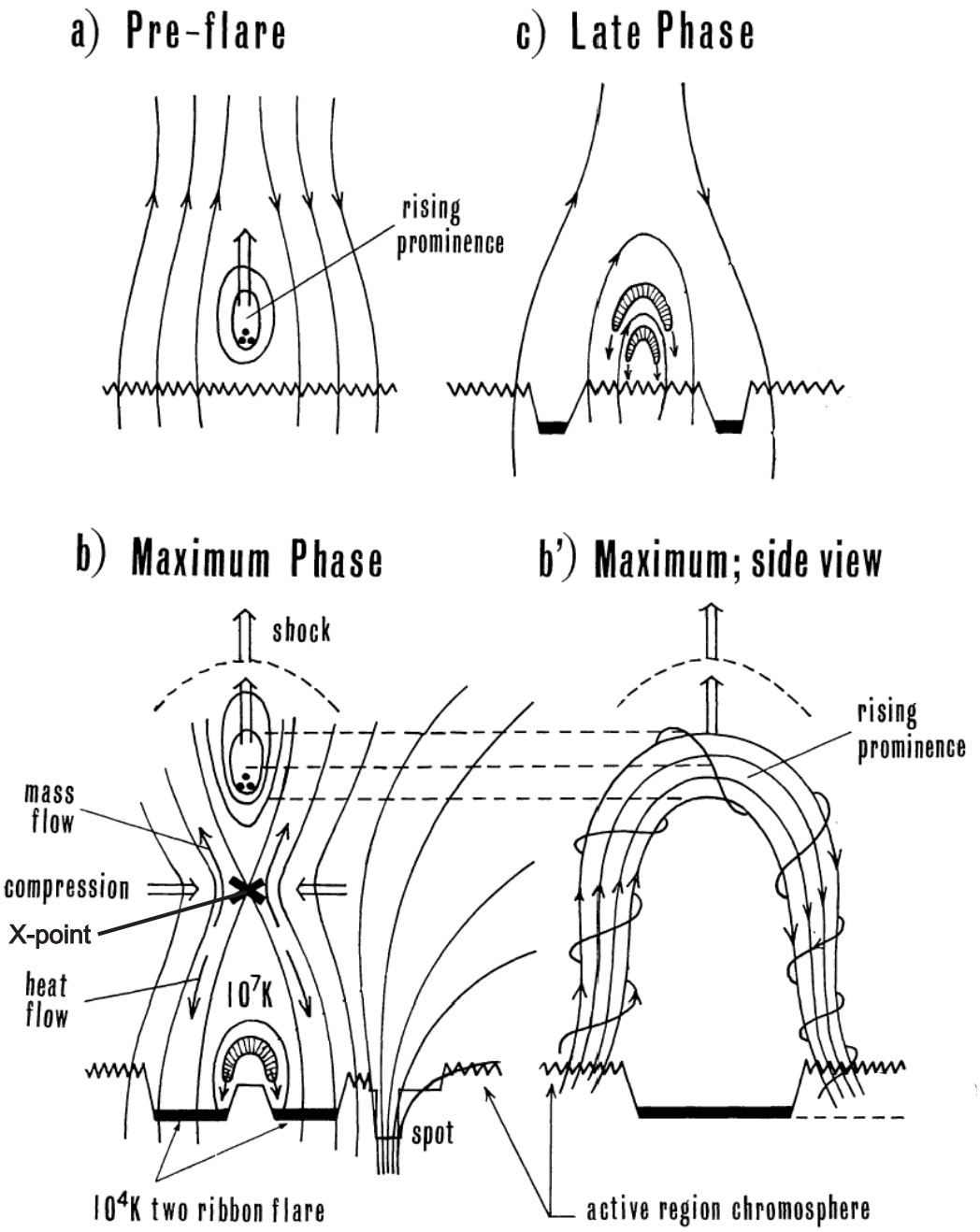

Figure 6.5: Cartoon depicting the main stages in the CSHKP model for eruptive events (Hirayama 1974). Panel (a) shows shows the initial stage where a flux rope is rising amongst overlying magnetic field. Panels (b) and (b') show the rising prominence from two points-of-view with magnetic reconnection occurring at the X-point in (b). Panel (c) shows the reorganisation of the magnetic system after the prominence has erupted.

is often referred to as the "standard model" as it explains various observations of solar flares and can also be applied to CMEs and prominence eruptions (see e.g., Shibata 1999, and references within).

Theoretical studies have suggested that when prominences become eruptive, the increase in velocity causes their radiative output to decrease (Labrosse et al. 2010) due to the Doppler dimming/brightening effect (Hyder & Lites 1970). Labrosse & McGlinchey (2011) have investigated this phenomena to see if this process can be used to investigate the plasma parameters of erupting prominences. They investigated four such prominences (one of which is the focus of Section 6.4) and found that in three cases they were able to measure a decrease in intensity with increasing velocity. However, when using their non-LTE model to explore this phenomenon further, they found that plasma conditions within the prominence (most particularly temperature and mass) play as important a role in changing intensity values as the velocity does, so their initial result may be misleading.

6.2.2 Onset Mechanisms

Most authors agree that a prominence eruption is caused when a flux rope experiences a perturbation leading to a loss of stability. The nature of this perturbation is still an open question with many mechanisms being put forward. Some of these "triggers" are discussed here.

Mass-Loading

Mass loading and off-loading are processes of mass transfer to or from a prominence and can both be eruption mechanisms. Changes in the total mass of the prominence material will undoubtedly lead to changes in its stability due to the force of gravity increasing or decreasing. For the mass loading scenario Wolfson & Dlamini (1997) and Wolfson & Saran (1998) found that an increase in prominence mass contributed to the stored magnetic energy of the structure, in some instances giving it enough energy to overcome the gravitational force keeping it down and erupt.

Alternatively, if the mass of the prominence decreases, this will compromise the balance between gravity and magnetic tension meaning that the prominence may start to move upwards. This motion will continue until the forces reach equilibrium again or, if too much mass as been lost, the prominence erupts outwards (Kuperus & Raadu 1974). Such a case was observed by Seaton et al. (2011) who measured material flowing down from a prominence structure that later erupted and caused a CME. They concluded that mass loss caused an initial rise of the prominence which in turn lead to reconnection which caused the structure to be accelerated upwards and ejected. In this case the mass loss was the eruption trigger but the authors note that they cannot comment on why the mass loss began in the first place.

Tether Release

Prominence "tethers" can be identified as overlying magnetic field lines which, alongside gravity, help to keep the prominence stable and combat the buoyancy of magnetic flux rope containing the prominence material. They are usually observed as barb structures such as those described in Section 6.1.1. There are various ways in which the loss of these tethers can lead to the eruption of a prominence. Firstly there is what is termed "tether-cutting" which is where the magnetic tethers are severed from the prominence due to magnetic reconnection below i.e., due to a flare or newly emerged magnetic flux (see e.g., Moore et al. 2001). Tether-cutting should be identifiable by observing the signatures of reconnection alongside evidence that the timing of this reconnection (such as a flare) coincides with the beginning of the upward motion of the prominence. In low energy events (such as one observed by Sterling & Moore 2003) the heating signature of reconnection may be lost in the background intensity. In this case the only evidence is in the timings of events but this will only support the tether-cutting model and not confirm it.

Another mechanism of eruption caused by tether activity is when a major tether no

longer holds down the prominence causing a loss-of-equilibrium which causes the other tethers to snap. This separate process of tether "straining" or "snapping" is used to refer to the instance where the tethers break due to the increase in the upward magnetic pressure. For example, if a tethered prominence experiences mass off-loading (as described above), the upward motion caused by the increase in buoyancy will increase the strain on the tethers causing them to lengthen and then snap.

Kink Instability

Eruption caused by a kink instability in the magnetic flux rope containing a prominence is a popular idea which has been well modeled and also observed. The left column of Figure 6.6 shows an observation of an erupting filament that has the signature helical shape observed in models of a twisted magnetic flux rope undergoing a kink instability. The right column shows a model by Török & Kliem (2005) which shows a remarkable similarity to the observations (Williams et al. 2005). Hood & Priest (1981) showed that a kink instability will occur when the twist of a flux rope (i.e., how tightly wound the magnetic field lines are) exceeds a critical value of around 2.49π. Once this occurs, the flux rope will rise exponentially (Török & Kliem 2004) as the kink expands outwards. Observationally, a kink could be induced in a flux rope due to the twisting motion of the prominence footpoints or a change in the intensity of the flux rope's electric current.

Other trigger mechanisms

The solar atmosphere does not consist of isolated structures. The inter-connectivity at work suggests that no system is unaffected by nearby activity (see e.g., Schrijver & Title 2011). This interaction of external factors can play a potential role in prominence eruptions. Nearby eruptions or active region activity could reasonably cause instabilities that could activate the rise of a previously steady prominence. This idea is explored in more detail in Section 6.5.3.

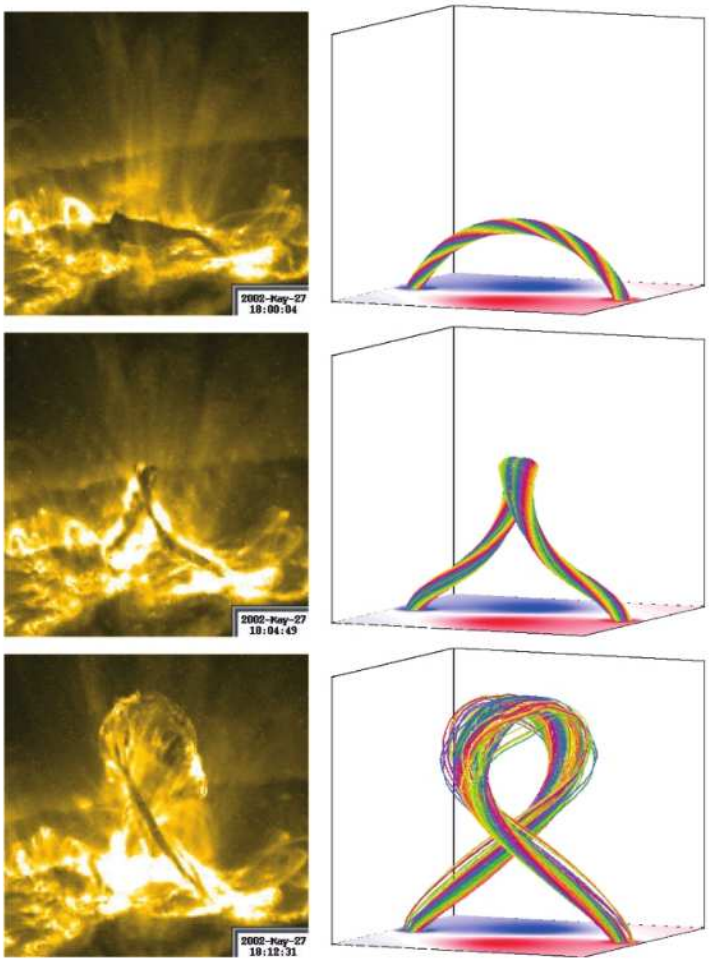

Figure 6.6: Series of images showing kink instability seen in both observations (left) of TRACE 195 Å and in a simulation of a kink-unstable flux rope (Figure from Török & Kliem 2005).

It is generally agreed that magnetic reconnection is necessary for the acceleration and release of most eruptive events. This does not seem to be the case for the polar-crown prominence discussed in Section 6.4 as no signatures of reconnection are observed. However, in a large number of other examples of eruptive events, reconnection plays a key part. It is unclear whether it can be the sole trigger of an eruption or if some other trigger (such as those described above) can upset the equilibrium which then goes on to cause reconnection and eruption.

In most cases it seems likely there is not a single trigger, but a combination of factors that leads to eruption. The trigger mechanisms described above are not extensive and

there are many more release methods in the literature e.g., the magnetic breakout model, photospheric shearing of the magnetic field, and MHD instability to name just three. The mechanisms discussed in this section are those thought to be important for the case study of an eruptive prominence investigated in Section 6.4. Evidence for and against the trigger mechanisms described above are presented in Section 6.5.

6.3 EUV Waves

The phenomena termed “EUV waves” may seem like a departure from the discussion of prominences but a short description is given here as these features are pertinent to the following sections.

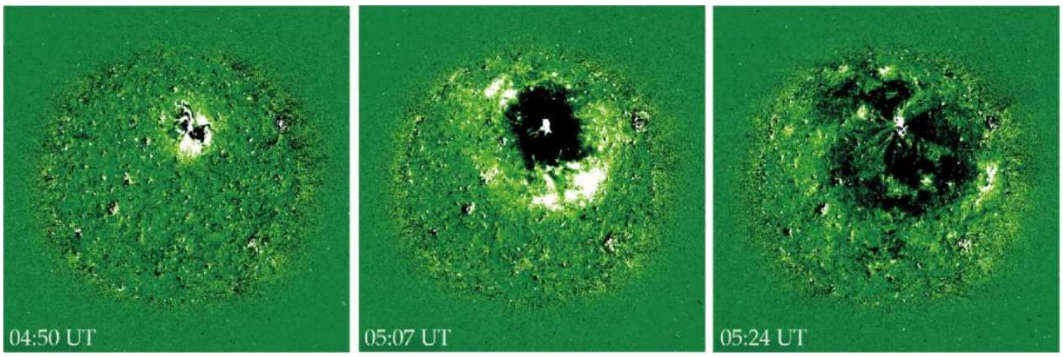

Figure 6.7: Example of EUV wave expansion seen in a running difference image. Adapted from Gallagher & Long (2011) and based on work by Thompson et al. (1998).

The Extreme ultraviolet Imaging Telescope (EIT) onboard SoHO first brought to light the existence of large-scale propagating intensity enhancements that were subsequently dubbed “EIT waves”. These features are associated with flaring active regions and CMEs and are observed as nearly circular intensity disturbances moving outwards from their source over the solar surface (see Figure 6.7). The velocities of these propagations cover a wide range and have been observed to have values between 100–700 km s^{-1} (Gallagher & Long 2011).

The term “EIT wave” has been replaced with “EUV wave” as they can be seen by any

EUV imager. As the name suggests, these features are mostly seen in 1-2 MK pass-bands although they have been associated with a chromospheric counterpart observed in Hα (Moreton & Ramsey 1960) and named "Moreton waves". Biesecker et al. (2002) studied the correlation between CMEs and EUV waves and found that all 173 waves they observed had an associated CME. This relationship was further cemented by Chen (2006) who studied examples of strong flares that had no CME component. They found that in these cases no EUV wave was produced suggesting a strong case for EUV waves being a CME-only phenomena.

The origin of EUV waves and their connection with CMEs has been a serious topic of debate in recent years with the various explanations falling into either wave or non-wave categories (see a review by Wills-Davey & Attrill (2009) and references within). A popular wave-based interpretation is that the eruption of a CME creates a fast mode MHD wave while the main pseudo-wave explanation suggests that the observed bright "wave" is created by magnetic reconnection from the expanding CME edges with the solar atmosphere. Patsourakos & Vourlidas (2009) disagree with this interpretation as they investigated an EUV wave using STEREO and found that the dual points-of-view and high cadence helped them to separate the CME component from the wave component. This allowed them to observe that both components evolve separately and thus that EUV waves are most likely a fast mode MHD wave phenomenon. This debate is still ongoing with strong proponents on both sides. Only high-cadence, multi-wavelength observations from multiple points of view will settle it either way.

6.4 13 June 2010 Prominence

As previously mentioned, prominences and filaments are the same structure observed from different points-of-view. Different types of observation (i.e., white light, Lyman-α,

Hα, Ca II H and K, and EUV filters such as He II 304 Å) can reveal different morphologies. It is advantageous to observe a prominence both on-disc and off-limb in order to fully investigate its structure. In the past this had to be done by waiting for the structure to rotate from the East limb to the centre of the disc or from the disc out to the Western limb. This rotation can take up to a week so crucial details in the fast evolving structure are lost.

The launch of the STEREO satellites in 2006 opened up a new way of viewing the Sun by giving scientists two new points-of-view: three when combined with instruments at Earth and the L1 point e.g., SDO, SoHO and ground based observations. These satellites, in combination with SDO, allow us to view prominences on-disc and on-limb simultaneously. Unfortunately STEREO lacks a magnetograph or the ability to image in Hα (items crucial for a full analysis of a prominence) but its two EUVI instruments can observe in four passbands that are comparable with AIA. The cadence and resolution have lower values (see Chapter 2) but the data can still give important information about the structure and evolution of the prominence.

By combining observations from SDO and STEREO we can take advantage of the different perspectives they offer and use a data set that is unprecedented in terms of coverage and spatial resolution, in order to study an erupting prominence in detail.

6.4.1 Observations of the polar-crown prominence

This section presents a case study of an eruptive polar-crown prominence, such as those discussed in Section 6.1. The data set examined here were taken on the 13 June 2010 utilising both STEREO-A/SECCHI/EUVI and SDO/AIA.

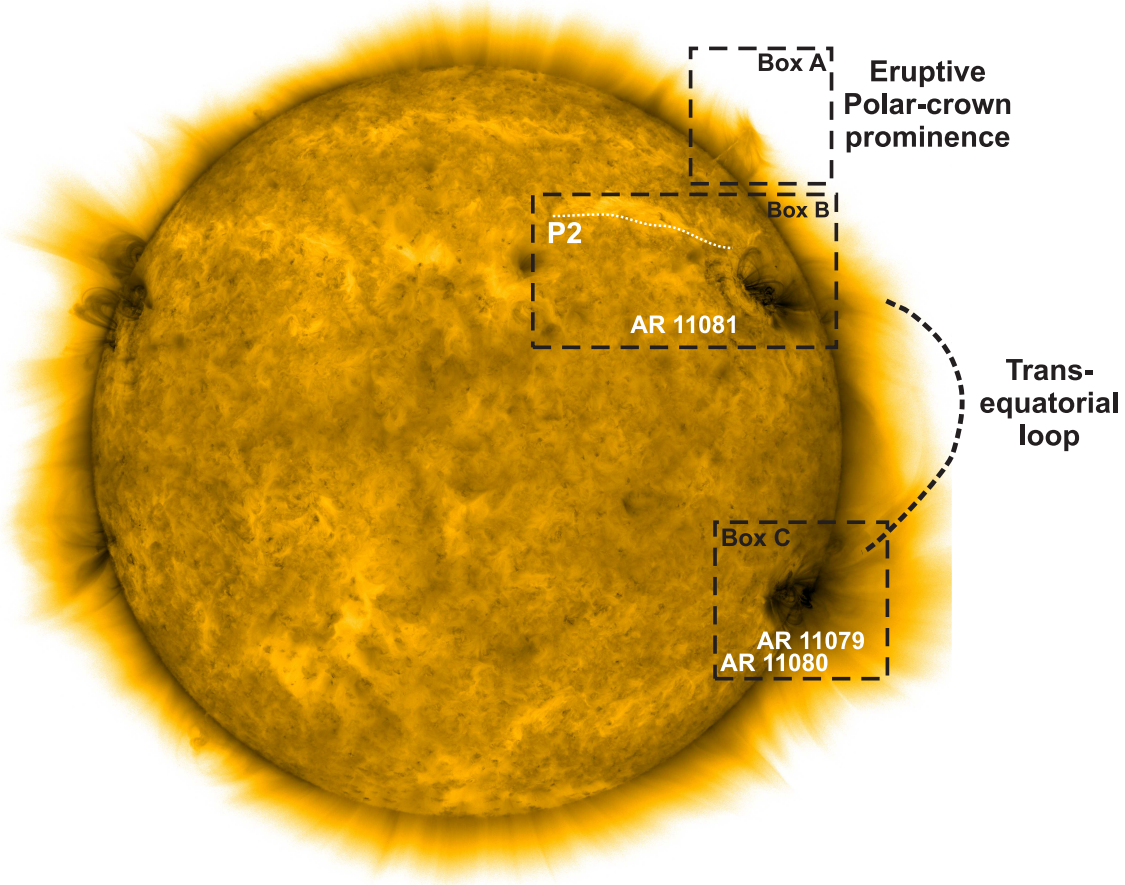

Figure 6.8: SDO/AIA 171 Å full-disc full-resolution negative intensity image showing the beginnings of the prominence eruption. The polar-crown prominence area is in Box A where the prominence barbs and an unusual U-shaped configuration of plasma can be observed more closely in Figure 6.9. Box B contains an area of nearby activity (AR 11081 and a second prominence P2) which is discussed further in Section 6.4.2. Box C shows an area of the Southern hemisphere where two side-by-side active regions are seen. This area is discussed in Section 6.4.2 and 6.5.2.

SDO/AIA multithermal observations

The prominence was observed on the North-West limb of the Sun as seen by SDO/AIA (see Figure 6.8) where it was identified as a polar-crown prominence with an associated cavity. Over the hours 00:00 to 12:00 UT this prominence was observed to slowly rise before erupting outwards as part of a CME. Over this time period, full-resolution data in four of the AIA passbands were utilised at a reduced time cadence of 3 minutes (instead of the high cadence 12 second data). This reduction was made to make the data-handling more manageable.

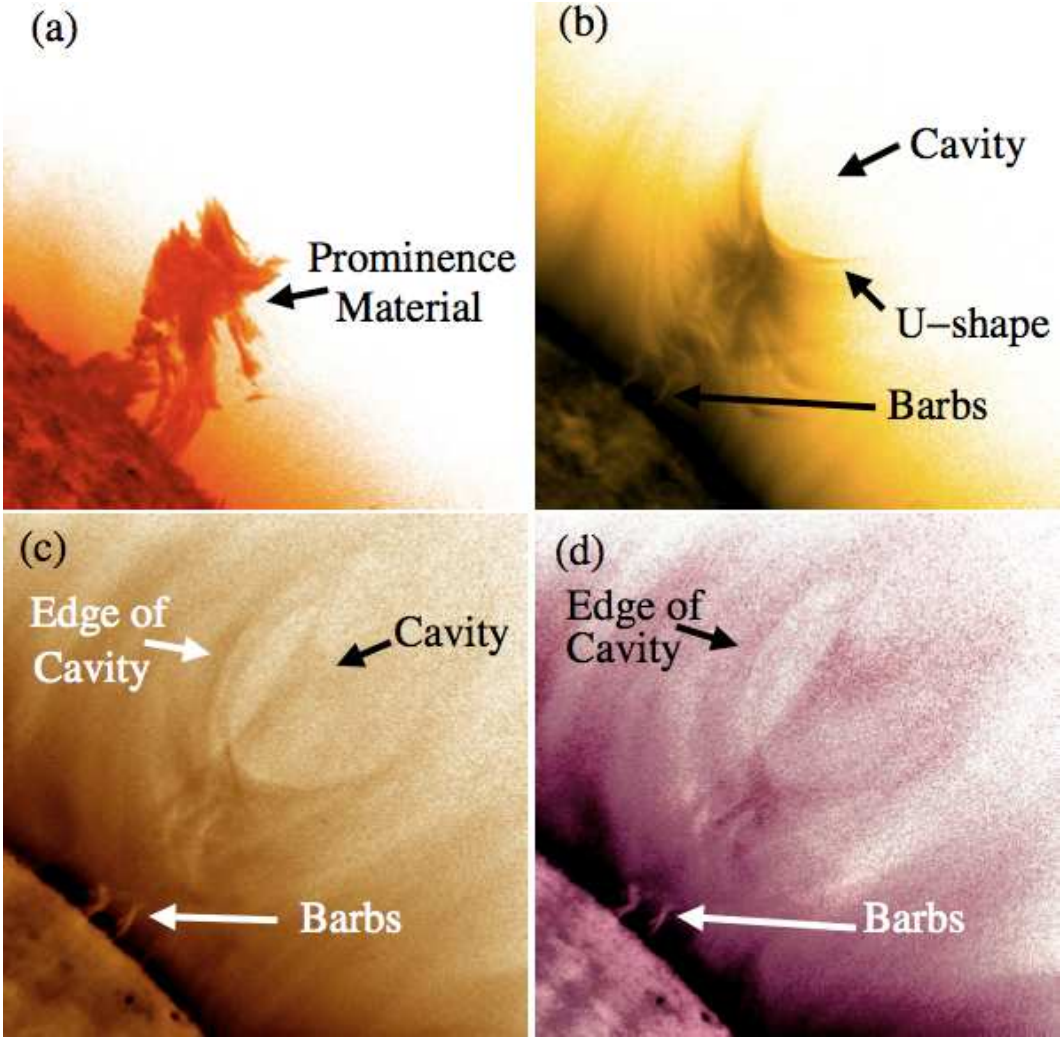

Figure 6.9: Off-limb close-up of the prominence structure observed by SDO/AIA in different wavelengths (a) 304 Å (b) 171 Å (c) 193 Å (d) 211 Å with the different structures labelled (negative image). The field of view is that of Box A in Figure 6.8. Figure from Régnier, Walsh & Alexander, 2011.

The structure of the prominence during the eruption can be seen in Figure 6.9 where the four passbands reveal different parts of the structure. Figure 6.9(a) shows cooler chromospheric material in He II at 304 Å (T~50,000 K) where the mass of the prominence above the solar limb is clearly seen. The top of this material has a slight U-shaped curvature that is confirmed in Figure 6.9(b) which shows Fe IX at 171 Å (T~0.6 MK). The structure of the cavity is now clearly apparent with the prominence material lying along the dipped magnetic field lines, leaving a cavity above. This area of depleted density, as well as two barb structures seen connecting the prominence to the solar limb, are also seen in Figures (c) and (d) which show Fe XII at 193 Å (T~1.6MK) and Fe XIV at 211 Å (T~2MK) respectively. The temperatures stated here are based on the instrument response function (shown in Figure 2.13).

Due to the observation date of 13 June 2010, only Level 1 "test" series data were available. This means that the data were corrected for bad pixels, spikes, jitter and pointing effects but the calibration was an early approximation. This shortcoming does not affect this study as the AIA data here have been used to study structure and not to make quantitative analyses of the intensity.

STEREO-A/EUVI observations

Whilst the SDO/AIA data set of the eruption event is high in both resolution and cadence, the single point-of-view of the SDO spacecraft can lead to difficulties when trying to interpret the 3D evolution of the structure located on the limb. With this in mind the position of the STEREO-A spacecraft was checked and found to be in a good vantage point for the eruption at this time (see Figure 6.10). Only EUVI data in the passbands 304 Å and 195 Å were abundant over the time range of the eruption and even then the time cadence was reduced compared to SDO (at around 5 minutes). The spatial resolution of these data is 3.2" (Aschwanden et al. 2008) compared with the superior ~1" resolution of AIA. The STEREO data was processed within the standard SSWIDL

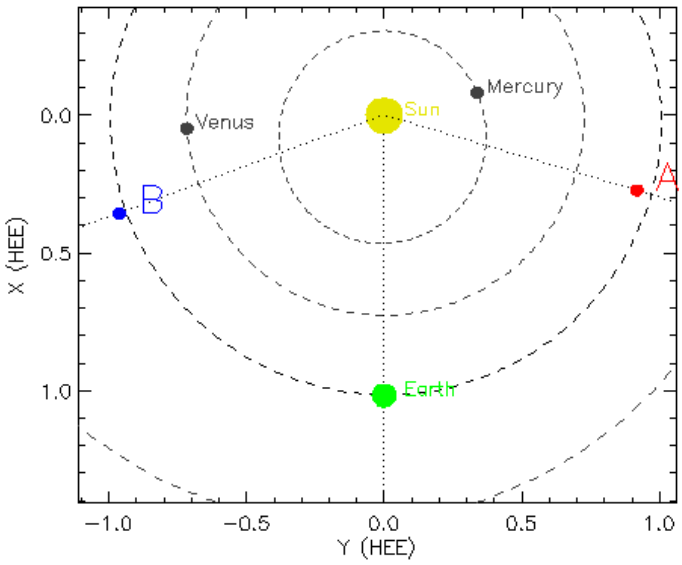

Figure 6.10: Sketch showing the relative positions of STEREO-A and B to the Earth and the Sun on the 13 June 2010 at 00:00 UT. The Ahead satellite is at a 74° separation from Earth while the Behind satellite is at a 69° angle.

routines using SECCHI_PREP.

STEREO-B was located round the other side of the Sun and only observed the very end of the prominence eruption when the material could be seen rising up over the Northern limb. Observations from STEREO-B will therefore not be discussed.

Previous observations

An additional perspective can be gained by going back seven days and viewing the prominence as it appeared at the disc centre (as would be the only option if no STEREO data was available). Figure 6.11 shows three full-disc images of the Sun on the 6 June 2010 in Hα (Big Bear Solar Observatory), and SDO/AIA 304 Å and 193 Å. The Hα image shows that this feature is indeed located along the polar-crown area and that it seems to have quite a fragmented structure. It is also seen in the AIA channels as a dark feature along this position. Figure 6.11 gives an indication of the length of the prominence and also confirms that the feature seen in Figure 6.9 is a rising prominence

and not some other magnetic field aberration.

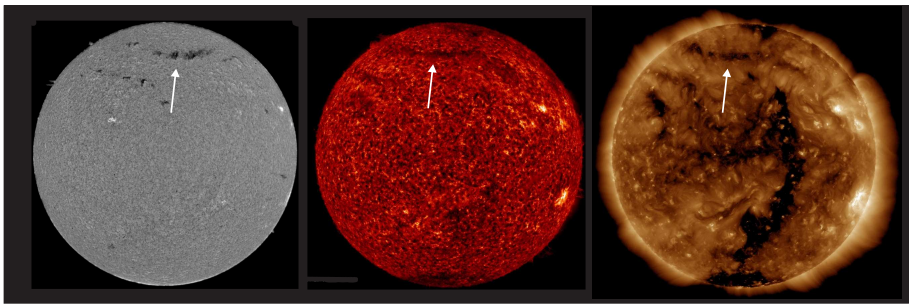

Figure 6.11: Images of the prominence seen from Earth seven days before the eruption when it was on-disc. The prominence can be clearly seen in all three images in the northern polar crown region. Left panel is a BBSO Hα image, an SDO/AIA 304 Å image is in the middle and the right shows an SDO/AIA 193 Å image.

6.4.2 External influences on polar-crown prominence

Figure 6.8 showed the polar-crown prominence within the context of the full solar disc. Boxes B and C highlight some other areas of interest that show lots of activity over the 12 hour observation window chosen. The Northern hemisphere includes an active region (AR 11081) and a secondary prominence (hereafter P2). The Southern hemisphere contains two close-by active regions (AR 11080 and 11079) which seem to be linked to the Northern hemisphere by a trans-equatorial loop. These features and the possible influences they have over the polar-crown prominence eruption are discussed here.

Northern Hemisphere activity

The West limb of the Sun on the 13 June 2010 had a number of interesting and dynamic features. The features of the Northern hemisphere are shown in Figure 6.12 and shows the major changes the area undergoes. Movie prom_5.mov shows the dynamic evolution of these features over the twelve hour data set. P2 is seen in the top-left of each image where it is observed to be a large quiet-sun prominence that remains very stable. It is observed to be magnetically connected to the nearby AR 11081 and shows brightenings

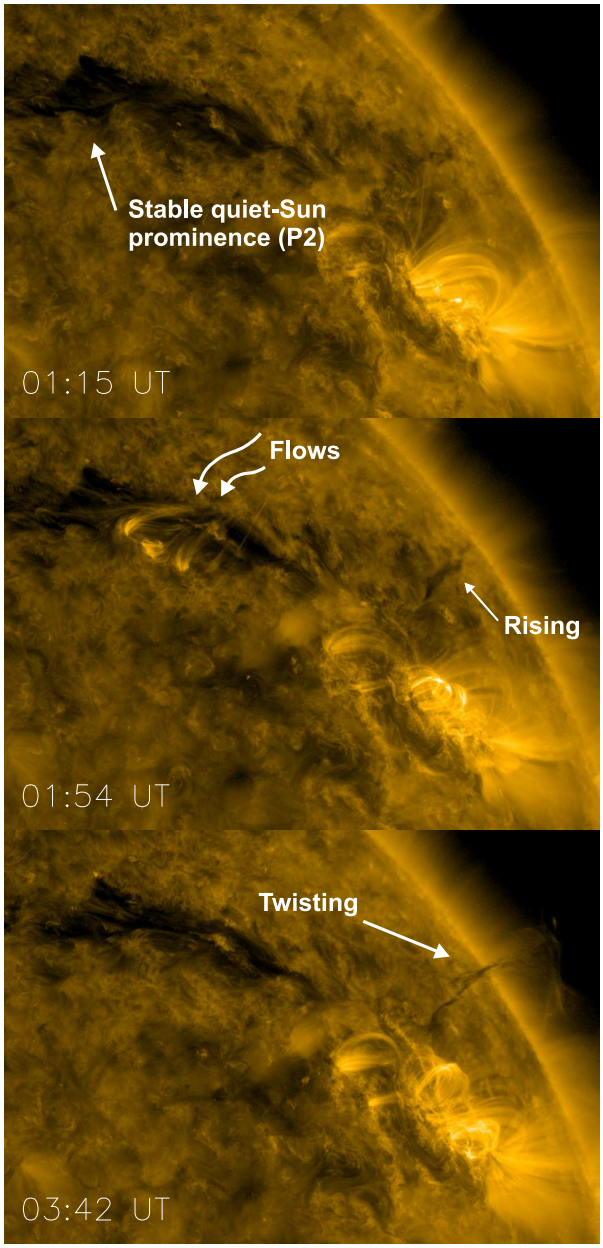

Figure 6.12: Time series of AIA 171 Å partial Sun images focusing on the active region (AR 11081) and second prominence (P2) seen in the Northern hemisphere. P2 is identified in the topmost image which remains stable but is observed to experience flows related to activity in the nearby active region. A section of this prominence and is seen to rise and twist over the course of the observation. This figure is a close up of the area labelled Box B from the full-Sun image in Figure 6.8.

associated with mass flow (Figure 6.12 middle panel) from the active region. The Western end of P2 is then seen to rise and twist in relation to activity in the active region. None of this activity however is seen to correlate with the motion of the polar-crown prominence.

Southern Hemisphere activity

Box C in Figure 6.8 highlights an area in the Southern hemisphere on the Western limb which shows a lot of activity. This area contains two active regions (AR 11080 and 11079) which are shown from a different perspective in Figure 6.13. This figure shows a full-disc STEREO-A/SECCHI/EUVI image in the 195 Å channel at 03:45 UT with the two ARs highlighted and enlarged. Figure 6.14 shows the AIA view of these active regions at the same time and also two hours later. The left image at 03:42 UT shows the active regions and also highlights the bottom of the trans-equatorial loop seen in the full-disc image (Figure 6.8). The right panel of Figure 6.14 shows the same region two hours later after a significant change has taken place. An M1 flare located in the further West active region (AR 11079) goes off at 05:33 UT leading to a CME (see Section 6.5.2).

The location of the flare and the front of the emerging CME are highlighted with a full account of the aftermath of this flare given in Section 6.5.2.

6.4.3 Analysis of polar-crown prominence eruption

Structural Evolution

The prominence cavity is observed in all four of the AIA channels shown in Figure 6.9. In 171 Å (b) it is seen as a collection of U-shaped structures with little material seen in the centre of the cavity. This paucity of material is also seen at different temperatures

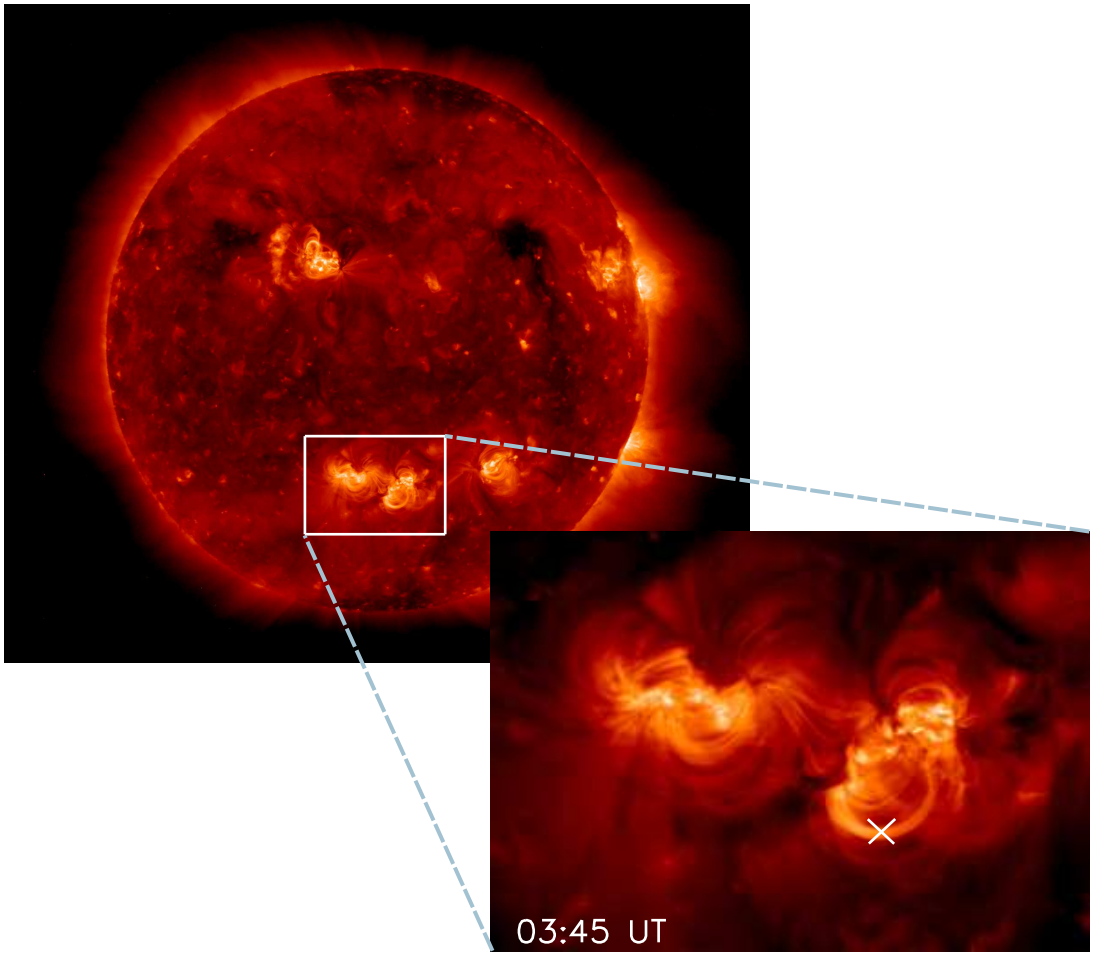

Figure 6.13: Full Sun STEREO/SECCHI/EUVI 195Å with highlighted and enlarged image of the Southern hemisphere active regions NOAA 11080 on the left and 11079 on the right. The 'X' indicates the site of the M1 flare which creates the EUV wave observed.

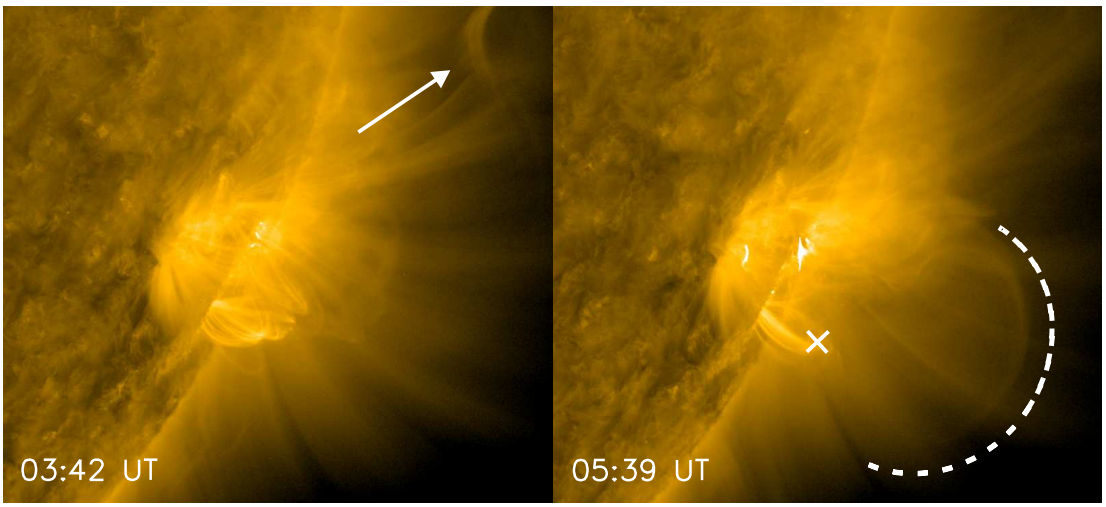

Figure 6.14: SDO/AIA 171 Å images of the Southern hemisphere active regions at 03:42 and 05:39 UT on the 13 June 2010. The white arrow on the left image highlights a curious trans-equatorial loop (discussed in the Future Work Section 7.3). The white 'X' on the right image indicates the site of an M1 flare that occurred at 05:33 UT causing a CME. The expanding front of this CME is also highlighted. The field of view in this image is the same as Box C in Figure 6.8.

suggesting that the prominence material lies along the lower edge the cavity i.e., in the dips of the magnetic field of the flux tube. Material seen "inside" the cavity in Figure 6.9 (c) and (d) is most likely foreground or background material along the line of sight.

Figure 6.15 shows that the U-shaped structure seen in 171 Å is maintained throughout the eruption giving credence to the idea that we are looking along the axis of an erupting flux rope (such as depicted in Figure 6.4). During the eruption it can be seen that the prominence splits into two separate structures as labelled in Figure 6.15: (1) that moves upwards with some material falling down after the main eruption and (2) part that doesn't erupt but seems to interact with the falling material later on. This movement can be more clearly seen in Movie prom_1.mov.

The prominence barbs are also highlighted in Figure 6.9 where they are seen as bright strands underneath the prominence. These are most clearly seen in 171 Å and 193 Å where they are seen in absorption against the bright limb. The two main barbs are shown more clearly in Figure 6.16 where a time series of images shows how they change over time. The top-left image (at 00:03 UT) shows the initial structure of the barbs with

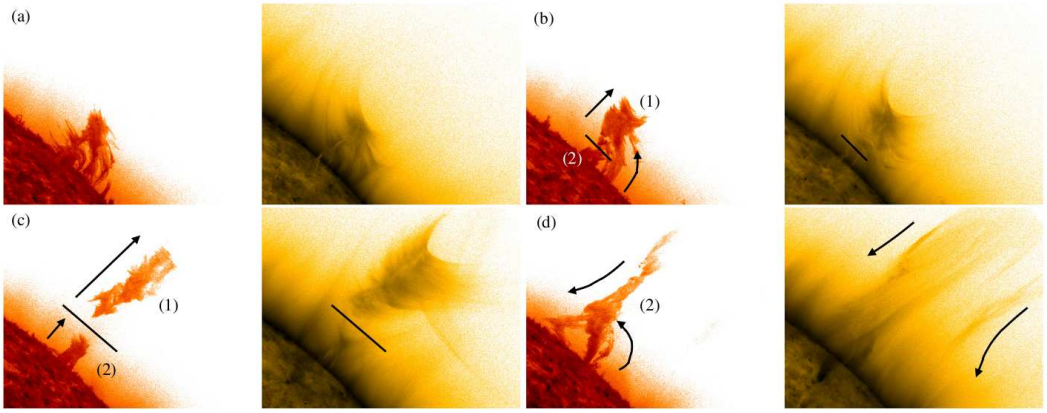

Figure 6.15: Series of four instances during the prominence eruption showing SDO/AIA 304 Å and 171 Å at times (a) 00:03:12 UT, (b) 03:24:11 UT, (c) 06:51:11 UT and (d) 09:00:11 UT. The arrows indicate the direction of the plasma motion during the eruption. Labels (1) and (2) identify the parts of the plasma that evolve differently over time. See Movie prom_1.mov for details of evolution. Image from Régnier, Walsh & Alexander, 2011.

two clear parts that seem to connect the base of the prominence to the solar surface. Over time the integrity of the barbs is seen to diminish as the prominence rises. There is also some twisting/un-twisting motion seen in the foremost barb that is shown in Movie prom_2.mov. It is unclear if this motion is a genuine un-twisting or just the apparent motion of the plasma. Unfortunately the structure is too close to the limb for magnetogram data and Hinode/EIS was not observing this region. Without magnetic or spectroscopic data being analysed the real motion is difficult to confirm.

The way in which the barbs and cavity evolve over time can be explored by plotting a time-distance graph over the course of the 12 hour observation window. This is shown in Figure 6.17 where cuts through the barb and cavity region are shown next to their corresponding time-distance plots. For the barb evolution it can be seen that there are two clear structures at the base of the prominence although it is difficult to determine where they lie in relation to one another along the line of sight. It is likely that the more Western barb lies further into the plane of the image i.e., they are not side-by-side. Both barbs undergo a dramatic change over the course of the observations and are seen to fragment and then decrease in intensity at different times. The evolution of the barbs and their possible role as an eruption trigger is discussed further in Section 6.5.1.

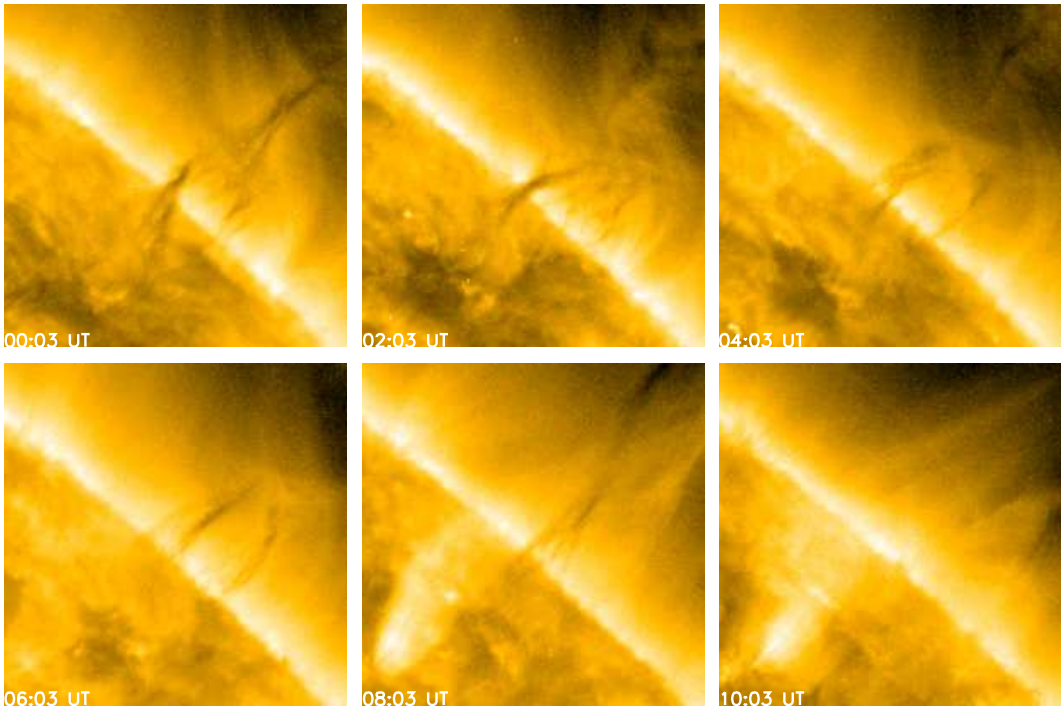

Figure 6.16: Sequence of images showing the evolution of the prominence barbs over time. See Movie prom_2.mov to see the evolution more clearly.

The STEREO-A/EUVI data set was used to add another perspective to the observation of the prominence. EUVI 304 Å added very useful information and can be seen in Figure 6.18 where AIA and EUVI images are shown side-by-side. This time series shows the 304 Å at 06:56, 08:06, and 09:26 UT i.e., after the eruption is well under way. Before this time the prominence was not identifiable in the STEREO images due to a combination of background and line-of-sight effects, and was only seen once it had risen higher in the atmosphere. The white dashed lines in the Figure 6.18 represent the basic shape of the prominence as it rises (this can be seen in Movie prom_6.mov). It is observed that the West side of the prominence lifts off first - a detail that would not be seen by just using SDO/AIA. This factor, along with the almost "flipped" nature of the prominence material seen in the lower panel of Figure 6.18 will help to discover what the more likely trigger mechanism of this prominence is (see Section 6.5.3).

The EUVI 195 Å data set did not clearly show the prominence eruption (as the material in this passband is too hot at around LogT~6.2) but another interesting feature was seen

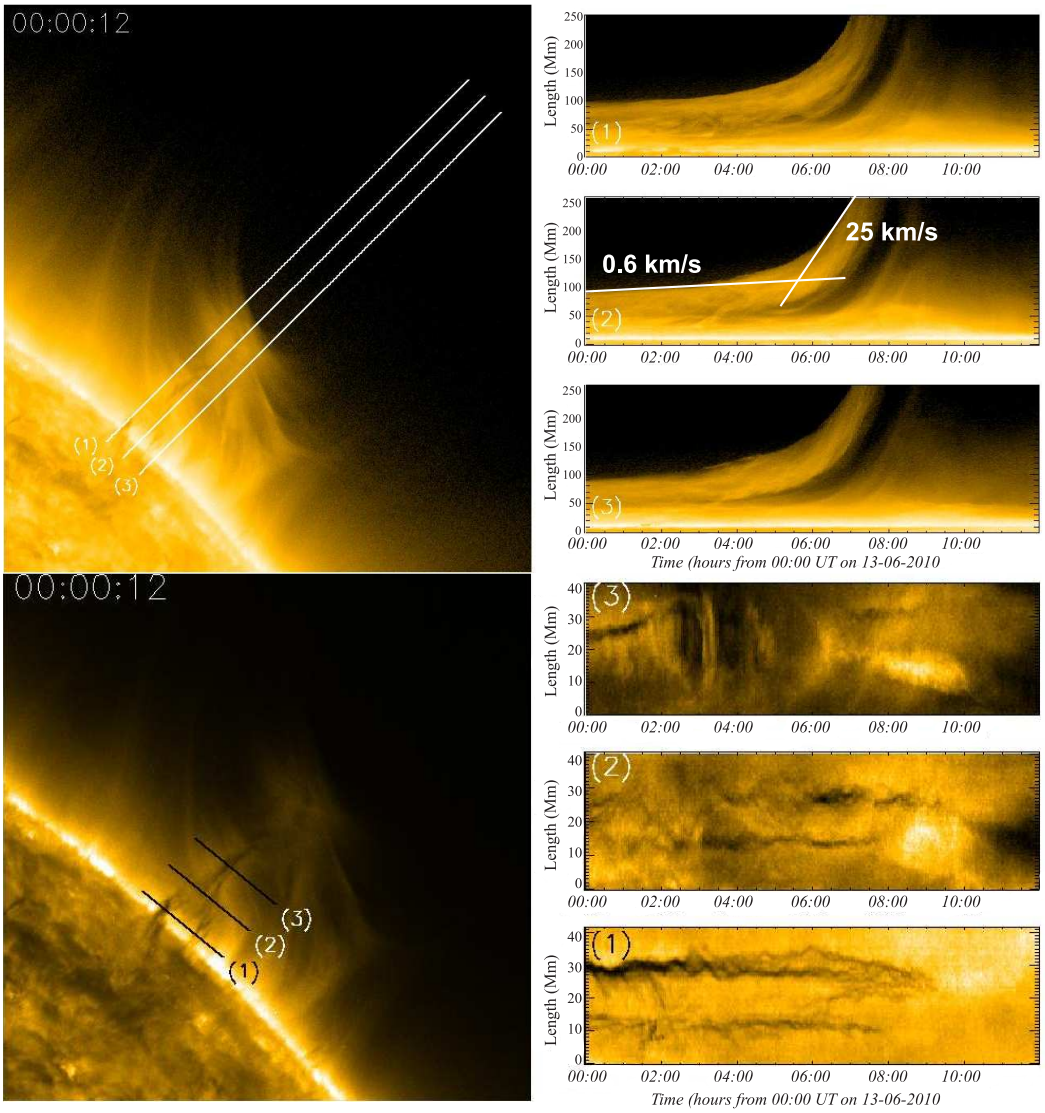

Figure 6.17: Top panel shows three cuts through the prominence cavity and how they evolve over time. The time-distance plots of each cut is shown on the right of the top panel with the calculated velocity of the cavity shown in the middle plot. The lower panel shows a similar examination of the prominence barbs with time-distance plots of three cuts shown in the right panel. Figure adapted from Régnier, Walsh & Alexander, 2011. Movies prom_3.mov and prom_4.mov show more details of these changes over time.

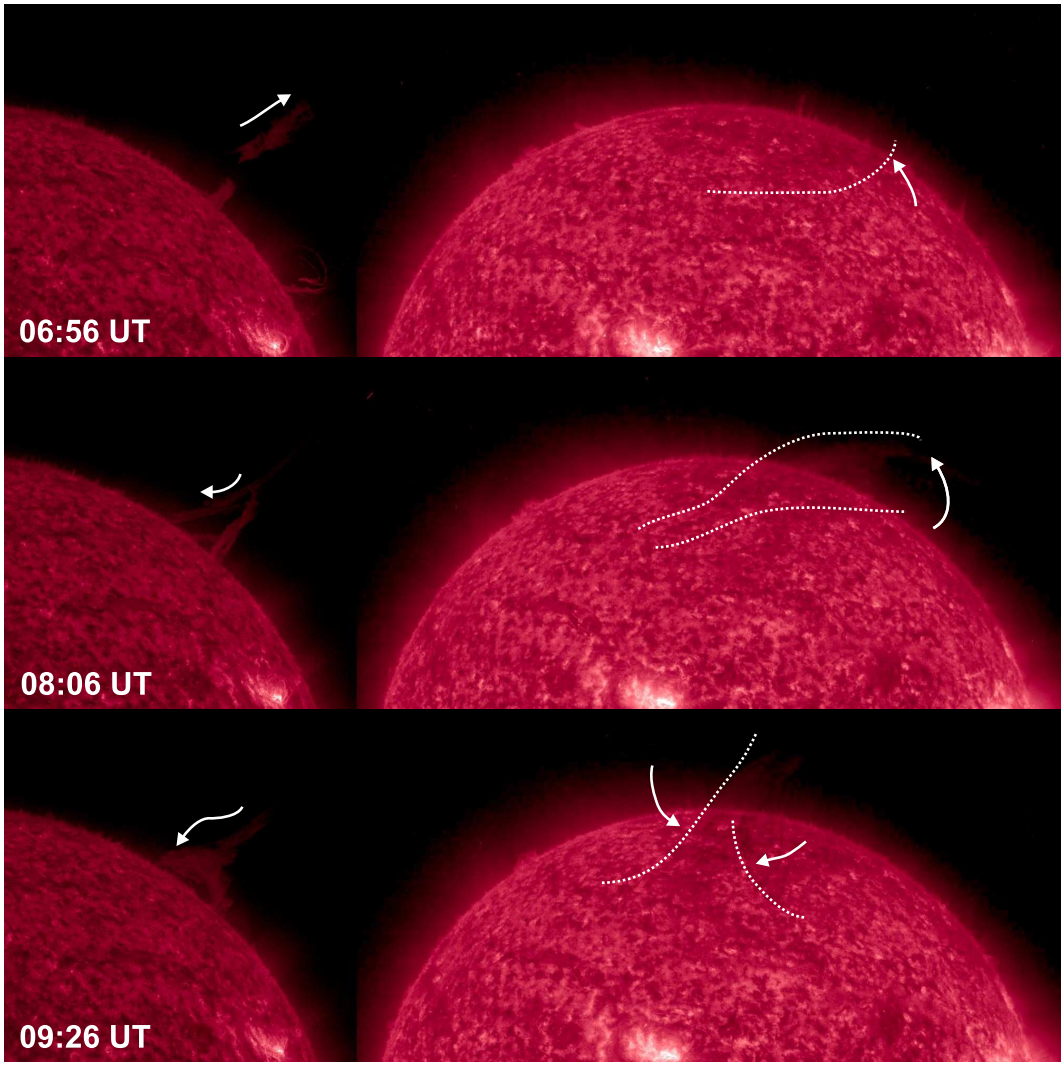

Figure 6.18: Series of same-time 304 Å images from SDO/AIA (left) and STEREO/SECCHI/EUVI (right) showing the evolution of the ejected material from two perspectives. The dotted white lines indicate where the moving material is located with arrows showing the direction of movement. See Movie prom_6.mov.

and is discussed in Section 6.5.2.

Dynamics

The wealth of SDO/AIA data for this eruption allow an accurate measure of the velocity of the cavity rise to be calculated. Looking at the middle plot on the right of Figure 6.17, the slope of the lower edge of the rising cavity has been used to approximate the velocity which appears to have at least a two-part trajectory. To begin with the prominence appears quite stable and has a slow rise of 0.6 km s^{-1} from 00:00 UT until around 03:00 UT. This is followed by a rapid acceleration as the eruption gets underway. The speed of the latter part of the eruption is measured to be 25 km s^{-1}. This is much less than the local sound speed (which is typically around 100–200 km s^{-1} (Gallagher & Long 2011)) but is of a similar value to velocities measured by other authors for the final ejection speed of a slow rising prominence. For example, Sterling & Moore (2003) studied a similar polar-crown prominence that was stable before it underwent a slow rise of ~1 km s^{-1} followed by a fast rise of ~10 km s^{-1}.

Over the course of the twelve hour observation, a radical change in the structure of the prominence is seen as it rises and is ejected. An interesting effect to note is the various flows that occur over short timescales - especially after the main phase of the eruption. Some of these can be seen in panel (d) of Figure 6.15 and also in Movie prom_1.mov and prom_5.mov. These flows from the prominence back down to the surface indicate that the prominence is still magnetically connected throughout the corona, even after it has erupted as a CME (shown in Figure 6.19 at three times). This suggests that mass-loss could play an important role in the prominence eruption.

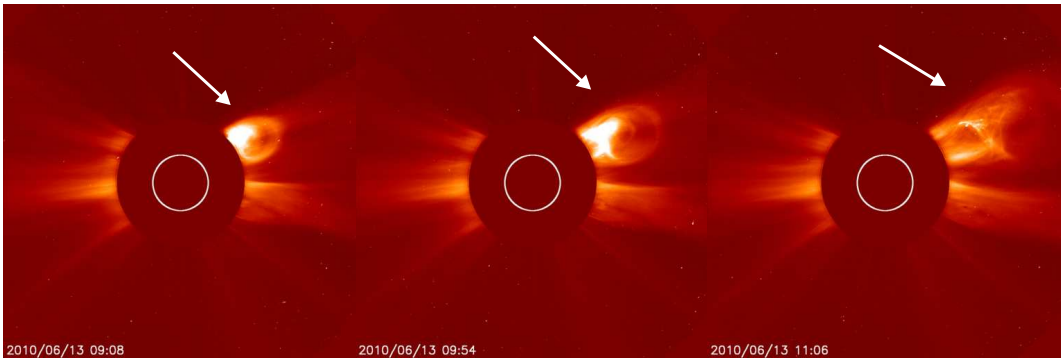

Figure 6.19: Series of SoHO/LASCO/C2 images showing the evolution of the CME that results from the polar-crown prominence eruption seen on the North-West limb.

6.5 Exploration of initiation methods

Section 6.2.2 describes the details of various ways in which an eruptive event can be triggered. The polar-crown prominence being investigated here was a very stable structure until it erupted on the 13 June 2010. It was observed in Hα to be quiescent in the polar-crown area for at least one solar rotation prior to eruption. This indicates that some kind of trigger mechanism is likely to be responsible. This section explores the more likely mechanisms, namely: tether cutting, perturbation by EUV wave, mass un-loading, and kink instability, and presents evidence to support or rule out these possibilities.

6.5.1 Barb Evolution - tether cutting and straining

As discussed in Section 6.2.2, the evolution of prominence barbs/tethers can play a crucial role in the eruption process. In the case of the 13 June 2010 polar-crown prominence, dynamic changes in the structure of the barbs were observed and could potentially give clues about what triggered the eruption. Initial observations of the barbs were introduced in Section 6.4.3 with the changes over time detailed here.

If we consider the clearer of the two prominence barbs (the one located at 30Mm on the time-distance plots in the lowest panel of Figure 6.17), the structure is seen to move in

an almost oscillatory fashion before becoming more thread-like at around 03:00 UT and disappearing completely at around 09:00 UT. This possible oscillation was investigated by making another time-distance plot of this barb along the position shown in Figure 6.20. This time-distance plot can be seen in the lower panel of Figure 6.21 where the oscillatory motion has been picked out by fitting a line to the motion using the highest intensity of the barb at each timestep. This fit is seen as a white line along the dark barb (this line ended at 06:00 UT when the background noise became to high to follow the barb any further). This fit was smoothed and the general trend of peaks and troughs were marked as dashed and dotted red lines respectively. Table 6.2 shows the times of these features and indicates that the times between these half-cycles changes from an average of 33 minutes in the slow-rise phase of the eruption to 16 minutes as the eruption accelerates. The point at which this change occurs is marked on Figure 6.21 by the red line at 02:54 UT which extends upwards to the top panel showing the cavity velocity change. This position does seem to identify where the gradient of the cavity velocity changes from a slow rise to something steeper - perhaps indicating a relation between the barb's oscillation and the eruption velocity of the cavity. However, the motion is not perfectly periodic and only covers 4-5 cycles so it is hard to tell if the barb's motion is a result of a real oscillation, a twisting/untwisting of the barb, or simple plasma motions along the line of sight. A clearer case of oscillation in a similar barb structure was observed by Isobe & Tripathi (2006) who measured a clear oscillation with a period of 120 minutes and concluded that the oscillations were indicative of a destabilising/restoring motion.

Additionally, due to the lack of reconnection signatures such as increased emission in the hotter AIA channels at the site of the barbs, it is unlikely that the trigger mechanism is tether-cutting. Additional evidence for this conclusion can be found by noting that in Figure 6.21 the cavity is seen to rise before any major changes in the barbs are observed. This may make a case for tether-straining as based on the various timings, the breaking up of the barbs could be attributed to the rise of the cavity. Unfortunately, this would give no clues as to the trigger mechanism itself as this straining is just a consequence of

Event (T-trough, P-peak)	Timestep (UT)	Duration of half-cycle (mins)
Start Time	00:11:10	-
T	00:36:11	25[a]
P	01:18:11	42
T[b]	01:48:11	30
P	02:21:11	33
T	02:54:11[c]	33
P	03:12:11	18
T	03:24:11	12
P	03:36:11	12
T	03:54:11	18
P	04:12:11	18
Flare in AR 11079	05:33:00	-
EUV wave arrival time	06:20:00	-

Table 6.2: Table relating to Figure 6.21 showing the timings of the peaks and troughs of the initial oscillation seen in the prominence barb.Times of the M1 flare in the southern hemisphere and the calculated arrival time of the EUV wave are also shown. [a]This may not be an accurate period as this assumes the peak of this half-cycle is at the start time. [b] This feature is a trough even though in Figure 6.21 it is a small peak. The general trend here is that of a trough. [c] This time indicates when the duration between peaks and troughs jumps from an average of 33 to 16 minutes. This time can also be associated with a change in velocity of the cavity.

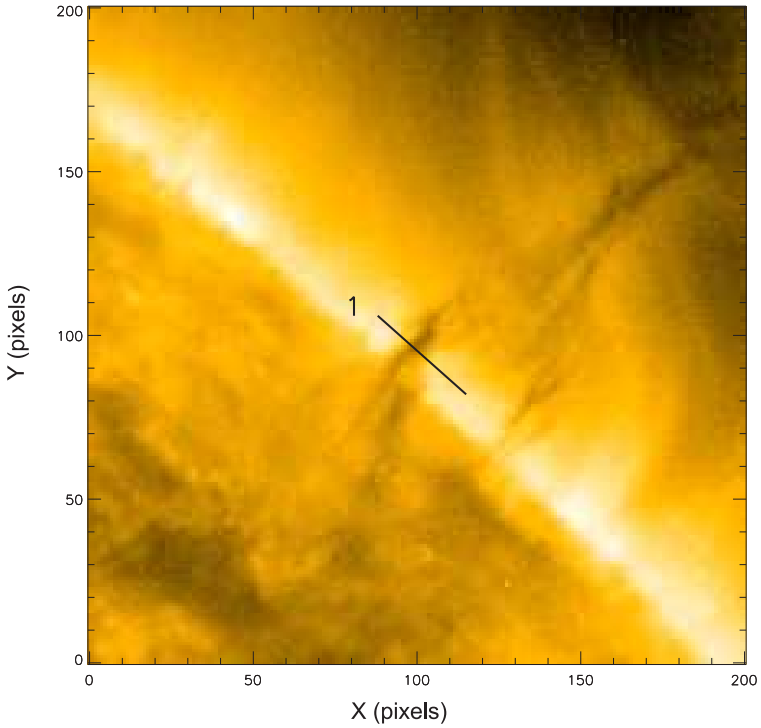

Figure 6.20: Close up of prominence barbs seen by SDO/AIA 171 Å showing the slice where the time-distance plot in Figure 6.21 is taken from.

the eruption and not the cause.

6.5.2 EUV Wave

While examining the STEREO-A/SECCHI/EUVI 195 Å data set over the time period of the Northern polar-crown prominence eruption, another interesting event was observed. At around 05:30 UT an M1 class flare is seen to go off in the Southern hemisphere active region (AR 11079 in Figure 6.8) and a clear EUV wave is seen to propagate outwards from it. It is possible the interaction of this EUV wave with the prominence is the reason why it suddenly erupts after such a long time being stable. Figure 6.22 shows a series of nine running difference images of the STEREO-A/EUVI 195 Å data. The EUV wave is clearly seen to start and then dissipate within a timescale of 20 minutes.

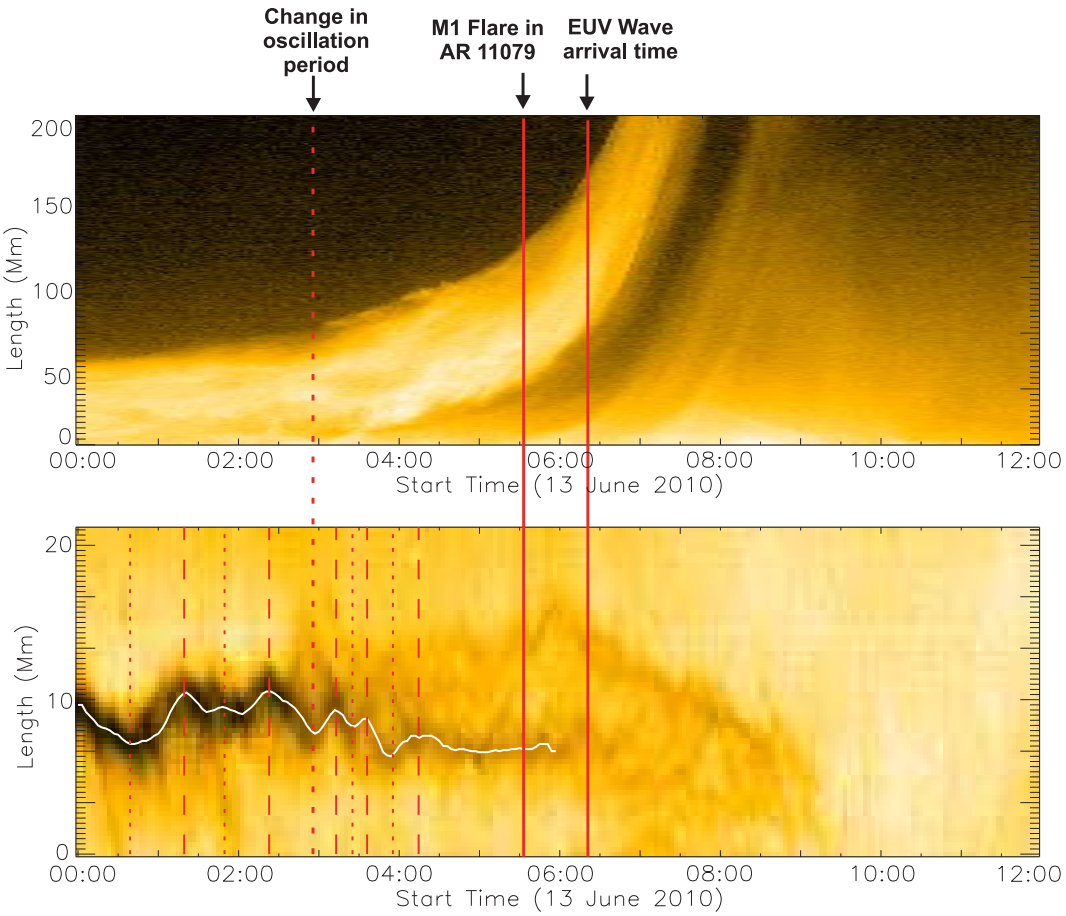

Figure 6.21: An examination of the barb oscillation and relation to cavity eruption speed. The lower plot shows a close up of the clearer of the two prominence barbs identified by the line in Figure 6.20. This time-distance plot shows the motion of the barb and the white line indicates the maximum intensity along this barb. The peaks and troughs have been marked with red dashed and dotted lines respectively. The top panel shows the same-time evolution of the prominence cavity in order to compare timings. Additional events such as a Southern hemisphere flare and EUV wave arrival time are marked.

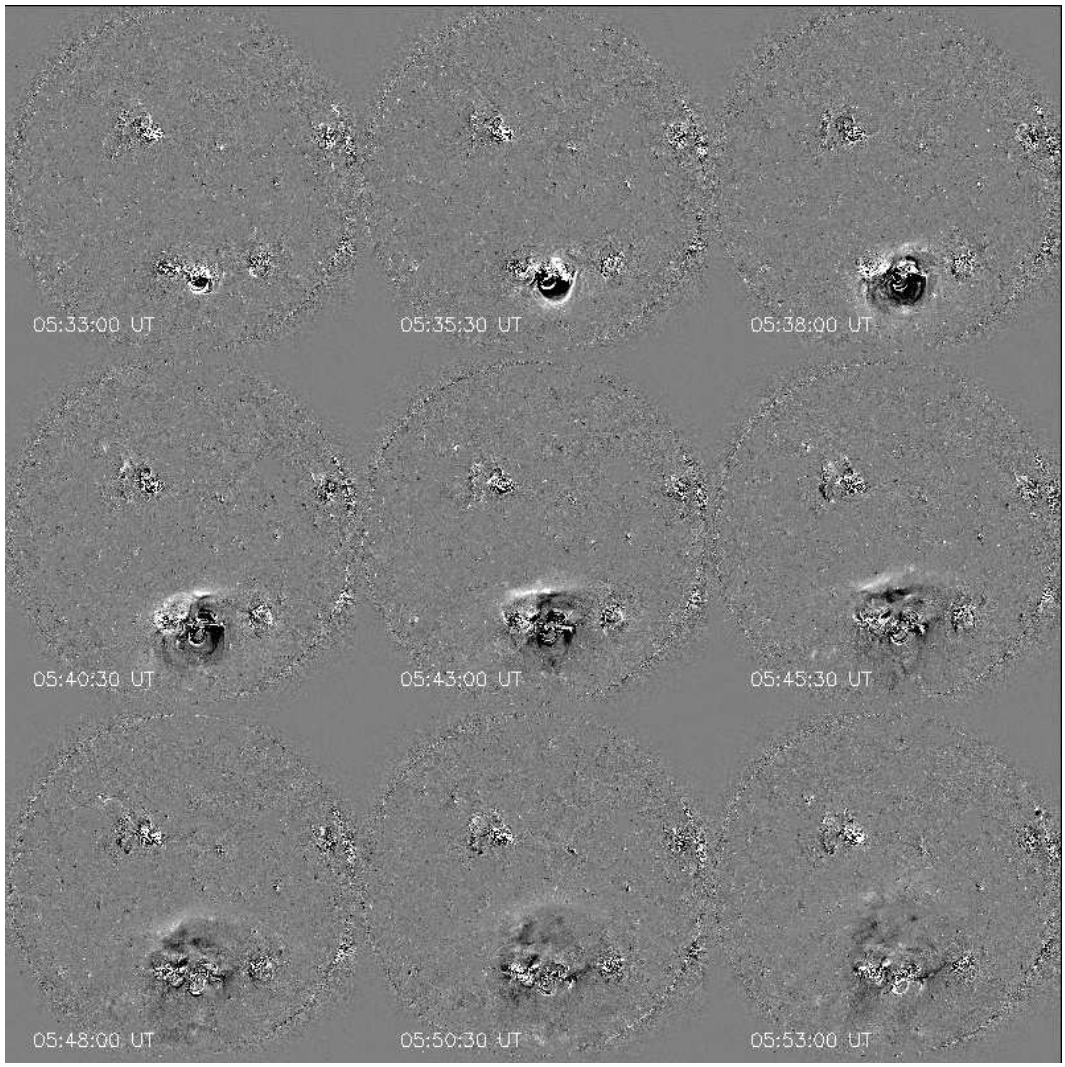

Figure 6.22: Series of full Sun running difference images from STEREO-A/SECCHI/EUVI 195 Å showing the expansion of the EUV wave over time from the active region in the Southern hemisphere. Movie prom_8.mov shows this expansion more clearly.

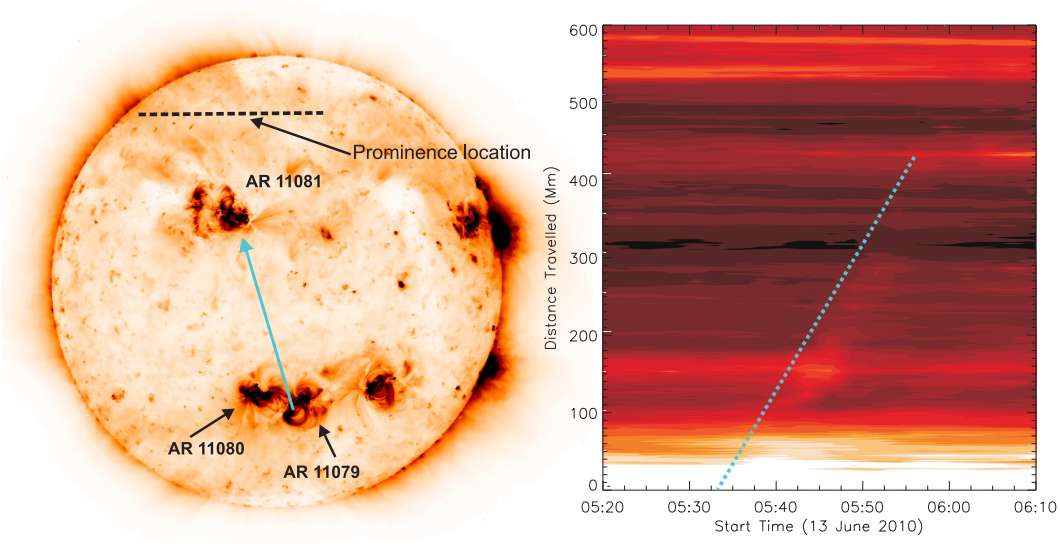

Figure 6.23: *Left:* full-Sun STEREO-A/EUVI 195 Å image showing the location of the various active regions and the polar-crown prominence under investigation. The M1 flare that causes the EUV wave is located in AR 11079 and the path along which its velocity is measured is indicated by the blue arrow. *Right:* time-distance plot created to measure the EUV wave speed. A clear diagonal motion is observed and has been highlighted by the dotted blue line. This line has been extended downwards to identify the initiation time of the EUV wave and agrees very well with the M1 flare time of 05:33 UT indicating the events are linked.

By taking a time/distance slice along the propagation path of the EUV wave, a time-distance plot was constructed (Figure 6.23). The left side of this figure shows a negative intensity image of the full Sun as seen by STEREO-A/EUVI in the 195 Å channel at 05:33 UT. The blue line represents the vector along which the speed was measured. The prominence is located further North in the polar-crown area (where the arrow indicates) but this vector was chosen as the propagation in this direction (i.e., towards AR 11081) was the most easily observed and so was more clearly seen in the time-distance plots. The left panel shows an example time-distance plot where a diagonal motion can clearly be seen. The gradient of this line was taken to be the velocity of the EUV wave and was calculated to be 330±50 km s^{-1}. The high uncertainty is due to the limited time cadence of the STEREO/EUVI data which made calculating the slope of the line difficult.

This speed is backed up by a study from Patsourakos et al. (2010) who studied the CME that was associated with the flare and EUV wave from AR 11079 using the same

combination of SDO/AIA and STEREO/SECCHI/EUVI. They measured the eruption speed of the CME and their results are seen in Figure 6.24 where the average speed of the CME front is around 300 km s^{-1}. This result ties in nicely with our measurement of the speed of the expanding EUV wave as it would be expected that the speeds have a similar magnitude.

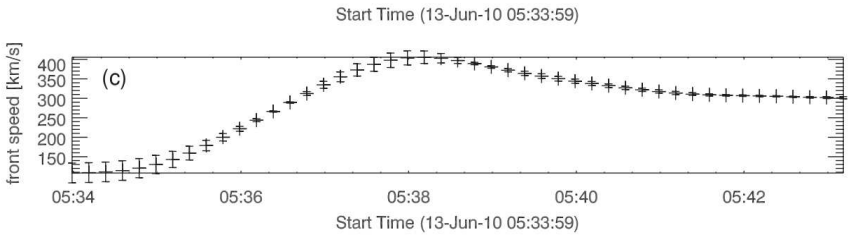

Figure 6.24: Results for Southern Hemisphere CME speed from Patsourakos et al. (2010).

With the measured EUV wave velocity of 330±50 km s^{-1}, the time taken for the wave to reach the Northern polar-crown area is 50±12 minutes meaning it would arrive at around 06:20 UT. This arrival time and the timing of the flare have been marked in Figure 6.21 as two solid red lines that extend over the two time/distance plots. It can be clearly seen that the eruption is well under way by the time the EUV wave would arrive. Thus, this EUV wave is likely to not have triggered the eruption as it arrives too late. It is also unlikely that a chromospheric counterpart of this EUV wave e.g., a Moreton wave, could have arrived early enough to perturb the prominence as the flare that created this wave occurs at 05:33 UT while the prominence is seen to start to rise about 90 minutes before this time.

6.5.3 Mass Off-loading

Another possible trigger mechanism that is supported by the observations is mass off-loading. This is a possible mechanism due to the down-flows of material that are observed in the four AIA channels, particularly at 304 Å. Figure 6.25 shows two instances where mass flows from the prominence down to the solar surface are seen with

SDO/AIA 304 Å. Downward mass flows are seen to occur throughout the 12 hour observation window with a lot of activity seen before the prominence erupts. Movie prom_1.mov shows this is greater detail.

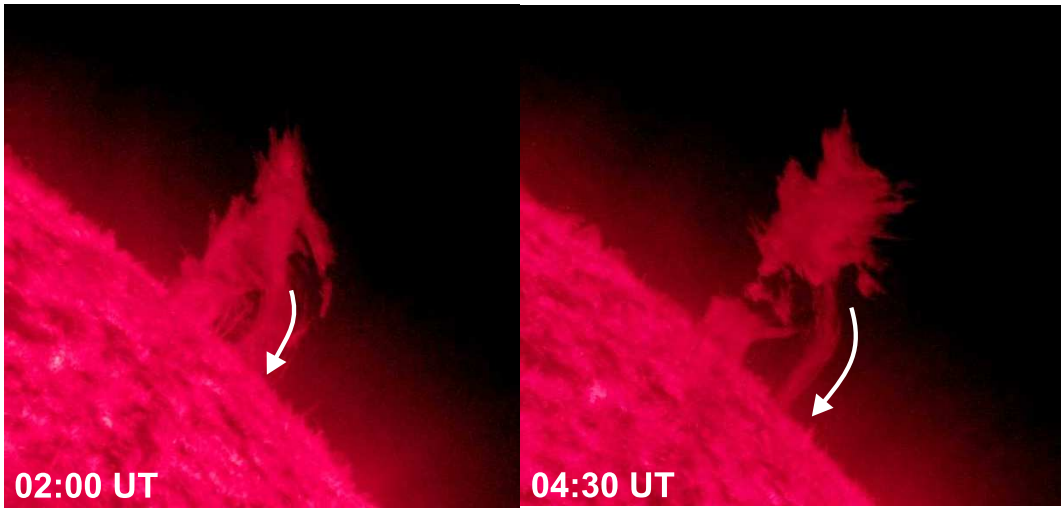

Figure 6.25: Images of of the prominence as seen by SDO/AIA 304 Å at two different times. The areas highlighted by the arrows are major mass flows that are observed (see Movie prom_1.mov) to flow from the prominence down towards the solar surface.

As mentioned in Section 6.2.2, the reduction of the prominence mass would lead to the magnetic tension force increasing, causing the structure to rise. This would cause increased strain on the barbs/tethers that connect the prominence with the lower atmosphere. This can be seen in Figure 6.21 where the barbs start to decrease in intensity after the prominence cavity has started to rise. Based on these observations it is likely that mass loss plays a significant role in the eruption of the prominence.

6.5.4 Kink Instability

Another mechanism that could be a contributing factor to the prominence eruption is a kink instability. Evidence for this process is seen in two ways: the near exponential rise of the prominence cavity, and the restructuring of the magnetic field post-eruption.

Rise of prominence cavity

As detailed in Section 6.2.2, an MHD instability in a magnetic flux tube (caused by some perturbation such as an increase in magnetic field line twist) implies an exponential rise over time (Schrijver et al. 2008). In order establish how likely a mechanism kink instability is for the case of the 13 June 2010 prominence, the nature of the cavity rise over time has to be quantified. This has been done by examining the time-distance plot made of a slice through the centre of the cavity (such as line 2 in Figure 6.17) which rises over time. The left section of Figure 6.26 shows a trimmed version of this time-distance plot where the edge of the cavity has been approximated by the solid black line. This edge was identified using a combination of image processing and user-defined selection with the mouse cursor. The error on this edge was estimated as the square root of the height of the prominence and has been plotted as two dashed lines above and below the defined edge. The edge of the cavity in this time-distance plot was not easy to define and these values of uncertainty represent a good visual fit of the data. In order to investigate whether or not the cavity rise was exponential, the logarithm of the cavity height over time was plotted. This is seen on the top-right panel of Figure 6.26 where the dotted line represents the best linear fit to the data. It can be seen the data is not a perfectly straight line (as you would expect if the rise was purely exponential). In order to quantify the fit more accurately, the rise was split into two time sections (00:00 UT - 04:51 UT and 04:51 UT - 06:57 UT) and a linear fit was applied to each section. The lower-right panel of Figure 6.26 shows these linear functions as a pink dashed line (Fit 2a) and a dot-dashed black line (Fit 2b). It is clear that Fit 2a is a good approximation of the height rise of the cavity in the first five hours but misses the final phase of the cavity rise. This is closely approximated by Fit 2b which gives a very good fit to the final two hours but is not a good fit to the rest of the data.

The right panel of Figure 6.26 has shown that the cavity rise over time can be loosely approximated by a single exponential function but is even better approximated by two exponential functions representing different time periods. The goodness of these fits is

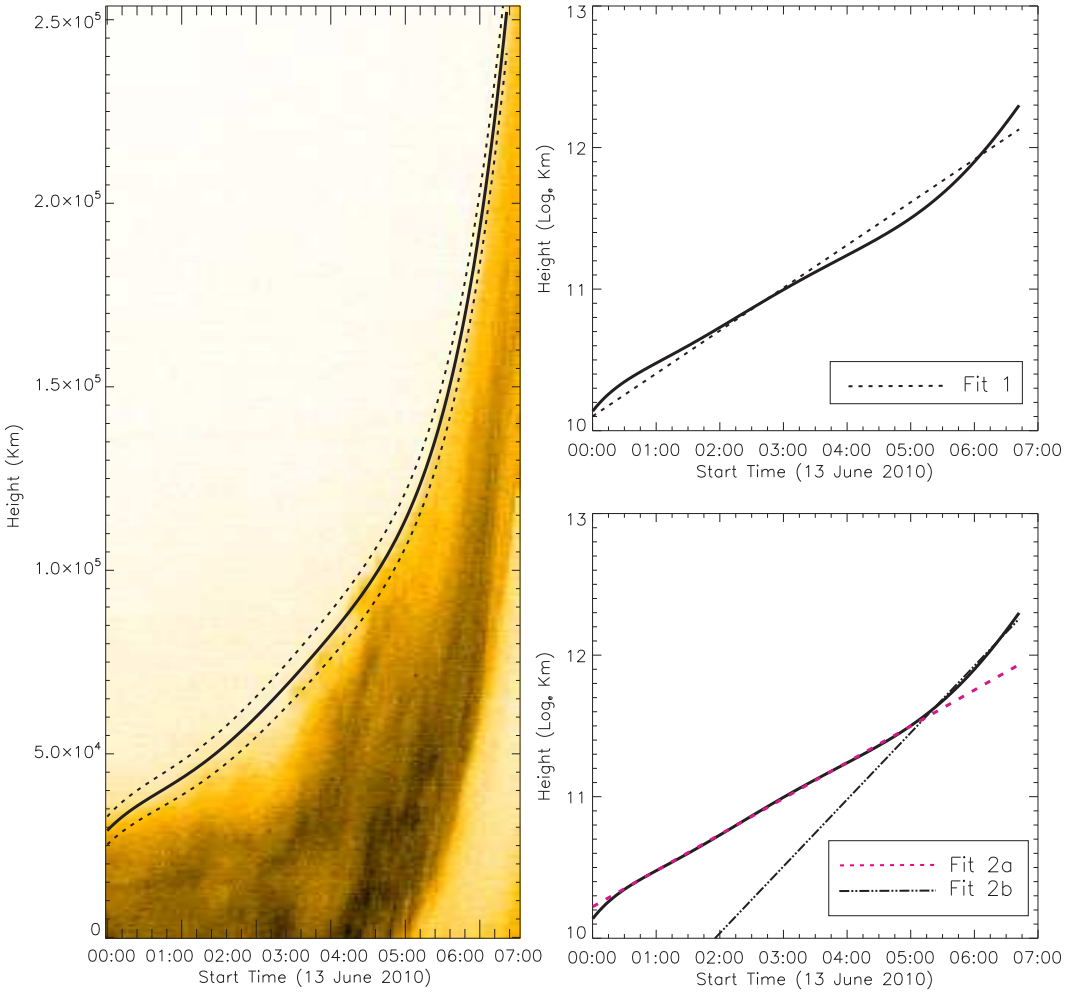

Figure 6.26: Left: scaled and trimmed time-distance plot of the rising prominence cavity with the edge defined by the black solid line. The two dashed lines show the uncertainty in this edge and have values δ=H$\pm\sqrt{H}$. Right: Two graphs showing the Log of the cavity height (H) and a best linear fit (top) and a two-part linear fit (bottom). It can be seen that two linear functions fit the cavity edge better than one.

shown in Figure 6.27 which shows how well these one and two-component fits match the data. The black solid line in each of the upper plots represents the edge of the cavity as defined previously. The left plot shows this edge over-plotted with an exponential function based on Fit 1 (black dashed line). The lower-left plot shows the residuals between the cavity edge and Fit 1 where the dashed lines represent the upper and lower limits of the uncertainty. It can be seen that initially (in the first 3.5 hours), this function does a good job of reproducing the cavity rise. However, it fails to accurately represent the latter part of the eruption. In order to combat this, Fit 2a and 2b were investigated to see how well a dual fit could recreate the data. The right panel of Figure 6.27 shows the cavity edge over-plotted with the two exponential functions based on Fit 2a and 2b. This clearly shows that the dual-exponential fit manages to follow the cavity rise throughout the 7 hour time period. The residuals for Fit 2a in the first five hours are very low and those for Fit 2b are within the acceptable errors.

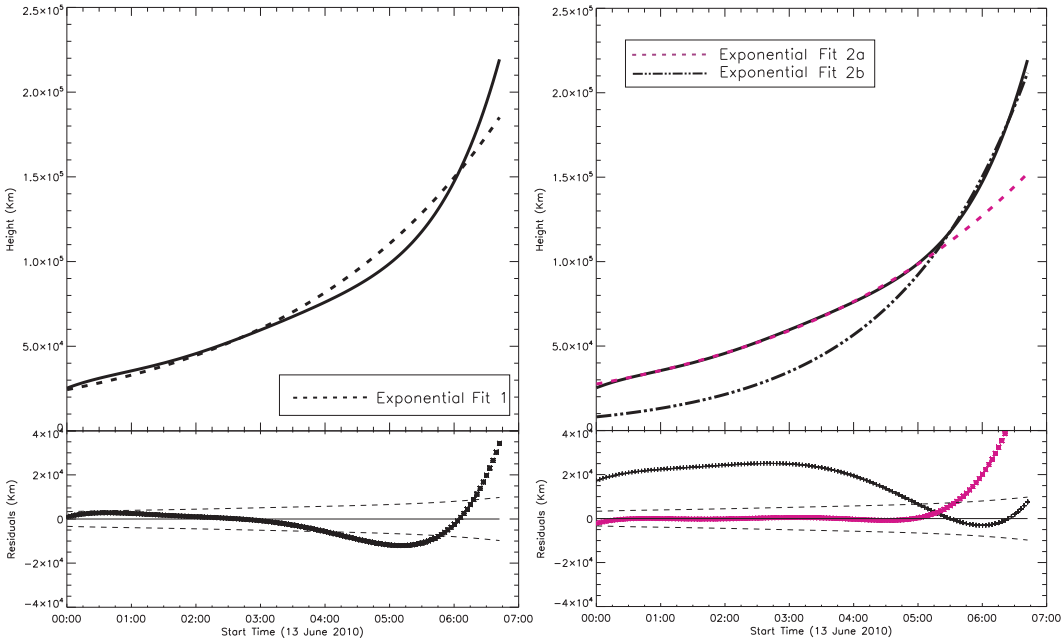

Figure 6.27: This graph follows on from Figure 6.26 and shows the cavity edge (solid black line in two upper plots) overplotted with an exponential fit based on the best single linear fit (left - Fit 1), and the two-part linear fit (right - Fit 2a and 2b). The residuals between these fits and the cavity edge are plotted below the two methods. The dashed lines on these plots represent the error values on the location of the cavity edge.

Clearly the cavity rise over time cannot be approximated as a single exponential function. A combination of Fits 2a and 2b give the most accurate fit to the data and reinforce our earlier statement about the cavity rise having two distinct velocity profiles. Other authors have noted that prominence eruption profiles can also be characterised by rise profiles such as a power law, constant acceleration, or linearly increasing acceleration (such as Williams et al. 2005), but that an exponential rise supports the idea that an instability is behind the rise. The validity of these additional rise profiles will be explored in Alexander, Régnier, & Walsh, 2012, (in prep), but it can be clearly seen that the prominence cavity rise is a two-part exponential suggesting that a kink instability is a likely eruption mechanism in this case.

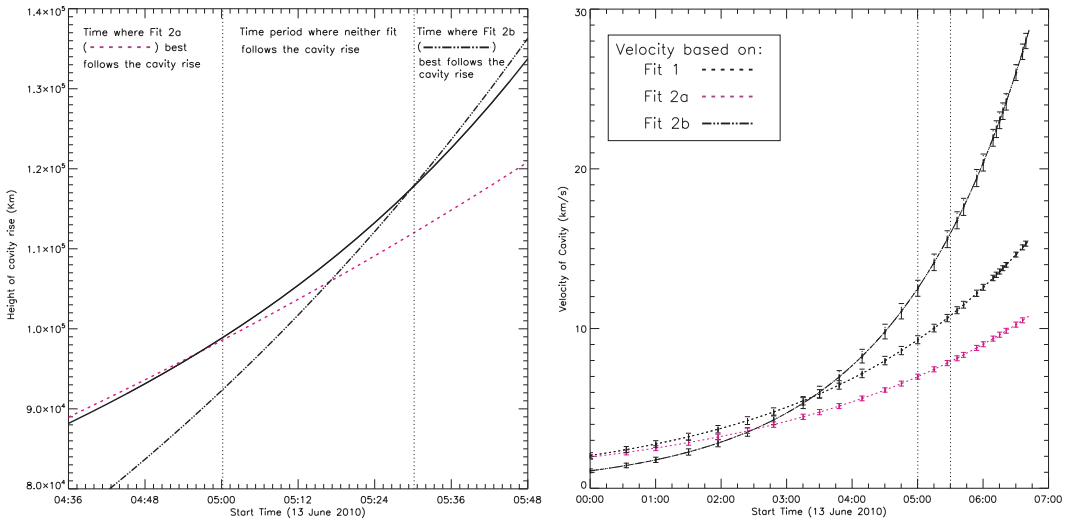

Figure 6.28: *Left:* close up of the time period when Fit 2b takes over from Fit 2a as the best representation of the cavity rise. *Right:* Velocity profiles of the cavity based on Fits 1, 2a and 2b. The dotted vertical lines highlight the half hour where none of the fits accurately follows the cavity rise and therefore the velocity measurements are less accurate.

These exponential fits can be used to infer a more accurate velocity of the cavity rise over time by plotting the differential of the height over time fits. Figure 6.28 shows these calculated velocities (right panel) and also a closer look at the point in time in which the two exponential fits diverge from the cavity edge they have been fitted to. A time period of around 30 minutes where neither Fit 2a or 2b is an accurate fit to the data is shown as two dotted lines on each plot in Figure 6.28.

In order to investigate this further, another measure of velocity derived straight from the observed rise profile is calculated. This was found by measuring the change in distance over time of the cavity edge (defined in the left plot of Figure 6.26) for every fifteen minute period over the seven hour observation time. The values of velocity derived from this method are shown in Figure 6.29 as a green line and compared to the velocity values calculated from Fit 2a and 2b. It can be seen that this profile agrees with Fit 2a (pink) very well for the first three quarters of the observation time. The initial deceleration seen can be attributed to the poorly defined cavity edge at this time caused by the high level of background intensity near the solar surface.

The velocity profiles in Figure 6.29 show that the cavity has an initial rise of 2 ±0.2 km s^{-1} (based on Fit 2a and the Fit from obs.) which increases over time to give a final eruption speed of 15–25 ±0.6 km s^{-1} (based on Fit 2b). The errors on the velocities of the exponential fits were brought forward from the errors in determining the cavity edge and look to have been underestimated for this cavity rise for Fits 2a and 2b. The errors in determining the height (H) of the cavity where therefore increased from $\Delta H = \sqrt{H}$ to $\Delta H = 10\%$ H for the 'Fit to obs.' case as this value more accurately reflects the uncertainty in defining the cavity edge.

The crossing point where Fit 2b takes over from Fit 2a in the right panel of Figure 6.27 occurs at 05:03 UT. It can be seen in Figure 6.28 that at this time there is quite a large disparity between the two velocities indicated by Fit 2a and 2b. Due to this difference in velocity, only velocity values in the initial rise phase (00:00 - 03:00 UT) and the final eruption (05:30 - 07:00 UT) can be stated with accuracy.

Post-eruption motions

Observations from STEREO-A/EUVI 304 Å (Figure 6.18) provide another clue to the origin of the prominence eruption. If we designate the end of the prominence seen by SDO/AIA as the 'East' end, and the end that is anchored further West than STEREO-A

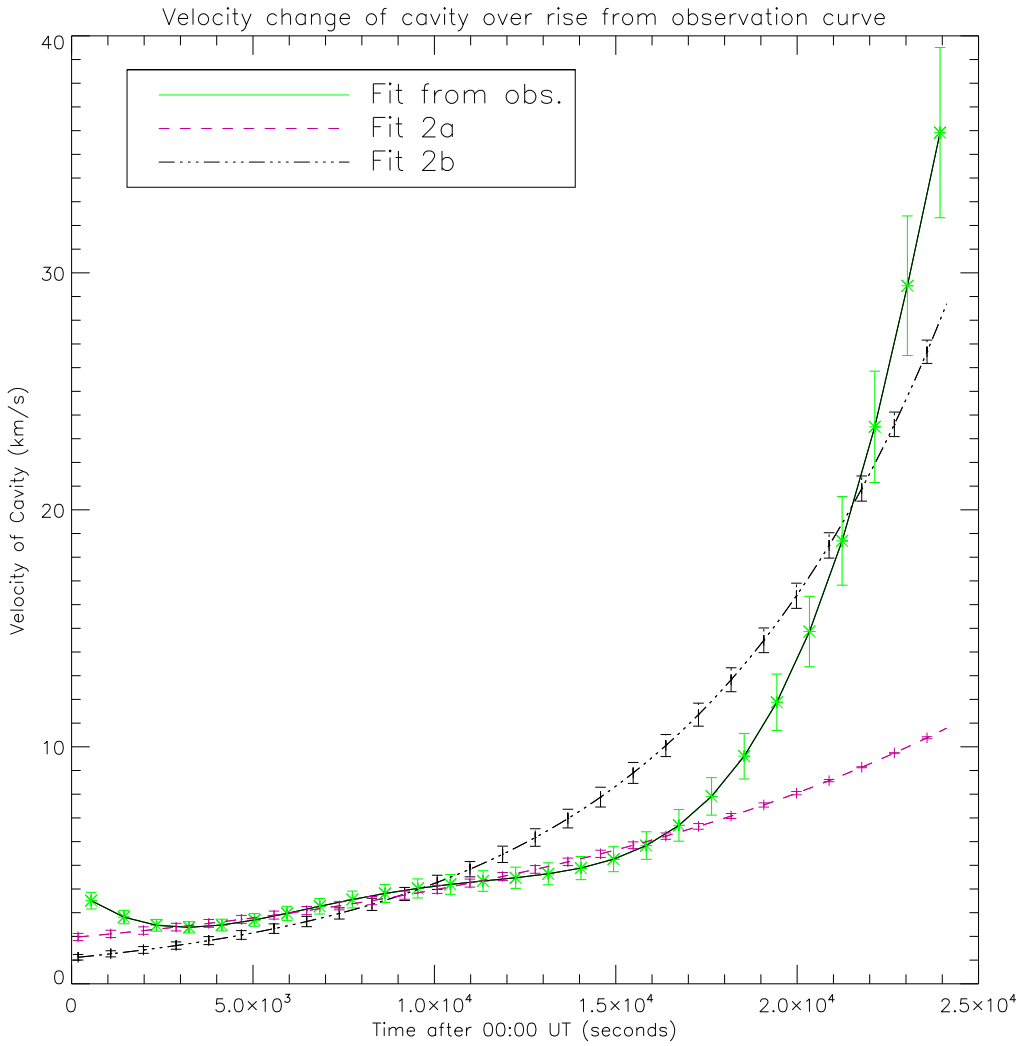

Figure 6.29: Further comparison of velocity profiles. The green line shows the cavity rise velocity calculated directly from the height over time observations of the cavity edge while the pink (Fit 2a) and black (Fit 2b) lines show the values obtained from the differential of the exponential fit curves fitted to the data. The error on the green curve has been estimated at 10% of the velocity.

can view (where West means towards the right hand side on each image) as the ‘West’ end, then it can be observed that the West end of the prominence begins to rise upwards before the East. A possible ‘kink’ shape is also seen after the eruption as the magnetic field reorganises itself. This is highlighted in the lower panel of Figure 6.18 where the plasma is observed to have a similar structure to that of a classic kink unstable flux rope as seen in Figure 6.6. Movie prom_7.mov shows this apparent ‘flip’ of the plasma more clearly although it is possible that this motion is simply caused by the remaining prominence material interacting with pre-existing coronal material. It is hard to be definite as the background intensity is comparable to the prominence intensity making it hard to pick out the exact plasma motions.

6.6 Conclusions

Using the dual perspectives of SDO and STEREO-A, the structure and evolution of a quiescent polar-crown prominence was investigated as it underwent a slow-rise and subsequent eruption. This study represents the most comprehensive observations of an eruptive prominence to-date as the full-disc, high temporal and spatial resolution of SDO/AIA, when coupled with the secondary point-of-view of STEREO-A reveal the most comprehensive 3D representation of the event.

The polar-crown prominence consists of a clear cavity component which is interpreted as a density depletion. The polar crown prominence material sits at the bottom of this cavity indicating the existence of a magnetohydrostatic equilibrium. The structure was observed to go from a stable state that was in this equilibrium, to an unstable state resulting in an eruption. The reason for this change has been explored by investigating various eruption triggers. There are several physical mechanisms that could be responsible for the prominence eruption and the extensive data set available can help to impose constraints on the possibilities. By ruling out certain mechanisms and finding evidence

to support others, the most realistic interpretation of events can be reached.

Based on the observations, the interaction of the EUV wave generated in the Southern AR 11079 did not trigger the polar-crown prominence eruption as its calculated arrival time was too late. Other external influences from the nearby Northern AR 11081 and secondary prominence were also not a factor in the eruption as none showed any correlated activity with the eruption timings. The motion of the prominence barbs have also been ruled out as triggers for the eruption. The oscillation seen in one of the barbs is most likely due to the effect of the rising of the prominence due to some other factor or combination of factors. It is also possible that this is not a true oscillation at all and is just an effect of plasma motions along the line-of-sight. Regardless of whether this motion is oscillatory, the barbs are seen to decrease in intensity and disappear as a result of the cavity rising suggesting that what we are seeing is tether-straining not tether-cutting.

The observations suggest that the most likely cause of the eruption is a combination of mass off-loading and some kind of instability (most likely a kink instability). The clear mass motions from the prominence towards the solar surface observed by SDO/AIA would cause the balance between gravity and magnetic tension to move away from equilibrium, leading to the prominence rising. This may be enough to cause the eruption or there may also be a contribution from a kink instability in the prominence flux rope. The prominence was observed over two solar rotations so it is possible that accumulated magnetic stress could have built up over time. Photospheric motions could also have led to the increase in twist in the magnetic field lines of the prominence flux rope. Without magnetogram data the only evidence to support the idea of kink instability being present is the near-exponential rise of the prominence cavity along with the observations of a kinking motion in the reorganisation of the magnetic field post-eruption.

The evidence for the eruption being caused by a combination of mass off-loading and kink instability is persuasive but it is also possible that the observations cannot reveal the real trigger. As mentioned previously, the ‘West’ end of the prominence is seen

to rise first so it is possible that some unknown process (beyond the field-of-view's of STEREO-A and SDO) occurred which triggered the eruption. If this is the case we are just seeing the effects of the eruption and not the trigger itself. This investigation emphasises that it is not always clear why an eruption has occurred and that in most cases, a combination of factors may be at work.

Future work would expand this study by looking at other examples of eruptive polar-crown prominences to see if the same signatures are seen. Ideally these additional examples would have the same type of dual point-of-view observations and have accompanying magnetogram and spectrometer data. This would allow the investigation of prominence structure, evolution and triggering mechanisms to be studied as thoroughly as current instrumentation allows. See Chapter 7 for more details.

Chapter 7

Final Conclusions and Future Work

This thesis has analysed and discussed multiple features of the corona from small to large-scale, but there is still scope for each topic covered to be taken further in the future. This chapter summarises the conclusions of each investigation and also outlines the particular actions and directions any future work could take and the future missions that could facilitate this.

7.1 XBP observations

Complete Hinode observations of an X-ray bright point observed on the 10^{th} to the 11^{th} of October 2007 were analysed over the entire lifetime of the XBP. Plasma parameters such as temperature, density, filling factor, cooling timescales, and magnetic field strength were calculated over the lifetime of the XBP to examine how they changed over time. The XBP was observed to exist over an area of cancelling magnetic field with the X-ray structure of the bright point having a good visual fit to the potential field extrapolation.

The temperature of the bright point was found to remain steady at around log T/K = 6.1

over the course of the cancellation suggesting that it was near isothermal. It was further concluded that the calculated temperature of the bright point was not necessarily the same as the peak formation temperature of the spectral lines in which it was observed. This reinforces the importance of carrying out detailed temperature analysis. The density of the bright point was calculated using the line ratio method and was found to have an average value of 5 ± 1 x 10^{9}cm^{-3} which was found to decrease by 40% over the course of the cancellation.

Doppler velocity changes of ±15 km s^{-1} in and around the bright point were observed to change on timescales shorter than could be observed. The time between consecutive EIS rasters was 30 minutes but even this relatively short time period was too long, with the corresponding Doppler velocity images showing large differences between files. The changes in the velocity flows could not be correlated with changes in the magnetic field for this reason.

Future expansion of this work could be achieved in two ways: further analysis of the XBP already studied, and including other bright points in the study for comparison and corroboration of results. These two options are detailed in the following sections.

7.1.1 Further morphology study

Using the various instruments onboard Hinode, the XBP's structure was examined at different atmospheric heights. The magnetic configuration of the upper photosphere was examined by looking at SOT/NFI Na I D line magnetograms, while the XBP's structure at coronal heights was investigated by looking at the various spectral lines imaged by EIS as well as the XRT imaging the bright point in several filters.

The comparison between the SOT Na I D 589.6Å magnetogram and the SoHO/MDI Ni I 6768Å magnetogram gave an additional perspective as the two spectral lines have different formation heights. Although the exact heights are still debated, it is thought

the MDI Ni I 6768Å line forms at around 125 km above the visible solar surface while the SOT Na I D 589.6Å line forms higher up between 300-500 km. No difference in the XBP shape from these two observations was detected due to the large difference in resolution between the two instruments. However, relying on magnetograms and coronal observations leaves an important portion of the atmosphere out - namely the chromosphere/transition region. The EIS He II 256.32Å line (T_{max} ~4.9) gives an important glimpse of the structure of the bright point in the chromosphere and showcases the bipolar structure interpreted as the footpoints of the XBP.

This study could be taken further by utilising other spectral regions that can be imaged by the SOT. As described in Section 2.2.2, these observations cover a number of wavelengths relating to photospheric and chromospheric heights. By combining observations from different instruments, we can follow the structure of the XBP from the photosphere, up through the chromosphere and transition region to the corona. Figure 7.1 shows a series of images taken at a particular instance in the observation period (11-Oct-2007 06.15 UT) progressing from low photospheric/chromospheric heights up to high coronal regions.

The top row shows three examples from SOT: (a) the Na I D chromospheric magnetogram showing the ongoing cancellation of the positive and negative polarities of the XBP, (b) the G-band 4305Å line showing the granulation pattern of the photospheric network with the outline of the two polarities overplotted, (c) the Ca II H 3968Åline also with the polarity contours overplotted. There are brightenings observed in both the G-band (around the granules) and Ca II H images in the areas outlined by the magnetic contours suggesting that strong magnetic fields are located in the same areas throughout the lower atmosphere.

The next two images (panels (d) and (e)) have been taken with EIS and show the XBP observed in He II 256.32 (log T/K = 4.9) and Fe XII 195.12 (log T/K = 6.2) lines, representing the chromosphere and corona respectively. It can be seen the XBP structure

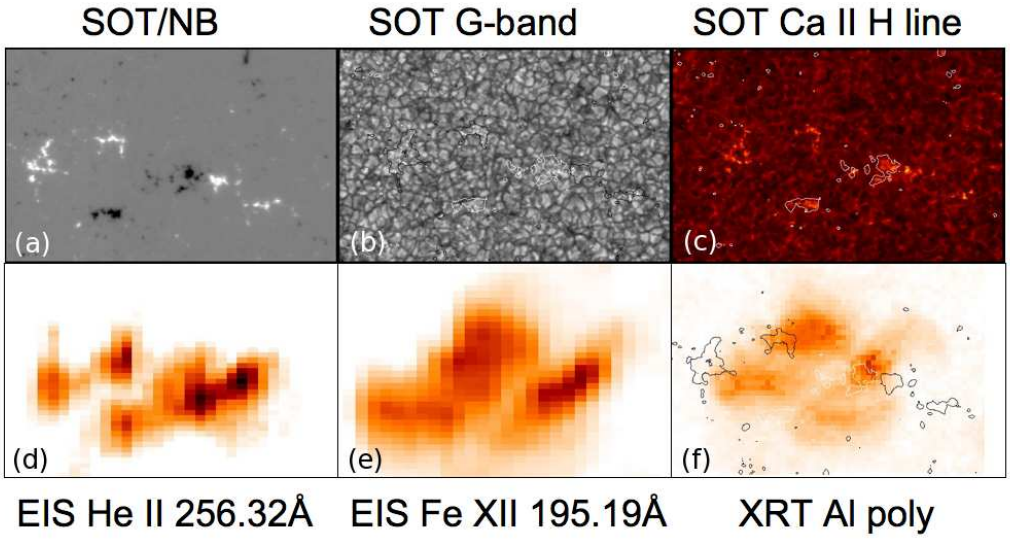

Figure 7.1: Series of images of the XBP at increasing atmospheric heights imaged with Hinode. The G-band and Ca II images have previously not been included in the analysis.

changes as the atmospheric height increases - in He II the bipolar structure of the XBP can be clearly seen but is not visible in Fe XII. Image (f) is taken with the Hinode X-ray Telescope (XRT) Al-poly/open filter and represents the hot coronal component of the bright point. Again the contours of the SOT/NB magnetic fragments have been overplotted to show the overall relation between the location of structures at the highest and lowest atmospheric heights observed.

Figure 7.1 shows a quick glance at the different structure of the bright point at various heights but this could be taken further by looking at how these different structures change over time as the magnetic field cancellation proceeds. This would allow the structure to be tracked from the photosphere up to the corona and could provide some additional information on how the velocity flows relate to the underlying material.

7.1.2 Widening the scope of this work

Expand study to include many more examples

Although the investigation into the structure and evolution of the XBP observed on the

11-Oct-2007 was thorough, it only involved one example and is therefore a case study rather than a full exploration of general XBP traits.

The launch of the Solar Dynamics Observatory has opened up the possibility of performing large-scale (possibly automated) surveys of XBPs. The high spatial and temporal resolution of the AIA instrument means that the emergence, lifetime and disappearance of XBPs could be studied to get a more statistically accurate picture of their structure and evolution. Although measurements of the bright point's temperature, density and velocity flows would not be possible without spectroscopic information, a lot of information on XBP morphology in relation to the magnetic field (measured using SDO/HMI) could be gathered.

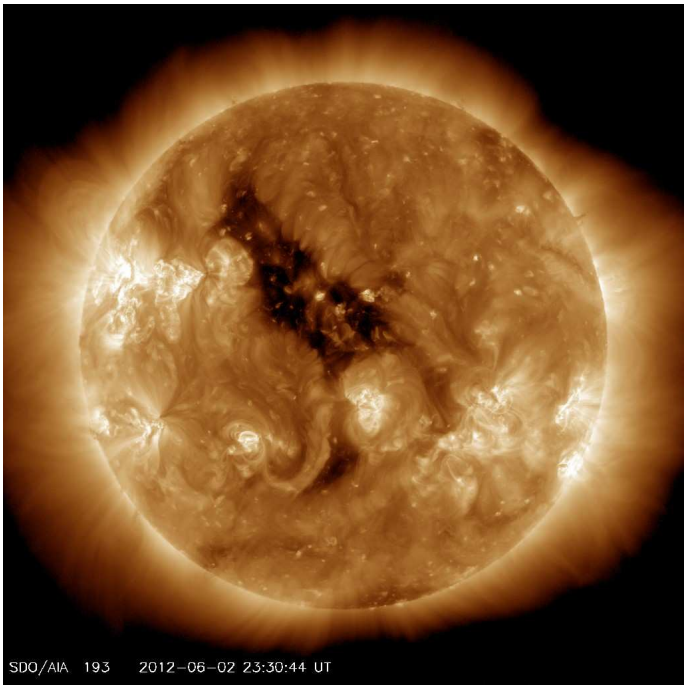

Figure 7.2: Full Sun image taken with the 193Å AIA channel showing a central coronal hole with many XBP visible all over the disc.

Figure 7.2 shows an example full-disc image taken in the SDO/AIA 193Å channel where many example of XBPs can be seen all over the disc. There even seems to be an example within the central coronal hole. Examining different types of XBP (both from cancelling and emerging magnetic fields) and also XBPs formed in different environments (e.g., quiet Sun, near active regions, and within the open field of coronal holes)

would allow for a fuller survey to be conducted. SDO can observe all these scenarios and study the entire evolution of many bright points as they move across the solar disc.

Deeper exploration into link between small-scale Doppler-motions and magnetic field

The investigation into the 11-Oct-2007 XBP could not link the Doppler motions observed to coronal magnetic field changes as these changes were observed to occur on timescales shorter than the EIS rasters could image. In order to investigate this further, additional XBP examples need to be observed either with specially designed EIS studies that will cover the area faster, or with one of the planned future spectrometers.

These include IRIS (Interface Region Imaging Spectrograph) which is to be launched in December 2012, and the spectrographs onboard Solar-C which has its provisional launch date set for Winter 2019. IRIS will be particularly good for examining flows especially in cooler lines and will be able to perform rapid raster scans with a cadence of 10 seconds. In combination with EIS it will be able to provide spectral information over all atmospheric heights. Solar-C will also image spectral lines from the photosphere up to the corona and will do so with a larger field-of-view and higher spatial resolution than IRIS. It is clear that the investigation of flows within XBPs will continue to be an interesting and viable research topic for many years to come and thus this work could easily be extended.

7.1.3 Relevant Future Missions for XBP work

There are numerous upcoming space missions that could facilitate the extension of the XBP work detailed above. In particular, the idea of exploring the structure and formation of XBP at lower atmospheric heights could be exploited by missions such as IRIS and CLASP which are designed to study the chromosphere and transition region. Solar-C will also be ideal for XBP work as it will contain similar but higher resolution

(in time/space) instruments than Hinode, allowing for the same type of case study to be performed in more detail than ever before.

IRIS

The Interface Region Imaging Spectrograph (IRIS) is an upcoming mission designed to obtain UV spectra and images that focus on the chromosphere and transition region. The satellite will obtain very high quality images with a spatial resolution of ~0.33" and temporal cadence of ~1 second. This would allow the fast evolving structure of XBPs in the lower atmosphere to be studied in much greater detail.

The main scientific objectives of IRIS are to study chromospheric features that are at the time/space resolution limit of current instrumentation. This will allow the structuring and dynamics of the chromosphere to be understood in more detail which will lead to progress in understanding how the magnetic field, and the mass and energy flows change at different atmospheric heights. The mission is expected to be launched in December 2012 and is a perfect complement so current missions such as SDO and Hinode.

CLASP

The Chromospheric Lyman-Alpha SpectroPolarimeter (CLASP, (Narukage et al. 2011)) is a sounding rocket experiment designed to measure the linear polarisation profiles of the Lyman-alpha line. The results from these measurements will allow the magnetic field in the upper chromosphere/transition region to be studied in detail for the first time.

This experiment is expected to be launched in Summer 2014 and will help to fill in the gaps of our current instrumentation. CLASP will be ideal to study the small-scale magnetic structure of XBPs in the chromosphere and could be used in combination with Hinode/SOT and SDO/HMI in order to track the magnetic field of an XBP throughout the solar atmosphere.

Solar-C[1]

The Solar-C mission is planned as a follow up to the highly successful Yohkoh (Solar-A) and Hinode (Solar-B) missions. Hinode has demonstrated the powerful combination that imaging and spectroscopic measurements can achieve so Solar-C has been designed to utilise the same combination of observables but at higher resolution. Gaps in the temperature coverage (particularly in the chromosphere/transition region) that current missions suffer from also aim to be addressed.

The satellite will fly three instruments:

- **SUVIT: Solar UV-Visible-IR Telescope.** This instrument will measure the chromospheric magnetic field by making intensity and spectro-polarimetric measurements of photospheric and chromospheric spectral lines. It will have 0.1”-0.2” spatial resolution and a cadence of 0.1-1 second for imaging and 1-20 seconds for SP. The field-of-view of the instrument is 180” x 180” which is comparable to Hinode/SOT. Figure 7.3 shows the main ways in which the two instruments differ.

- **EUVS/LEMUR: EUV/FUV High Throughput Spectroscopic Telescope.** This instrument will measure the intensity, velocity, temperature and density of solar plasma by analysing spectral lines in the wavelength range 17-21nm and 46-128nm. The instrument will have a spatial resolution of 0.28” and temporal resolution of <10 seconds (for 0.28” steps) and <1 second (for 1” steps). Figure 7.4 shows a comparison between this instrument and current UV spectrometers. This instrument would be ideal to address the issue found in Chapter 3 and detailed above in future work i.e., that Hinode/EIS could not track the plasma velocities quickly enough to observe the changes as they occurred within the XBP. This new instrument has much higher cadence so it is possible it would be possible to tie the velocity changes to the magnetic field changes.

[1]Information on Solar-C and its instruments as well as Figures 7.3 and 7.4 were found at http://hinode.nao.ac.jp/SOLAR-C/Documents/Solar-C_e.pdf

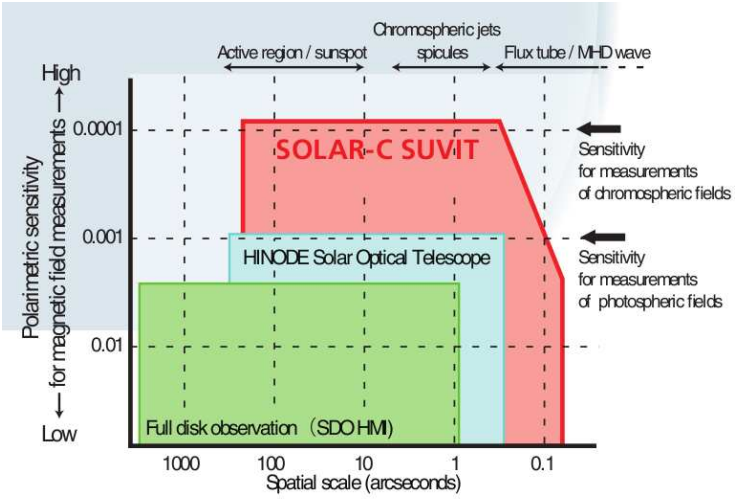

Figure 7.3: Comparison between Solar-C/SUVIT, Hinode/SOT and SDO/HMI in terms of magnetic sensitivity and the size of the features they can image. SUVIT will clearly take observations into new levels of detail. Image credit JAXA.

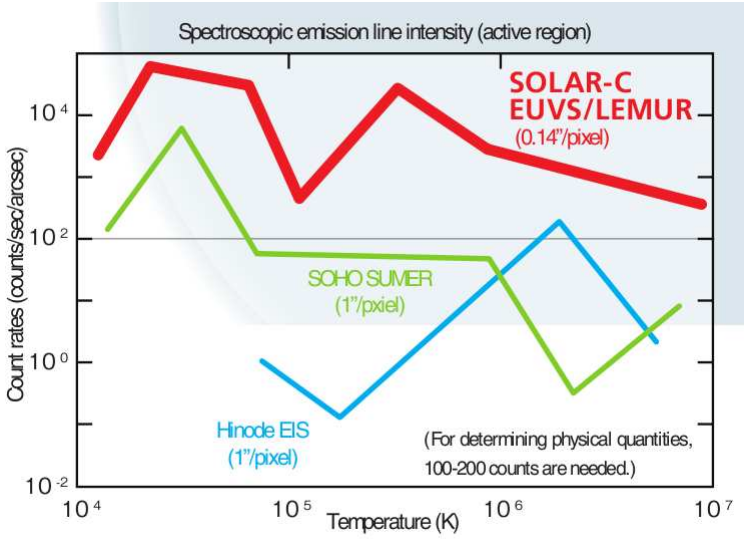

Figure 7.4: Comparison of Solar-C EUVS/LEMUR to current instrumentation. Image credit JAXA.

- **XIT: X-ray Imaging Telescope.** This instrument comprises of two parts - the Photon Counting Imaging Spectroscopy Soft X-ray Telescope (XIT-PC), and the Ultra High Spatial Resolution Normal Incidence EUV Telescope (XIT-NI). The XIT-PC will conduct the first x-ray imaging spectroscopic observations of the

corona allowing coronal structures across a wide range of temperatures to be studied. The XIT-NI will perform large field-of-view (400” x 400”) imaging of the X-ray corona at very high spatial resolution (0.2-0.3” compared to the Hinode/XRT’s 2” resolution.)

The provisional launch date for Solar-C is set for Winter 2019 which gives time for the observations gathered by other missions such as IRIS and CLASP to be thoroughly studied. Solar-C will help to bridge any remaining gaps in the observations and enable scientists to study the whole solar atmosphere at high resolution. This will hopefully allow fundamentals about heating and mass/energy flows to be uncovered and move our understanding of the Sun forward another step.

7.2 Work on DEMs with the MSHD simulation

The work described in Chapter 4 involved the investigation of the parameter space of the MSHD simulation and how changes in various parameters affected the resulting DEM distributions and intensity values. As the model parameter space was altered, a number of changes in the resulting DEMs were observed. In most cases these changes were subtle and could be explained by the changing physics of the system. The cooling simulation showed the most unique changes where the total energy of the system could be identified by examining the evolution of the intensity values and DEM shape.

The results from the various investigations of parameter space were then used to measure the effectiveness of a particular DEM solver code. The iterative solver code XRT_DEM_iterative2.pro was examined for a number of the simulations and it was found that in the majority of cases it did an excellent job of reconstructing the original model intensity values and DEM distribution. The only instance where the solver did not do well was in the case where the model DEM was very narrow i.e., only covering a few temperature bins. This highlights the under-constrained problem of using DEM solvers and

shows that this particular solver works best when the original DEM being reconstructed is smoother and more multithermal.

There are a number of ways in which this work could be taken forward in the future which are described in the following sections.

7.2.1 Exploring the cooling simulation further

Section 4.2.5 detailed the investigation into a subset of the simulations that had had their nanoflare energy releases moved into the first quarter of the simulation rather than uniformly over the entire simulation time. This allowed the behaviour of the loop as it cooled to be observed and described in terms of the corresponding intensity and DEM distribution changes.

This type of 'cooling' simulation was only performed for three cases where the total energy going into each simulation was the variable factor i.e., strand number, number of bursts, and location of heating was kept the same, while the total energy was increased by an order of magnitude each time by increasing the average nanoflare energy by the same order.

In future work, it would be very interesting to observe the cooling behaviour of the other simulations which explore additional model parameters. Viall & Klimchuk (2011) also studied a simulated cooling loop and found a similar result to that presented in Section 4.2.5 where the total energy going into the simulated loop had a unique effect on the order of the intensity peaks in each channel. Additional authors such as Winebarger et al. (2003b), Aschwanden et al. (2000b), Schrijver (2001), and Landi et al. (2009) have also studied observations of cooling plasma so it would be interesting to compare their observations to the results of the cooling MSHD model to test the validity of the model further.

7.2.2 Testing other DEM solvers - a first look

Chapter 5 described the comparison between the results from the MSHD model and the outputs of the iterative solver XRT_DEM_iterative2.pro. In the majority of cases the iterative solver was able to provide a solution that matched the model intensity and DEM distribution well. It was only in cases where the model DEM was particularly narrow that the solver was less effective.

Another type of solver that was described in Section 5 is called the Convex-hull solver and is a direct inversion method as opposed to an iterative method. This solver runs much faster than the iterative one so it would be interesting to see if it matches the model DEM and intensity values just as well. Figure 7.5 shows some preliminary results based on giving the solver code the intensity values from the MSHD model case study data.

The top two plots show two example DEM solutions out of the hundreds that were calculated by the Convex-hull solver. They show that even though both solutions are equally valid (in that they can both reproduce the original model intensity values when folded back through the temperature response), their distribution over the temperature bins can be very different. The bottom-left plot shows all the Convex-hull DEM solutions overplotted on one another and is useful to give a first indication of which bins are the most important to the fit. These are the bins in which many of the solutions have a contribution and can be identified by the high-number of plots creating a darker line as in LogT=6.2. The bottom-right plot shows these solutions overplotted with the original DEM from the case study. It can be seen that the solver seems to match the DEM distribution in many of the bins.

The goodness-of-fit between the Convex-hull solutions and the original MSHD DEM is harder to quantify than with the iterative solver. As shown in the top two plots of Figure 7.5, the Convex-hull solutions are not spread evenly over all the temperature bins. Each DEM solution has a non-zero component in six temperature bins which varies from

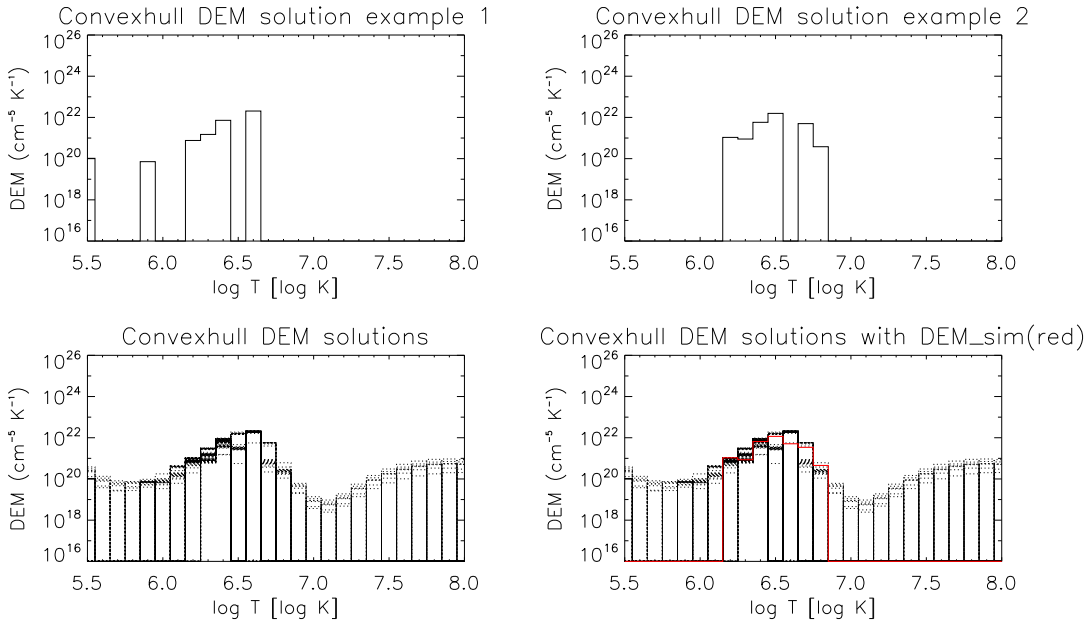

Figure 7.5: Example of results from Convex-hull solver. Top plots show two example solutions. Bottom-left plot shows all the valid solutions overplotted while the bottom-right plots shows these solutions overplotted with the original MSHD DEM from the case study these solutions are based on.

solution to solution.

The case study in Section 5.2 detailed how to identify which temperature bins are most important for the model DEM and based on this, many of the Convex-hull solutions can be eliminated i.e., only solutions with non-zero contributions in the important bins could be considered further. Figure 7.6 shows a more detailed comparison between the solver solutions and the model DEM. This plot shows the 20 Convex-hull solutions out of the 123 calculated, that fulfill this criteria. They are overplotted on the MSHD model DEM which has been coloured according to temperature bin importance. It can be seen that in the most important bins (coloured red), the solver solutions come close to the real values in many cases.

Future work would aim to quantify this fit and come up with a definitive way to identify the best solution out of the series the Convex-hull solver produces. As with the investigation of the iterative solver, conclusions on the Convex-hull solver's applicability to real data would have to be quantified i.e., if no 'real' DEM is available for comparison,

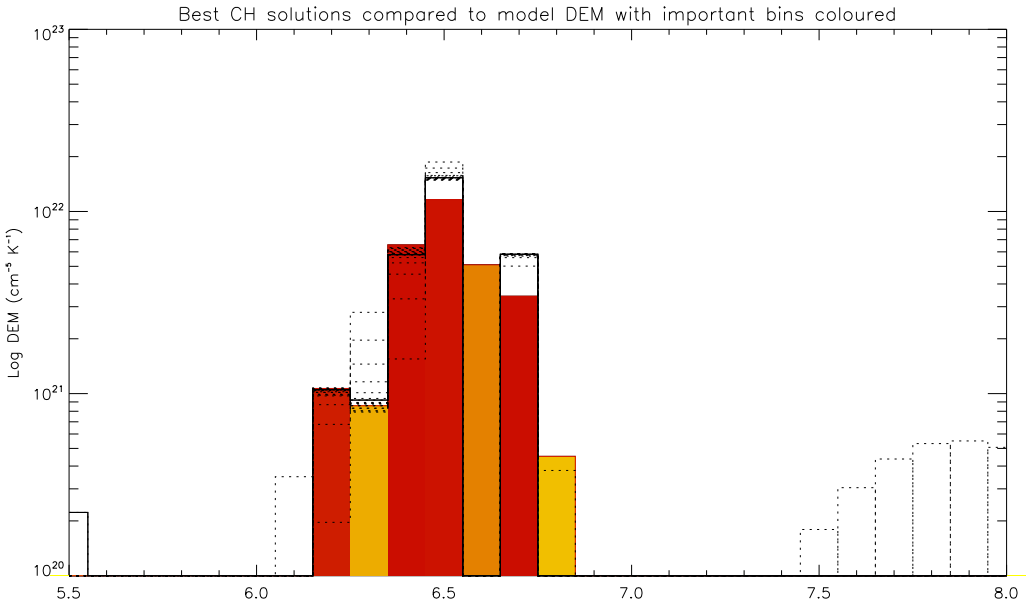

Figure 7.6: Plot showing the MSHD model DEM coloured according to temperature bin importance overplotted with the 20 Convex-hull solutions (out of 123) which had non-zero contributions in the four most important bins.

how would the best solution be identified?

7.2.3 Application to real observations

In order to properly tie together (i) the work on investigating the parameter space of the MSHD model and (ii) the investigation of the ability of the iterative solver to reconstruct the model values, real examples of SDO/AIA data should be looked at. Future work on this topic will cover a number of examples of loops with similar lengths/widths to the model i.e., either by looking for 100Mm long loops in the data or adjusting the model length/width to match the observations.

Figure 7.7 shows an example of a loop observation taken with SDO/AIA in the six channels used by the DEM solvers. The small box in each plot represents an area of the loop footpoint where the intensity in each channel was averaged over 9 pixels. The large box in the 211Å channel shows the area used to measure the background

intensity in each channel. This loop region is perhaps not the best example to use due to the complicated structure of the loops within the active region. The footpoint region highlighted was chosen as there seemed to be many overlying loops whose appearance varied from channel to channel i.e., in this case there was not a clear loop to pick whose position was the same in each channel.

The six values of intensity from this observation were then passed to the Convex-hull and iterative solvers to see what they would interpret. Figure 7.8 shows the results of the solver fits. The top plot shows the collection of solver solutions from the Convex-hull code, the middle plot shows the solutions from the iterative solver code, and the bottom plot shows the two sets of solutions overplotted for comparison.

It can be seen that the overall pattern displayed by both solver solutions is very different. However, this does not infer that the two solvers have interpreted the data differently as these plots show all 101 solutions of the iterative solver and all 1878 solutions of the Convex-hull solver. The case study in Section 5.2 outlined how to cut the number of iterative solvers down to the set of 'best' solutions and so future work would aim to do the same for the Convex-hull solutions.

However, these solutions cannot be cut down to a smaller sample size based on how well they reconstruct the original intensity values as each solution does an equally good job. Perhaps one way to cut down the solutions would be to keep the ones that have the smoothest progression across temperature (i.e., not the solutions with the 'picket-fence' type distribution seen in the top-left plot of Figure 7.5) or solutions that don't have contributions at less physically likely temperatures i.e., over logT=7. This cut off would obviously be scaled depending on the type of target being analysed i.e., quiet Sun compared to active region or flare site.

Future work will involve (i) processing data of similar examples of long-lived loop structures observed with AIA (ideally at least 15-20 examples), (ii) calculating the background-corrected intensity values observed along the loop (ideally averaging over

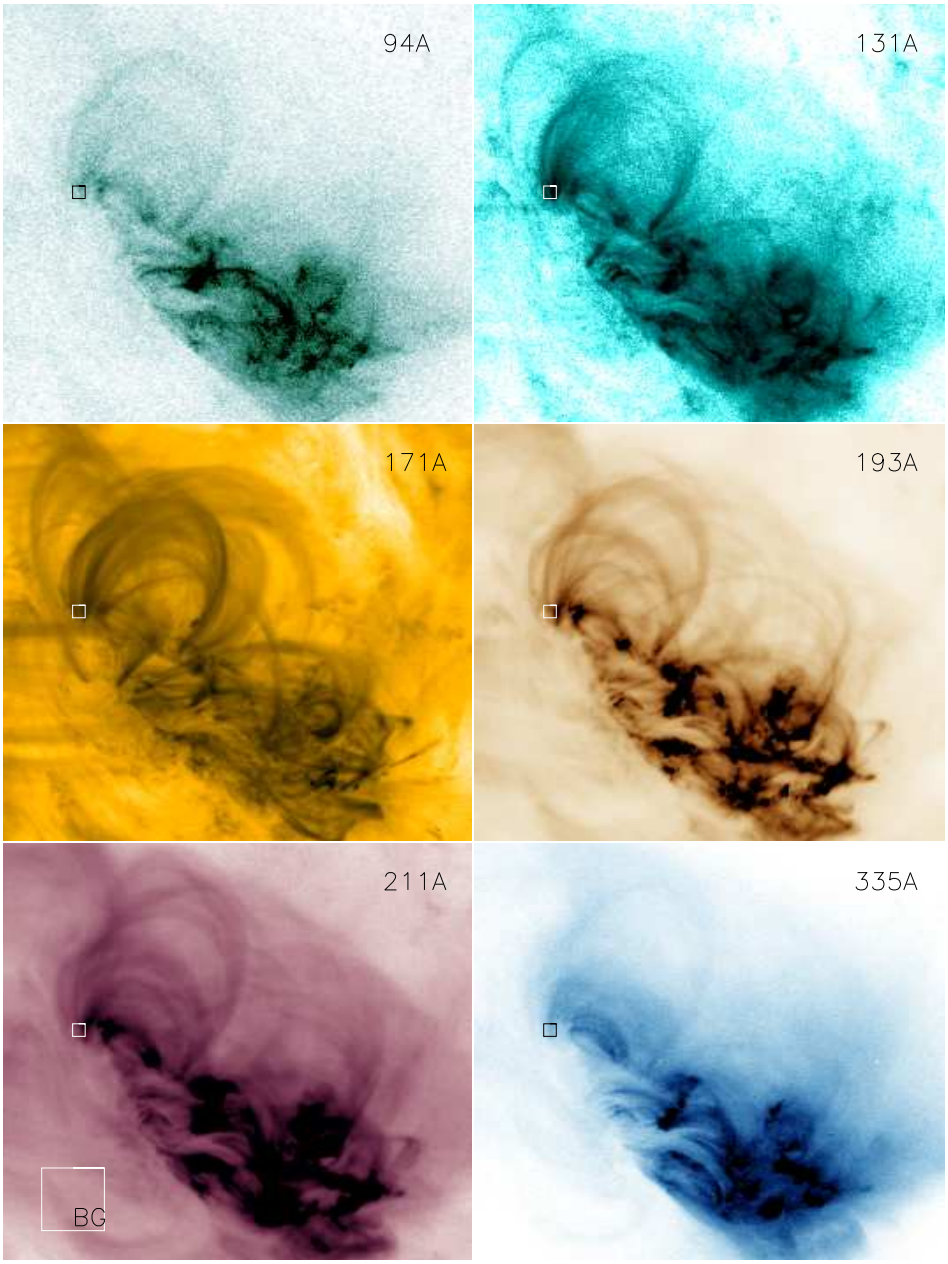

Figure 7.7: SDO/AIA observations of loops within an active region in the six channels required for reconstruction by DEM solver. The small box in each case shows the pixels chosen to be examined while the large box in the 211Å frame shows the location of the area chosen to represent the background intensity levels.

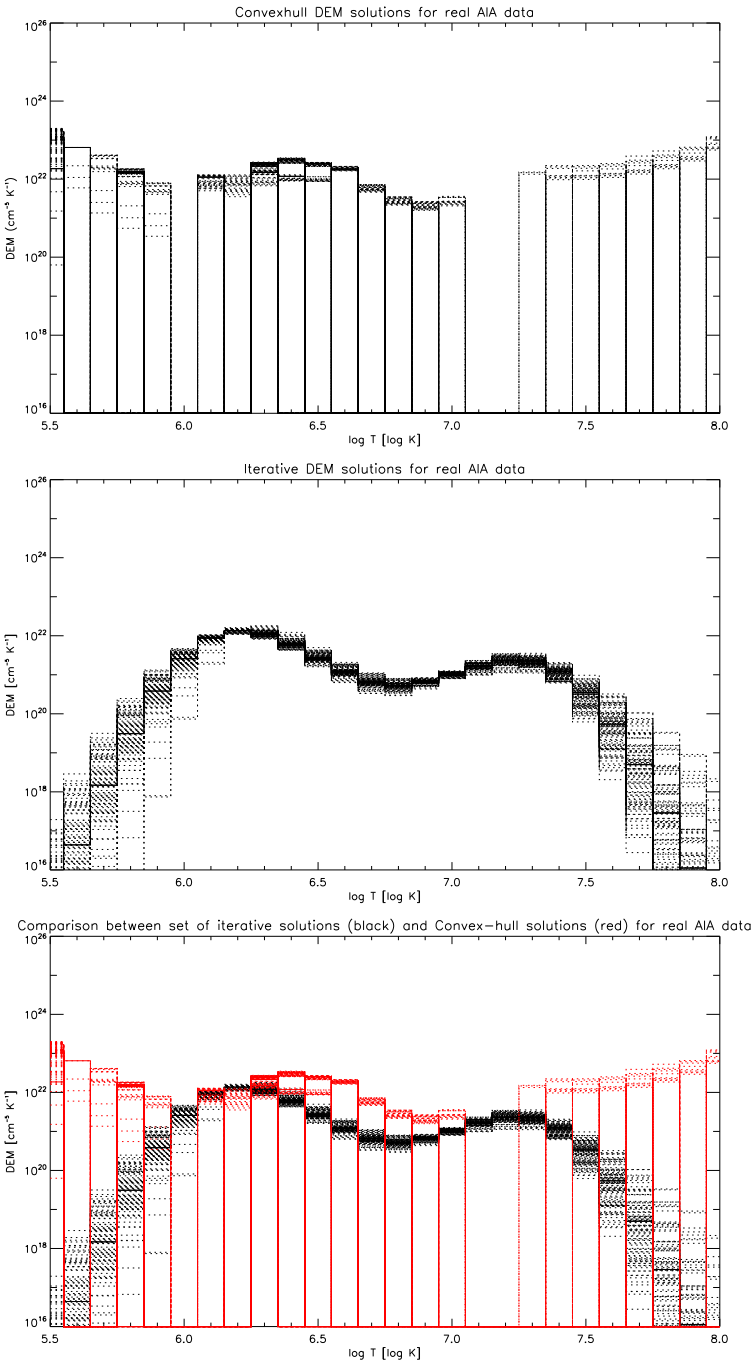

Figure 7.8: First look at results with solver codes applied to real AIA data. Top plot shows the collection of solver solutions from the Convex-hull code, the middle plot shows the solutions from the iterative solver code, and the bottom plot shows the two sets of solutions overplotted for comparison.

several pixels and multiple exposures to avoid erroneous fluctuations), (iii) using these intensities in conjunction with the two DEM solvers in order to get an idea of the temperature distribution of the plasma, (iv) finding an accurate way to reduce the number of Convex-hull solver solutions to the most physically likely ones, and (v) tying the MSHD model into the real observations by using the AIA data to constrain the model.

The under-constrained nature of the solvers will also be addressed by including data from other instruments in order to try and constrain the high and low temperature regions. The inclusion of spectra from Hinode/EIS in the analysis would allow a more accurate determination of the limits of the DEM. Plotting EM loci curves in conjunction with a DEM distribution created from imager data would help to constrain the shape of the DEM as the characteristic temperature of the spectral data is much more accurate than using imager temperature response functions which can include multiple spectral lines. EIS can image a large number of spectral lines over a wide range of formation temperatures while the thicker filters of XRT can provide additional information on the behaviour of the hotter plasma. The inclusion of data from both these instruments (EIS and XRT) as well as using AIA data would allow the most accurate spread of plasma temperature to be concluded.

7.2.4 Relevant Future Missions for Loop work

As well as being ideal for XBP analysis, future missions such as IRIS, CLASP and Solar-C (detailed above), will provide high quality data that could be used to extend the loop/DEM work presented in Chapters 4 and 5 in a number of ways. The improved accuracy of the spatial resolution of these instruments will make the multi-stranded nature of the corona much clearer and comparison with multi-stranded models more applicable. The higher quality spectra Solar-C will obtain will also be ideal to help further constrain the DEM of observed plasma.

A very recent mission named The High Resolution Coronal Imager (Hi-C)[2] was launched on the 11th of July 2012 on a NASA sounding rocket from the White Sands Missile Range in New Mexico.

The mission has been a collaborative effort between NASA, UCLan and the Harvard Smithsonian Astrophysical Observatory and aims to observe the solar corona with the highest spatial resolution ever achieved. The rocket flight will allow the telescope to observe a partial view of the Sun in 193 Å for a total of ~10 minutes before coming back down to Earth to be collected. This will produce around 6 images per minute with a spatial resolution of 0.2-0.25" (i.e., 5 times better than SDO/AIA).

The aims of this mission are to (i) observe very fine-scale structures in the corona to see if the multi-stranded nature of coronal feature can be quantified, and (ii) to test out the imager technology for the next generation of solar imagers. This first objective ties in very well with the multi-stranded work already performed and would allow future work on the MSHD model to be compared to observations that best illustrate the multi-stranded nature of coronal loops.

7.3 Prominence work

The work carried out to examine the eruption of the polar-crown prominence observed on the 13 June 2010 observed the structure of both the prominence and its overlying cavity in multiple wavelengths as the structure evolved over time. The cavity was found to be an area of depleted density above the main prominence material. The eruption of this structure was observed as a slow rise followed by an acceleration phase which led to the release of a coronal mass ejection. The eruption was observed by SDO/AIA and STEREO-A/EUVI with the dual points-of-view of the two instruments providing a very

[2]Information on Hi-C was attained from various online resources such as the NASA press release at http://www.nasa.gov/centers/marshall/news/news/releases/2012/12-064.html

useful perspective on the changing structure of the prominence.

Many possible initiation methods were looked at to see if the cause of the prominence eruption could be pinned down. An EUV wave originating in the southern hemisphere was found to have no connection to the eruption as it arrived at the polar-crown area after the eruption was well underway. Tether-cutting of the prominence barbs was also ruled out as the prominence is observed to rise before the barbs undergo any 'cutting'. It is concluded that the most likely cause of the eruption is a combination between mass un-loading (due to the flows of material observed to move from the prominence to the solar surface) and a form of kink-instability (inferred due to the exponential nature of the cavity rise observed).

This section outlines the ways in which the investigation of the erupting polar-crown prominence could be expanded upon in the future.

7.3.1 Expansion of work done so far

The investigation of the prominence eruption on the 13 June 2010 had many components. The eruption was not observed in isolation as there were numerous regions of activity on the Sun at the time which may or may not have been interlinked. The investigation looked into various trigger mechanisms and concluded that the most likely causes were a combination of mass un-loading and some type of kink instability. Future work on this subject could look into a number of details more closely.

Barb Oscillation Investigation

The behaviour of the prominence barbs was studied and a periodicity was observed to be present before the prominence erupted. This motion is not necessarily indicative that the barb structures are oscillating - the same motion could be observed when looking at the the barb being stretched upwards and untwisting. Whatever the cause, identifying

if the motion is truly present can be confirmed by the use of wavelet analysis. This is a type of Fourier analysis which allows the time dependence of existing periods to be studied. Figure 7.9 shows the first results of running the oscillation pattern seen in Figure 6.21 through a wavelet analysis code (figure provided by Mike Marsh, UCLan).

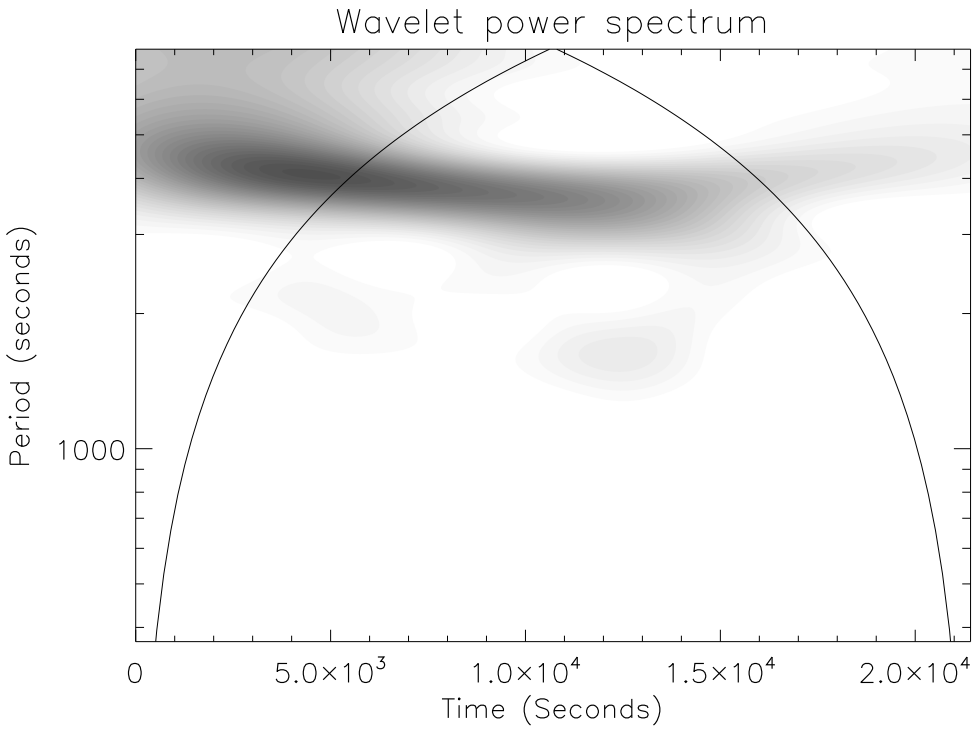

Figure 7.9: Wavelet power spectrum for the prominence oscillation highlighted in Figure 6.21. The curved solid lines represent the cone of influence within which the data can be relied upon. The power shown at the 4000s period mark suggests an oscillation is present.

The curved line in the plotting area represent the cone of influence and indicate that only data within this area should be relied upon. The x-axis refers to the time range the data is over while the y-axis gives the corresponding period detected. A fuller explanation of this type of plot can be found in Marsh et al. (2002, 2003). This shows that there is a clear signal (dark grey area) at around 4000 seconds which ties into the ~60 minute period described in Table 6.2. This first look demonstrates that oscillations are present and will be investigated further to see what it can add to the discussion of the changing barb structure in relation to the eruption.

Further investigation of associated phenomena

As stated previously, there are a lot of different structures/events occurring on the Sun around the time of the eruption. In particular, the trans-equatorial loop seen in Figures 6.8 and 6.14 is a factor that was not fully explored in Chapter 6.

Figure 7.10 shows the western limb of the Sun as seen by SDO/AIA in 171Å. The trans-equatorial loop connecting the southern and northern hemispheres can be seen in both the difference image (left) and the normal 171Å image (right). This loop is long-lived and indicated that the two hemispheres are magnetically linked. The magnetic connection of the loop appears to change after the EUV wave passes by it on its way North. It is possible that this magnetic connectivity between the two hemispheres could allow information on the SH flare to run ahead of the EUV wave meaning that the prominence eruption could at least be influenced by the wave even if it was not the cause. This is purely speculative so future work could look more closely at any possible flows along the trans-equatorial loop and investigate its magnetic connectivity in more detail.

CME associated with prominence eruption

After the prominence eruption, a large coronal mass ejection is observed. This is shown in Figure 7.11 where it is observed by SoHO/LASCO C2 and C3. This could form another aspect to the investigation of the eruption as the structure and speed of the CME could be linked back to the prominence shape and eruption speed.

7.3.2 Expansion of work into other examples

As with the XBP work, the study of the erupting prominence observed in the polar-crown on the 13 June 2010 was thorough but only included one example. In order to

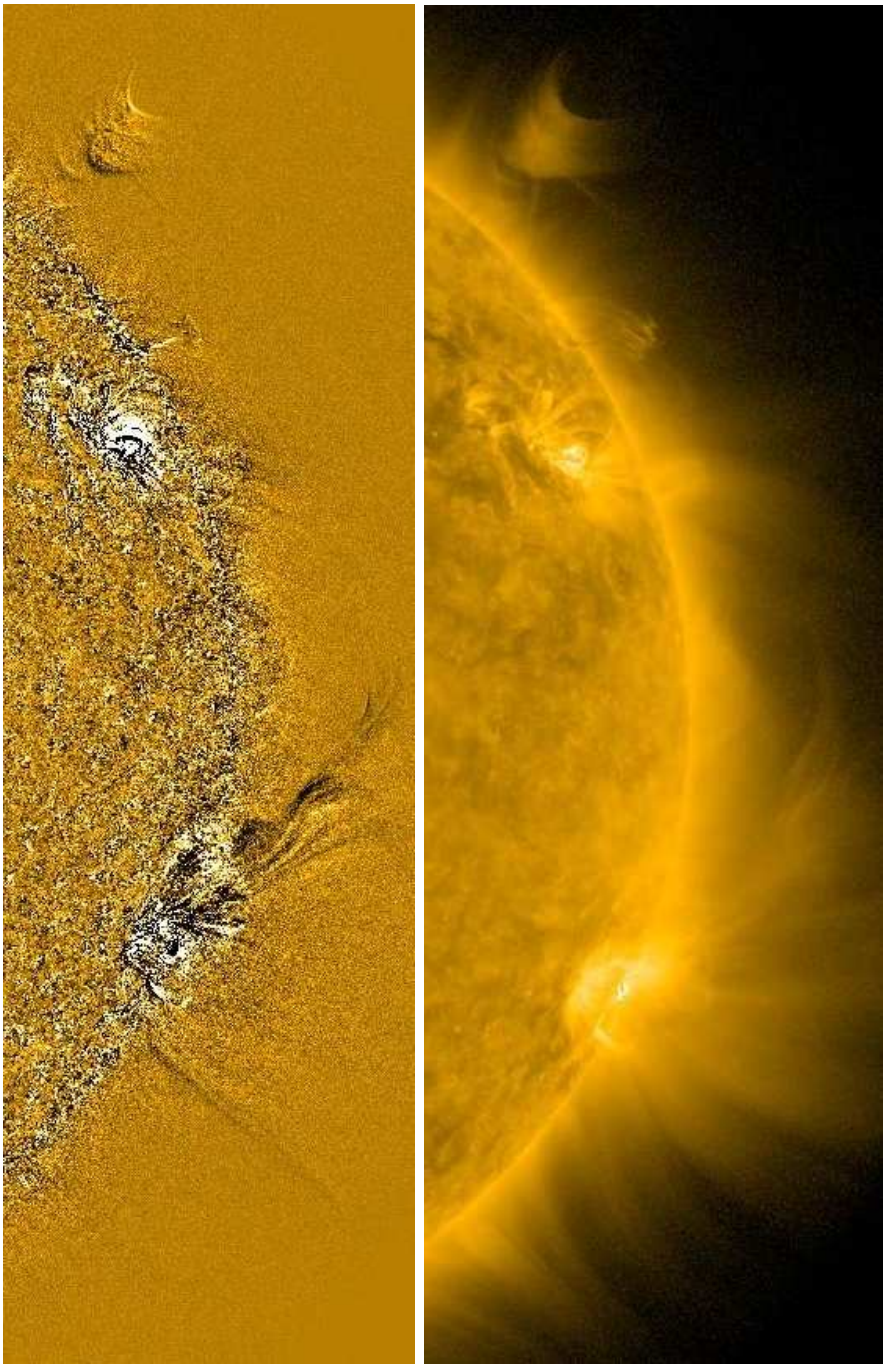

Figure 7.10: Figure showing the Western edge of the Sun where a trans-equatorial loop is seen. The left-hand plot shows a difference image of the loop seen in SDO/AIA 171Å while the right-hand plot shows the original image.

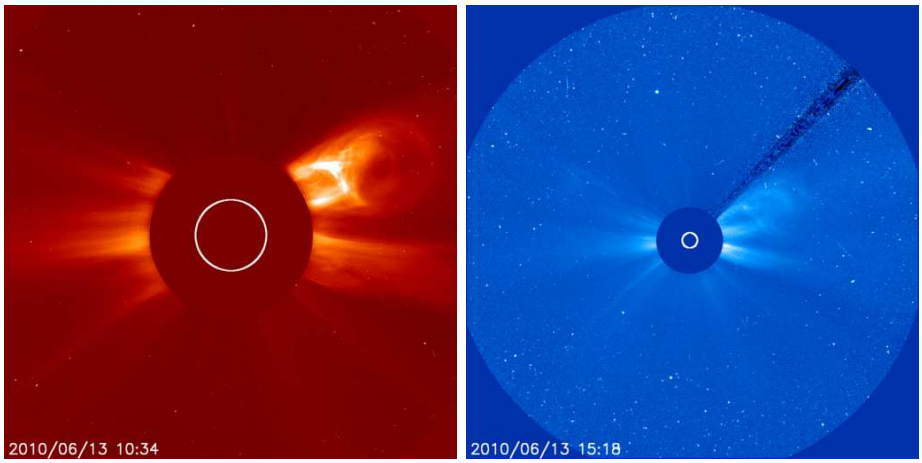

Figure 7.11: SoHO/LASCO images of the CME resulting from the prominence eruption seen in C2 (left) and C3 (right).

fully investigate the cause of the eruption, similar cases of polar-crown prominence/-cavity eruptions could be investigated.

With SDO in place, prominence cavities are more easily observed. Previously instruments such as SoHO/EIT also observed cavities but these were harder to see due to the reduced resolution of the instrument. Figure 7.12 shows a comparison of the full-disc Sun seen at 171Å in EIT (left) and AIA (right). The AIA image shows the prominence cavity and barbs much more clearly suggesting that AIA would be able to detect (perhaps automatically) many more of these structures for comparison.

The improvement of AIA over EIT is further shown in Figure 7.13 where a close up of the prominence can be seen in both 171Å (right) and 304Å (left). The AIA images show the fine detail of the U-shaped structure of the prominence material much more clearly than EIT.

Additional studies of prominence eruptions would ideally have concurrent spectroscopic and magnetic observations as well as thorough coverage by SDO and one of the STEREO satellites. This would allow for a 3D interpretation of the eruption to be viewed.

Once many examples observed with multiple instruments have been analysed, this information could be used alongside various models in order to examine the structure and

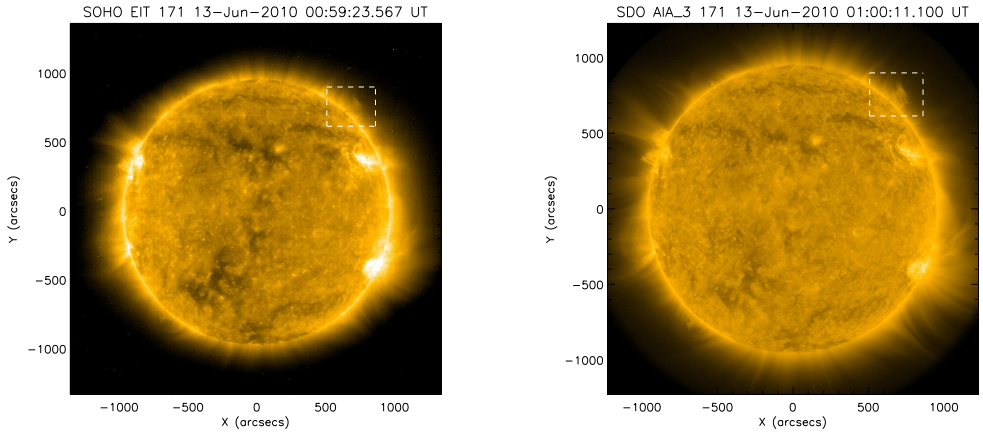

Figure 7.12: Comparison between full-disc SoHO/EIT 171Å (left) and SDO/AIA 171Å (right) for identification of the prominence cavity. The cavity and barbs are seen more clearly in the AIA image due to its higher resolution.

possible release mechanisms more closely.

7.3.3 Relevant Future Missions for Prominence work

Chapter 6 outlined the importance of combining observations when analysing prominence eruptions, particularly the importance of two points-of-view. In the future, STEREO may not be available to offer an additional perspective as the angular separation of both satellites from Earth will be too large to complement Earth/L1 bound satellite observations (although some instruments may be turned back on once the pair have returned from the far-side of the Sun). No follow up is currently planned for STEREO so future missions will have to improve upon current prominence observations by utilising the increased imaging and temporal resolution that missions such as IRIS, CLASP and Solar-C (detailed above) will provide. This will allow the small-scale and fast evolving features of prominence eruption to be studied in more detail i.e., the evolution of the barb structures and the possible flow of mass to and from the prominence.

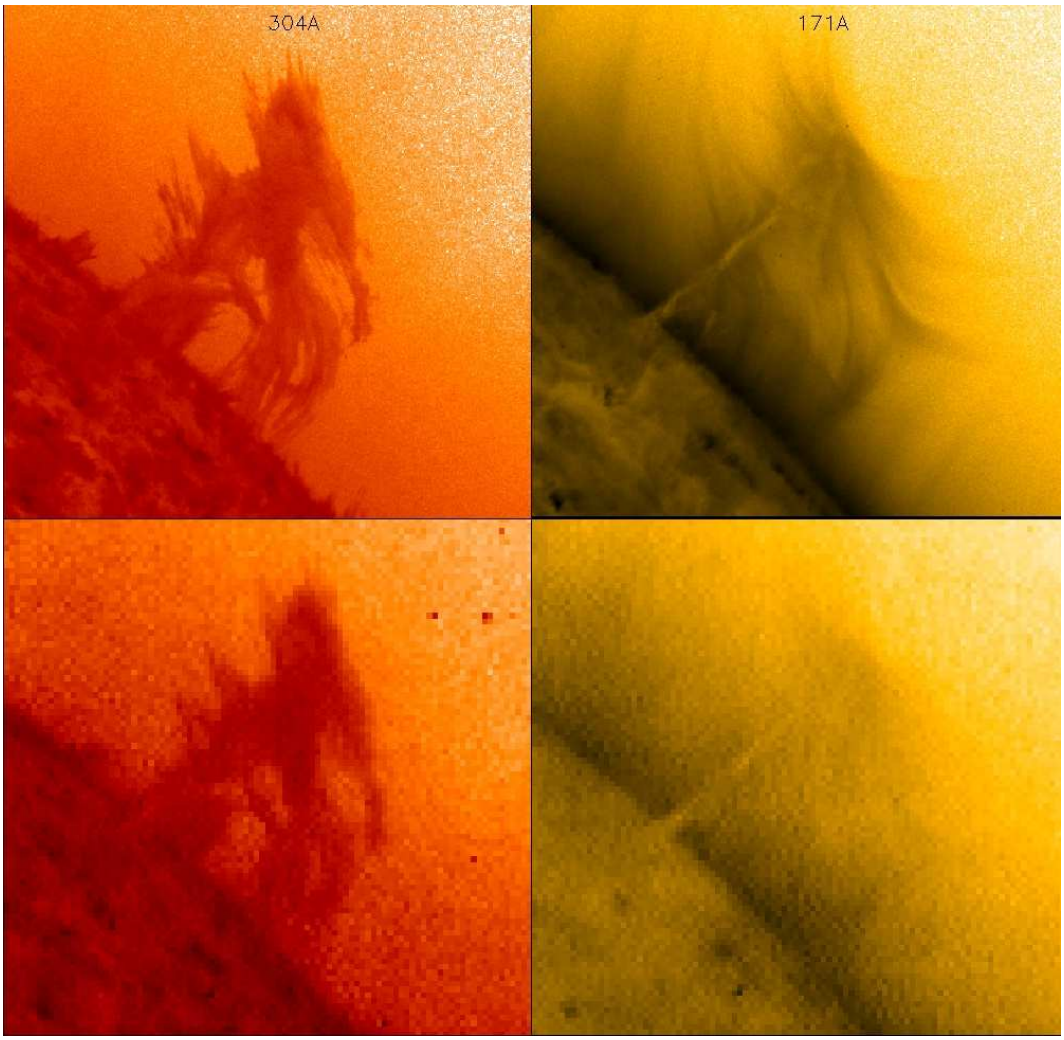

Figure 7.13: Top: Close up of prominence with SDO/AIA in 304Å (left) and 171Å (right). Bottom: same field-of-view observed with SoHO/EIT in the same channels.

Appendix A

List of published articles from this work

Copies of the published journal articles written during the course of this work are included in this section:

1. Alexander et al. (2011), ‘Hinode observations and 3D magnetic structure of an X-ray bright point’.
   Available at: http://adsabs.harvard.edu/abs/2011A%26A...526A.134A

2. Régnier et al. (2011), ‘A new look at a polar crown cavity as observed by SDO/AIA. Structure and dynamics’.
   Available at: http://adsabs.harvard.edu/abs/2011A%26A...533L...1R

The End

Bibliography

Alexander, C. E. 2008, *MSc. dissertation, UCL.*, ,

Alexander, C. E., Del Zanna, G., & Maclean, R. C. 2011, *Astron. Astrophys.*,, 526, A134

Arber, T. D., Longbottom, C. L., Gerrard, C. L., & Milne, A. M. 2001, *Journal of Computational Physics*, 171, 151

Aschwanden, M. J. 2008, Journal of Astrophysics and Astronomy, 29, 3

Aschwanden, M. J. & Boerner, P. 2011, *Astrophys. J.*,, 732, 81

Aschwanden, M. J., Nightingale, R. W., & Alexander, D. 2000a, *Astrophys. J.*,, 541, 1059

Aschwanden, M. J., Nitta, N. V., Wuelser, J.-P., & Lemen, J. R. 2008, *Astrophys. J.*,, 680, 1477

Aschwanden, M. J. & Parnell, C. E. 2002, *Astrophys. J.*,, 572, 1048

Aschwanden, M. J., Schrijver, C. J., & Alexander, D. 2001, *Astrophys. J.*,, 550, 1036

Aschwanden, M. J., Schrijver, C. J., Winebarger, A. R., & Warren, H. P. 2003, *Astrophys. J. L.*,, 588, L49

Aschwanden, M. J., Tarbell, T. D., Nightingale, R. W., et al. 2000b, *Astrophys. J.*,, 535, 1047

Aschwanden, M. J., Winebarger, A., Tsiklauri, D., & Peter, H. 2007, *Astrophys. J.*, 659, 1673

Babcock, H. W. 1961, *Astrophys. J.*, 133, 572

Biesecker, D. A., Myers, D. C., Thompson, B. J., Hammer, D. M., & Vourlidas, A. 2002, *Astrophys. J.*, 569, 1009

Bougeret, J. L., Goetz, K., Kaiser, M. L., et al. 2008, *Space Sci. Rev.*, 136, 487

Brosius, J. W., Rabin, D. M., & Thomas, R. J. 2007, *Astrophys. J. L.*, 656, L41

Brown, D. S., Parnell, C. E., Deluca, E. E., Golub, L., & McMullen, R. A. 2001a, *Solar Phys.*, 201, 305

Brown, D. S., Parnell, C. E., Deluca, E. E., Golub, L., & McMullen, R. A. 2001b, *Solar Phys.*, 201, 305

Cargill, P. J. 1994, *Astrophys. J.*, 422, 381

Cargill, P. J. & Klimchuk, J. A. 1997, *Astrophys. J.*, 478, 799

Cargill, P. J. & Klimchuk, J. A. 2004, *Astrophys. J.*, 605, 911

Carmichael, H. 1964, NASA Special Publication, 50, 451

Chae, J., Denker, C., Spirock, T. J., Wang, H., & Goode, P. R. 2000, *Solar Phys.*, 195, 333

Chae, J., Moon, Y.-J., Park, Y.-D., et al. 2007, *Pub. Astron. Soc. Japan*, 59, 619

Charbonneau, P., McIntosh, S. W., Liu, H.-L., & Bogdan, T. J. 2001, *Solar Phys.*, 203, 321

Chen, P. F. 2006, *Astrophys. J. L.*, 641, L153

Cheng, C.-C. 1980, *Astrophys. J.*, 238, 743

Cirtain, J. W., Del Zanna, G., DeLuca, E. E., et al. 2007, *Astrophys. J.*, 655, 598

Cook, J. W., Cheng, C.-C., Jacobs, V. L., & Antiochos, S. K. 1989, *Astrophys. J.*,, 338, 1176

Culhane, J. L., Harra, L. K., James, A. M., et al. 2007, *Solar Phys.*,, 243, 19

Del Zanna, G. 2003, *Astron. Astrophys.*,, 406, L5

Del Zanna, G. 2008a, *Astron. Astrophys.*,, 481, L69

Del Zanna, G. 2008b, *Astron. Astrophys.*,, 481, L49

Del Zanna, G., Landini, M., & Mason, H. E. 2002, *Astron. Astrophys.*,, 385, 968

Del Zanna, G. & Mason, H. E. 2003, *Astron. Astrophys.*,, 406, 1089

Del Zanna, G. & Mason, H. E. 2005, Advances in Space Research, 36, 1503

Del Zanna, G., O'Dwyer, B., & Mason, H. E. 2011, *Astron. Astrophys.*,, 535, A46

Delaboudinière, J.-P., Artzner, G. E., Brunaud, J., et al. 1995, *Solar Phys.*,, 162, 291

Dennis, B. R. 1985, *Solar Phys.*,, 100, 465

Dere, K. P. 2008, *Astron. Astrophys.*,, 491, 561

Dere, K. P. 2009, *Astron. Astrophys.*,, 497, 287

Dere, K. P., Landi, E., Mason, H. E., Monsignori Fossi, B. C., & Young, P. R. 1997, *Astron. Astrophys. Suppl.*,, 125, 149

Domingo, V., Fleck, B., & Poland, A. I. 1995, *Solar Phys.*,, 162, 1

Drake, J. F. 1971, *Solar Phys.*,, 16, 152

Fleck, B., Couvidat, S., & Straus, T. 2011, *Solar Phys.*,, 271, 27

Fletcher, L., Dennis, B. R., Hudson, H. S., et al. 2011, *Space Sci. Rev.*,, 159, 19

Forbes, T. G. 2000, *J. Geophys. Res.*,, 105, 23153

Gallagher, P. T. & Long, D. M. 2011, *Space Sci. Rev.*,, 158, 365

Galvin, A. B., Kistler, L. M., Popecki, M. A., et al. 2008, *Space Sci. Rev.*,, 136, 437

Gibson, S. E., Foster, D., Burkepile, J., de Toma, G., & Stanger, A. 2006, *Astrophys. J.*,, 641, 590

Gilbert, H. R., Holzer, T. E., Burkepile, J. T., & Hundhausen, A. J. 2000, *Astrophys. J.*,, 537, 503

Golub, L. 1996, *Astrophys. Space Sci.*,, 237, 33

Golub, L., Deluca, E., Austin, G., et al. 2007, *Solar Phys.*,, 243, 63

Golub, L., Deluca, E. E., Sette, A., & Weber, M. 2004, in Astronomical Society of the Pacific Conference Series, Vol. 325, The Solar-B Mission and the Forefront of Solar Physics, ed. T. Sakurai & T. Sekii, 217

Golub, L., Krieger, A. S., Silk, J. K., Timothy, A. F., & Vaiana, G. S. 1974, *Astrophys. J. L.*,, 189, L93+

Gopalswamy, N. 2006, Journal of Astrophysics and Astronomy, 27, 243

Grevesse, N. & Sauval, A. J. 1998, Space Science Reviews, 85, 161

Habbal, S. R. & Withbroe, G. L. 1981, *Solar Phys.*,, 69, 77

Habbal, S. R., Withbroe, G. L., & Dowdy, Jr., J. F. 1990, *Astrophys. J.*,, 352, 333

Handy, B. N., Acton, L. W., Kankelborg, C. C., et al. 1999, *Solar Phys.*,, 187, 229

Harvey, K. L. 1985, Australian Journal of Physics, 38, 875

Harvey, K. L., Strong, K. S., Nitta, N., & Tsuneta, S. 1994, in Astronomical Society of the Pacific Conference Series, Vol. 68, Solar Active Region Evolution: Comparing Models with Observations, ed. K. S. Balasubramaniam & G. W. Simon, 377–+

Haugan, S. V. H. 1997, The Component Fitting System (CFIT) for IDL, CDS software note no. 47, Tech. rep.

Hirayama, T. 1974, *Solar Phys.*,, 34, 323

Hood, A. W. & Priest, E. R. 1981, Geophysical and Astrophysical Fluid Dynamics, 17, 297

Howard, R. A., Moses, J. D., Vourlidas, A., et al. 2008, *Space Sci. Rev.*,, 136, 67

Hudson, H. S. 1991, *Solar Phys.*,, 133, 357

Hyder, C. L. & Lites, B. W. 1970, *Solar Phys.*,, 14, 147

Isobe, H. & Tripathi, D. 2006, *Astron. Astrophys.*,, 449, L17

Jordan, C., Ayres, T. R., Brown, A., Linsky, J. L., & Simon, T. 1987, *Mon. Not. Roy. Astron. Soc.*,, 225, 903

Judge, P. G. 2010, *Memorie della Societ Astronomica Italiana*, 81, 543

Kankelborg, C. C., Walker, II, A. B. C., Hoover, R. B., & Barbee, Jr., T. W. 1996, *Astrophys. J.*,, 466, 529

Kashyap, V. & Drake, J. J. 1998, *Astrophys. J.*,, 503, 450

Klimchuk, J. A. 2006, *Solar Phys.*,, 234, 41

Klimchuk, J. A. 2009, in Astronomical Society of the Pacific Conference Series, Vol. 415, The Second Hinode Science Meeting: Beyond Discovery-Toward Understanding, ed. B. Lites, M. Cheung, T. Magara, J. Mariska, & K. Reeves, 221–+

Klimchuk, J. A. & Cargill, P. J. 2001, *Astrophys. J.*,, 553, 440

Kopp, R. A. & Pneuman, G. W. 1976, *Solar Phys.*,, 50, 85

Kosugi, T., Matsuzaki, K., Sakao, T., et al. 2007, *Solar Phys.*,, 243, 3

Krieger, A. S., Timothy, A. F., & Roelof, E. C. 1973, *Solar Phys.*,, 29, 505

Kuperus, M. & Raadu, M. A. 1974, *Astron. Astrophys.*,, 31, 189

Labrosse, N., Heinzel, P., Vial, J.-C., et al. 2010, *Space Sci. Rev.*,, 151, 243

Labrosse, N. & McGlinchey, K. 2011, ArXiv e-prints

Landi, E., Del Zanna, G., Young, P. R., Dere, K. P., & Mason, H. E. 2012a, *Astrophys. J.*,, 744, 99

Landi, E., Del Zanna, G., Young, P. R., et al. 2006, *Astrophys. J. S.*,, 162, 261

Landi, E., Miralles, M. P., Curdt, W., & Hara, H. 2009, *Astrophys. J.*,, 695, 221

Landi, E., Reale, F., & Testa, P. 2012b, *Astron. Astrophys.*,, 538, A111

Leighton, R. B. 1964, *Astrophys. J.*,, 140, 1547

Leighton, R. B., Noyes, R. W., & Simon, G. W. 1962, *Astrophys. J.*,, 135, 474

Lemen, J. R., Title, A. M., Akin, D. J., et al. 2012a, *Solar Phys.*,, 275, 17

Lemen, J. R., Title, A. M., Akin, D. J., et al. 2012b, *Solar Phys.*,, 275, 17

Lin, Y., Engvold, O., Rouppe van der Voort, L., Wiik, J. E., & Berger, T. E. 2005, *Solar Phys.*,, 226, 239

Longcope, D. W. 1998, *Astrophys. J.*,, 507, 433

Longcope, D. W. 2005, *Living Reviews in Solar Physics*, 2, 7

Longcope, D. W. & Klapper, I. 2002, *Astrophys. J.*,, 579, 468

Luhmann, J. G., Curtis, D. W., Schroeder, P., et al. 2008, *Space Sci. Rev.*,, 136, 117

Mackay, D. H., Gaizauskas, V., & Yeates, A. R. 2008, *Solar Phys.*,, 248, 51

Mackay, D. H., Karpen, J. T., Ballester, J. L., Schmieder, B., & Aulanier, G. 2010, *Space Sci. Rev.*,, 151, 333

Madjarska, M. S., Doyle, J. G., Teriaca, L., & Banerjee, D. 2003, *Astron. Astrophys.*, 398, 775

Marsh, M. S., Walsh, R. W., & Bromage, B. J. I. 2002, *Astron. Astrophys.*, 393, 649

Marsh, M. S., Walsh, R. W., De Moortel, I., & Ireland, J. 2003, *Astron. Astrophys.*, 404, L37

Mazzotta, P., Mazzitelli, G., Colafrancesco, S., & Vittorio, N. 1998, *Astron. Astrophys. Suppl.*, 133, 403

Miesch, M. S. 2005, Living Reviews in Solar Physics, 2, 1

Moore, R. L., Sterling, A. C., Hudson, H. S., & Lemen, J. R. 2001, *Astrophys. J.*, 552, 833

Moreton, G. E. & Ramsey, H. E. 1960, *Pub. Astron. Soc. Pac.*, 72, 357

Munro, R. H., Gosling, J. T., Hildner, E., et al. 1979, *Solar Phys.*, 61, 201

Narukage, N., Tsuneta, S., Bando, T., et al. 2011, in Society of Photo-Optical Instrumentation Engineers (SPIE) Conference Series, Vol. 8148, Society of Photo-Optical Instrumentation Engineers (SPIE) Conference Series

Noci, G. 2003, *Memorie della Societ Astronomica Italiana*, 74, 704

Noglik, J. B. & Walsh, R. W. 2007, *Astrophys. J.*, 655, 1127

Nolte, J. T., Solodyna, C. V., & Gerassimenko, M. 1979, *Solar Phys.*, 63, 113

Norton, A. A., Graham, J. P., Ulrich, R. K., et al. 2006, *Solar Phys.*, 239, 69

O'Dwyer, B., Del Zanna, G., Mason, H. E., Weber, M. A., & Tripathi, D. 2010, *Astron. Astrophys.*, 521, A21+

Parker, E. N. 1988, *Astrophys. J.*, 330, 474

Parnell, C. E., Priest, E. R., & Golub, L. 1994, *Solar Phys.*, 151, 57

Parnell, C. E., Smith, J. M., Neukirch, T., & Priest, E. R. 1996, *Physics of Plasmas*, 3, 759

Patsourakos, S. & Vourlidas, A. 2009, *Astrophys. J. L.*,, 700, L182

Patsourakos, S., Vourlidas, A., & Stenborg, G. 2010, *Astrophys. J. L.*,, 724, L188

Pérez-Suárez, D., Maclean, R. C., Doyle, J. G., & Madjarska, M. S. 2008, *Astron. Astrophys.*,, 492, 575

Peter, H. 2001, *Astron. Astrophys.*,, 374, 1108

Plowman, J., Kankelborg, C., Martens, P., et al. 2012, ArXiv e-prints

Priest, E. R., Foley, C. R., Heyvaerts, J., et al. 2000, *Astrophys. J.*,, 539, 1002

Priest, E. R., Longcope, D. W., & Heyvaerts, J. 2005, *Astrophys. J.*,, 624, 1057

Priest, E. R., Parnell, C. E., & Martin, S. F. 1994, *Astrophys. J.*,, 427, 459

Reale, F. 2010, Living Reviews in Solar Physics, 7, 5

Reale, F. & Peres, G. 2000, *Astrophys. J. L.*,, 528, L45

Reale, F., Peres, G., Serio, S., DeLuca, E. E., & Golub, L. 2000, *Astrophys. J.*,, 535, 412

Reale, F., Testa, P., Klimchuk, J. A., & Parenti, S. 2009, *Astrophys. J.*,, 698, 756

Régnier, S., Walsh, R. W., & Alexander, C. E. 2011, *Astron. Astrophys.*,, 533, L1

Sarkar, A. & Walsh, R. W. 2008, *Astrophys. J.*,, 683, 516

Sarkar, A. & Walsh, R. W. 2009, *Astrophys. J.*,, 699, 1480

Scherrer, P. H., Bogart, R. S., Bush, R. I., et al. 1995, *Solar Phys.*,, 162, 129

Scherrer, P. H., Schou, J., Bush, R. I., et al. 2012, *Solar Phys.*,, 275, 207

Schmelz, J. T., Kashyap, V. L., Saar, S. H., et al. 2009a, *Astrophys. J.*,, 704, 863

Schmelz, J. T., Kashyap, V. L., & Weber, M. A. 2007, *Astrophys. J. L.*,, 660, L157

Schmelz, J. T., Saar, S. H., DeLuca, E. E., et al. 2009b, *Astrophys. J. L.*,, 693, L131

Schrijver, C. J. 2001, *Solar Phys.*,, 198, 325

Schrijver, C. J., Elmore, C., Kliem, B., Török, T., & Title, A. M. 2008, *Astrophys. J.*,, 674, 586

Schrijver, C. J. & Title, A. M. 2011, Journal of Geophysical Research (Space Physics), 116, 4108

Seaton, D. B., Mierla, M., Berghmans, D., Zhukov, A. N., & Dolla, L. 2011, *Astrophys. J. L.*,, 727, L10+

Shibata, K. 1999, *Astrophys. Space Sci.*,, 264, 129

Solanki, S. K. 1998, *Space Sci. Rev.*,, 85, 175

Sterling, A. C. & Moore, R. L. 2003, *Astrophys. J.*,, 599, 1418

Sturrock, P. A. 1966, *Nature*,, 211, 695

Tandberg-Hanssen, E., ed. 1995, Astrophysics and Space Science Library, Vol. 199, The nature of solar prominences

Taroyan, Y., Bradshaw, S. J., & Doyle, J. G. 2006, *Astron. Astrophys.*,, 446, 315

Testa, P. & Reale, F. 2012, *Astrophys. J. L.*,, 750, L10

Thompson, B. J., Plunkett, S. P., Gurman, J. B., et al. 1998, *Geophys. Res. Lett.*,, 25, 2465

Tian, H., Curdt, W., Marsch, E., & He, J. 2008, *Astrophys. J. L.*,, 681, L121

Török, T. & Kliem, B. 2004, in ESA Special Publication, Vol. 575, SOHO 15 Coronal Heating, ed. R. W. Walsh, J. Ireland, D. Danesy, & B. Fleck, 56

Török, T. & Kliem, B. 2005, *Astrophys. J. L.*,, 630, L97

Tripathi, D., Klimchuk, J. A., & Mason, H. E. 2011, *Astrophys. J.*,, 740, 111

Tripathi, D., Mason, H. E., Dwivedi, B. N., del Zanna, G., & Young, P. R. 2009, *Astrophys. J.*,, 694, 1256

Tripathi, D., Mason, H. E., Young, P. R., & Del Zanna, G. 2008, *Astron. Astrophys.*,, 481, L53

Tsuneta, S., Ichimoto, K., Katsukawa, Y., et al. 2008, *Solar Phys.*,, 249, 167

Tsurutani, B. T., Mannucci, A. J., Iijima, B., et al. 2006, Advances in Space Research, 37, 1583

Ugarte-Urra, I. 2004, PhD thesis, AA(Armagh Observatory, College Hill, Armagh BT61 9DG, N. Ireland, UK.)

Ugarte-Urra, I., Doyle, J. G., Walsh, R. W., & Madjarska, M. S. 2005, *Astron. Astrophys.*,, 439, 351

Ugarte-Urra, I., Winebarger, A. R., & Warren, H. P. 2006, *Astrophys. J.*,, 643, 1245

Vaiana, G. S., Davis, J. M., Giacconi, R., et al. 1973a, *Astrophys. J. L.*,, 185, L47

Vaiana, G. S., Krieger, A. S., & Timothy, A. F. 1973b, *Solar Phys.*,, 32, 81

Vaiana, G. S., Speybroeck, L. P., & Krieger, A. S. 1970, Bulletin of the American Physical Society, 15, 611

Viall, N. M. & Klimchuk, J. A. 2011, *Astrophys. J.*,, 738, 24

Wagner, W. J. 1984, *Annual review of astronomy and astrophysics*, 22, 267

Walsh, R. W., Bell, G. E., & Hood, A. W. 1997, *Solar Phys.*,, 171, 81

Wang, Y.-M., Hawley, S. H., & Sheeley, Jr., N. R. 1996, Science, Volume 271, Issue 5248, pp. 464-469, 271, 464

Warren, H. P., Brooks, D. H., & Winebarger, A. R. 2011, *Astrophys. J.*,, 734, 90

Warren, H. P., Ugarte-Urra, I., Doschek, G. A., Brooks, D. H., & Williams, D. R. 2008, *Astrophys. J. L.*,, 686, L131

Webb, D. F. & Hundhausen, A. J. 1987, *Solar Phys.*,, 108, 383

Weber, M. A., Deluca, E. E., Golub, L., & Sette, A. L. 2004, in IAU Symposium, Vol. 223, Multi-Wavelength Investigations of Solar Activity, ed. A. V. Stepanov, E. E. Benevolenskaya, & A. G. Kosovichev, 321–328

Welsch, B. T., Fisher, G. H., Abbett, W. P., & Régnier, S. 2004, *Astrophys. J.*,, 610, 1148

Williams, D. R., Török, T., Démoulin, P., van Driel-Gesztelyi, L., & Kliem, B. 2005, *Astrophys. J. L.*,, 628, L163

Wills-Davey, M. J. & Attrill, G. D. R. 2009, *Space Sci. Rev.*,, 149, 325

Winebarger, A. R. & Warren, H. P. 2004, *Astrophys. J. L.*,, 610, L129

Winebarger, A. R., Warren, H. P., & Mariska, J. T. 2003a, *Astrophys. J.*,, 587, 439

Winebarger, A. R., Warren, H. P., Schmelz, J. T., et al. 2012, *Astrophys. J. L.*,, 746, L17

Winebarger, A. R., Warren, H. P., & Seaton, D. B. 2003b, *Astrophys. J.*,, 593, 1164

Wolfson, R. & Dlamini, B. 1997, *Astrophys. J.*,, 483, 961

Wolfson, R. & Saran, S. 1998, *Astrophys. J.*,, 499, 496

Woods, T. N., Eparvier, F. G., Hock, R., et al. 2012, *Solar Phys.*,, 275, 115

Wuelser, J.-P., Lemen, J. R., Tarbell, T. D., et al. 2004, in Society of Photo-Optical Instrumentation Engineers (SPIE) Conference Series, Vol. 5171, Society of Photo-Optical Instrumentation Engineers (SPIE) Conference Series, ed. S. Fineschi & M. A. Gummin, 111–122

Yang, S. H., Zhang, J., Jin, C. L., Li, L. P., & Duan, H. Y. 2009, *Astron. Astrophys.*,, 501, 745

Young, P. R., Del Zanna, G., Mason, H. E., et al. 2007, *Pub. Astron. Soc. Japan,*, 59, 727

Young, P. R. & Landi, E. 2009, *Astrophys. J.,*, 707, 173